

GRAPHENATED POLYANILINE NANOCOMPOSITE FOR THE DETERMINATION OF
POLYAROMATIC HYDROCARBONS (PAHs) IN WATER



By

OLUWAKEMI OMOTUNDE TOVIDE

A thesis submitted in fulfilment of the requirement for the degree of Philosophiae Doctor in
the Department of Chemistry, University of the Western Cape, South Africa.

UNIVERSITY of the
WES Supervisor CAPE

Professor Emmanuel I. Iwuoha

Co-supervisors

Dr Jahed Nazeem

Professor Priscilla G. Baker

November, 2013.

KEYWORDS

Graphenated Polyaniline Nanocomposite for the Determination of Polyaromatic Hydrocarbons (PAHs) in Water

Oluwakemi Omotunde Tovide

Keywords

Graphenated-polyaniline

Graphene

Polyaniline

Metal oxide

Nanocomposite

Polyaromatic hydrocarbons

Persistent organic pollutants

Wastewater

Electrocatalyst

Cyclic voltammetry

Glassy Carbon Electrode

Electrochemical sensor



ABSTRACT

Graphenated polyaniline nanocomposite for the determination of (PAHs) in water

O.O. Tovide

PhD Thesis, Department of Chemistry, University of the Western Cape, November 2013.

The thesis presents a simple, sensitive, low cost and a novel graphenated polyaniline doped tungsten trioxide nanocomposite, as an electrochemical sensor for the detection and quantitative and determination of PAHs, which are ubiquitous, toxic, as well as dangerous organic pollutant compounds in the environment. The selected PAHs (anthracene, phenanthrene and pyrene) in wastewater were given priority as a result of their threat to human nature and that of the environment. In order for a healthy, non-polluted and well sustainable environment, there is need for an instrument that is capable of detecting and quantifying these organic pollutants onsite and also for constant monitoring. The nanocomposites were developed by chemical and electrochemical methods of preparations, exploiting the intrinsic properties of polyaniline, graphene and tungsten trioxide semiconducting materials. Chemically, graphene-polyaniline (GR-PANI) nanocomposite was synthesised by in situ polymerisation method, then casted on a surface of glassy carbon electrode to form GR-PANI modified electrode. The properties of the prepared electrode were investigated through morphological and spectroscopic techniques, which confirmed the formation of the composite. The electroactivity of the prepared modified electrode revealed great improvement in cyclic and square wave voltammetric response on anthracene. A dynamic range of 2.0×10^{-5} to 1.0×10^{-3} M and detection limit of 4.39×10^{-7} M was established.

The electrochemical method involves electrochemical deposition of mixture of tungsten trioxide and aniline monomer onto the surface of a graphene modified electrode, to form a composite of graphenated polyaniline doped tungsten trioxide (PANI|WO₃|GR) and then used as an electrocatalyst on a glassy carbon electrode. Morphological and spectroscopic characterisations such as Fourier transform infrared spectroscopy (FT-IR), RAMAN, Scanning electron microscopy (SEM), Transmission electron microscopy (TEM), Atomic force microscopy (AFM) and Ultra violet visible (UV-vis) spectroscopy confirmed the successful synthesis of graphene, polyaniline and the doped polyaniline film with tungsten trioxide as well as their intercalation with graphene thin film. The properties of the prepared films were also investigated by electrochemical methods. The cyclic and square wave voltammetric results revealed the electrocatalytic activities of the PANI|WO₃|GR sensor towards the oxidation of phenanthrene, anthracene and pyrene. The limit of detection for phenanthrene was 0.123 pM (1.23×10^{-4} nM) over a dynamic range of 1.0 to 6.0 pM. A dynamic linear range of 1.0 to 10.0 pM was attained with a limit of detection of 0.136 pM (1.36×10^{-4} nM) for anthracene. Pyrene gave a limit of detection of 0.132 pM (1.32×10^{-4} nM) over a linear dynamic range of 1.0 to 10.0 pM. The PANI|WO₃|GR sensor showed an excellent sensitivity, reproducibility and long-term stability to the various PAHs studied and the limit of detection (LOD) determined were comparable with WHO standards and specification for PAHs which is 1.12 nM (1120 pM) in water. This study offered a new technology that can be useful in real time determination of PAHs.

DECLARATION

I declare that the *Electrochemical response of novel graphenated polyaniline nanocomposite for the determination of polyaromatic hydrocarbons* is my work, that it has not been submitted for any degree or examination in any other University, and that all sources I have used or quoted have been indicated and acknowledged by means of complete references.



Oluwakemi Omotunde Tovide

November 2013.

Signature-----

ACKNOWLEDGEMENT

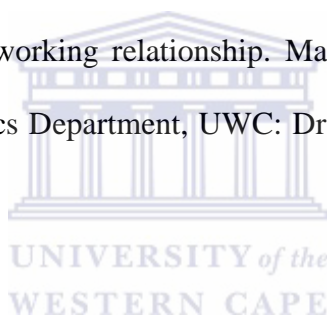
First and foremost I offer my sincerest gratitude to Almighty God. I give Him all the glory, honour and adoration for seeing me through this journey, giving the strength and wisdom through the Holy Spirit and letting me know that it is never too late to become a Doctor.

I owe my deepest and immense gratitude to my supervisor Professor Emmanuel I. Iwuoha whom God has blessed me with and has chosen to be my Angel on guard and guidance, for his mentorship throughout the journey and making me to believe in myself that I can do it. I will forever be grateful for your kindness. Goethe said, “Treat people as if they were what they ought to be and you help them to become what they are capable of being.” You have treated me as though I were capable of reaching the stars. Because of you, I have. ‘You are Awesome indeed’. My gratitude also goes to the most intelligent and adorable mother I have ever come across, Professor Priscilla G. Baker, you have been so wonderful to me. And Dr. Nazeem Jahed, thank you for being there to cheer and to guide. Thank you all for your support, encouragement and excellent supervision throughout the research time.

I acknowledge the help of our senior researcher, Dr. Tesfaye Waryo, for his academic support and relentless effort in making sure that every material needed was at my disposal throughout the research period. Special thanks to Dr. Stephen Mailu for his encouragement during my challenging moments of the research work and for his assistance during my writing of the thesis. I say thank you from the bottom of my heart for your help and support.

To my friends, colleagues and loved ones in SensorLab: Dr. Fanelwa Ajayi, Dr. Chinwe, Mr. Nuralli Mohamed, Dr. Natasha Ross, Dr. Masikini Milua, Dr. Abebaw Tsegaye, Christopher Sunday, Olubunmi Omoyeni, Lundi Ngqongwa, Bilibana Mawethu, Hlamulo Makelani, Gcineka Mbambisa, Euodia Hess, Godfrey Fuku, Busiswa Matyholo, Noluthando Mayedwa, Lindsay Wilson, Candice Rassie, Gertrude Fomo, Samantha Fiona, Unathi Gcilitshana, Salma Zbeda, Lindsay Wilson, Sara Ibrahim and K.W. Pokpas. SensorLab MSc students, Nanoscience students, SensorLab PhD students that I did not remember to mention and all Post doctoral fellows in SensorLab, you are all gratefully acknowledged.

All members of the Chemistry Department, University of the Western Cape, South Africa, I say thank you for your cordial working relationship. Many thanks to the members of the Electron Microscope Unit, Physics Department, UWC: Dr. Subelia and Mr. Adrian for their help in analyzing my samples.



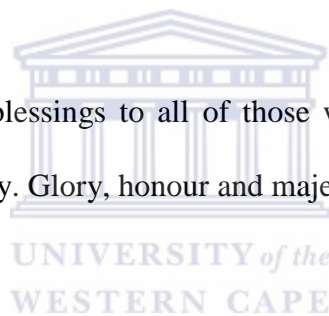
It is with profound gratitude that I acknowledge the following people: All members of the Celestial Church of Christ, Iba Parish 1, Nigeria, all members of the Celestial Church of Christ, mercy of the Lord Parish, South Africa, all ministers and members of the Redeemed Christian Church of God, Household of God Parish, South Africa, for their support and prayers throughout my journey.

To all my colleagues and friends from Lagos State University: Dr. Morunke Saibu, your contribution in making this dream come true is wholeheartedly appreciated, My daddy in the Lord and mentor, Dr. John Alegbe, you are a gem. Dr. Wale Olowu, Dr. Olusola Ademola,

Dr. Tony Ojekale, Dr. Albert Amosu, Sunday Vodah, I sincerely appreciate your support.
Thank you.

I give my profound gratitude to all my family members especially my loving husband Superior Evangelist Michael Mautin Tovide for your patience, encouragement and constant prayers. My mother Muyinat Abiodun Lawal, thank you so much for your love and constant prayers throughout my journey. To all my children, for their patience and endurance during my absence studying for this degree, you all have made living worthwhile and I missed you a great lot. To all my siblings, family friends, both in Nigeria and South Africa, a big thank you for your love and care.

Lastly, I offer my regards and blessings to all of those who supported me in any respect during the completion of my study. Glory, honour and majesty are unto God for his greatness.
Thank you Lord Jesus.



DEDICATION

I dedicate this thesis to

Almighty God,

My mother,

My darling husband

Michael Mautin Tovide

And

My Family



UNIVERSITY *of the*
WESTERN CAPE

ACADEMIC OUTPUTS

1. **Oluwakemi Tovide**, Nazeem Jaheed, Nurali Mohamed et al and Emmanuel I. Iwuoha. Graphenated polyaniline-doped tungsten oxide nanocomposite sensor for real time determination of phenanthrene. *ElectrochimicaActa* (in press).
2. **Oluwakemi Tovide**, Nazeem Jahed, Nurali Mohammed et al. and Emmanuel Iwuoha. Electrochemical response transductions of graphenated-polyaniline nanosensor for environmental anthracene. *Advances in Biological, Ecological and Environmental Sciences, and Engineering* (in press).
3. Njagi Njomo, Tesfaye Waryo, Milua Masikini, Chinwe O. Ikpo, Stephen Mailu, Gcineka Mbambisa, **Oluwakemi Tovide** et al. and Emmanuel I. Iwuoha. Graphenated Ta(IV)O and poly(4-styrene sulphonic acid) doped polyaniline nanocomposite as cathode material in an electrochemical capacitor. *ElectrochimicaActa* (in press).
4. Christopher E. Sunday, Mawethu Bilibana, **Oluwakemi Tovide** et al. and Emmanuel Iwuoha. Modulation of the matrix effect of nafion on tris(bipyridine)ruthenium(II) electrochemical probes by functionalization with 4-nitrophenyl azographene-gold nanocomposite. *ElectrochimicaActa* (in press).

PRESENTATIONS

Oluwakemi O.Tovide, Priscilla G. Baker and Emmanuel I. Iwuoha, Graphenated polyaniline nanosensor systems for real time determination of persistent organic pollutants (POPs) in wastewater for 2nd International Symposium on Electrochemistry: Electrochemistry for

Energy at the University of the Western Cape, Bellville, South African from 19-20th July, 2012 (ElectroChemSA 2012) (oral).

Oluwakemi O.Tovide, Priscilla G. Baker and Emmanuel I. Iwuoha, Graphenated polyaniline nanosensor systems for real time Determination of polyaromatic hydrocarbons, 13th Tropical Meeting of the International Society of Electrochemistry at the International Convent Centre of the Council for Scientific and Industrial Research (CSIR ICC), Pretoria, South Africa, from April 7th to 11th 2013 (poster).



TABLE OF CONTENT

KEYWORDS.....	ii
ABSTRACT.....	iii
DECLARATION	v
ACKNOWLEDGEMENT	vi
DEDICATION.....	ix
ACADEMIC OUTPUT	x
TABLE OF CONTENT.....	xii
LIST OF FIGURES	xxix
LIST OF TABLES	xxix
LIST OF SCHEMES.....	xxx
LIST OF ABBREVIATIONS.....	xxxi
CHAPTER ONE.....	1
INTRODUCTION	1
1.1. Background.....	1
1.2. Problem statement.....	3
1.3. Rationale and motivation.....	4
1.4. Research aim and objectives.....	6
1.4.1. AIM.....	6
1.4.2. Objective of the study includes:	6
1.5. Research framework.....	6
1.6. Thesis statement.....	7
CHAPTER TWO	8
LITRATURE REVIEW	8
2.1. Wastewater.....	8
2.1.2. Persistent organic pollutants (POPs).....	11



2.2. Polyaromatic hydrocarbons.....	12
2.2.1. Formation and characteristics of PAHs.....	13
2.2.2. Toxicity: exposure and carcinogenicity of PAHs	16
2.2.2.1. Exposure	16
2.2.2.2. Toxicity and Carcinogenicity.....	17
2.2.3. Occurrence, sources and distribution in the environment.....	17
2.2.3.1. Natural sources.....	18
2.2.3.2. Anthropogenic sources.....	18
2.2.3.3. PAHs in sources to the aquatic environment	19
2.2.3.4. Distribution of PAHs in sources to the Marine environment.....	21
2.2.3.5. Point sources	21
2.2.3.6. Distribution of PAH in Marine water.....	22
2.2.3.7. Distribution of PAH in Marine sediments	22
2.3. Characterisation of the monitored PAHs.....	23
2.3.1. Anthracene (ATN)	23
2.3.2. Phenanthrene (PHE).....	24
2.3.3. Pyrene (PYR).....	26
2.4. Method of detection of polyaromatic hydrocarbon (PAHs).....	27
2.5. Conducting polymers (Intrinsically conducting polymers, ICP)	28
2.5.1. Conductivity in conducting polymer	31
2.5.2. Polarons	32
2.5.3. Bipolarons	34
2.5.4. Solitons.....	34
2.6. Synthesis of polymer.....	38
2.6.1. Chemical oxidative polymerisation.....	40
2.6.2. Electrochemical polymerisation.....	42
2.7. Polyaniline.....	44
2.7.1. Structure and oxidation state of polyaniline	44
2.7.2. Conductivity in polyaniline.....	47

2.7.3. Synthesis of polyaniline	49
2.7.8. Doping in polyaniline	52
2.8. Nanocomposite	52
2.8.1. Polymer nanocomposites	53
2.8.2. Methods of preparation of polymer nanocomposite	58
2.9. Graphene	58
2.9.1. Properties of graphene	62
2.9.2. Methods of graphene synthesis.....	67
2.9.2.1. Mechanical exfoliation and cleavage	67
2.9.2.2. Epitaxial growth on silicon carbide.....	69
2.9.2.3. Chemical vapour deposition (CVD).....	69
2.9.2.4. Chemically derived graphene.....	70
2.9.3. Graphene based composites	75
2.9.3.1. Polymer-graphene based nanocomposite.....	75
2.10. Tungsten trioxide	80
2.11. Sensor and sensor devices	82
2.11.1. Chemiresistor or conductometric sensors.....	85
2.11.2. Potentiometric sensor	85
2.11.3. Amperometric/Voltammetric sensors	87
2.11.4. Electroanalytical techniques	88
2.11.4.1. Voltammetry	88
2.11.4.2. Instrumentation	89
2.11.4.2.1. The potentiostat.....	91
2.11.4.2.2. Electrochemical cell and electrodes	91
2.11.4.2.3. Electrodes.....	91
2.11.4.2.4. The reference electrode (RE)	92
2.11.4.2.5. Counter electrode (CE)	92
2.11.4.2.6. Working electrode (WE).....	92
2.11.4.3. Cyclic voltammetry	93
2.11.4.4. Square wave voltammetry (SWV)	100

2.11.4.5. Electrocatalysis	101
2.11.4.6. Chemically modified electrode	103
2.11.5. Electrochemical impedance spectroscopy (EIS).....	106
2.11.5.1. Bode plot.....	110
2.11.5.2. Equivalent electrical circuit	112
2.11.5.2.1. Solution resistance (R_s)	114
2.11.5.2.2. Charge transfer resistance (R_{ct}).....	114
2.11.5.2.3. Warburg impedance	115
2.11.5.2.4. Coating capacitance	117
2.11.5.2.5. Constant phase element (CPE).....	117
2.11.5.2.6. EIS characterisation of a polymer thin film	118
2.11.5.2.7. Impedance modelling using equivalent electrical circuit.....	119
2.11.6 Microscopy and Spectroscopy techniques	122
2.11.6.1. Ultraviolet-visible (UV-vis) spectroscopy	122
2.11.6.2. Fourier transforms infrared spectroscopy (FT-IR).....	124
2.11.6.3. Raman spectroscopy	125
2.11.6.4. Atomic force microscopy (AFM).....	127
2.11.6.5. X-ray diffraction (XRD)	129
2.11.6.6. High Resolution Transmission Electron Microscopy (HR-TEM)	130
2.11.6.7. High resolution scanning electron microscope (HR-SEM).....	132
CHAPTER THREE	134
MATERIALS AND METHODS.....	134
Introduction.....	134
3.1 Reagents.....	134
3.2. Measurements and instrumentations	135
3.3 Preparation of materials	136
3.3.1. Synthesis of graphite oxide	136
3.3.2. Preparation of graphene	137
3.3.3. Preparation of polyaniline by chemical polymerisation	139
3.3.4. Preparation of graphene-polyaniline nanocomposite (GR-PANI).....	139

3.3.5. Preparation of the graphene polyaniline modified electrode	141
3.3.6. Preparation of polyaniline-tungsten oxide-graphene film (PANI WO ₃ GR)	141
3.3.6.1. Optimisation of the PANI film.....	141
3.3.6.2. Optimisation of hydrogen peroxide	142
3.3.6.3. Preparation of polyaniline-tungsten oxide-graphene film.....	142
3.4. Characterisation of graphene-polyaniline (GR-PANI) modified electrode and Polyaniline–tungsten oxide–graphene (PANI WO ₃ GR) nanocomposite	144
3.4.1. Electrochemical characterisation.....	144
3.4.1.1. Cyclic voltammetry (CV).....	144
3.4.1.2. Electrochemical impedance spectroscopy (EIS)	144
3.5. Morphological characterisation	144
3.6. Application of the GR-PANI modified electrode as sensor on anthracene.....	144
3.7. Application of polyaniline–tungsten oxide-graphene nanocomposite as polyaromatic hydrocarbon nanosensor	145
3.7.1. Choice of electrolyte	145
3.7.2. Preparation and determination of PAHs.....	146
3.7.2. Interferences, stability and reproducibility studies	146
CHAPTER FOUR.....	148
RESULTS AND DISCUSSION-PART 1	148
4.1. Introduction	148
4.2.2. High resolution transmission electron microscopy (HRTEM)	151
4.2.3. Fourier Transform InfraRed (FT-IR).....	152
4.2.4. Atomic force microscopy (AFM)	153
4.2.5. X-ray diffraction (XRD)	154
4.2.6. Raman spectroscopy.....	155
4.2.7. UV –Vis spectroscopy.....	157
CHAPTER FIVE	158
RESULTS AND DISCUSSION-part 2	158
5.1. Introduction	158

5.2. Characterisation of graphene-polyaniline (GR-PANI) nanocomposite	159
5.2.1. Cyclic voltammetry.....	159
5.2.2. Scan rate dependence of the modified electrode	161
5.3. Morphology and spectroscopic characterisation	163
5.3.1. Electrochemical Impedance Spectroscopy (EIS) of GR-PANI GCE.....	163
5.3.2. Scanning electron microscopy (SEM).....	166
5.3.3. High resolution transmittance electron microscopy (HR-TEM)	166
5.3.4. Fourier transmission infrared (FT-IR).....	168
5.3.5. X-ray diffraction (XRD)	170
5.4. Response of modified electrode on anthracene	171
5.4.1. Electrochemical Application of the modified GR-PANI electrode for anthracene Detection	172
5.4.1.1. Electrochemical behaviour of the modified electrodes	172
5.4.1.2. Effect of scan rate	174
5.4.1.3. Analytical application of the modified electrode	175
5.5. Interferences, stability and reproducibility studies	175
CHAPTER SIX.....	180
RESULT AND DISCUSSION-part 3.....	180
6.1. Introduction	180
6.2. Spectroscopic and morphology characterisation	181
6.2.1. UV-visible spectroscopy	181
6.2.2. High resolution scanning electron spectroscopy	183
6.2.3. High resolution transmission electron microscopy (HRTEM)	186
6.2.4. Raman micro spectroscopy	188
6.3. Electrochemical characterisation of the modified film on glassy electrode.....	190
6.3.1. Results of the optimised parameters.....	190
6.3.1.1. Characterisation of the PANI electrode for optimisation.....	190
6.3.1.2. Optimisation of hydrogen peroxide concentration for WO ₃ synthesis.....	195

6.3. Electrochemical Characterisation of PANI WO ₃ GR electrode.....	197
6.3.1. Cyclic voltammetry of PANI WO ₃ GR electrode in HCl.....	201
6.4. Electrochemical Impedance Spectroscopy (EIS) of PANI WO ₃ GR GCE.....	202
6.5. Electrochemical Application of the modified PANI WO ₃ GR electrode on some polyaromatic hydrocarbons (PAHs).....	204
6.5.1. Electrocatalytic oxidation of phenanthrene	204
6.5.1.1. Effect of scan rate	206
6.5.1.2. Cyclic voltammetry response at different concentration of phenanthrene.....	207
6.5.2. Reproducibility, stability and interference studies	209
6.5.3. Electrochemical responses of the PANI WO ₃ GR GCE anthracene sensor.....	210
6.5.3.1. Effect of scan rate	212
6.5.3.2. Cyclic voltammetry response at different concentration of anthracene.....	214
6.5.4. Reproducibility, stability and interference studies.....	219
6.5.5. Electrocatalytic oxidation of pyrene (PYR).....	219
6.5.5.1. Effect of scan rate	221
6.5.5.2. Cyclic voltammetry response of different concentration of pyrene.....	222
6.5.6. Reproducibility, stability and interference studies.....	226
CHAPTER SEVEN	227
CONCLUSIONS AND RECOMMENDATIONS	227
7.1. Conclusion.....	227
7.2. Future work and Recommendation	230
References.....	231

LIST OF FIGURES

Figure 1. Extraction of water and reused along the supply chain (a) and a typical example of wastewater discharge directly into the water bodies from a source point (b).....	10
Figure 2. The chemical structure of some of the 16 PAHs listed as priority.....	14
Figure 3. Structure of Anthracene.....	23
Figure 4. Structure of Phenanthrene.....	24
Figure 5. Structure of Pyrene.....	26
Figure 6. Overview of some applications of conducting polymers.....	30
Figure 7. Distorted geometry of the excited state (lattice relaxation) results in a reduction of the ionization potential ΔIP (i), accommodation of charged within two ‘polaron’ states within the semiconductor gap (ii) (a) and A geometry representation of (i) a single polaron [radical ion coupled to a lattice distortion, having spin $1/2$, charged $\pm e$ and (ii) a doubly charged bipolaron [spinless di-ion coupled to a lattice distortion], having a spin 0 and charged $\pm 2e$ (b).	33
Figure 8. Schematic illustration of doped polyaniline showing the formation of charge carries polarons (radical cations) and bipolaron (dications).....	35
Figure 9. Structure, conductivities ($S\text{ cm}^{-1}$) and type of doping (n or p) for some conducting Polymers.....	38
Figure 10. Schematic illustration of oxidation of aniline showing initial product of oxidation to resulting polymer.....	40
Figure 11. Schematic illustration of chemical synthesis of polymer (e.g. polyaniline).....	41

Figure 12. Structure of polyaniline.	46
Figure 13. Structure of Polyaniline in its different form of oxidation states.	46
Figure 14. Different structures of polyaniline in its doped form.	47
Figure 15. Schematic illustration of doped form of polyaniline (emeraldine salt) for protonation.	48
Figure 16. Possible reaction mechanism to generate polyaniline from polymerisation of aniline.....	50
Figure 17. Electropolymerisation of Polyaniline in 1 M HCl solution at a potential scan rate of 50 mV/ s and window potential between -200 and +1100 mV	51
Figure 18. Schematic illustration of some materials of polymer nanocomposites.	55
Figure 19. Graphitic forms of graphene showing the different types of dimension.	60
Figure 20. A typical structure of natural graphite.....	61
Figure 21. Schematic illustration of graphite stacked layered sheets to single layer of graphene.....	61
Figure 22. The electronic configuration of graphene in the ground and excited state.....	64
Figure 23. Illustration of hybridisation in graphene.	64
Figure 24. Schematic view of the sp^2 hybrid orbitals and (b) View of hexagonal lattice in graphene.....	66
Figure 25. Schematic view of energy band in (a) 3-D and (b) 2-D graphene.....	66
Figure 26. Schematic diagram of structure of graphene oxide (GO).....	71

Figure 27. Schematic representation of electrochemical sensor.	85
Figure 28. A typical conventional set up in electrochemical cell.	90
Figure 29. Illustration of a typical linear sweep voltammetry.	94
Figure 30. Illustration of a typical cyclic sweep voltammetry.....	94
Figure 31. A typical illustration of cyclic voltammogram for a reversible reaction.....	98
Figure 32. A typical SWV containing the forward, reverse and difference currents.....	101
Figure 33. Schematic diagram of electrocatalytic process on the surface of a modified electrode.....	103
Figure 34. Illustration of a sinusoidal current response to potential perturbation as a function of time in a linear system.....	107
Figure 35. A typical Nyquist plot showing some kinetics.....	110
Figure 36. Bode plot with one time constant.	111
Figure 37. A typical simple equivalent electrical circuit.	112
Figure 38. A typical equivalent circuit (a) and Nyquist plot of a polymer membrane (b). ...	119
Figure 39. Equivalent circuit for simulating the impedance spectra of bare carbon electrode (BC) and polyaniline carbon (PC) electrodes.	120
Figure 40. UV-vis spectrum of graphene oxide.....	123
Figure 41. FT-IR Spectra of Graphene oxide.	124
Figure 42. Raman spectrum of graphene.	127

Figure 43. Atomic force microscope with a controlling computer.....	128
Figure 44. AFM topography image of graphene on a SiO ₂ substrate.....	128
Figure 45. Presentation of x-ray diffraction pattern of graphene oxide and graphite.....	130
Figure 46. A typical HRTEM (a) and an example of image (b).....	132
Figure 47. A typical HRSEM (a) and an example of image (b).....	133
Figure 48. Sample of synthesised solution of (a) graphite oxide and (b) reduced graphene oxide (graphene).	138
Figure 49. Schematic representation of the mechanisms in the preparation of graphene.....	149
Figure 50. SEM images of (a) graphene oxide (GO) and (b) graphene (GR).	150
Figure 51. Energy dispersive X-ray spectrum of graphene oxide.	150
Figure 52. HRTEM images of (a) graphene oxide and (b) graphene.	151
Figure 53. Energy dispersive X-ray spectrum of graphene.	152
Figure 54. FTIR spectra of (a) graphite, (b) graphene oxide and (c) graphene.	153
Figure 55. AFM image of graphene sheets with height profile.	153
Figure 56. XRD pattern of (a) graphite, (b) graphene oxide and (c) graphene.....	154
Figure 57. Raman spectra of (a) graphene and (b) graphite oxide.....	156
Figure 58. UV- visible spectra of (a) graphene oxide and (b) graphene.....	157

Figure 59. Cyclic voltammograms of (a) modified graphene GCE (potential window -200 to +800 mV) , (b) PANI GCE, (c) GR-PANI GCE and (d) GR-PANI GCE at different scan rate in 1 M HCl. Potential window: -200 to +1200 mV.	161
Figure 60. Plot of scan rate dependence curves of anodic peak current $I_{p,a1}$ (a) and $I_{p,a2}$ (b).....	163
Figure 61. Nyquist plots of the EIS measurement of (a) GCE, (b) PANI GCE and (c) GR-PANI GCE in 1 M HCl. Inset is the Randle's equivalent circuit for fitting.	165
Figure 62. SEM images of (a) GO, (b) GR, (c) GR-PANI and (d) PANI.	167
Figure 63. HRTEM pictures of (a) GO, (b) GR, (c) PANI and (d) and GR-PANI.	168
Figure 64. FTIR spectra of (a) GR, (b) GR-PANI, (c) PANI and (d) GO.	169
Figure 65. XRD patterns of GR (a), PANI (b) and GR-PANI nanocomposite (c).	170
Figure 66. Cyclic voltammograms of GR-PANI GCE in acetonitrile/water (80:20 v/v) with 0.1 M LiClO ₄ at scan rate of 50 mV s ⁻¹	173
Figure 67. Cyclic voltammograms of bare GCE before modification, after modification and response of modified electrode at addition of 100 μM (1.0 x 10 ⁻⁴ M) of anthracene in acetonitrile/water containing 0.1 M LiClO ₄ (a) and GR-PANI GCE, PANI GCE and bare GCE in the presence of 100 μM (1.0 x 10 ⁻⁴ M) of anthracene (b) at scan rate of 50 mV s ⁻¹ and potential window of -200 to +1400 mV.	174
Figure 68. Cyclic voltammograms of (a) GR-PANI GCE in acetonitrile/water (80:20 v/v) with 0.1 M LiClO ₄ , in the presence of 1.0 x 10 ⁻⁴ M anthracene and (b) a plot of the scan rate dependence of its anodic peak currents.	175

Figure 69. Cyclic voltammograms of (a) modified GR-PANI GCE upon the addition of different concentrations (20 – 1000 μM) of anthracene (at high concentrations), (b) at lower concentrations, (c) plot of calibration curve for GR-PANI GCE anthracene sensor at high concentrations and (d) at low concentrations.....	177
Figure 70. Square Wave Voltammograms of (a) modified GR-PANI GCE upon the addition of different concentrations of anthracene (high concentrations), (b) plot of calibration curve of the anodic peak current versus concentrations, (c) addition at lower concentrations and (d) plot of calibration curve at lower concentrations of anthracene.	178
Figure 71. UV Vis absorption spectra of (a) GR and (b) PANI, PANI WO ₃ GR and PANI WO ₃	183
Figure 72. HRSEM images of (a) PANI, (b) WO ₃ , (c) PANI WO ₃ , (d) GR, (e) PANI WO ₃ GR and EDX result of the elemental analysis of nanocomposite formed (f).	185
Figure 73. Electron dispersive X-ray results of the elemental composition of PANI WO ₃ GR nanocomposite.	185
Figure 74. HRTEM images of (a) GR, (b) PANI, (c) PANI WO ₃ , (d) PANI WO ₃ GR nanocomposite, (e) EDX analysis and (f) STEM image of nanocomposite.	187
Figure 75. Electron dispersive X ray analysis of PANI WO ₃ GR.....	188
Figure 76. Raman spectra of (a) PANI, (b) PANI WO ₃ and (c) PANI WO ₃ GR films.....	189
Figure 77. Raman spectrum of graphene (GR).	190
Figure 78. Cyclic Voltammograms for electropolymerisation of polyaniline in 1 M HCl at scan rate of 50 mV s ⁻¹ and window potential of -200 to +1200 mV.....	191

Figure 79. Cyclic voltammograms of PANI GC electrode in 1 M HCl at different scan rate.	192
Figure 80. Cyclic voltammograms for the electropolymerisation of PANI film at (a) 50 mV s ⁻¹ , (b) 100 mV s ⁻¹ and (c) 200 mV s ⁻¹ in 1 M HCl.	194
Figure 81. Cyclic voltammograms of PANI WO ₃ in the presence of different concentrations of H ₂ O ₂ (a) and at 0.08 M of H ₂ O ₂ overlay with PANI (b).	196
Figure 82. Cyclic voltammograms for the electrodeposition of (a) PANI, (b) PANI WO ₃ and (c) PANI WO ₃ GR films on a glassy electrode in a solution of 1 M HCl, at potential window of -600 mV to + 1000 mV and overlay of bare GCE, PANI GCE, PANI WO ₃ GCE and PANI WO ₃ GR GCE in a solution of 1 M HCl at scan rate of 50 mV s ⁻¹	198
Figure 83. Cyclic Voltammograms of (a) PANI WO ₃ GR electrode at different scan rates (5, 10, 15, 20, 25, 30, 40 and 50 mV s ⁻¹) in 1 M HCl and (b) a plot of scan rate dependence anodic peak current.	201
Figure 84. Nyquist plot of the EIS measurement of (a) bare GCE, (b) PANI WO ₃ GR GCE, (c) PANI WO ₃ GCE and (d) PANI GCE in the presence of 1 M aqueous solution of HCl. Inset is Randles equivalent circuit Nyquist plots obtained.	202
Figure 85. Cyclic voltammograms of (a) PANI WO ₃ GR GCE before addition and (b) after addition of 5.0 x 10 ⁻³ nM of phenanthrene analyte in 1 M HCl at scan rate of.....	205
Figure 86. Cyclic Voltammograms of 5.0 x 10 ⁻³ nM of phenanthrene at PANI WO ₃ GR GCE (a), PANI WO ₃ GCE (b) and PANI GCE (c) in 1 M HCl at a scan rate of 30 mV s ⁻¹	206

Figure 87. Cyclic Voltammograms of PANI WO ₃ GR GCE upon the addition of 5.0 x 10 ⁻³ nM of phenanthrene in 1 M HCl at different scan rates (a) and a plot of scan rate dependence of its anodic peak current (b).....	207
Figure 88. Cyclic Voltammograms of PANI WO ₃ GR GCE in 1 M HCl, in the presence of phenanthrene at 30 mV s ⁻¹ (a) and a calibration plot for PANI WO ₃ GR GCE phenanthrene sensor versus concentrations of phenanthrene (b).	208
Figure 89. Square wave voltammograms of (a) PANI WO ₃ GR electrode at every successive addition of phenanthrene in 1 M HCl at a scan rate of 30 mV s ⁻¹ , (b) response at lower concentrations and (c) and a calibration plot for PANI WO ₃ GR GCE phenanthrene sensor versus concentrations of phenanthrene.	209
Figure 90. Cyclic voltammograms of PANI WO ₃ GR GCE in 1 M HCl (a) before and (b) after the addition of 5.0 x 10 ⁻³ nM of anthracene in 1M HCl at scan rate of 30 mV s ⁻¹ and potential window of +0 to +2000 mV.....	211
Figure 91. Cyclic Voltammograms of 5.0 x 10 ⁻³ nM of anthracene at PANI GCE (a), PANI WO ₃ GCE (b) and PANI WO ₃ GR GCE (c) in 1 M HCl at a scan rate of 30 mV s ⁻¹ ..	212
Figure 92. Scan rate dependence cyclic voltammograms of PANI WO ₃ GR GCE sensor in 1 M HCl containing 5.0 x 10 ⁻³ nM anthracene.....	213
Figure 93. A plot of scan rate dependence of its anodic peak current.	213
Figure 94. Cyclic voltammograms of the PANI WO ₃ GR GCE in 1 M HCl in the presence of different concentrations of anthracene at scan rate of 30 mV s ⁻¹ and potential window of +0 to +2000 mV.	215

Figure 95. Calibration plot for PANI WO ₃ GR GCE anthracene sensor versus different concentrations of anthracene.....	216
Figure 96. Square wave voltammograms of the PANI WO ₃ GR GCE in 1 M HCl at every addition of concentrations of anthracene at scan rate of 30 mV s ⁻¹ and potential window of +0 to +2000 mV.....	216
Figure 97. Square wave voltammograms of the PANI WO ₃ GR GCE in 1 M HCl at lower concentrations of anthracene at scan rate of 30 mV s ⁻¹ and potential window of +0 to +2000 mV.....	217
Figure 98. Calibration plot for PANI WO ₃ GR GCE anthracene sensor at lower concentrations.	218
Figure 99. Cyclic voltammograms of PANI WO ₃ GR GCE in 1 M HCl before (a) and after the addition of 5.0 x 10 ⁻³ nM pyrene (b).....	220
Figure 100. Cyclic Voltammograms of 5.0 x 10 ⁻³ nM of pyrene at PANI GCE (a), PANI WO ₃ GCE (b) and PANI WO ₃ GR GCE (c) in 1 M HCl at a scan rate of 30 mV s ⁻¹ and potential window of +0 to +2000 mV.....	220
Figure 101. Scan rate dependent cyclic voltammograms of PANI WO ₃ GR GCE sensor in 1 M HCl containing 5.0 x 10 ⁻³ nM pyrene.	221
Figure 102. A plot of the scan rate dependence of its anodic peak currents.....	222
Figure 103. Cyclic voltammograms of the PANI WO ₃ GR GCE in 1 M HCl at increasing concentrations of pyrene at scan rate of 30 mV s ⁻¹	223
Figure 104. Calibration plot for PANI WO ₃ GR GCE pyrene sensor at different concentrations.	223

Figure 105. Square wave voltammograms of the PANI|WO₃|GR|GCE in 1 M HCl at different concentrations of pyrene and at a scan rate of 30 mV s⁻¹.224

Figure 106. Square wave voltammograms of the PANI|WO₃|GR|GCE in 1 M HCl at lower concentrations of pyrene at scan rate of 30 mV s⁻¹.225

Figure 107. Calibration plot at lower concentrations of pyrene.225



LIST OF TABLES

Table 1. Some of the unique properties of graphene.	63
Table 2. Common circuit elements	113
Table 3. Equivalent circuit model and dependent variables as fit parameter.	118
Table 4. CV peak parameters of GR-PANI and PANI modified electrodes.	160
Table 5. CV peak parameters of GR-PANI and PANI modified electrodes.	160
Table 6. Impedance data obtained from the Randle equivalent circuit fitting from Figure 61	165
Table 7. Band gap energy values calculated from the UV-vis spectra	182
Table 8. Obtained data of cyclic voltammetric analysis from Figure 81	199
Table 9. Values for the fitted parameter of Randles equivalent circuit Nyquist plots from Figure 84	203
Table 10. The relative sensitivities, LOD, low concentration linear range obtainable for the different polymer systems.....	229

LIST OF SCHEMES

Scheme 1. Research framework.....	7
Scheme 2. Schematic illustration to the synthesis of graphene.	137
Scheme 3. Schematic illustration of chemical synthesis of graphene-polyaniline nanocomposite via in situ polymerisation.....	140
Scheme 4. Schematic diagram of the deposition of PANI WO ₃ film on graphene modified electrode.....	143
Scheme 5. Possible products expected from the oxidation of anthracene.	172
Scheme 6. Schematic diagram showing Pathway to degradation of phenanthrene	206



LIST OF ABBREVIATIONS

DDT	Dichlorophenyl trichloroethane
PCBs	Polychlorinated biphenyls
PAHs	Polyaromatic hydrocarbons
POPs	Persistent organic pollutants
WHO	World health organization
USEPA	United state environmental protection agency
PHE	Phenanthrene
ANT	Anthracene
PYR	Pyrene
LMW	Low molecular weight
HMW	High molecular weight
CNT	Carbon nanotubes
ICPs	Intrinsic conducting polymers
PA	Polyacetylene
PANI	Polyaniline
PPy	Polypyrrole
PTh	Polythiophene
PPv	Poly(p-phenylenevinylene)
PEDOT	Poly(3,4-ethylenedioxythiophene)
LUMO	Lowest unoccupied molecular orbital
HOMO	Highest occupied molecular orbital
DP	Degree of polymerisation
ES	Emeraldine salt
PNC	Polymer nanocomposite
0D	Zero dimensional

1D	One dimensional
2D	Two dimensional
3D	Three dimensional
HOPG	Highly ordered pyrolytic graphite
GIC	Graphitic intercalation compound
CVD	Chemical vapour deposition
Ni	Nickel
Co	Cobalt
Pt	Platinum
GO	Graphite oxide
rGO	Reduced graphene oxide
GR	Graphene
CMG	Chemically modified graphene
CARGO	Chemically reduced active graphene oxide
PS	Polystyrene
WO ₃	Tungsten oxide
WO ₃ .H ₂ O	Tungstite
H ₂ WO ₄	Tungstic acid
Ag/AgCl	Silver-silver chloride
CE	Counter electrode
WE	Working electrode
RE	Reference electrode
ΔE_p	Peak separation
$E_{p,a}$	Anodic peak potential
$E_{p,c}$	Cathodic peak potential
$I_{p,a}$	Anodic peak current

$I_{p,c}$	Cathodic peak current
E°	Formal potential
CV	Cyclic voltammetry
SWV	Square wave voltammetry
CME	Chemically modified electrode
EIS	Electrochemical impedance spectroscopy
EEC	Equivalent electrical circuit
R_s	Solution resistance
R_{ct}	Charge transfer resistance
CPE	Constant phase element
UV-vis	Ultraviolet visible
FTIR	Fourier transform infrared
AFM	Atomic force microscope
XRD	X-ray diffraction
HRTEM	High resolution transmission electron microscope
HRSEM	High resolution scanning electron microscope
EDX	Energy dispersive X-ray microanalysis
HCl	Hydrochloric acid
GR-PANI	Graphene-polyaniline film
GCE	Glassy carbon electrode
PANI WO ₃	Polyaniline-tungsten oxide film
PANI WO ₃ GR	Polyaniline-tungsten oxide-graphene film

CHAPTER ONE

INTRODUCTION

1.1 Background

One of the basic necessities that determine a healthy life is an environment that is free of contaminant and which is expectant of human beings and other living organism. However, human actions through anthropogenic activities have greatly impacted the rate of supply of the major nutrients that constrain the productivity, composition, and diversity of terrestrial ecosystem. The releasing of harmful contaminants into the environment causing instability and harm to the ecosystem is termed as pollution. Unwanted changes in the environment then occurred, which involves the physical, biological and chemical changes in air, water and land, affecting human life in one way or the other. It has become a serious issue in developing countries due to rapid growth, development, industrialization, agricultural and lack of regulations. Pollution is the root cause of many diseases that kills and disable human organism. Water is said to be polluted when there is any physical, biological or chemical change in water quality that adversely affects living organisms or makes water unsuitable for use which then becomes a great threat to the life of human beings as well as the ecosystem. Unmanaged wastewater can be a source of pollution, a hazard for the health of human populations and the environment alike. The principal contaminants include toxic chemicals, nutrients and biodegradable organics, bacterial as well as viral pathogens [1]. These contaminants are either in solution or as particulate matter and are carried along in the water from different sources and affect water quality. They can have (bio-) cumulative, persistent and synergistic characteristics affecting ecosystem health and function, food production, human health and wellbeing, and undermining human security. The prime water pollutants including, dichlorodiphenyltrichloroethane (DDT), polychlorinated biphenyls (PCBs) and polyaromatic

hydrocarbons (PAHs), persist in the natural environment and giving rise to bioaccumulation in the tissues of aquatic organisms [2]. These prolonged and persistent organic pollutants are transferred up the food chain and they can reach levels of concern in fish species that are eaten by humans. Moreover, bacterial and viral pathogens can pose a public health risk for those who drink contaminated water or eat raw shellfish from polluted water bodies. Polyaromatic hydrocarbons (PAHs) are among the most persistent organic and major environmental pollutants that need constant monitoring due to their toxicity [3]. They are chemical compounds made up of carbon and hydrogen atoms forming two or more fused aromatic rings without any heteroatom or substituent [4]. PAHs are lipophilic in nature; even though, few of them can slightly dissolve in water. They are ubiquitous in the environment, produced as by-product of combustion of fossil fuels, coal tar deposits, oil, through anthropogenic activities or naturally by forest fires, volcanoes, plants, fungi and bacteria [5]. They are widely distributed in soil, air, water, also in ocean, river sediments and sludge [2]. PAHs are organic compounds that are persistent in the environment and liable to bioaccumulation through the food web [6], thus, causing adverse effect on human health and the environment. They are being identified as carcinogenic, teratogenic and mutagenic contaminants even at relatively low levels, thus a great concern. [7-8]. Their resistance to degradation has actually allows them a long environmental half-life, and the toxicity as well as release of these chemicals consecutively over time results in their accumulation and will impose global environmental problem. As a result, government and environmental scientists worldwide have gone thorough research so as to decrease and manage their risk to people and the environment. Recent studies have focused on developing methods for monitoring traces of PAHs. However, analysis and monitoring have generally focused on some selected 16 PAHs highlighted by the US Environmental Protection Agency (EPA) [9-10]. Because PAHs are hydrophobic in nature, thus, their persistent in the aquatic environment and could even exist in micro level, once in the water system, it becomes

difficult to treat even by conventional methods due to their persistency and non-reactivity in water [11]. Degradation of organic pollutants from contaminated water by electrochemical method through oxidation has shown to be an adaptable, non-discriminating, reliable and efficient technique that is capable of decreasing the extensive variety of organic pollutants [12-15]. In this study an electrochemical method, in form of an electrochemical sensor based on polyaniline /tungsten oxide/graphene nanocomposite is developed. The composite is used to modify glassy carbon electrode through application of positive potentials at which the contaminated water is simply passed through the electrode in an electrochemical cell, oxidation occurred directly on the surface of the electrode, and hence an identification and determination of the specific PAHs- anthracene, phenanthrene and pyrene which are some of the carcinogenic PAHs selected to be among the priority pollutants by EPA.

1.2. Problem statement

The concern about the human health risks associated with the exposure to mutagenic, teratogenic and carcinogenic polyaromatic hydrocarbons in the environment has brought about the interest in the development of a suitable method of analysis that is cheaper and easier to use in identifying and quantifying them. Despite the effectiveness of conventional methods in terms of high accuracy and low detection limit of the techniques which includes: immunoassay, gas chromatography and high performance liquid chromatography (HPLC) with UV-vis absorbance or fluorescence, and capillary electrophoresis (CE) equipped with laser-induced fluorescence, that have been reported and adopted, however, they have limitations; in that, they are very costly, time consuming, laboratory borne, they need a lot of skill in the operation and sometime suffer from low detection limit. Furthermore, a large amount of sample volume and solvent are needed in separation and extraction procedures. Apparently, there is the need to overcome all these challenges. Consequently, a cheaper, faster, easier to use, low power

consuming, miniaturizable, user friendly, and on site analytical device suitable to compliment or substitute for these classical methods is developed in form of a graphenated polyaniline nanocomposite based electrochemical sensor for the detection and quantitative determination of PAHs.

1.3. Rationale and motivation

The discovery of polymer nanocomposite opened a new dimension in the field of materials science. In particular, the use of inorganic nanomaterials as fillers in the preparation of polymer/inorganic composites has attracted increasing interest owing to their unique properties and numerous potential applications in the automotive, aerospace, construction and electronic industries [16-20]. Recently, carbon-based nanofillers such as carbon black, expanded graphite, foliated graphite, carbon nanotubes (CNTs) and graphene have been introduced to the preparation of polymer nanocomposite [21-24]. Among the carbon compositing materials, carbon nanotubes (CNTs) have proven to be very effective as conductive fillers. The only drawback of CNTs as nanofiller is their higher production cost; therefore, the mass production of CNT based functional composite materials is very difficult. Graphene is two dimensional carbon nanofiller with one-atom-thick planar sheet of sp^2 bonded carbon atoms that are densely packed in a honeycomb crystal lattice. It is regarded as the "thinnest material in the universe" with tremendous application potential [25-26]. Graphene is predicted to have remarkable properties, such as high thermal conductivity, superior mechanical properties and excellent electronic transport properties [27-28], [29], [30-31]. These intrinsic properties of graphene have generated enormous interest for its possible implementation in a myriad of devices [32].

The main thrust of this study is to use the synergism of electrochemical and molecular electronic concepts in the development of novel nano-structured or nanometer scale sensor devices for environmental analysis of anthropogenic persistent organic pollutants (POPs)

contained in industrial and domestic wastewater systems. Our current interests are on polyaromatic hydrocarbons (PAHs) including anthracene, phenanthrene, pyrene, benzo[a]anthracene and benzo[a]pyrene. These compounds are known to have varying degrees of toxic, mutagenic or carcinogenic activities. The World Health Organization (WHO) has set aside some guidelines concerning the pollution of polyaromatic hydrocarbons. A concentration below 15 ng L^{-1} for each polyaromatic hydrocarbon and 700 ng L^{-1} for benzo[a]pyrene has been recommended by the WHO [33]. Also, the recommended concentration of 8 PAHs in drinking water has been estimated to be lower than 200 ng L^{-1} and concentration range of 0.1 to 830 ng L^{-1} should not be exceeded in surface water. The European Union as well as the United State Environmental Protection Agency (USEPA) has also specified permissible limits for the 16 priority PAHs [34].

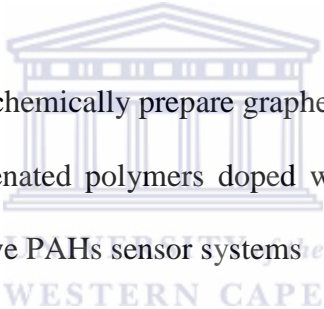
Presently, instrumental methods of analysis involving chromatographic (TLC, GC, HPLC) [35-37], spectroscopic (UV-Vis, IR, MS) [37-38] or coupled techniques (GC-MS) [39], are heavily relied upon for environmental analysis. These instrumental techniques are usually expensive, amenable on-site applications require extensive pre-treatment stages before analyte quantification and they failed to indicate whether the compounds are accessible for assimilation by living organisms. The rationale for this proposed study is the need for relatively low cost, miniaturized and easy-to-use hand-held nanosensor systems for onsite application, which to a great extent maintains sample integrity. Environmental impedimetric and chemosensor devices containing intrinsically conducting polymer (ICP) nanotubes that have been graphenated and doped with tungsten oxides will be developed and applied for real-time determination and speciation of PAHs associated with industrial wastewater effluents.

1.4. Research aim and objectives

1.4.1. AIM

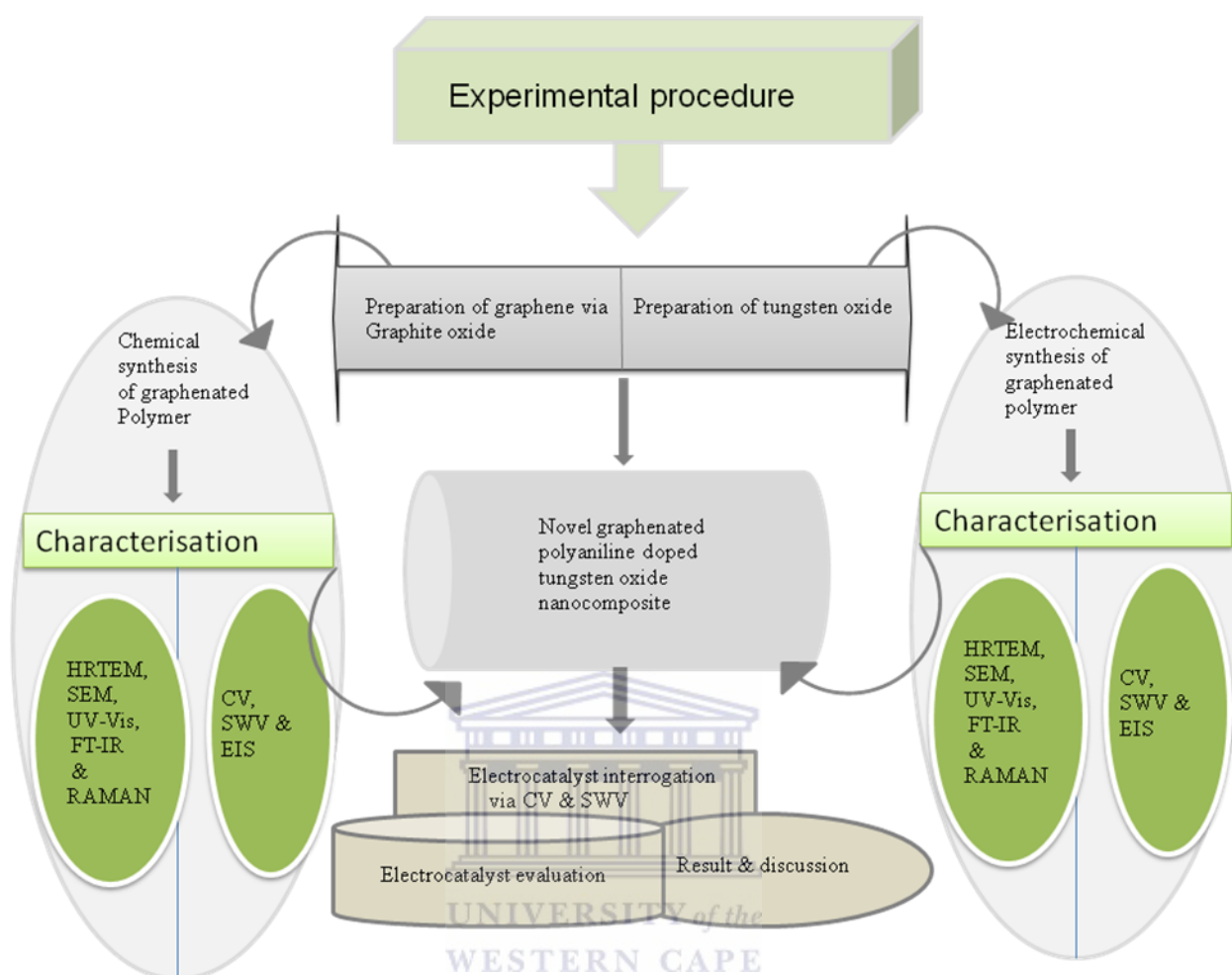
To develop a novel method for harnessing the properties of electro conductive polymers in sensor technology by using polymeric nanotubes blends in the preparation of high performance sensor devices. Success in this will have a long term impact for the development and promotion of scientific and technical knowledge in the field of chemistry for industrial agricultural, research, medical, pharmaceutical, environmental or other peaceful purposes.

1.4.2. Objective of the study includes:

- 
- (i) To prepare graphene.
 - (ii) To electrochemically and chemically prepare graphenated polymers.
 - (iii) To produce novel graphenated polymers doped with transition metal oxides for the production of ultra-sensitive PAHs sensor systems
 - (iv) To characterize, interrogate and model the responses of the graphenated PANI sensor composite by instrumental, electrochemical, microscopic impedimetric and spectroscopic techniques.
 - (v) To develop high performance gold, platinum and carbon disc or screen-printed nano-sensor devices.
 - (vi) To determine the detection limit, sensitivities and analytical linear ranges of the PANI sensor systems with respect to various PAHs.

1.5. Research framework

The study of the objective is illustrated in the scheme below.



Scheme 1. Research framework.

1.6. Thesis statement

Graphenated polyaniline nanocomposite should have suitable electrochemical and electrocatalytic properties that make them applicable for real time determination of polyaromatic hydrocarbons.

CHAPTER TWO

LITRATURE REVIEW

This chapter presents a literature review comprising of impact of wastewater and persistent organic pollutants (POPs) on the environment, properties, toxicity, effect, distribution and various sources of PAHs. Nanocomposites based on polyaniline, graphene and tungsten oxide, their method of synthesis and possible application. Also, a brief background of the characterisation techniques used in the study is discussed.

2.1. Wastewater

The activities by human on the environment have a created a great impact on the biological and diversity of our aquatic ecosystem. The aquatic environment is affected through discharge of contaminated water into the environment thus polluting the water of downstream users. As an illustration, water that passes through the hydrological system from the mountain summit to the sea, is been captured by the activities of human society who took this water into their custody and put it through processes such as diversion, extraction as well as treatment, then reused it to sustain the communities and economies throughout the watershed which include agriculture, industrial and municipal [40]. However, the activities failed to return the extracted water in the same condition that it was captured but discharged it into the environment, constituting wastewater. An astounding value of about 80 to 90% of all wastewater generated in the developing counties have been reported to have being discharged directly into surface water bodies [41]. Through this, the biological diversity of aquatic ecosystem is impacted and the basic integrity of life is disrupted [42-43].

Wastewater can be regarded as any water that has been adversely affected in quality by anthropogenic influence via liquid waste discharged by domestic residences, commercial properties, industry, and/or agriculture including a wide range of potential contaminants such PAHs at higher concentrations via bioaccumulation [40, 44-45]. It becomes obviously a source of pollution, especially when not well managed, endangering the health of human populations as well as the environment. About 60 per cent of global ecosystem service was reported by the millennium ecosystem assessment [46] to have been degraded or used unsustainably as result of wastewater. It can among other things be polluted with countless of diverse components of persistent organic pollutants such as pathogens, organic compound, synthetic chemicals, nutrients, organic matter and heavy metals, which can either, be in solution or as particulates matters, distributing into different sources and have (bio-) accumulative, persistent and synergistic characteristics that can affect the ecosystem health and function, food production, human health as well as wellbeing [40], according to the illustration in Figure 1, about 70 per cent of water has been used in other productive activities before entering urban areas, which are left at the mercy of just 8 per cent and the rest percentage shared by the industry [47-48]. **Figure 1a** showed the illustration of extraction of water and reused along the supply chain and **Figure 1b**, a typical example of wastewater discharged directly into the water bodies from a source point.

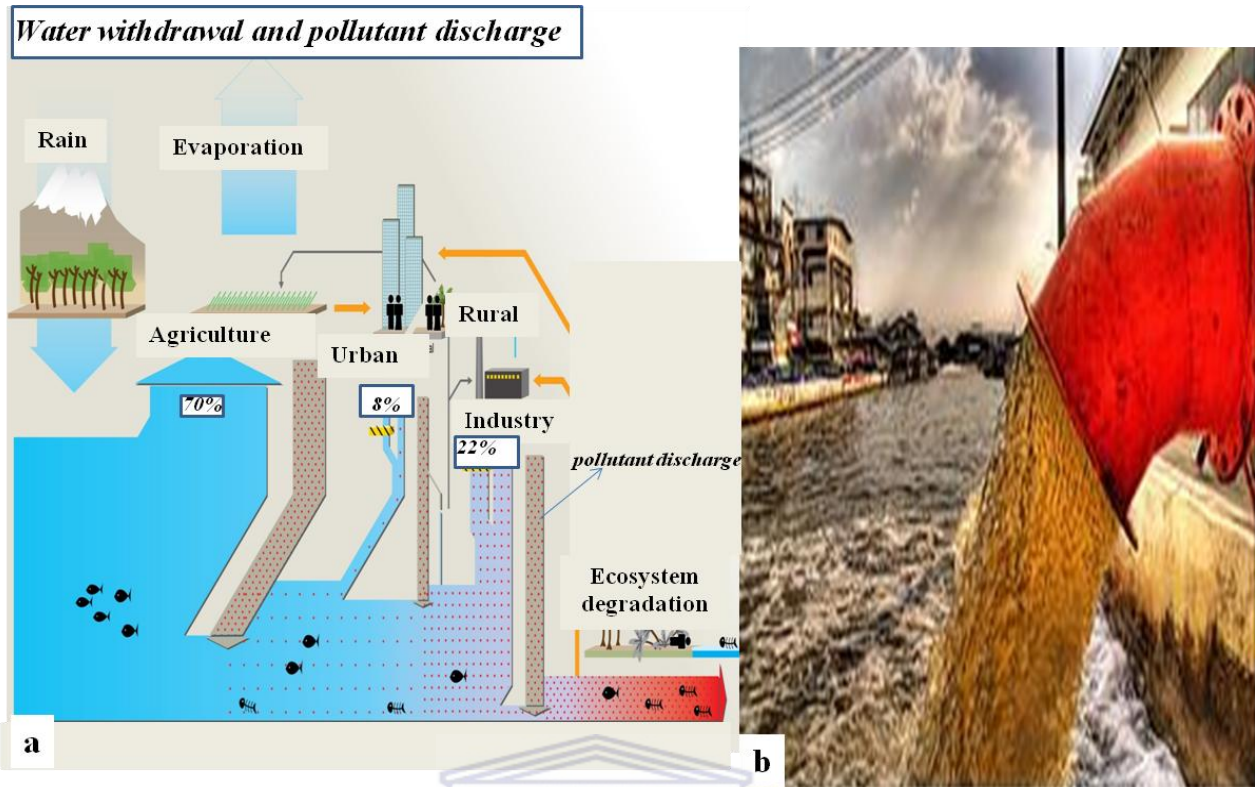
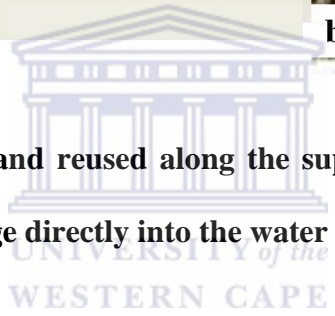


Figure 1. Extraction of water and reused along the supply chain (a) [40] and a typical example of wastewater discharge directly into the water bodies from a source point (b).



2.1.2. Persistent organic pollutants (POPs)

Persistent organic pollutants (POPs) are chemical substances that have the ability to persist in the environment, bioaccumulate through the food web, and pose a risk of causing adverse effects on human health and the environment [49]. This group of priority pollutants consists of pesticides such as dichlorodiphenyltrichloroethane (DDT) [50], industrial chemicals (such as polychlorinated biphenyls (PCBs), polyaromatic hydrocarbon (PAHs), generated accidental by-products of industrial processes (such as dioxins and furans) or combustion processes (e.g. PAHs). They are released into the environment through natural and various human activities of which human activities makes the greater contributor. Comprehensively, reported studies have it that POPs are among the most dangerous pollutant released into the environment by human [51]. The following can be generally associated with Persistent organic pollutant (POPs):

-They are toxic, a source of deleterious health effect such as birth defects (teratogenic), mutagenic, damage of immune and respiratory systems as well as critical organs. The hormone system dysfunction such as damage to the reproductive system, sex-linked disorder, and shortened lactation periods for nursing mothers, as well as endocrine disruption having developmental and carcinogenic effects, are all associated with POPs [52].

-They resist breakdown in water but soluble in fatty tissue, which makes them to be bioavailable to mammals. They bioaccumulate exponentially up the food chain [53], attaining the greatest magnitudes in mammals and humans [54]. Besides, these substances have been reported to bioconcentrate under typical environmental conditions [49, 52, 55]. A factor of about 70,000 times concentration of the same POPs has been reported to bioconcentrate in the tissue of fish by Jacobs *et al.* [56].

-They are semi-volatile, thus, capable of travelling great distances through cycles of evaporation and atmospheric cycling and deposited via wind and water, regionally and globally [49, 55, 57]. POPs have been found continentally and in every major climate zone, including

remote regions such as oceans and deserts. They are also found in the body fat of human beings and every wildlife species. Thus, exposure to these contaminants by every individual could cause the health effect. Although, some of the POPs in the Stockholm convention [57] are no longer produced in the United States, people can still be at risk from POPs that are persisted in the environment [58].

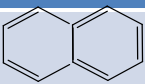
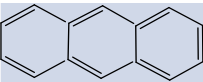
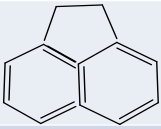
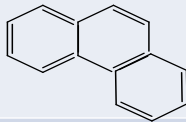
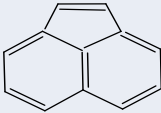
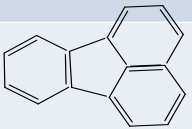
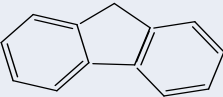
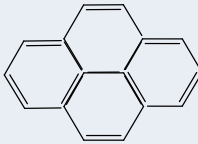
2.2. Polyaromatic hydrocarbons

Among the most persistence organic pollutants extensively studied in the environment, polyaromatic hydrocarbons (PAHs) are more ubiquitous. They are in the air, water, soil and food, the more dangerous they are to plants, animal and human [7]. PAHs are organic compounds that contain more than one fused benzene rings, e.g. naphthalene to anthracene with the lower molecular weight (two or three aromatic rings) and chrysenes to coronenes with higher molecular weight (four to seven atomic rings). Polycyclic aromatic hydrocarbons are lipophilic, in the sense that they can mix more easily with oil than water, with the larger compounds being less water-soluble and less volatile. Hence, PAHs are found primarily in soil, sediment and oily substances, than in water or air. They are product of incomplete combustion, either through natural or anthropogenic activities, and are generally found in complex mixtures. The natural sources comprises of forest fires, volcanic eruption, fossil fuel, pyrolysis of organic materials etc. [59]. The main sources of PAHs is through anthropogenic activities which comprises of combustion of fossil fuels inform of burning of coal oil and natural gas, petroleum spills, run offs from agriculture, industrial effluents etc. PAHs can be found to adsorb unto airborne particles when in gas phase and are capable of adsorbing on particulate matters when dissolved in water, for instance, groundwater, wastewater and drinking water. Reaction with pollutants like ozone, nitrogen oxide and sulfur dioxide can occur also when in the atmosphere [60]. Because of the prevalent sources and persistence properties,

bioaccumulation and ubiquitous nature of PAHs, it has been considered as carcinogenic, mutagenic and teratogenic [61]. The emission and adsorption of PAHs in the air and water respectively, and the tendency to be transported more farther than expected [62]. Spillage of fuel like petroleum, oil as well as coal product has resulted in emission of PAHs, causing deleterious effect on the aquatic life and environment [5, 63]. The detection and determination of PAHs revealed a high level of toxic effect on green alga and some organism in the aquatic environment [64]. Furthermore, PAHs have increasingly attracted the awareness that it can lead to biochemical, immunologic, genetic, and reproductive effects, and have been extensively observed in fish and other animals from marine and freshwater environments upon exposure [65-66]. The vulnerability to PAHs and potential health risk connected to the distribution has recently raised the interest and greater focus by researchers.

2.2.1. Formation and characteristics of PAHs

PAH are numerous classes of organic compounds which comprises of two or more units of benzene rings fused together. They can occur as complex mixtures without heteroatom or substituent. They are non-polar and hydrophobic in nature, thus, they are only soluble to some extent in water and their solubility also depends on their molecular weight, i.e. the higher the molecular weight, the less soluble they are. Their persistence in the environment due to bioaccumulation and biodegradation has resulted in the recognition of some of these compounds as priority pollutants in wastewater. Among the 16 PAHs listed as priority compounds by the environmental protection agency (EPA) are Acenaphthene, Acenaphthylene, Anthracene, Fluorene, Phenanthrene, Pyrene etc. according to **Figure 2** [33, 67].

NAME	CHEMICAL STRUCTURE	CHEMICAL FORMULA	NAME	CHEMICAL STRUCTURE	CHEMICAL FORMULAR
Naphthalene		$C_{10}H_8$	Anthracene		$C_{14}H_{10}$
Acenaphthene		$C_{12}H_{10}$	Phenanthrene		$C_{14}H_{10}$
Acenaphthylene		$C_{12}H_8$	Fluoranthene		$C_{16}H_{10}$
Fluorene		$C_{13}H_{10}$	Pyrene		$C_{16}H_{10}$

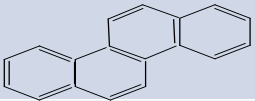
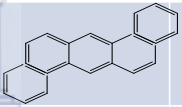
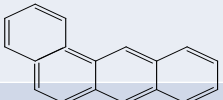
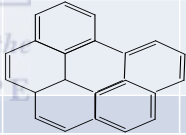
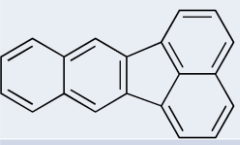
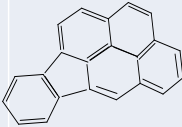
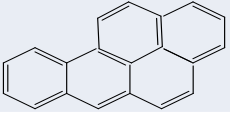
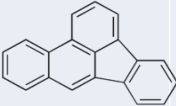
NAME	CHEMICAL STRUCTURE	CHEMICAL FORMULA	NAME	CHEMICAL STRUCTURE	CHEMICAL FORMULAR
Chrysene		$C_{18}H_{12}$	Dibenzo(a,h)anthracene		$C_{22}H_{14}$
Benzo(a)anthracene		$C_{20}H_{12}$	Benzo(g,h,i)perylene		$C_{22}H_{12}$
Benzo(k)fluoranthene		$C_{20}H_{12}$	Ideno(1,2,3c,d)pyrene		$C_{22}H_{12}$
Benzo(a)pyrene		$C_{20}H_{12}$	Benzo(b)fluoranthene		$C_{20}H_{12}$

Figure 2. The chemical structure of some of the 16 PAHs listed as priority.

The physical and chemical characters of PAHs can be associated to their molecular weights. In terms of vapourisation, oxidation and reduction properties, their resistivity increase with

increase in molecular weight hence aqueous solubility decreases which resulted into the difference in their behaviour, distribution, as well as their effect on biological system in the environment. The lower molecular weight PAHs tends to be more soluble and volatile than the higher molecular weight PAHs which are readily soluble in organic solvents. Their hydrophobic nature enables them to be able to absorb onto suspended particulate in the aquatic environment [68]. Hence, they settled and accumulate onto the bottom sediments which determine their persistence and susceptibility to biodegradation in the aquatic environment. PAHs with high boiling points are highly lipophilic and difficult to dissolve in water [69]. Wang *et al*, Mai *et al*, and Yunker *et al*. [70-72], have all investigated the distribution and concentration of PAHs in aquatic environment Weig *et al*. [73] reported the concentration of PAHs in the contaminated environment to be in excess of 1000 ng/L and to have been associated with urban runoffs, sewage outfalls and wastewater from industrial area discharges. These high concentrations of PAHs could go into human body through food webs, and cause deleterious effect on human health. Hence, investigating the concentration and distribution of PAHs in the environment will provide an important record and useful background for risk assessment, future studies, wastes disposal and management. Several are available and have been employed in the detection.

2.2.2. Toxicity: exposure and carcinogenicity of PAHs

2.2.2.1. Exposure

Polyaromatic hydrocarbons represent a greater part of group of persistent organic pollutant (POP) and ubiquitous compounds in nature. They formed the main hazards released by various petroleum hydrocarbons or coal tar derived product, variety of combustion processes and industrial processes to the environment. PAHs are transported into all tissues of the human body containing fat, stored in liver and kidneys spleen, adrenal glands and ovaries, and thereby, accumulate by repeated and long-term exposure [74]. Exposure to PAHs through tobacco smoke, wood smoke and consumption of foods formed the major sources of the united state population to PAHs [74]. Others include vehicle emission, residential heating, cultural burning, waste incineration and emission from industrial processes. Burning of coal, wood, gasoline or other product burnt in soil can also be a source of exposure [75]. Human can also be exposed to PAHs via water consumption, either in surface water or sediment. PAHs can undergo processes like volatilization, oxidation and biodegrading, and binding to suspended particles or sediment through adsorption or accumulates in plants or aquatic organisms. Due to the wide exposure, they have the tendency to be transported to the human tissues and stored in fats, liver and kidney and repeatedly bio accumulate and causing deleterious effect to human health [76]. In addition, main exposure of the united state population to PAHs, include inhalation of tobacco smoke, wood smoke, air from traffic emission and consumption of food contaminated with PAHs [77]. The levels of exposure to PAHs by humans and biological response play a major role in investigating the risk associated with PAHs. The variability in human activities, concentrations and inhalation rate can then be estimated. However, different PAHs species have different properties and this account for their behaviour and toxicity in the environment.

Risk assessment and toxicity of the groups of PAHs are often estimated on the basis of benzo[a]pyrene (Bap) concentration [78].

2.2.2.2. Toxicity and Carcinogenicity

A wide range of effect due to toxicity including blood cell damage that leads to anaemia, immune-toxicity, mutagenic, damage to foetus has been associated with PAHs. Carcinogenic effect has been extensively studied to be the most serious toxicity of PAHs [8]. The earlier studies on carcinogenicity of coal tar extract have been related to these observations about PAHs. Hence, benzo[c]fluorene was found to form major constituents of coal tar, in strongly induced DNA-adduct formation [79-81]. The annual number of lung cancer cases attributed to carcinogenic PAH compound was estimated at 58 persons per million in 2005 [82]. Cancer sufferers of Beijing inhabitants in 2007 were reported to be 1.7% through inhalation of PAH in ambient air [83]. Some PAHs have been reported to be a causative agent of lung deceases [84], as well as pancreatic [85]. Prostate and cervical cancers in humans and animal models have also been reported to be associated with PAHs [86-87]. Lee *et al.* [88], in a community-based case-control study through pap smear screening and biopsy examination, reported a high level of cervical tumorigenesis in chefs that were exposed to PAHs in kitchens with poor fume ventilation during the main cooking life.

2.2.3. Occurrence, sources and distribution in the environment

Polycyclic aromatic hydrocarbons (PAHs) are the common and prevalent environmental contaminants that occurred in atmosphere, water, soil, sediment and organism [89-92]. They are usually generated from natural processes and anthropogenic activities and then introduced into the environment via diverse routes. Due to their hydrophobic and solubility nature, they have the affinity to be associated with the particulate phase, subjecting to major processes such

as volatilisation, adsorption, and dissolution onto these particles and eventually onto the sediments of lakes, marine, sea water etc. with consequences for bioaccumulation [93-94].

2.2.3.1. Natural sources

Naturally, PAHs can be in three different forms; high temperature pyrolysis of organic material, low to moderate temperature diagenesis of sedimentary organic materials to form fossil fuel, and direct biosynthesis by microbes and plant [93]. Thus, the main contributors to natural sources can be associated with burning of forest fire, agricultural burning and plain fires whereby the PAHs from these sources are liable to adsorb onto suspended particulate and eventually enter the terrestrial and aquatic environment as atmospheric fallout [95-96]. Once in the atmosphere, they may undergo photolytic and chemical (ozone) transformations, in which they however, remains in the atmosphere for a long period due to degradation. As such, they are distributed globally, even appearing in such places like remote areas, e.g. Antarctica [97]. Other natural sources include bituminous fossil fuels, for instance, coal and crude oil deposits consequently to diagenesis. PAHs of low molecular weight (LMW) such as phenanthrene, as well as high molecular weight (HMW) such as pyrene, benzo[a]anthracene, benzo[a]pyrene etc. have all been identified with carbon coal [98]. Volcanoes activities as well as biosynthesis by algae and bacteria also contribute to natural sources of PAHs [93].

2.2.3.2. Anthropogenic sources

Anthropogenic activities are those that are derived from human activities. And one of the major contributors is incomplete combustion of organic matter at high temperature, especially during pyrolysis. Anthropogenic can generally be divided into two categories: direct discharges into aquatic environment and discharges into atmosphere [93]. Sources of PAHs discharged directly into water body are: accidental spillage, leakages from fluids containing PAHs e.g. wastes oils and gasoline, industrial and domestic wastewaters, urban runoff, and discharges originating

from landfills, use of creosoted pilings for docks and other shoreline structures while atmospheric discharges can further be categorized into: mobile and stationary categories. The mobile category includes contributors from vehicular petroleum and diesel petrol. Emission of exhaust fumes from vehicles formed the main emitters, others include, automobile, railways, ships and aircraft via the use of diesel, coal, gasoline, oils and lubricant. Urban area are the major contributors in mobile sources of PAH emission [99]. Emission of PAHs from these sources via exhaust fumes are adsorbed onto particulates where photolytic degradation or deposition onto street surfaces could occur, after which they are precipitated and washes into drainage system and eventually flushed into the aquatic environment. Stationary category entails a large variety of incomplete combustion process including residential heating, industrial activities, incineration agriculture activities and power generation which results in high accumulation of PAHs concentration [100]. PAHs are added into the environment from these sources either through pyrolysis, or during industrial processes. The PAHs are adsorbed onto particulate in the air if not degraded and then deposited onto the water, as well as the surrounding terrestrial environment [89-90].

2.2.3.3. PAHs in sources to the aquatic environment

Polyaromatic hydrocarbons (PAHs) in aquatic environment can be found to originate from three different sources: pyrogenic, petrogenic and diagenetic [101]. Pyrogenic PAHs are four to six benzene rings that are mostly dominated by non-alkylated PAHs compounds. Pyrogenic PAHs are formed during combustion in forest fire or biomass, volcanoes and anthropogenic activities e.g. wood ovens, industry etc. [101]. Emission could also be from shipping and long-range transport from land areas or flaring at offshore oil installations [102].

Petrogenic PAHs are also enriched in 2- and 3-ring, lower molecular weight (LMW) and are majorly alkylated compounds. They are formed during the conversion of organic matters to

petroleum and coals [103], or anthropogenic as a result of oil spills [104]. The alkylated structure of petrogenic PAHs reflects the ancient plant material from which the compounds are formed [105]. Diagenetic PAHs refer to PAHs from the biogenic precursors, like plant terpenes, leading to the formation of compounds such as retene and derivatives of phenanthrene and chrysene [106]. Perylene is another common diagenetic PAH, although its exact formation process remain unclear, because an anaerobic process appears to be involved [107]. While diagenetic PAHs are frequently found at the background level in the recent sediments, they often dominate the assemblage of PAHs present in older sediments deposited human industrial activity [108]. A potential fourth source of PAHs is biogenic, i.e. purely from bacteria, fungi, plant or animals in sedimentary environments without any contributions from diagenetic processes [109]. Unlike petrogenic PAHs, they are not strongly varied in chemical structures but are usually found individually or in easy mixtures e.g. perylene, found in sediments of Northern Barents Sea [110]. Wu *et al.* [111] supported the observation that the composition of PAH molecules in the sediments differed from the commonly found in petroleum, and that most PAHs in aquatic environments originated from pyrogenic sources. However, petrogenic PAHs can also occur alone or in combination with pyrogenic PAHs. Generally, petrogenic PAHs appear to be associated with local or point sources, such as refineries and other petroleum industries, and adjacent to road and navigational routes. This is in contrast with the distribution of pyrogenic PAHs, which occur on broader geographic scales [112]. Finally, diagenetic PAHs occur at the background levels, although anthropogenic sources (e.g. perylene) can contribute to these types of PAHs. Thus, a strong relationship exists between PAHs source and distribution, with pyrogenic PAHs often dominating in the aquatic environment in terms of concentration and geographical distribution [112]. Another important difference between pyrogenic and petrogenic PAHs is that petrogenic PAHs do not occur in the sedimentary record to the same extent as pyrogenic PAHs, fewer petrogenic PAHs are released

into the environment. However, pyrogenic PAHs associated with soot and carbon appeared to be far more persistent and largely protected from various forms of environmental degradation [112].

2.2.3.4. Distribution of PAHs in sources to the Marine environment

The major sources of PAHs to the costal marine environment include urban runoff, wastewater effluents, industrial outfalls, atmospheric deposition, and spills and leaks during the transport and production of fossil fuels [112]. These compounds are environmentally important because of their carcinogenic or mutagenic nature.

2.2.3.5. Point sources

Point sources are those that are directly discharged into the marine environment from identifiable pipes or outfalls. Municipal wastewater facilities and industrial outfalls are majorly the point sources for most estuaries. The concentration of total PAHs in wastewater from North American and European municipalities ranges from $< 1 \mu\text{g L}^{-1}$ to $625 \mu\text{g L}^{-1}$ [112]. A high value of $216.5 \mu\text{g L}^{-1}$ has been observed for the Los Angeles county sanitation District which, unlike most other wastewater facilities, receives a large fraction of effluent from petroleum refineries. This effluent is dominated by two- and three- ringed PAHs (naphthalene, phenanthrene, and substituted naphthalene, phenanthrene) which is consistent with a strong signal from petroleum, either derived from refinery effluent or from urban runoff, and has been observed in Rhode Island, USA, wastewater effluents [113]. High concentration ($625 \mu\text{g L}^{-1}$) associated with oil shipping and refinery operation has been reported from effluents in the Eastern Mediterranean Sea [114]. Concentration ranges for wastewater treatment plants that serve primarily for domestic waste are generally less than $5 \mu\text{g L}^{-1}$ [74]. Sewage sludge generated from the treatment of wastewater contain level of PAHs in the order of $1.6 \mu\text{g L}^{-1}$ dry

weight, range 1.2 - 5.3 $\mu\text{g L}^{-1}$, depending upon the fraction of industrial waste in the treatment stream [74].

2.2.3.6. Distribution of PAH in Marine water

The concentration of total PAHs in the marine water are quite variable ranging from undetectable to 11 $\mu\text{g L}^{-1}$ [74]. The concentration ranges are so large that even within a relatively small geographic region; it is difficult to distinguish between areas. Generally, gradient does however occur where offshore concentrations are the lowest. [74]. PAHs in water partition between dissolved and particulate fraction, depends upon the solubility of the individual PAHs and the availability of binding substrate such as suspended particulate, according to the distribution of PAHs in seawater sample from the USA, UK and China [74]. Naphthalene is either the most, or nearly the most, dominant PAHs in the sample from the Hong Kong vicinity [115].

2.2.3.7. Distribution of PAHs in Marine sediments

The distribution of PAHs in the marine sediment is largely controlled by their solubility and hydrophobicity, making sediment their primary repository. As such, PAHs have been measured in sediment from a great number of regions around the globe. The distribution of individual PAH compound in sediments sample is generally dominated by 4, 5, and 6- ring species [74]. This is in contrast to the constituents in the dissolved or vapour phase or air, precipitation and seawater, which tends to be dominated by 2- and 3-ring species. The specific ratio of parent PAHs and parent to alkyl homolog distributions of PAHs are useful to determine the dominance of petrogenic versus pyrogenic sources. Parent compounds that do not contain alkyl constituents are indicative of pyrogenic sources such as, soot and other combustion-derived materials whereas, PAH distributions, dominated by alkyl constituents are representatives of petroleum sources [74].

2.3. Chemistry of the monitored PAHs

2.3.1. Anthracene (ATN)

Anthracene is a member of the low molecular weight polyaromatic hydrocarbon. It is a colourless and solid compound consisting of three fused aromatic rings with a chemical formula of $C_{14}H_{10}$, varying in appearance from colourless to pale yellow crystal like coal, **Figure 3**. It is hydrophobic because of non-polarity of the chemical structure [116], but it is soluble in a variety of organic solvents, such as toluene, ethanol, methanol, benzene, and carbon disulfide. Anthracene like other PAHs is a constituent of coal tar and commonly generated during combustion processes and pyrolysis of organic matters, Oil and petrol spillage into water bodies and is one of the numbers of polycyclic aromatic hydrocarbons (PAHs) on EPA's priority pollutant list. Exposure to anthracene arises through various ways such as oil spillage into water bodies, tobacco smoking, drinking water, breathing air or ingesting food that has been contaminated with combustion product. Eating grilled and charring food is another means of exposure to anthracene. It appears to aim at stomach, intestines, and lungs, liver, fat tissues, once in the body and there has been indication that it is probable to be an inducer of tumour [117-118]. Exposure to high doses of anthracene for a short time can cause damage to the skin, burning, itching and edema and a build-up of fluid in tissue can also occur when anthracene is ingested.

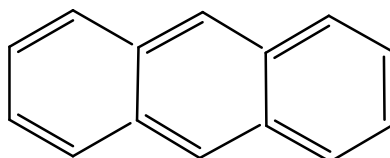


Figure 3. Structure of Anthracene.

2.3.2. Phenanthrene (PHE)

Phenanthrene (PHE) is a member of group of polycyclic aromatic hydrocarbon. It is composed of three fused rings of benzene with a molecular formula of $C_{14}H_{10}$. It is a colourless crystal-like solid with a faint odour, but can also appear as a white powder having blue fluorescence **Figure 4**. It has a boiling and melting point of 332 °C and 101 °C respectively. Phenanthrene is nearly insoluble in water but soluble in most low polarity organic solvent such as acetonitrile, benzene, toluene, carbon tetrachloride, chloroform, and ether or acetic acid. Phenanthrene is more stable than its linear isomer anthracene, based on the clar's rule, a theory for stabilizing hydrogen-hydrogen bonds [119]. The name phenanthrene is a composite of phenyl and anthracene [120] and the reactions of phenanthrene typically occur at the 9 and 10 positions including its oxidation reaction to form phenanthrenequinone [121-122], and has also been identified as one of the priority pollutant by the United States Environmental Protection Agency [37, 67, 123].

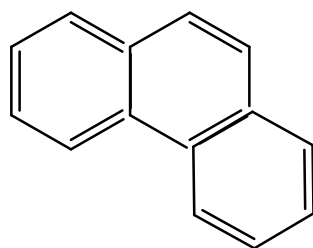
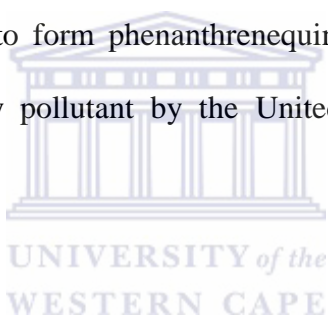
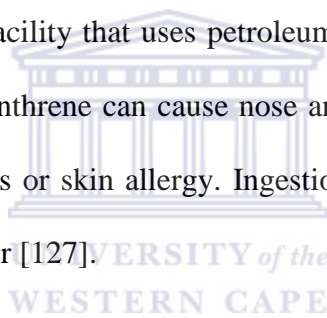


Figure 4. Structure of Phenanthrene.

Phenanthrene is among the persistent organic pollutants and a hydrophobic contaminant that is widely distributed in the environment, occurring as natural constituents of fossil fuels and their anthropogenic pyrolysis products [124]. It is widely distributed in the aquatic environment and has been identified in surface water, tap water, wastewater, and dried lake sediments. It has also been identified in seafood collected from contaminated waters and in smoked as well as charcoal-broiled foods [37, 67]. Exposure to phenanthrene is thus mainly from the environment. Fumes from vehicle exhaust, coal, coal tar, asphalt, wildfires, agricultural burning and hazardous waste sites are all sources of exposure. Eating foods grown in contaminated soil or by eating meat or other food contaminated with phenanthrene [125]. Exposure to phenanthrene can also be from working in a plant that makes coal tar, asphalts and aluminium, or that burns trash, facility that uses petroleum or coal, where wood, com and oil are burned [126]. Inhaling phenanthrene can cause nose and throat irritation, skin contact can result to rash, skin, burns, blisters or skin allergy. Ingestion through food or water can affect the fat tissues, kidney and the liver [127].



2.3.3. Pyrene (PYR)

Pyrene is among the group of polycyclic aromatic hydrocarbons (PAHs) and also a persistent organic pollutant, consisting of four fused benzene rings, resulting in a flat aromatic system. It is a colourless solid with a chemical formula of $C_{16}H_{10}$. The melting point ranges between 145 – 148 °C and boils at 404 °C [128]. Pyrene is ubiquitous in the environment as a by-product of the manufactured gas process and other incomplete combustion organic compounds [128]. It is present at thousands of sites throughout the United States and has been shown to be involved in the bacterial co-metabolism of the potent carcinogen benzo[a]pyrene [129]. Exposure to pyrene could be by eating smoked fish or meats [130]. It has also been found in surface and drinking water as well as in ambient air [128]. Subchronic oral exposure to pyrene produced nephropathy, decreased kidney weights, increased liver weights, although, slight haematological changes has been discovered in mice [131].

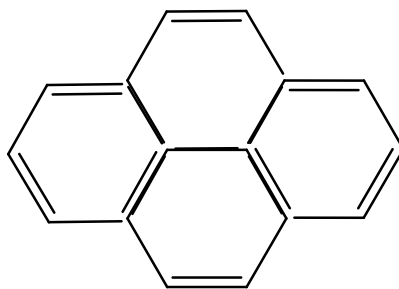


Figure 5. Structure of Pyrene.

2.4. Method of detection of polyaromatic hydrocarbon (PAHs)

Polyaromatic hydrocarbons (PAHs) have been traditionally detected and quantified by using several analytical techniques which include high performance liquid chromatography (HPLC) with UV-vis absorbance or fluorescence [132-133], titrimetry [134], mass spectroscopy [135], gas chromatography-mass spectrometry (GC-MS) [136], immunoassay and capillary electrophoresis (CE) equipped with laser-induced fluorescence [137], with acceptable accuracy, precision and specificity. However, they are not cost effective and methods of analysis are time consuming; a lot of chemical derivatisation procedure as well as large amount of organic solvent are required. Many of them are too cumbersome and not portable enough for field analysis. Moreover, it needs the assistance of an analytical chemist. Therefore, a suitable and cost effective method of analysis that can overcome all the above mentioned limitations of classical method, in form of Electroanalytical method is developed. Electroanalytical methods are regarded as a better and efficient method of determining PAHs in the environment. It has recently attracted a great deal of attention due to its adaptability and which has allowed its application in treatment and quantification of gases liquids and solids. It is environmentally friendly unlike other methods because the main reagent is electron which is referred to as “clean reagent” [138-139]. Other advantages include its energy efficiency whereby potential, voltage drops and side reaction are controlled, electrodes and cells can be designed to minimise power losses owing to poor current distribution. Consequently, electroanalytical method has found several applications in environmental science such as, electrochemical method of monitoring environmental carcinogens [140], electro-dialysis treatment of nitrogen in wastewater [141]. Electrodeionisation by direct and indirect anodic oxidation [142-143], to mention a few. Another point of interest in this present work is in the choice of electrolyte as the medium for detection of analyte. Acetonitrile, as a common and generally choice of electrolyte in the quantification of polyaromatic hydrocarbon is a non-aqueous electrolyte and

need the assistance of a supporting electrolyte to enhance conductivity and current migration. However, considering PAHs in their aqueous environment, it becomes our interest to use an electrolyte that is aqueous, more conducting and that can also allow the detection of PAHs in the aqueous environment. In this work, the choice of aqueous hydrochloric acid (HCl) as the working electrolyte in the detection and quantification of polyaromatic hydrocarbon goes along with the fact that HCl is a strong electrolyte due to its ability to ionize completely in water; it is more electrically conducting and has affinity for electroactive species, hence, the choice of HCl as the working electrolyte [144-145].

In this work and for the first time, an electrochemical method for the determination of PAHs has been developed in form of graphenated modified polyaniline doped tungsten oxide, constructed by electrodeposition of a mixture of polyaniline and tungsten trioxide on the surface of a graphene modified glassy carbon electrode which was then, used as an electrochemical sensor.

Review work on conducting polymer, graphene and metal oxide is further outlined in the chapter below.

2.5. Conducting polymers (Intrinsically conducting polymers, ICP)

A polymer can be referred to as a large molecule (macromolecule) composed of repeating structural units or chains typically connected by covalent chemical bonds. It essentially refers to a large class of natural and synthetic materials with a variety of properties and purposes [146-147]. Familiar examples of polymers comprises of plastics and proteins [148]. A simple example is Polyethylene [149]. However, polymers are not just limited to be mostly carbon backbones, an element like silicon can also form recognizable materials such as silicones, e.g.

polydimethylsiloxane [150-151]. The bases for the backbone of DNA can also be traced to Phosphodiester bonds. Natural polymers such as protein and nucleic acid have essentially contributed to biological processes and the main constituent of wood and papers are from a natural polymer cellulose [152-153]. The reality that polymers have been considered as insulators has not hindered their usage as inactive semiconductors especially due to their light weight and greater ease of fabrication. The appearance of conducting polymers which are conjugated can be dated back to the 70s and has opened up new era in the world of research. The new class of polymers possessing high electronic conductivity (*electronically conducting polymers*) was discovered by three collaborating scientists, Alan J. Heeger, Alan G. MacDiarmid and Hideki Shirakawa. They played a major role in this breakthrough, and which later earned them the Nobel Prize for Chemistry in 2000 “the discovery and development of electronically conductive polymers”. The preparation of polyacetylene and its large increase in conductivity after doping revealed the first conductive polymer by the group and the earliest to be recognized in the field of research [154]. Though, the polymers due to their extended π -conjugation has made doping possible, making them electrically conducting [155-156], but, they are surrounded with some limitations, which includes their poor processability and instability to surrounding environment, and this has rendered them unappealing for technological applications. Recently, conjugated conducting polymers with ease of processability (hence, soluble) and which will not lose their stability even in the doped form has been prepared [157]. This has generated much more interest in applied science and technology as a result of their unique electrical and physical properties, controllable chemical and electrochemical properties, chemical stability, high electron affinity and low cost [158], and readily available for various applications in areas such as biosensor [159-160], rechargeable batteries [161-162], light emitting diodes (LED) [163-165], electrochromic display devices [166-167], transistor and data storage devices [168-169], electromagnetic

interference (EMI) shielding [170-171], chemical sensors [172-173] and actuator [174] have been explored.

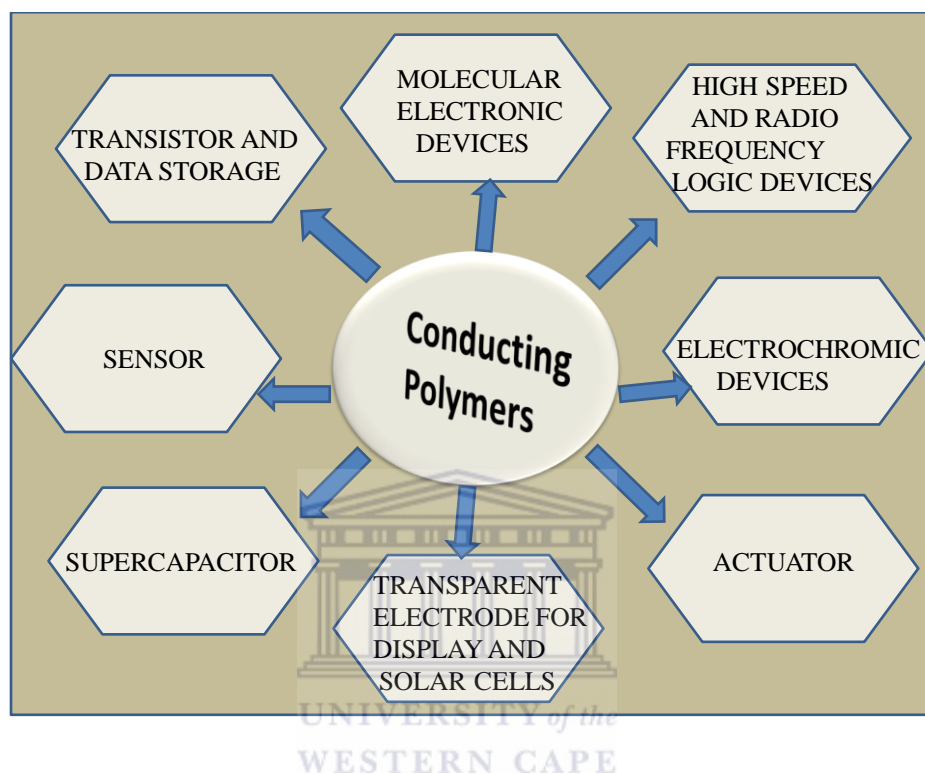


Figure 6. Overview of some applications of conducting polymers.

The emergence of conjugated conducting polymers preferably referred to as intrinsically conducting polymer (ICPs) has constituted a significant goal in modern research [175-176]. The various ICPs includes polyacetylene (PA), polyaniline (PANI), polypyrrole (PPy), polythiophene (PTh), poly(p-phenylenevinylene) (PPV), poly(3,4-ethylene dioxithiophene)(PEDOT), polyfuran and their derivatives [159]. These common forms of ICPs in their neutral states are however converted into semi-conductive or conductive states through chemical or electrochemical redox reactions. To broaden the functions or improve the performances of these polymers, ICPs are often doped with other functional materials to form composites. The variability of the conductivity i.e. the ease with which the polymers can be

reversibly switched between insulating and conducting form is an interesting and exploitable property [177]. Poly(acetylene) the simplest intrinsically poly conjugated polymer opened up the first synthesis and initiated the progress in the scientific investigation of conducting polymers properties hence, the reaction of poly(acetylene) with bromine or iodine vapours rendered the polymer conductive [178]. Further studies demonstrated that the reaction is redox and consists of neutral polymer chains which transformed into polycarbocations at the insertion of the bromine or iodine anion in order to neutralize the positive charge imposed on the polymer in the course of doping reaction, i.e. a counterion is formed which is the reduced form of the oxidising agent (corresponding to a p-type doping) or the oxidised form of the reducing agent (corresponding to n-type doping) [179-180].



2.5.1. Conductivity in conducting polymer

The following are the characteristics for a polymer to be electrically conducting:

- It has to behave like a metal, that is, its electrons must be in a movable state and not bound to the atoms.
- Polymers must consist of alternating single and double bonds, called conjugated double bonds.
- Every bond contains a localized “sigma” bonds which is the bases of a strong chemical bond. Similarly, every double bond also contains a less strongly localized “pi” bond which is weaker in conjugation.
- Electrons must be easily removed (oxidation) or added (reduction) without much interference of the “sigma” bonds which is primarily responsible for holding the polymer together. The process known as doping is of two types, the p- and n- type of

doping and can be achieved chemically or electrochemically. Consequently to electro-neutrality, doping requires the incorporation of a counter-ion.

The mechanism of conduction in conducting polymers is very complex due to its wide magnitude of conductivity which involved different mechanisms within different regimes. In order to understand the mechanism behind doping and conductivity in conducting polymer, the concepts of polarons, bipolarons, and solitons have been proposed, consequently, the nature of charges appearing on the polymer chains upon doping and the electronic band in the polymers has also been examined [181-183].

2.5.2. Polarons

The polaron is a radical ion (spin $\frac{1}{2}$) associated with a lattice distortion, and the presence of localized electronic states in the gap referred to as polaron states. The ability of a charge to significantly cause deformation around the lattice is the manifestation of a strong electron-phonon coupling which is thus denoted as P^+ or p^- depending on the sign of the charge. The level of polarons is within the upward shift of the highest occupied molecular orbital (HOMO) and the downward shift of the lowest unoccupied molecular orbital (LUMO), as a result, charge localization process is favourable relative to the band process, thus a localized electronic state in the gap [144]. This is different compared to a case of inorganic semiconductor as shown in **Figure 7**. In the **Figure 7a**, the level of the midgap are the level of the distorted region and are effectively added to the undistorted states described as the HOMO and LUMO. The formation of these distorted level is favourable since it gives rise to an overall reduction in energy which is referred to as binding energy, associated with the formation of a polaron. However, there could also be a bi-polaron being formed at this stage, **Figure 7b**

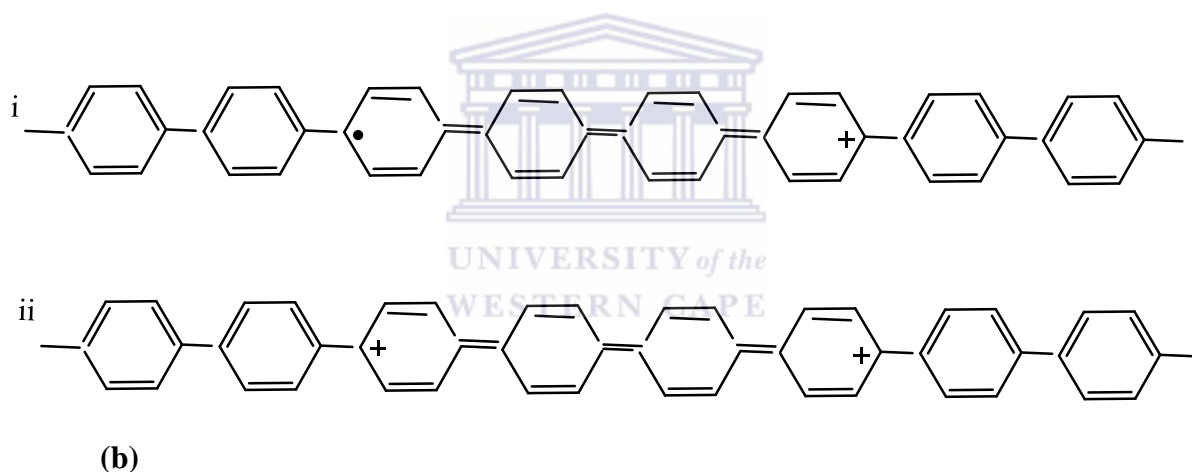
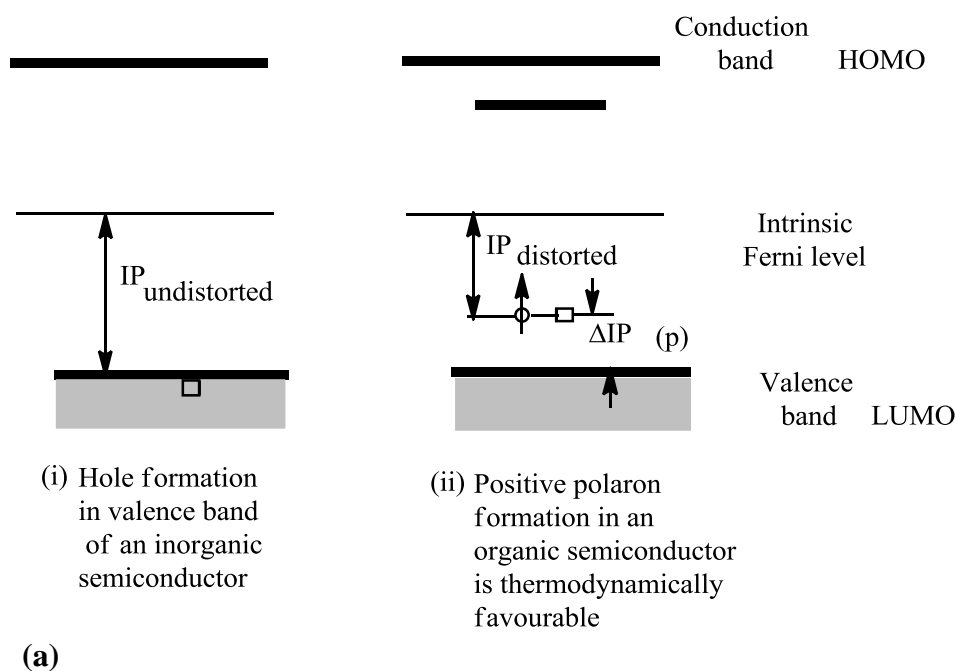


Figure 7. Distorted geometry of the excited state (lattice relaxation) results in a reduction of the ionization potential ΔIP (i), accommodation of charged within two ‘polaron’ states within the semiconductor gap (ii) (a) and A geometry representation of (i) a single polaron [radical ion coupled to a lattice distortion, having spin 1/2, charged $\pm e$ and (ii) a doubly charged bipolaron [spinless di-ion coupled to a lattice distortion], having a spin 0 and charged $\pm 2e$ (b). [144]

2.5.3. Bipolarons

A bipolaron is a bound pair of two polarons, formed when two polarons (i.e. the combination of electron and distortion) of like charges come to interact in a conjugated system. Of course, the two polarons must be close enough to share the same distortion and develop a lower energy, which effectively leads to attraction between the two polarons. If the interaction is large enough, then a bound bipolaron will be formed. This can be related to, theory of conductivity of a material consisting of two electrons coupled through a lattice vibration, i.e. a phonon. The formation of a bipolaron implies that the energy gained by the interaction with the lattice is larger than the coulomb repulsion between the two charges of same sign confined in the same location. Bipolarons and polarons process leads to carrier mobility which results in high conductivity of the polymers i.e. in doped conducting polymers such as polythiophene [145].



2.5.4. Solitons

Owing to the quasi one dimensional nature of conjugate polymers, the interaction between the electron and the carbon backbones in the system leads to instability in relation to the dimerisation of the lattice, which is usually portrayed as an alteration of single and double bonds. As a result, an excitation state referred to as, solitons occurred. Solitons can be referred to as mobile charge or neutral defect or “kink” in the polymer chain that propagate down the chain and reduces the barrier of interconversion. Compared to a polaron, a solitons has an unusual spin charge separation: a neutral solitons has spin $\frac{1}{2}$ while a charge solitons is spinless. Polaron, bipolaron and solitons are commonly believed to play major roles role in doping [183-184]. The formation of the charged carriers in doped polyaniline [147] shows that controlling the concentration of dopant can lead to an enhancement in conductivity due to formation of

charge carrier i.e. polarons/bipolaron which are facilitate through manipulation from the external potential and the coulombic field of counterion distributed along the chains [147].

Figure 8 showed the schematic illustration of doped polyaniline showing the formation of charge carries polarons (radical cations) and bipolaron (dications).

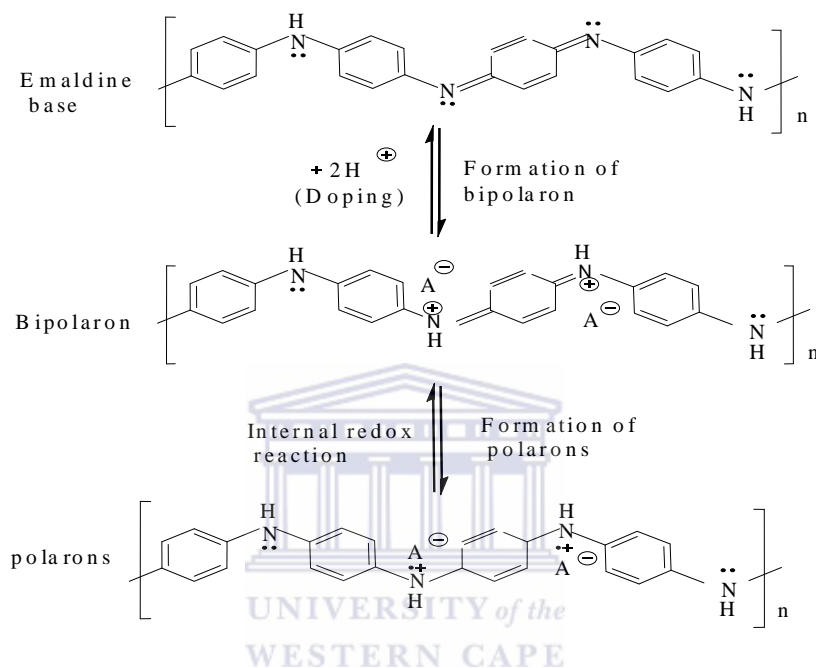
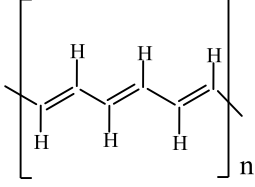
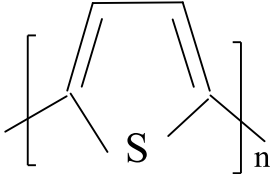
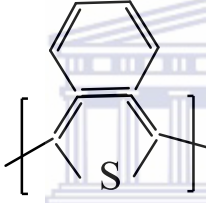
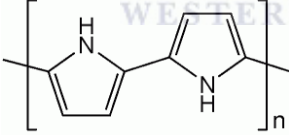
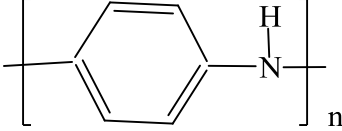
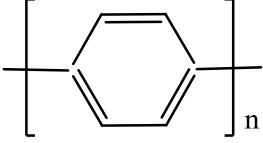


Figure 8. Schematic illustration of doped polyaniline showing the formation of charge carries polarons (radical cations) and bipolaron (dications).

The bases of conductivity in heterocyclic conjugated polymer can be attributed to the nearby sp^2 hybridised carbon centres in the polymer back bones. A valence electron on each centre resides in a p_z orbital, which is orthogonal to the three sigma-bonds. During doping, by oxidation, the electron in these delocalized orbital attained high mobility and some of these electrons are removed. Thus, a conjugated p-orbital is formed as a one dimensional electronic band. In this case, the electrons within this band are partially emptied and are mobile. Theoretically, an unfilled band can accept electrons if the same material is doped by reduction.

As a matter of fact, most organic conductors are doped oxidatively to give p-type materials. Delocalisation is limited by both disorder and coulombic interactions between electrons and hole, and generally, materials with conductivities less than $10^{-8} \text{ S cm}^{-1}$ are considered insulators, while those between 10^{-8} and 10^3 S cm^{-1} are semiconductors and those with conductivities greater than 10^3 S cm^{-1} are considered conductor [185-186].

The uniqueness for the conducting properties of conjugated polymers is actually derived from the delocalisation of p-electron bonding along the polymer chain. The ease at which the system can be oxidised or reduced is very important and this account for the choice of π – bonding system which can easily be twisted without much interference of the σ (sigma)-bonds which is mainly the dependable bond that is holding the polymer together. Unlike poly(acetylene) and purposely because of its limitations, heterocyclic conjugated polymers in the form of poly(aniline), poly(pyrrole), poly(thiophene), poly(furan) and their derivatives, which are known to be thermally stable due to their aromaticity can be easily prepared by electrochemical or chemical oxidation of their neutral polymers. The mechanisms of the two types of preparations lead to the polymers in their doped (oxidised) state. The neutral polymer can thus be obtained when they are reduced by electrochemical or chemical methods. Some various types of conducting polymers, structures, conductivities (S cm^{-1}), and type of doping (n or p) for some conducting polymers are listed out in **Figure 9**

Name of Polymer	Structure	Conductivity (S cm ⁻¹)	Type of doping
Poly(acetylene)		200-1000	n, p
Polythiophene		10-100	P
Polyisothianaphthene		1-50	P
Polypyrrole		40-200	P
Polyaniline		5-200	n, p
Poly(para-phenylene)		500	n, p

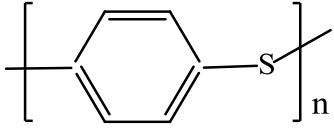
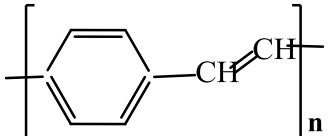
polyparaphenylene sulfide		3-300	P
polyparaphenylene vinylene		1-1000	P

Figure 9. Structure, conductivities ($S\text{ cm}^{-1}$) and type of doping (n or p) for some conducting Polymers.

2.6. Synthesis of polymer

Polymers that can be transformed into conductive polymers have more than one techniques of preparation, but the significant lead, is the incorporation of the extended π electron conjugation. Among several techniques for the preparation of polymers, oxidative coupling of the monocyclic precursor through standard polymerisations are mostly and extensive preparation techniques, and can either be chemical or electrochemical polymerisation [187]. Other various methods which include conventional [188], polycondensation [189], photochemical [190-191], plasma polymerisation, chain polymerisation, step growth polymerisation, concentrated emulsion polymerisation, chemical vapour deposition, solid-state polymerisation [152] to mention a few, have also been employed but with reported disadvantage such as, use of costly chemicals and time consumption [154].

The two different methods that have been extensively and generally used for the synthesis of conductive polymers are then discussed, i.e. **Electrochemical and chemical polymerisation.**

The reaction mechanism of the two techniques is based on oxidative coupling of monomer to produce polymer. Oxidative polymerisation is usually adopted in synthesising polymeric (oligomeric) products from various classes of monomers (aromatic amines, phenols,

thiophenols, aromatic hydrocarbons and heterocycles [192]. The monomers used are normally characterised by pronounced electron donor properties and high oxidation tendency. These properties, in particular, are intrinsic to aromatic amines, phenols and thiophenols or sulphur- and nitrogen-containing heterocyclic compounds due to the presence of electron donor substituent in benzene or heterocyclic ring. Oxidation of monomer takes place under the action of inorganic (or organic) oxidising agent (chemical oxidation) or the applied potential (electropolymerisation). During this process, cation or cation radical sites are generated in monomer (polymer) molecule, thus initiating polymer growth. In oxidation polymerisation, the oxidation reaction mechanism is illustrated on the chemical structure of polyaniline in **Figure 10**. A number of different initial products are likely to be generated which may be associated to differences in reaction condition. This frequently have a deep effect on the material's oxidation state, particle size, molecular weight, and degree of aggregation. The initial oxidation produces cation $[(\text{phNH}_2)]^+$ which can react with another aniline molecule through para position to produce polyaniline. Reaction can alternatively take through ortho or para positions but with much less probability than para. At the ortho position, reaction leads to further oxidation which produces phenazine-like moieties along the backbone of the polymer. Furthermore, aniline reacting through tail to tail, or head to head coupling will produce benzidine or azobenzene moieties respectively [193-194].

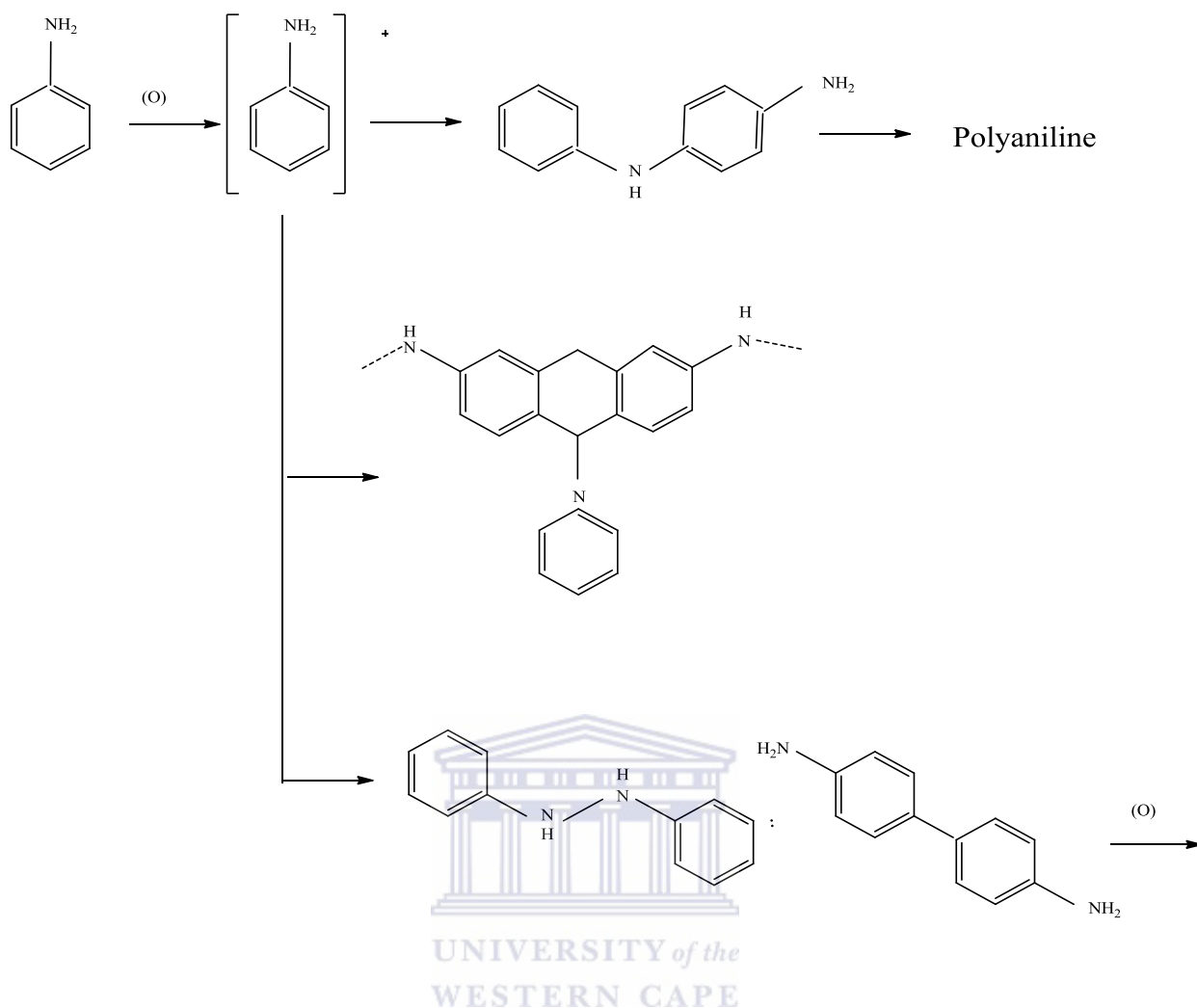


Figure 10. Schematic illustration of oxidation of aniline showing initial product of oxidation to resulting polymer [194].

2.6.1. Chemical oxidative polymerisation

The method is broadly used to synthesize large amount of conducting polymers and does not involve the use of electrode. The oxidation of the monomers to cation radical and the coupling of these cation radicals to form dication in a repetitive process and in the presence of an oxidising agent, to produce polymer, is referred to as chemical oxidative polymerisation. In a chemical synthesis, the monomer is exposed to an oxidising reagent in a basic medium e.g. ammonium persulfate (APS) or anhydrous FeCl_3 , the reaction is then initiated, resulting in the

formation of the polymer in its doped and conducting state. **Figure 11** showed a typical illustration of chemical oxidation reaction of polymer e.g. polyaniline. A neutral polymer can as well be achieved if the material is made to pass through a strong reducing agent such sodium borohydride, hydrazine or ammonia [195].

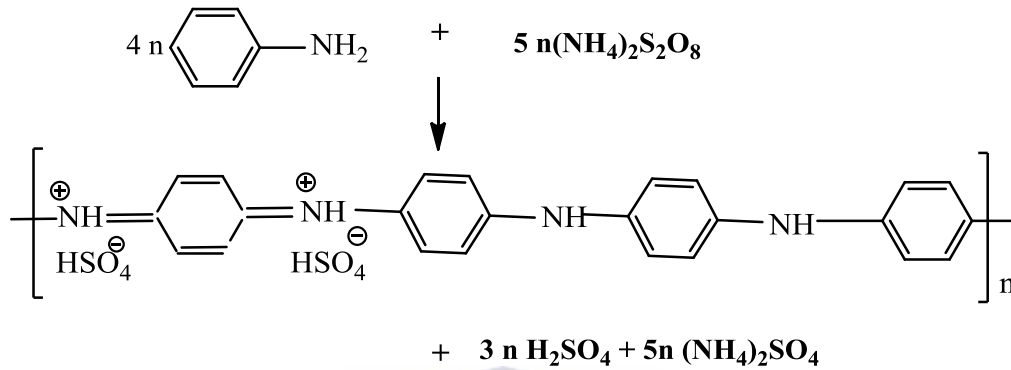
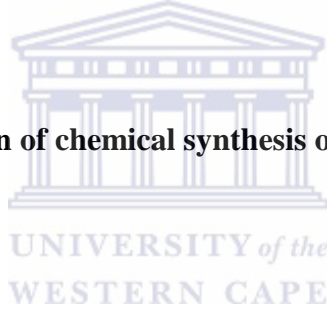


Figure 11. Schematic illustration of chemical synthesis of polymer (e.g. polyaniline).



2.6.2. Electrochemical polymerisation

In **electrochemical polymerisation**, the use of electrode is alternatively involved. The process is usually carried out in a single or dual-compartment cell by adopting a standard cell three electrode configurations in a supporting electrolyte normally dissolved in an appropriate solvent. The condition of method can be through potentiostatic (under voltage condition), potentiodynamic or galvanostatic (under current condition), using a suitable power supply. Electrochemical method of synthesis is a simple method to take up, and apart from the advantage of obtaining a conductive polymer which is doped at the same time, the process allows a broadly choice of cation ion and anions as “dopant ion” for use [196-199]. The synthesis method by electropolymerisation also depends on oxidation reaction, although reduction reaction is also possible [175].

Simple aromatic benzoid (e.g. aniline) and heterocyclic (pyrrole) are more preferably synthesised using this method especially where it involves a polymer thin film electrode. The conducting polymers of the monomers are easily controlled and can be obtained in an oxidised, high conducting state. However, the oxidation state of the polymer can be fine-tuned electrochemically, e.g. potential cycling between the oxidised, conducting state and the neutral, insulating state or by using a suitable redox compound. Therefore, the fate of the reactive specie depends on the experimental condition such as, the composition of the solution, temperature, potential or the rate of change in potential galvanostatic current density, material of the electrode and even the state of electrode surface.

In the synthesis of a polymer, studies revealed the mechanism to usually involve, a monomer dissolved in a solution of a supporting electrolyte by an external potential and leading to the formation of a cation radical as the initial reaction step, followed by a dimerisation reaction and then a stepwise chain growth proceed via the association of a radical ion or the association of a cation radical with a neutral monomer. Usually, the oxidation is accompanied by transfer of two

electrons ($2e^-$) per monomer unit, whereby, elimination of two protons ($2H^+$) occurred from each monomer unit to yield a neutral dimer, the dimer is oxidised and the process is repeated until the electroactive polymer film is deposited onto the conducting substrate. Thus, the deposited polymers is typically in its oxidised state [doped form], more reason for the presence of a supporting electrolyte to compensate for the positive charges along the polymer backbone [198].



2.7. Polyaniline

Among the family of intrinsically conducting polymers (ICP), polyaniline (PANI) has been found to be attractive and extensively studied owing to the good environmental stability, ease of synthesis, low cost, high electrical conductivity, and mechanical flexibility, attained by the polymer. It has unique multiple oxidation states as well as acid /base doped/dedoping response which has actually make it excellent for acid/base chemical vapour sensor. All these properties have prompted its potential application in various devices such as supercapacitors[200], sensor[201], electrochromic[202], actuators[203]. Other application includes its use for making electromagnetic shielding[171], antistatic coating and flexible electrodes [204]. Although, as earlier reported by researchers [205-207], the discovery of polyaniline, can be dated back to its intermittent report in the early 20th century. Investigation continued until 1862, when the ultimate report included the electrochemical method for the determination of small quantities of aniline [208-210]. The hypothesis then survived through some experiments by A.G. MacDiarmid and his co-workers, by demonstrating that the conductive state of polyaniline occurred from the protonic doping of emeraldine form of polyaniline [211-213]. This conductive polymer, polyaniline, continued to extensively gained attention, offering chances to deal with basic matters of importance to technology including e.g. metal-insulator [214].

2.7.1. Structure and oxidation state of polyaniline

The structure of polyaniline in its mixed oxidation state is shown in **Figure 12**, n equals the degree of polymerisation (DP) and the oxidation state is determined by the y values: Pernigraniline ($y = 0$) is the completely oxidised form of polyaniline (with imine links instead of amine links). Leucomeraldine ($y = 1$) represent the fully reduced form of polyaniline while emeraldine ($y = 0.5$) contains an equal fraction of both reduced and the oxidation form as

shown in **Figure 13**. Emeraldine form of polyaniline is often referred to as base (EB), is neutral, if doped, (i.e. the imine nitrogen has been protonated by an acid.) it is called emeraldine salt (ES), termed as protonation [215]. The polyaniline structure showed two main units, diiminoquinone-diaminobenzene as shown in Figure 11, during protonation, these two trapped unit in the emeraldine base are delocalized and the resulting emeraldine salt is formed. Thus, emeraldine base is best considered as the most useful form of polyaniline [216], apart from been highly stable at room temperature, the doped form, which is emeraldine salt (ES), is highly electrically conducting [217]. The two other forms of polyaniline, leucoemeraldine and pernigraniline are poor conductors, even in their doped state. This transformation of polyaniline to different forms with different colours, apart from the oxidation state, showed part of the uniqueness in its properties compared to other polymers. The emeraldine salt (green colour) obtained as the product from the polymerisation of aniline in acidic medium (electrolyte) can easily be further oxidised to pernigraniline (dark blue colour), which can further be treated with alkali to form violet pernigraniline. However, emeraldine salt can also be reduced to leucoemeraldine. All the various stage of reduction and oxidation conformation and colours has led to the differences in the conductivity of polyaniline which has provided its application in some devices such as supercapacitors electrochromic [218-219]. **Figure 14** showed the different structure of polyaniline in its doped form, from fully reduced leucoemeraldine via protoemeraldine to fully oxidised pernigraniline.

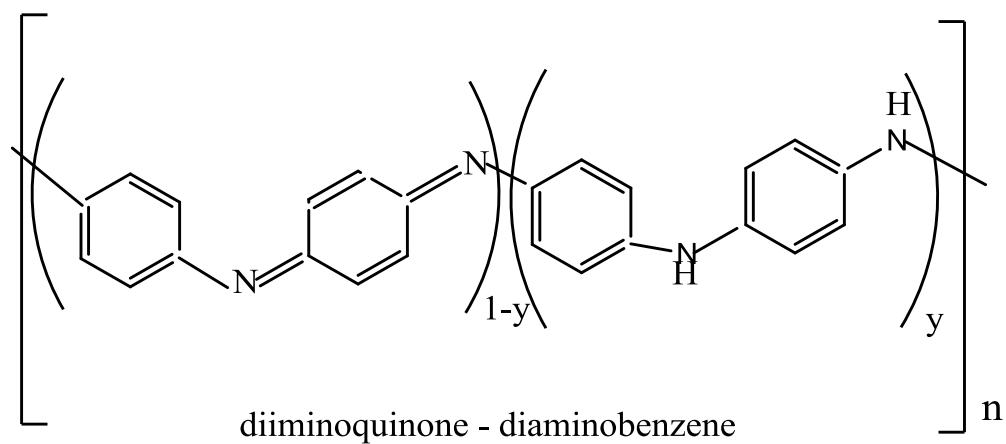


Figure 12. Structure of polyaniline.

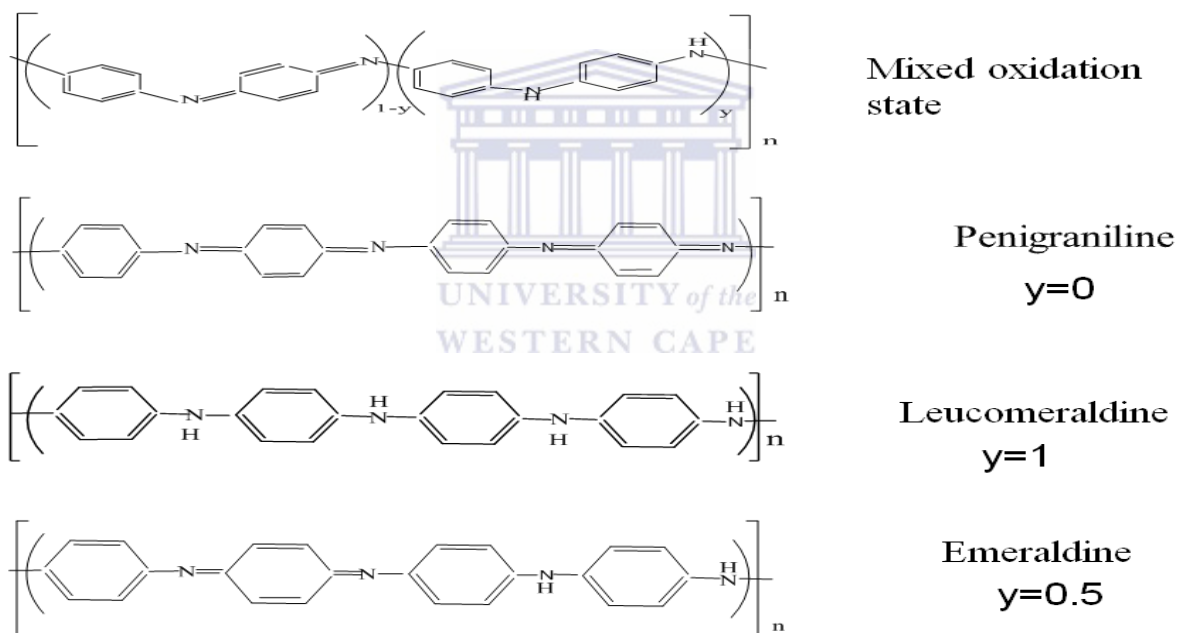


Figure 13. Structure of Polyaniline in its different form of oxidation states.

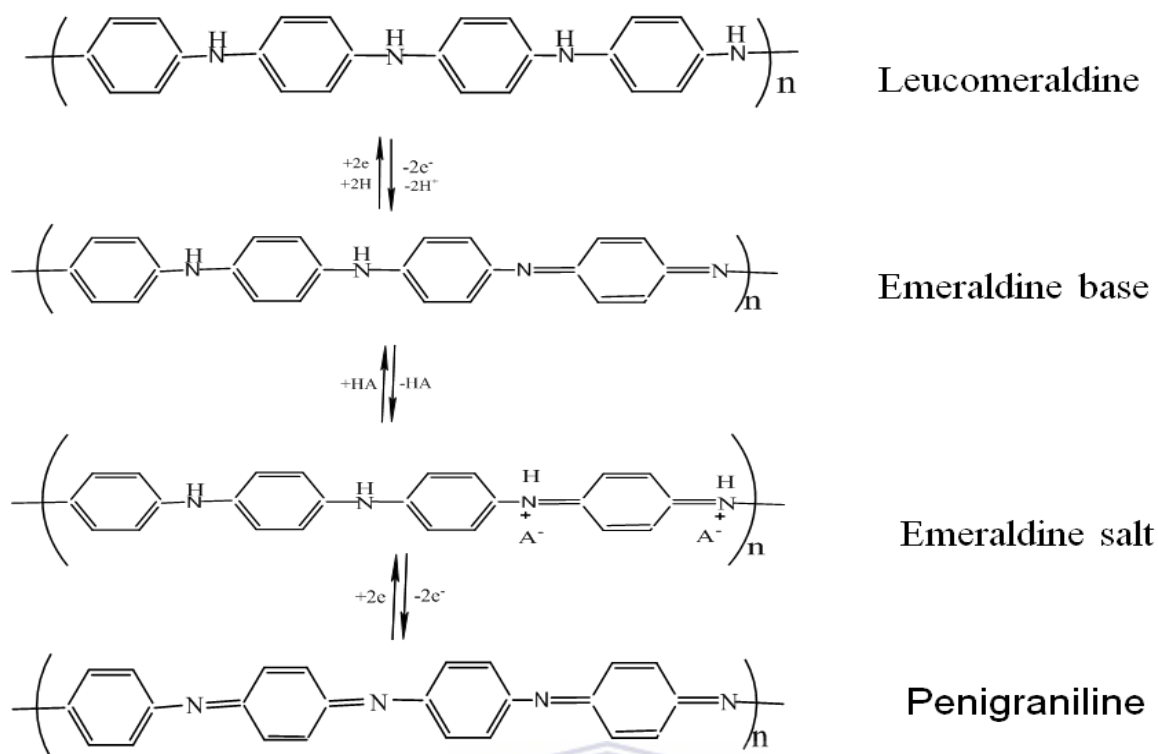
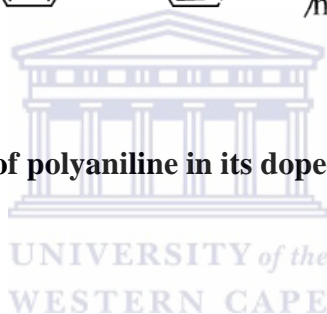


Figure 14. Different structures of polyaniline in its doped form.



2.7.2. Conductivity in polyaniline

Conductivity in polyaniline makes it one of its uniqueness compared to other electroconducting polymers, in that, the formation of the radical cation in the mechanism as well as the conjugation double bond system involve nitrogen atoms, whereas, in other electroconducting polymers, the formation of their radical cation ions involve carbon atom. As a result, the electrical conductivity of polyaniline reliance is on both the level of oxidation and reduction. Thus, the emeraldine form of polyaniline provides the opportunity to be protonated by doping to form a conducting form of emeraldine salt as illustrated in **Figure 15**. According to the bipolaron and polaron model proposed for emeraldine salt conductivity by Wallace *et al.* [220], and later established by Patil *et al.* [221], that formation of polaron as charge carrier elucidates

the high conductivity in polyaniline. Reported studies by Xue *et al.* [222] revealed that the degree of doping can actually determines the rate of conductivity, studies also reported that the highest conductivity of polyaniline can be attained at 50% degree of doping, which is associated with the emeraldine salt of polyaniline [220, 222-224], and the conductivity level and variation in their order of magnitude to be $10^{-2} \text{ S cm}^{-1}$ for undoped emeraldine and up to 10^3 S cm^{-1} for doped emeraldine [220].

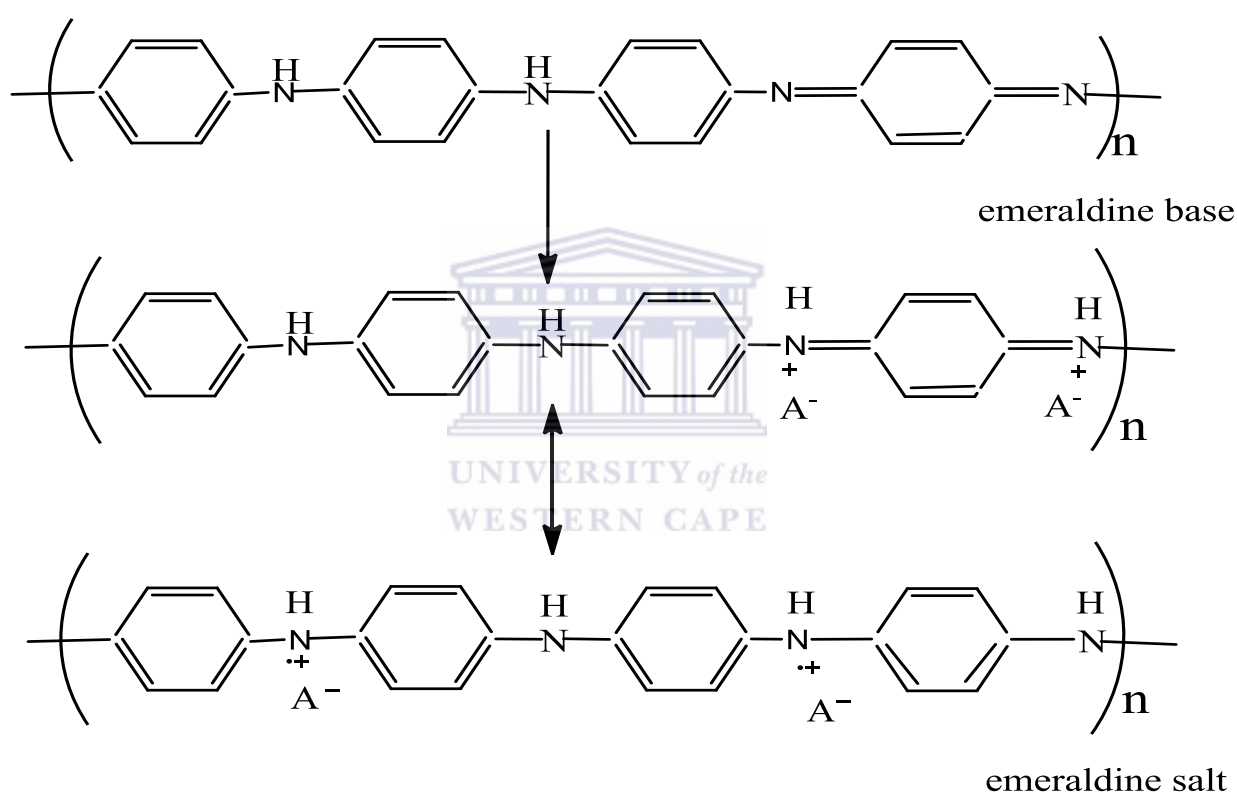


Figure 15. Schematic illustration of doped form of polyaniline (emeraldine salt) for protonation.

2.7.3. Synthesis of polyaniline

The method of synthesis commonly adopted to prepare polyaniline is electrochemical and chemical oxidative polymerisation method. The chemical oxidative polymerisation method of synthesis, involving the presence of an oxidising agent in acidic medium has been illustrated in **Figure 11**. The **electrochemical method** of preparing polyaniline is most widely and reliably used owing to its ability to direct the experimental condition for suitable purposes. The initiation and termination step of the reaction can be controlled as well as the scanning potential with electrochemical method of preparing polyaniline. However, studies have reported that, the type of polyaniline formed in terms of structural morphology, properties, type of film deposited on the substrate (thin or thick film) and type of substrate used and even conductivity, can be associated with the reaction conditions such as, type of supporting electrolyte and the pH [225-226], concentration of the choice of monomer [227], the applied potential and type of solvent [220] and using suitable redox compound [228-229]. Furthermore, choices of techniques that can be employed during synthesis of polyaniline by polymerizing aniline are, a constant potential (potentiostatic); constant current (galvanostatic); and a potential scanning/cycling or sweeping, and each with its different results. Polymer powder which glued weakly on the surface of the electrode has been formed at constant potential [230-231], while an experiment performed through electro-oxidation of aniline by potential sweeping, produced an evenly distributed, thin film that remained stuck on the surface of the electrode [232-233]. The general mechanism involved in the electrochemical synthesis of polyaniline from aniline monomer is illustrated in **Figure 16**, showing the radical cation from aniline monomer which is considered to be the rate determining step of the reaction, coupling to generate dimerisation, removal of two H^+ ion to generate a neutral dimer, and further chain propagation through oxidation of the neutral dimer into dimer radical that can react with a monomer or dimer, giving rise to elongation of the polyaniline backbone. The chain

propagation finally leads to formation of a polymer (e.g. polyaniline film on the electrode [227, 234])

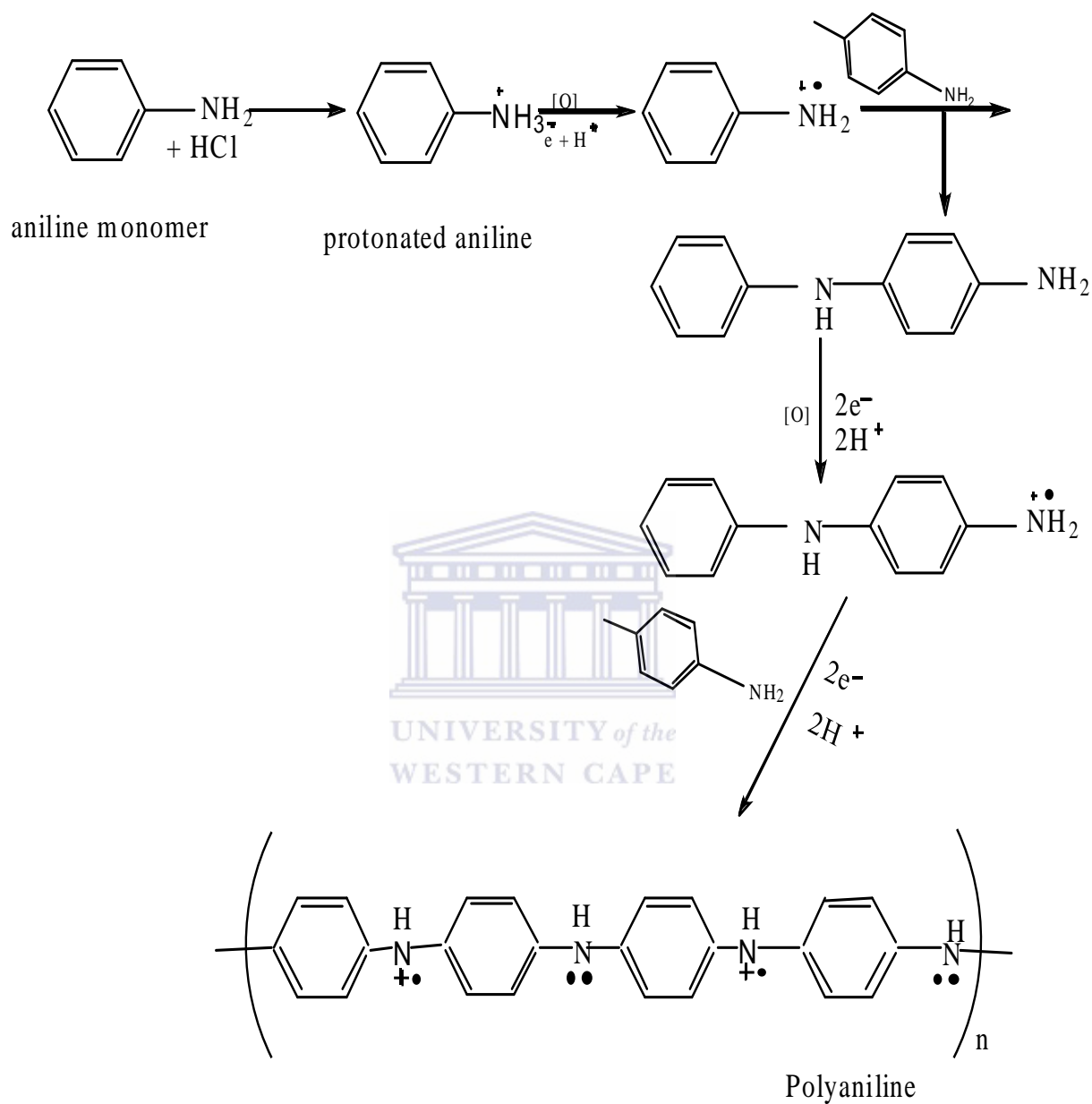


Figure 16. Possible reaction mechanism to generate polyaniline from polymerisation of aniline.

An electrochemical synthesis of a polyaniline performed using a glassy carbon electrode can be shown from the cyclic voltammograms in **Figure 17** below. Analysis was carried out in 1 M HCl solution at a potential scan rate of 50 mV/ s by cycling the potential between -200 and +1100 mV. The polyaniline showed a well redox activity. The two main anodic peaks assigned A and B, are reported to be corresponding to the transformation of leucoemeraldine base to emeraldine salt and emeraldine salt to pernigraniline salt of polyaniline while the reverse, C' and A' are both corresponding to the conversion of pernigraniline salt to emeraldine salt and emeraldine salt to leucoemeraldine base. The redox couple B/B' in the centre of the CV is regarded as an impurities such as the benzoquinone and the hydroquinone in the polyaniline. An increase observed in the redox peaks gave an indicated of formation of a conducting polymer on the electrode. This has also been confirmed and reported from studies [235-238].

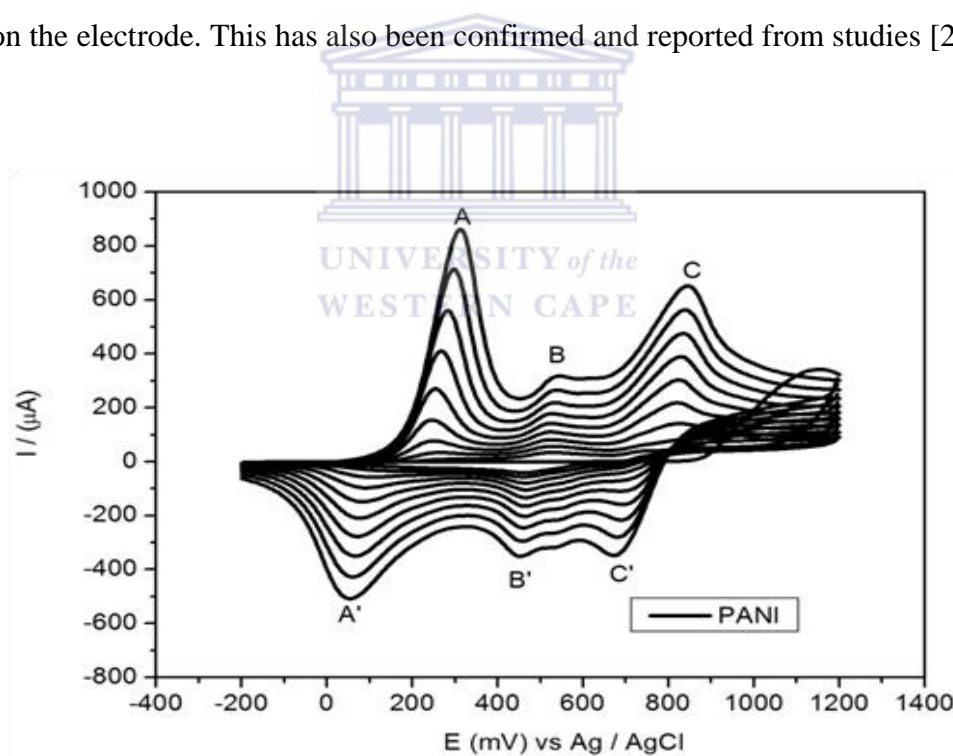


Figure 17. Electropolymerisation of Polyaniline in 1 M HCl solution at a potential scan rate of 50 mV/ s and window potential between -200 and +1100 mV

2.7.8. Doping in polyaniline

The basic method behind doping as earlier mentioned are the quasi-particles, referred to as polaron, bipolaron and solitons according to charges and spin distribution, especially in conjugated polymers. These formed the bases behind their conductivity in any suitable environment. Usually, polyaniline has appeared as a promising candidate among these groups of polymer owing to its ability to exist in a variety of protonation and oxidation forms as earlier illustrated in Figure 13. The protonated emeraldine, produced during the oxidative polymerisation of aniline in aqueous acid, is electrically conducting due to the presence of the cation radical in its structure. These positive charged units on the structure are then balanced by negative charged counterion (conjugated base) from any dopant such as chloride or sulphate ions which are usually inserted during electrochemical polymerisation and as well referred to as protonic acid doping. However, the concentration of dopant from studies reported to have profound effect on the morphology, conductivity and electrocatalytic activity of polyaniline and the polarisation method [179]. Experimental studies by Nair *et al.* [239], also reported the order of growth of polyaniline to increase with the increase in the size of the dopant.

2.8. Nanocomposite

The research on composite has brought about the benefit to develop a material that can offer possible properties and can precisely be suitable for a certain requirement. Nanocomposite can be regarded as a material that consists of two or more phases of solid, metal, gels, colloids or polymers in different dimensional, where one of the phases could be bulky and the other in a nano-dimensional phase combining together. Consequentially, the property of the nanocomposite is differing from the individual component materials as a result of the differences in structure and chemistry. Organic/inorganic materials as a class of nanocomposite

have captured the interest of researcher. Important effort is focused on the ability to get control of the nanoscale structure by means of innovative synthetic approaches. The properties of nanocomposite material depend not only on the individual parents but also on their morphology and interfacial characteristics.

2.8.1. Polymer nanocomposites

Polymer nanocomposites (PNC) consist of a polymer or copolymer having nanoparticles or nanofillers dispersed in the polymer matrix. These may be of different shape (e.g., platelets, fibres, spheroids), but one dimension must at least be in the range of 1–50 nm. These polymer nanocomposites belong to the category of multi-phase systems (viz. blends, composites, and foams) that consume nearly 95% of plastics production. These systems require orientation of the dispersed phase, controlled mixing/compounding, stabilization of the achieved dispersion, and the compounding strategies for all multi-phase systems, including PNC. However, nanomaterial of conducting polymers is of special interest as their properties are considerably different from the properties of corresponding macroscopic materials. Usually, a change in surface properties is observed when a conducting polymer is surrounded by a dopant, either nanomaterial or bulky substances such as nanotubes, nanoclusters, nanoparticle nanocrystals quantum dot, graphene transition metal oxide etc. as illustrated **Figure 18**. This however, forces the polymer backbones to interact with the molecules. A nanocomposite with different morphology is formed and which is capable of solubilising the conducting polymer. Nanomaterial of polyaniline can effectively provide a controlled electrochemical catalysis, orientation and solubilisation, as a result of the formation of micelles and obviously enhancing the quality of the polymer which has given them potential in application such as sensors.

Conducting polymer nanomaterial for a sensor construction has gained a lot of recognition owing to the large surface area. Therefore, some properties of the nanomaterial that may have

influence on the sensitivity of the devices should be given more concern, in terms of sizes, shapes and surface area of the nanomaterial. There is increase in surface area-to-volume ratio as the particles get smaller, leading to an increase in dominance of the behaviour of atoms on the surface area of particle over that of those interior of the particle. This higher surface area of the nano-particles affects the properties of the particles when they are reacting with other particles, the interaction with the other particles within the mixture is more and then increasing the strength, heat resistance and many other properties as well as factors do change for the mixture. Controlling these can invariably improve the material properties and function of the device. Fabricating conducting polymer nanocomposite-based sensors with high sensitivity as well as fast response time should also be of great desire and attraction. Conducting polymer nanocomposite with large specific surface area has been predicted to be an excellent sensing materials [240]. A relatively long time response has been noticed as a result of slow penetration in bulky polymer fabricated sensor [241-242]. Band gap in nano tubes has been controlled through particle sizes [243-244], mechanical properties have also been studied to be size dependent [245]. The yield strength and hardness of microstructure polycrystalline materials typically increases with decrease in size particles.

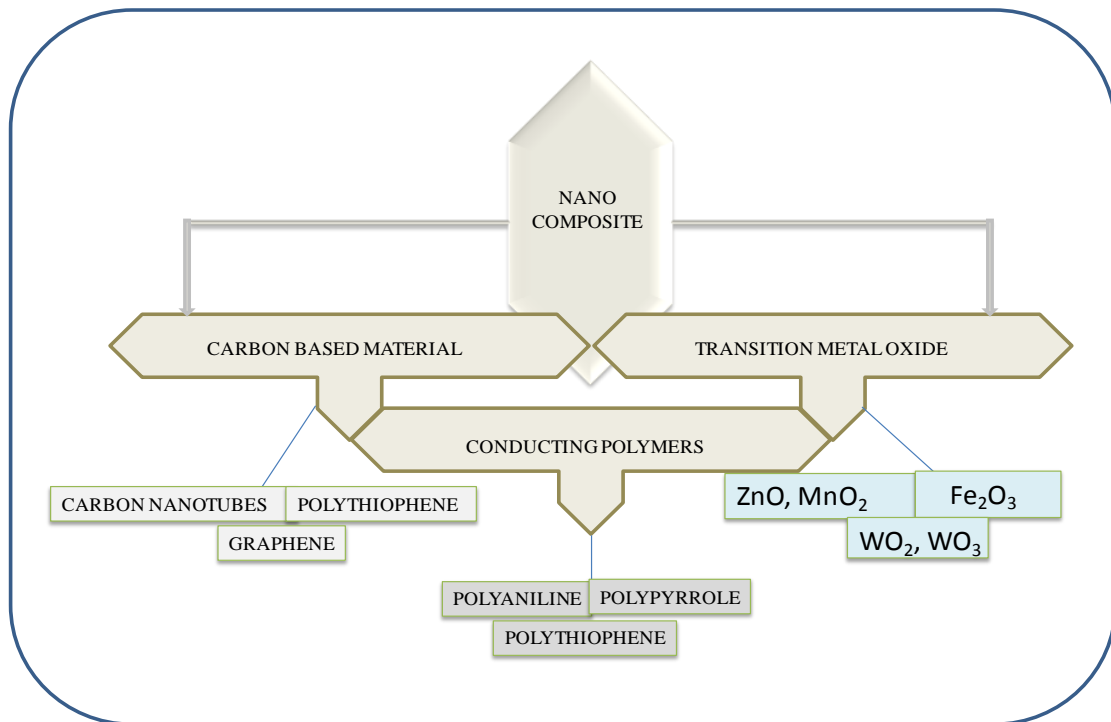


Figure 18. Schematic illustration of some materials of polymer nanocomposites.

The behaviour of materials formed from nanocomposites is different in comparison with conventional composites with microscale structure. Owing to the small size of the structural unit and the high surface-to-volume ratio [246], the properties of composite materials are greatly influenced by the degree of mixing between the two phases [209]. In conventionally filled polymers, the constituents are immiscible, resulting in a coarsely blended macrocomposite with chemically distinct phases, which resulted in poor physical attraction between the organic and inorganic components, leading to agglomeration of the inorganic components and therefore, weaker materials are achieved [247]. Besides, the micrometer size particles act as strains as a result of the concentration, whereas, in nanocomposite, problem of strains are avoided for the fact that the components are combined at nanoscale. Therefore, the structure of the composite also depends largely on the extent to compatibility of the organic and the inorganic component [247]. However, in polymer nanocomposite preparation, Clays

are usually used as additives because they are composed of layered silicates that can intercalate organic molecules. Analysis of smectite clay has shown that there are several levels of organization within the clay minerals. The smallest, primary particles are on the order of 10 nm and are composed of stacks of parallel lamellae with an average of 10 sheets per particle. Macroaggregates are formed by a lateral joining of several primary particles, and aggregates are composed of several primary particles and microaggregates. So, the lack of affinity between the hydrophilic silicate and the hydrophobic polymer makes it difficult to achieve a homogeneous mixture [248]. Therefore, Compatibility between the silicate clay layers and the polymers is achieved by ion exchange reactions. While the interlayer cations of silicate clays are usually Na^+ , Ca^{2+} , or K^+ ; exchange reactions with an organic cation increases the organophilicity of the clay layer surface. This lowers the surface energy and improves wetting with the polymer matrix [247]. In the cause of this, two particular characteristics of layered silicate particles are exploited in nanocomposite preparation; one, the silicate particles can be dispersed into individual layers, with a thickness of ~ 1 nm, and two, is the ability to fine-tune their surface chemistry through the exchange reactions with organic and inorganic cations [249]. Therefore, to prevent agglomeration and make the surface of the ultrafine particles stabilised, repulsive interparticle forces are then essential. The use of ionic surfactants is usually employed [250], as such, cation exchanged silicate are easily dispersed in an organic matrix, forming composites of two types which are: Intercalated structures where there can be an increased but relatively constant separation between the silicate layer [247-248]. Here the polymer chains are able to intercalate between the host layers in a crystalline repetitive manner to form a well ordered composite [249]. Exfoliated nanocomposite is another type, in which the unstacked mineral blocks are highly diffuse in the polymer, with a random interlayer distances and orientation [247, 249]. Therefore, in forming polymer nanocomposites, two types of

nanocomposites are thermodynamically achievable and which are; intercalation and exfoliation nanocomposites.



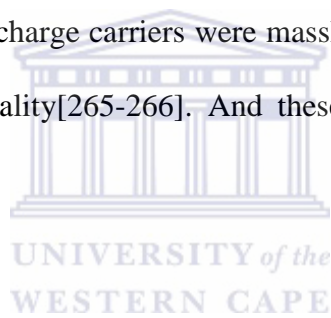
2.8.2. Methods of preparation of polymer nanocomposite

Quite a number of methods of preparation have been employed in the preparation of polymer nanocomposite. Apart from the sol-gel process [251-252] and monomer/polymer grafting to clay layers [253]. Others method of synthesis that are later discussed includes melt method, solution mixing and in-situ intercalative polymerisation method.

2.9. Graphene

Graphene is a leading light on the horizon of technology especially in chemistry, physics and materials science and as such now speedily on the increase. This strictly two-dimensional material exhibits outstandingly and surprisingly high crystal and electronic quality. Regardless of its short history, has already made known a large amount of its potential applications including field emission, electronics, sensor and energy. By and large, graphene represent a theoretically new class of materials that are only one atom thick and, this basic concept has opened up a new ways into a technology that has never ceased to amaze and keep on to yield productive sights for more applications in the world of science and technology. Graphene is the two dimensional allotrope of carbon, a one atom thick planar sheet of sp^2 -bonded carbon-carbon distance of 0.142 nm forming a densely packed honeycomb crystal lattice in structure. [254]. The name was invented in 1962 by Hanns-peter Boehm who combined graphite and the suffix-ene, describing graphene as the single layers of stacked sheets of graphite [255]. This interesting material was discovered later in 2004 from University of Manchester by A.K Geim and his co-workers, through a simple scotch tape experiment which later awarded them, a noble price in 2010 [256-257]. This breakthrough has recently resulted in an award of a £1 billion grant by the European Union at the program for research and innovation, on 'Graphene and Human brain project' presented by the commission as part of its EU budget proposal for

2014 to 2020, (EU press report 2013) [258]. This gave an indication that research on graphene is one of an emerging translational nanotechnology and will continue to make profound impact in various aspects of technology. Regarded as a two dimensional honeycomb lattice, graphene is the basic structural and mother of all other dimensional allotropes of carbon as shown in **Figure 19**. It can be wrapped up into Zero dimensional (0D) fullerenes, rolled into one dimensional (1D) nanotubes or stacked into three dimensional (3D) to form graphite [259]. Conversely, graphene though described as an integral part of 3D material, had been alleged not to exist freely [260-261], and thermodynamically unstable regarding its structure formations of different dimensions. The notion was later proved wrong, when a free standing graphene was surprisingly discovered and supported by numerous experiments to back it up [262], and finally confirmed with certainty that its charge carriers were massless Dirac fermions [254, 263-264], as well as exhibiting high crystallinity[265-266]. And these discoveries led to a blast in the interest of graphene.



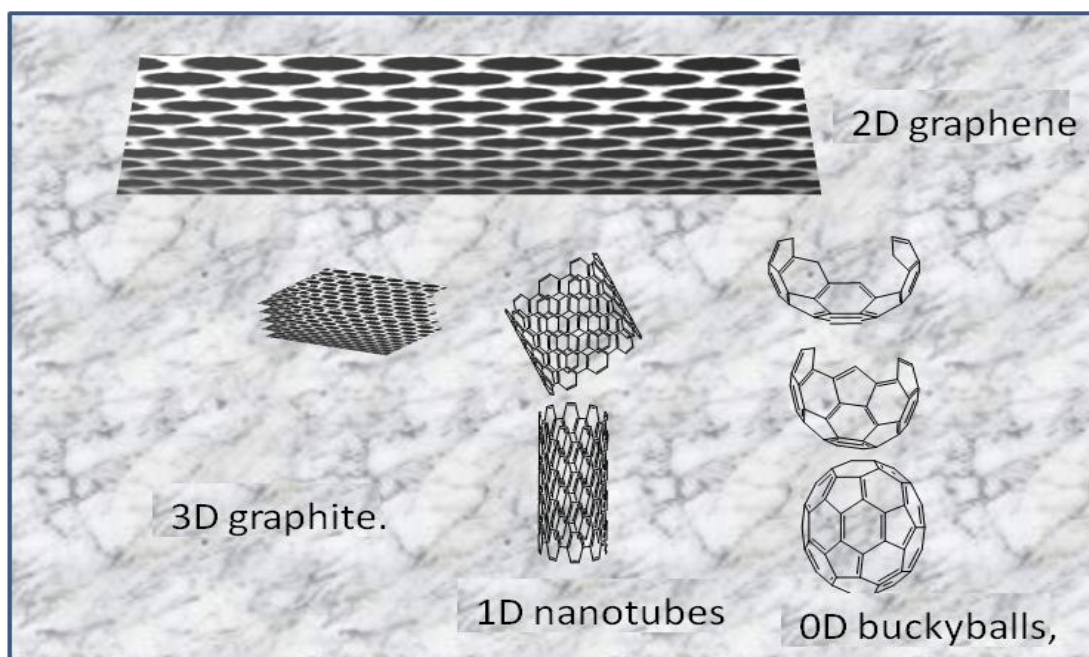


Figure 19. Graphitic forms of graphene showing the different types of dimension.

Consequently, graphite has been known as an abundant and naturally occurring mineral [267-268] and allotrope of carbon [269]. It is basically referred to as draw or write, and then applicable in pencil [270-271]. Hence, when one writes with a pencil on a sheet of paper, graphene stacks is actually been produced and somewhere among these stacks are individual graphene layers. Unlike other forms of carbon e.g. diamond, graphite is an electrical conductor, due to its electronic structure [272-273], and much more stable than other forms of carbon. Thus, use in such application as counter electrodes for dye-sensitized solar cells [274-275]. The morphology of graphite revealed layers of planar structure of carbon atoms arranged in a honeycomb lattice to each other with a separation of 0.142 nm and the distance between the plane is 0.335 nm, bounded by weak dispersed forces.(van der Waals forces) [276]. The van der waals forces adjacently binding the sheets together can be removed by different

experimental approaches that brings about the possible route to single layer of graphene sheet [277-278].

This advance allowed easy production of high-quality and crystalline graphene and opened ways to massive experimental activities unabatedly [277]. A typical structure of a natural graphite and layer of graphene sheet from graphite is illustrated in **Figure 20** and **Figure 21** respectively below.



Figure 20. A typical structure of natural graphite.

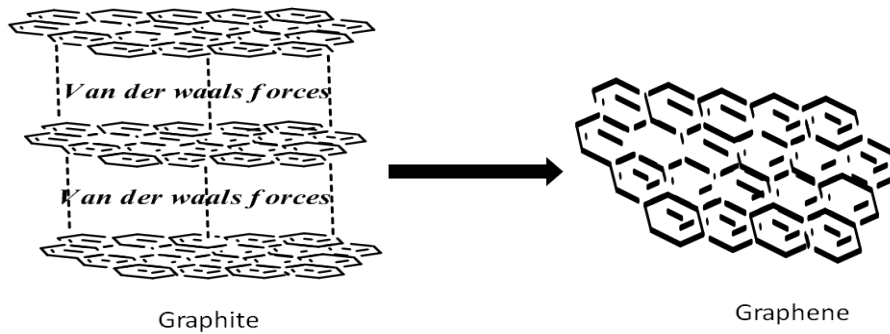


Figure 21. Schematic illustration of graphite stacked layered sheets to single layer of graphene.

2.9.1. Properties of graphene

Graphene has distinctively emerged as an exciting material, capturing the interest of every individual in the world of research, strictly owing to its intrinsic and exceptional properties which include excellent electron mobility through its atom thick sp^2 bonded 2-D structure [254], current density, superior thermal conductivity [279-280], high mechanical and tensile strength [264, 281-282], optical transmittance [283] and fascinating transport phenomena such as quantum Hall Effect [284] and surface area of over $2,600\text{m}^2/\text{g}$ [285]. **Table 1** presents the outstanding properties of graphene. These intrinsic properties as well as its easy availability, have enabled graphene to find potentials in numerous applications, for example, electronic devices [286], field emitters[287], batteries [288-289], solar cells [290-291], electronic display [292], sensors [293], thermally and electrically conducting composite, and structural composite with enhanced mechanical properties [294].

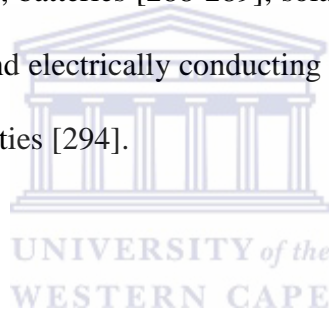


Table 1. Some of the unique properties of graphene.

Property	Graphene	Reference
Electron mobility	15000 cm² Vs⁻¹	[279]
Resistivity	10⁻⁶ Ω cm	[279]
Thermal conductivity	4.84 – 5.3 × 10³ Wn⁻¹ K⁻¹	[279]
Coefficient of thermal expansion	-6 × 10⁻⁶ K⁻¹	[279]
Elastic modules	0.5 – 1 TPa	[264]
Tensile strength	130 GPa	[264]
Transmittance	> 95% for 2 nm thick film > 70% for 10 nm thick film	[283]

The remarkable electronic properties of graphene can be attributed to the nature and major character of bonding in sp² hybridisation. Hybridisation (i.e. combining of atomic orbitals to form hybrid orbitals) in carbon atom which is the primary and elementary constituent of graphene, is associated with 6 electrons with an electronic configuration of 1s²2s²2p². This represents the atomic ground state configuration, where the four valence electron that initiates bonding are, the two electrons in 2s subshell and two electrons in the 2p subshell. This is illustrated in **Figure 22**. For hybridisation to take place, one of the 2s electron is promoted into the empty 2p orbitals and this resulted into an excitation state where a bond can then be

formed. However during hybridisation, the number of hybrid orbitals formed determines how many numbers of atomic orbitals are mixed and this is what brings about the different forms of hybrid orbitals sp , sp^2 , sp^3 etc.

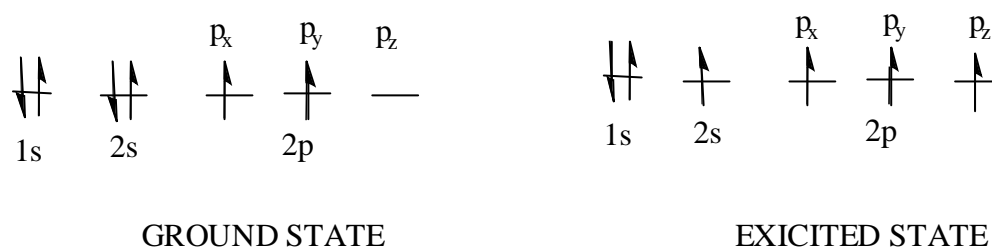


Figure 22. The electronic configuration of graphene in the ground and excited state.

In graphene, sp^2 hybridised orbitals are responsible for bonding. From the excited state, three atomic orbitals, 2s and two 2p ($2p_x$ and $2p_y$) mixed to form three hybrid orbital for each of the carbon atoms leaving an unmixed 2p orbital which represent the unbonded fourth electrons in the orbital and also participate in bonding by contributing the one electron per carbon atom. This is illustrated in **Figure 23**.

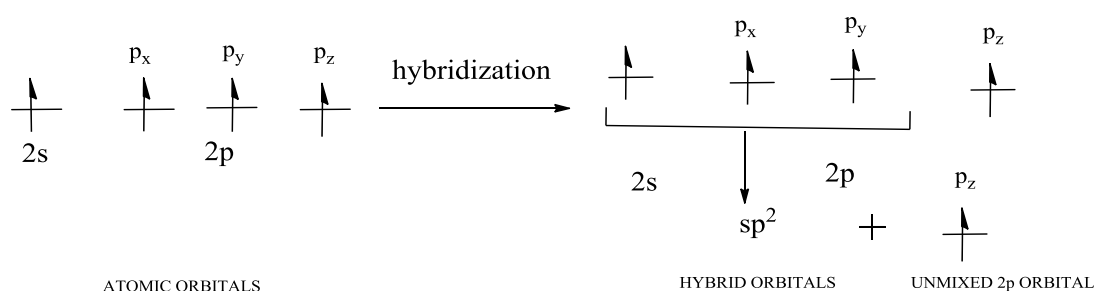


Figure 23. Illustration of hybridisation in graphene.

Each carbon atom is sp^2 hybridised and is been represented by the three equal lobes pointing outwards in a plane and forming sigma bond with sp^2 of the neighbouring carbon atoms and one $2p_z$ which occupies a pi orbital that participate in bonding, extending vertically above and

below the plane as shown in **Figure 24a**. Hybridisation of these three equal formed lobes spreads and one $2p_z$ which occupies a pi orbital that participate in bonding, creates movement of electrons across the whole graphene sheets and forming delocalisation of the π electrons over the whole structure. The carbon-carbon distance is estimated to be 0.142 as shown in **Figure 24b**, behaving like massless relativistic particles [262] and interacting with the periodic field of the hexagon crystal lattice that later forms Dirac fermions, described as cone like energy bands [295]. This uniqueness makes graphene an extremely good electrical conductor compared to ordinary semiconductor and also contributes to other remarkable properties of graphene.

Considering the astonishing electronic quality exhibited by graphene as crystal, it is quite dissimilar from a three –dimensional material like silicon. The energy of quasiparticles which can be described by energy bands, in graphene, the behaviour is different compared to an ordinary semiconductor. In an ordinary semiconductor, the conduction and valence band are separated by a band energy referred to as band gap and which obviously represents the amount of energy required to increase the electron from the valence band to the conduction band and with a parabolic band structure **Figure 25a**. But as for graphene, the band structure showed valence band and the conduction band to be smooth sided cones which meets at a point (k) referred to as, Dirac point **Figure 25b** [296].

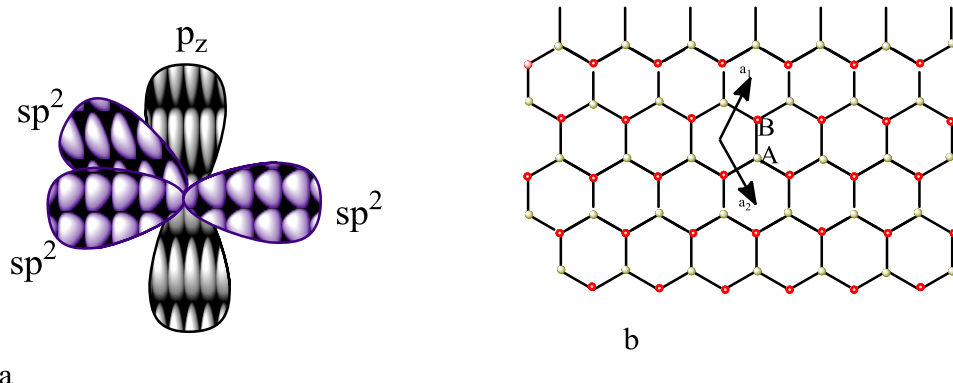


Figure 24. Schematic view of the sp^2 hybrid orbital and (b) View of hexagonal lattice in graphene [297].

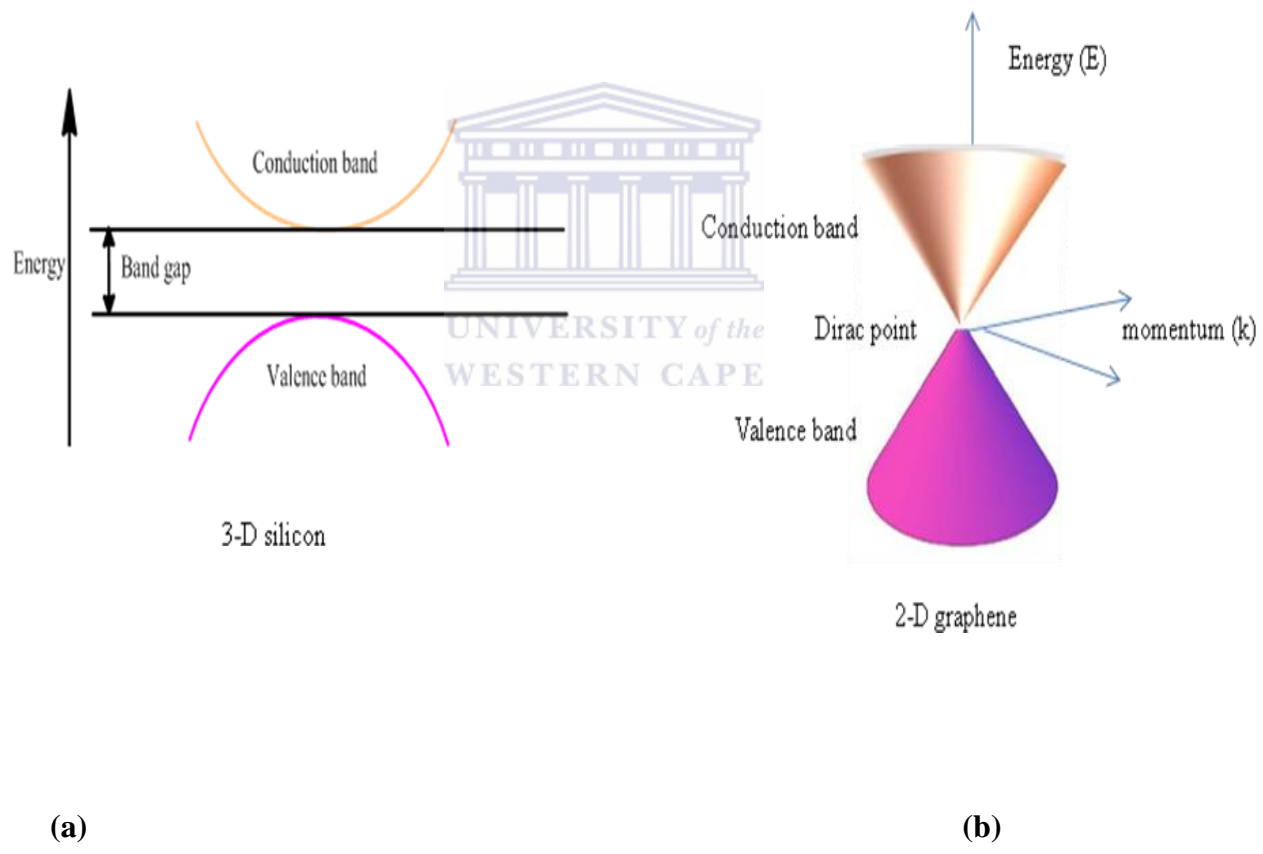


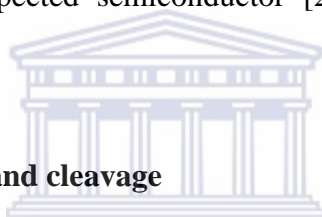
Figure 25. Schematic view of energy band in (a) 3-D and (b) 2-D graphene [296].

An exciting result of the above exceptional band structure in graphene is the ability of the electrons to move freely without collision and at enormous distance, thus their capability of

greater electrical conductivity (10 to 100 times) than a normal semiconductor even at room temperature (e.g. silicon) thus, a promising candidate such as electronic, sensor, computing, biomedical and in many other applications.

2.9.2. Methods of graphene synthesis

In an attempt to come up with a technique that can yield a quality and large amount of graphene, numerous preparation methods have been developed and even currently in process, but each one with a unique characteristic. Nevertheless, a 2-D crystal with a single atomic plane graphene is the priority. Emphasis has been made on number of layers of graphene to play a vital role in actually coming up with a material that serves the purpose in terms of electronic properties and an expected semiconductor [264, 296]. Some of the numerous approaches are discussed:



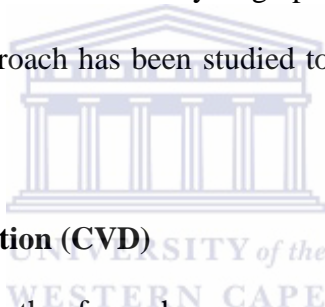
2.9.2.1. Mechanical exfoliation and cleavage

Exfoliation technique has been the earliest attempt of synthesis of graphene from bulk of highly ordered pyrolytic graphite (HOPG) [262, 264]. Novoselov and his workers, through mechanical exfoliation, were the first to obtain a free standing single graphene sheet by use of cohesive tape enough to break the weak van der waals forces binding the bulky layers of graphite and repeatedly peeling the crystals into increasingly thinner pieces, a method referred to as scotch tape method [25]. Although, a large defect free material with excellent electronic properties compared with other techniques is achieved by this approach, it is only limited by the size of the isolated graphene flakes obtained, only a few micrometres in size are usually produced and also has the tendency of restacking or crumple [298]. The exfoliation technique opened up diverse ways of modification by researchers so that they can come up with techniques that can avoid the limitations and more especially an intrinsic, stable and pure 2-D crystal [266], which can be visible by naked eyes. Other means of mechanical exfoliation is

through chemical oxidation of graphite, the graphite oxide is then exfoliated to provide large amount of graphite oxide monolayer which unavoidably yielded a substance with defects as a result of the chemical treatment [299]. A defect free monolayer graphene among other researchers has then been demonstrated [31, 300]. Although, a high cost of solvent (N-methylpyrrolidone) and high boiling point which can actually affects the graphene deposition are involved. Through the use of surfactants, Lotya *et al.* [301] and Green *et al.* [302], have been able to produce a graphene monolayer that is however stabilised against aggregation and thickness controlled. Similarly, exfoliation can be through absorption of small molecules between the layers of graphite or by non-covalently attaching molecules of polymers onto the sheets of the graphite to form graphite intercalation compounds (GICs) [303]. Agglomeration in graphite is however reduced by this method and the graphitic layer is protected by the guest molecules. Thus, the interaction of the molecules with graphite layer by charge transfer can either increase the in plane electrical conductivity or decreases the conductivity when it forms covalent bonds, due to the interruption of the conjugated sp^2 system. A high quality single layer graphene that is stable has also been produced through expansion of graphite, using concentrated sulphuric acid which has proven to be the best ultrasonic solvent to offer an optimum condition of preparation. This acid intercalated expandable graphite (EG) could be prepared by means of ultrasound irradiation, chemical oxidation or electrochemical process [304-305]. Chia *et al.* [306] and Li *et al.* [307] has reported a hundred times in volume of graphite expanded at high temperature. Other approaches that have shown potentials to the preparation of graphene sheets besides mechanical exfoliation are epitaxial growth from silicon carbide (SiC), chemical vapour deposition (CVD) and chemically derived graphene method.

2.9.2.2. Epitaxial growth on silicon carbide

In variation to mechanical exfoliation approach of producing graphene is the epitaxial growth on silicon carbide. This process requires the heating of silicon carbide at a very high temperature (above 1100 °C) to get reduced to graphene. The epitaxial graphene produced from this process depends on the size of the silicon carbide substrate and this can have influence some properties like the thickness, motilities (with extreme large temperature dependence), carrier density [308] as well as some of the electronic band structure of the graphene produced [309] and quantum Hall effect [285]. Improvement on the substrate quality and better understanding of the growth process can actually improve the quality of the graphene produced and to achieve a monolayer graphite [310]. However, the modified graphene produced from this approach has been studied to have a lot of advantages in device application [311-312].



2.9.2.3. Chemical vapour deposition (CVD)

This approach involves the growth of graphene on metal substrates. A single crystal of ruthenium has been illustrated to yield a sample of graphene with high purity, via either thermal decomposition [313-314] at high temperature of about 1000 K or by controlled segregation of carbon from bulk of the substrate. Metal substrate like iridium and many other transition metals like nickel (Ni), cobalt (Co) and platinum (Pt) could possibly yield a graphene that is uniformly thick and weakly bonded but slightly rippled [315]. This has enabled an extensive usage in electronic, catalysts or sensing applications [316]. Graphene growth on nickel substrate has also been described by Reina *et al.* and Lahiri *et al.* [317-318].

2.9.2.4. Chemically derived graphene

Preparation of graphene through chemical route involves the extraction of graphene from graphite by chemical method. A process whereby graphite oxide (GO) is synthesised through oxidative treatment of graphite based on Hummers method. Using oxidants such as concentrated sulphuric acid, nitric acid and potassium permanganate, with modifications from different individual researchers to suit applications, which invariably showed that the level of oxidation depends on the method, reaction condition and precursor (graphite) used [319-321]. Albeit, there is still substantial debate about the specific structure of graphene oxide over the years, and even till date the definite model is yet to be determined.

Many review work on the structure has been presented by different authors and their groups [322-325]. The graphite oxide (GO) produced compared to pristine graphite oxide bears oxygen functional groups such as hydroxyl and epoxy groups on the basal planes as well as carboxyl and carbonyl group at the edges of the layers of graphite oxide [325-326]. The van der waals interaction between the layers of graphite oxide is then altered by these oxygen functionalities and resulting in the hydrophilic nature as well as easy intercalation of water molecules between the layered sheets, and a well stable colloidal dispersion during exfoliation [327-328]. This exfoliation process gives rise to single layered sheets of graphene oxide which however shares the same chemical properties with graphite oxide but different features structurally [265, 299]. The oxygen functional groups situated on the basal plane and edges of the sheets has actually provided a reactive site for a variety of surface modification reaction to achieve a functionalized graphene-oxide and graphene-based materials, and apart from its low cost, easy access, scalability and widespread and ability to convert to graphene which have attracted much interest [329-330], graphene oxide (GO) is rendered electrically insulating by consisting of defects as well as disorders [265, 331], which can be attributed to disruption of

the conjugated electronic structure by these functional groups, brought about during oxidation. However, important progress has been made to produce thin film sheet with decrease in the hydrophilic character and essentially restoring the electrical conductivity through chemical reduction of the homogeneous GO suspension [300, 331-332]. These has enabled the usage in a wide range of applications in graphene based electronics and optoelectronic devices such as field effect transistors, chemical/bio sensors, organic solar cells and transparent electrodes. A typical structure of graphene oxide is shown in **Figure 26**.

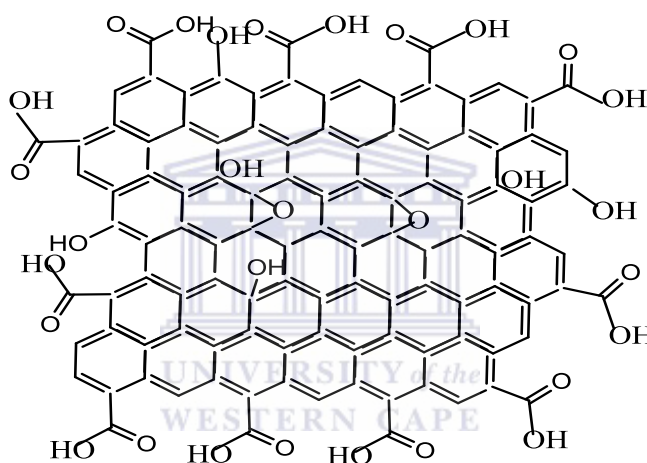


Figure 26. Schematic diagram of structure of graphene oxide (GO).

So far, the reduction process is still one of the essential reactions of graphene oxide due to the similarities between reduced graphene oxide and pristine graphene.

In the attempt by researchers to use graphene in a large scale application such as graphene based composite, chemical conversion of graphene oxide is the obvious and attractive route to large quantities of graphene like materials. These reduction methods could be through chemical, thermal and electrochemical method. Several chemical reducing agents including hydrazine [331, 333-334], sodium borohydride [335-336] and other chemical agents such as

hydrohalic acid (HBr) [337] and lithium aluminium hydride, has been employed in the chemical reduction of graphene oxide. Environmentally friendly (that does not involve the use of strong acids) methods of reduction, such as vitamin c and aluminium powder has also been used [338-339]. Hydrazine hydrate compared to other strong reductant, does not react with water and has been found to be one of the best options among reductant for reducing graphene oxide and also to produce a thin and graphite like sheet [294, 299]. Using sodium borohydride is another possible route to reduction of graphene oxide in aqueous solution and has been recently reported to be more effective than hydrazine [335]. Reduction of graphene oxide thermally, has also been reported [340]. This is carried out by direct heating of graphene oxide in a furnace at high temperature of about 1050 °C, whereby, a stable carbon oxide species is created thermodynamically; the stacked structure is then exfoliated through the extrusion of carbon dioxide generated Kudin *et al.* [341] reported a notable effect in the structure and about 30% lost in the mass of GO during exfoliation which has resulted in topological defect. It is tentatively accepted to be effective considering the bulk conductivity measurement of 1000-2300 S m⁻¹. However, the defect might have an effect on the mechanical properties when compared to a chemically reduced sample [342-343].

Another promising route of reducing graphene oxide is the electrochemical reduction method thus refers to as the electrochemical removal of oxygen functionalities. In this process, substrates electrodes such as ITO, glass, plastic and so on, can be utilised. A thin film of graphene oxide is deposited on the electrode and reduction can be performed using sweep voltammetry by scanning at window potential from an initial or minimum value (-0.6, 0.7 V) to a final or maximum value (-0.87, 1.1 V) in a solution (such as sodium phosphate buffer, sodium chloride) as a working electrolyte. A reduction peak observed around -0.87 V during the first 300s indicated a reduction of graphene oxide which gradually decreased to a background current level of about 5000s [344]. A controllable synthesis of graphene oxide has

also been reported by Zhou *et al.* [345]. The use of dangerous reductant and strong chemicals are avoided in electrochemical method and disposal of by product is also not required. While the route showed to be efficient, however, reduction of large amount of graphene oxide on the electrode becomes a compromising issue where scalability is involved and which happened to be the basic need when large amount of graphene is necessary, compared to a chemical method of reduction [27].

The reduction of graphene oxide through chemical means to achieve a pristine graphene sheet has been reported to usually results in agglomeration of the prepared graphene sheets [294, 346]. The graphene sheets became hydrophobic and cannot be easily dissolve in polar solvent, even after it is treated with ultrasonication, they tend to re-stack. In this regards, the accessibility of surface area is reduced and this may affect polymer nanocomposite reinforcement with graphene. Functionalisation then becomes necessary to avoid re stacking and to produce a stable aqueous dispersed graphene sheets in water and even in organic solvent. The functionalisation process, both covalent and non-covalent way of functionalizing GO has been reported to produce stable dispersions of chemically modified graphene (CMG) platelets in polar solvents and also to improve on well-suitability with diverse polymer matrices [347-348]. Covalent functionalisation reaction of graphene oxide can be by; exploiting the chemistry of oxygen groups on GO prior to reduction, functionalities based on grafting molecules on the basal planes of graphene/ covalent bonds between free radicals or dienophiles and C=C bonds of pristine graphene, and via modification of graphene. Several reported works include, the post-assembly modification of graphene oxide papers with primary alkylamines via solution and vapour phase intercalation with the latter process being significantly slower, has been presented by Stankovich *et al.* [349]. Comptone *et al.* [350] has also demonstrated an excellent processibility of the obtained chemically reduced active graphene oxide (CARGO) dispersions *via* free-standing CARGO papers that exhibit tunable electrical

conductivity/chemical activity and can be used as lithium-ion battery anodes with enhanced Coulombic efficiency. Direct exfoliation of graphite to graphene in aqueous media with diazaperopyrenium dications has been demonstrated to minimise agglomeration of graphene sheets in solution by Sampath *et al.* [351]. Non-covalent functionalisation method depends on the van der Waals forces, electrostatic interaction or π - π -stacking of the GO or derivatives of graphene [352-353]. In this method, the chemical structure of the graphene sheets is however protected, electronic/optical properties and solubility of the nanosheets are also controlled effectively, thereby retaining the high charge carrier mobility compared to covalent functionalisation [354-355]. A lot of experiment has been reported using this approach. A stable dispersion of reduced graphene in various organic solvents was successfully achieved via non covalent functionalisation with amine-terminated polymers by Cho *et al.* [356]. Bai *et al.* [357] reported non covalent functionalisation of graphene via π - π -interactions to yield a well dispersible graphene. Polymeric surfactant has also been found interesting as non-covalent means of inducing solubility of graphene [358-359]. Stankovich *et al.* [265] prepared a stable dispersion of graphitic nanoplatelets by coating reduced graphite oxide with poly(sodium 4-styrenesulfonate) (PSS).

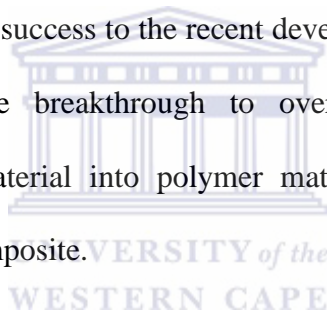
2.9.3. Graphene based composites

The intrinsic and unique properties of graphene sheets, as earlier mentioned have opened an opportunity for applications in composite materials. Quite a lot of polymers, nano particles and metal oxides semiconductors have been formed based on the remarkable properties of graphene which also include large surface area, mechanical, superior electrical and thermal properties. When compared with carbon nano tubes (CNTs), graphene has also proven to be effective conductive fillers [360]. One of the drawbacks of CNTs is their higher production cost which has hindered their mass production based functional materials to be difficult [361]. The development of such composites of graphene, not only need enough and scalable amount of graphene but also, must be homogenously well dispersed to improve their efficient integration with various matrices. The production of graphene oxide (GO) which is prepared from the oxidation of graphite, and the reduced graphene oxide (rGO) has however offered the possibility of exploring this two dimensional carbon sheet with the matrices in composites. Thus the recent interest in graphene oxide as carbon based nanofiller for polymer nanocomposite.

2.9.3.1. Polymer-graphene based nanocomposite

Amalgamation of nanomaterials, (nanoparticle or nanofiller) with polymer to form polymer nanocomposite has been a thing of interest in the research field owing to the unique properties (such as mechanical, electrical and thermal) that are usually stumbled upon in the cause of synthesis and has opened up many advantages to the development and improvement in the properties of many nanocomposites required to meet a specific challenge in a particular application and coupled with diverse ways of preparation, such as, colloidal dispersion, in situ polymerisation, electrochemical method etc. The incorporation of nanoparticles for reinforcement of polymers matrix composite has further contributed to the focus on the

material synthesis and are able to be employed in different areas of application [362]. Graphene, as fillers for polymer matrix composites have shown an immense possibilities for a variety of important applications. Recently, researchers have made successful effort on graphene oxide and graphene polymer composite. As previously discussed, graphene, a two – dimensional, atomically thin sheet of sp^2 of carbon atoms has higher surface to volume ratio, better electrical thermal and mechanical properties than carbon nanotubes (CNTs - inaccessibility of the inside surface to the polymer matrix is also a major contributor). Thus, a synergic reinforcement can be provided by graphene with polymer matrix properties for exceptional properties and better processibility in composites and applications in various devices such as sensor [293], supercapacitors [363], solar energy and automotive industries, to mention a few. However, the key success to the recent development is the improvement in bulk synthesis of graphene and the breakthrough to overcome several challenges in the incorporation of this unique material into polymer matrix towards the realization of the polymer graphene based nanocomposite.



2.9.3.2. Preparation of polymer-graphene based nanocomposite

The goal behind the preparation of polymer-graphene based nanocomposite is to produce new materials that are of high qualities and have maximum improvement in the final properties. A well homogeneous dispersion of graphene as well as effective external loading through synergic interaction between the filler and polymer matrix is however important. The supporting polymer for the nanocomposite is also considered, especially where it involves the π -conjugated conducting polymers (CPs), specifically, intrinsic conducting polymers (ICPs). These conducting polymers have conjugated backbones which can allow them to offer high electrical conductivity and good optical properties but do not display similar mechanical properties to other commercially available polymers. Preparation methods that can provide

covalent linkages between the fillers and the polymer matrices might be necessary because most dispersion methods involve interaction through non covalent weak dispersive forces. Several procedures that have been employed include, in-situ intercalative polymerisation, solution and melt intercalation process.



2.9.3.3. Solution mixing

Generally, the solution mixing procedure is based on solvent system, and usually involves the mixing of colloidal suspension of GO or graphene derivative material with polymer of interest by simple stirring or cut off mixing. In the process, the GO or modified graphene layers are allowed to swell in the presence of the solubilised polymer. [294], and the resulting suspension can then be precipitated. Precipitation can be done using a non-aqueous solvent in order to allow the polymer chains to be more enclosed with fillers upon precipitation, then the precipitated composite is extracted and dried for further processing and application. Solution mixing has always been one of the generally widespread methods of preparing polymer composite because it is simple and does not require the utilization of a special instrument, and can allow for a large scale production. However, the solubility or the dispersion of GO or graphene in the polymer solution is of great concern, especially with polymer solution in organic solvent. This can be solved by first dispersing GO and the graphene derivatives through ultrasonication before mixing with polymer solution.[364-365].

On the other hand, high-speed shearing can also be used as mixing method in the presence of an ice bath to prevent excess heating during the process or better still the suspension is directly spin coated onto a substrate and solvent can then be evaporated. Nevertheless, re aggregation of the (GO or graphene derivatives) in the composite might occur during the process of evaporation and this may be unfavourable to the properties of the composite [366]. As a result, it becomes imperative to modify GO and graphene derivatives with small functional molecule so as to prevent re-aggregation and as such increase the solubility in different kind of solvent. This can be initiated by phase transfer techniques [367] or surfactant [368]. Lyophilisation methods has also been extensively studied and reported to achieve a stable and well dispersed GO sheets prior to mixing with polymer matrix because of the hydrophilic nature of GO or

chemical modified graphene and thus enabled them to be frequently processed in either water or organic solvent [369].

Solution mixing of graphene polymer nanocomposite and have been studied and reported to allow GO and graphene derivatives graphene fillers into various types of polymers. Chen *et al.* [370] and Eda *et al.* [371] have successfully produced homogeneous aqueous colloidal suspension of graphene oxide sheets chemically cross-linked polystyrene (PS) to prepare PS/FGS composite.

2.9.3.4. Melt mixing.

In contrast to solution mixing, melt mixing process does not involve the use of solvent. The graphene derivatives of GO (fillers) and the polymer matrices are mixed mechanically at high temperature in the molten state using conventional method [372], exfoliation then follows to form nanocomposites. This method is frequently considered cheaper but do not give the same solubility of fillers as in solvent mixing or in situ polymerisation method. However, this method can be an optional technique for polymers that cannot be process by adsorption or in-situ polymerisation [372]. Varieties of polymer nanocomposites have been extensively prepared using this method. Kalaitzidou *et al.* [373] reported to achieve a high percolation threshold in nanocomposites made of polypropylene reinforced with exfoliated graphite nanoplatelets (PP/EG) using mixing process. Polyethylene terephthalate (PET)/graphene nanocomposite has been prepared and reported to give a high electrical conductivity of 2.11 S m^{-1} with only 3.0% of graphene, using melt mixing method of preparation [374].

2.9.3.5. In situ intercalative polymerisation

In situ polymerisation process of preparing polymer/graphene nanocomposite generally involves the mixing of the graphene or modified graphene (filler) in the liquid monomer,

whereby, the filler is made to disperse within the solution monomer. Polymerisation, which can either be initiated by heat or radiation, then follows in the presence of the dispersed filler. Several polymer nanocomposite that has been prepared using this method include, polystyrene(PS)/graphene nanocomposite [375]. Chen *et al.* [370] fabricated an electrically conducting polystyrene/graphite nanosheets nanocomposite films with much lower percolation threshold and much higher conductivities via in situ polymerisation. Preparation of polystyrene sulfonate (PSS)/LDH nanocomposite, poly(methyl methacrylate) (PMMA)/EG and polypropylene/graphene oxide (PP/GO) [375-377] have been reported via this method.

2.10. Tungsten trioxide

Tungsten oxide (WO_3) is a chemical compound containing oxygen and the transitional metal tungsten. It can be obtained as an intermediate in the recovery of tungsten from its minerals.[378], occurs naturally in form of hydrates such as tungstite ($\text{WO}_3 \cdot \text{H}_2\text{O}$). Among the widely studied metal oxide semiconductors, e.g. TiO_2 [379], ZnO [380-381], Fe_3O_4 [382], MoO_3 , [383] etc., tungsten oxide (WO_3) has been very attractive, and has gained a lot of recognition, due to its unique properties. As an n-type semiconductor with a band gap of 2.6 to 2.8 eV [384], it has greatly been utilised in so many devices, especially as a photoconductive material. Its ability to exist in multiple oxidation state due to intercalation of electrons and protons and been able to switch colours, has prompted its use in electrochromic and chemical devices. Its economic stability and strong adherence to the substrate as well as a cathodically ion insertion material, has contributed to its other advantages over other transition metal oxide [385]. However, the process of injection and extraction of electrons and metal cation (Li^+ , H^+ , Na^+ and K^+) during intercalation which give rise to the formation of tungsten bronze has actually played a major role in the conductivity properties of tungsten oxide. The so formed

tungsten bronze has provided electrical and optical properties that are different from the pristine oxide, thereby improving its electrochromic properties [386]. This has enabled tungsten oxide to also find further and wider application in commercial devices and displays e.g. photocatalyst [387], optochromic, optical devices, electrochromic [388], electrocatalysis, energy-saving devices e.g. smart windows in cars and buildings [389]. Several approaches to the synthesis of tungsten oxide have been reported and each has however resulted in different forms of tungsten oxide, which include monoclinic, mesoporous and crystalline nanostructure tungsten oxide. These physical and chemical approaches involve sol-gel method [390], vapour and solution phase procedure [391], thermal evaporation [392] etc. Electrochemical method of synthesis through deposition has also been accomplished and reported to give a thin nanostructured film of tungsten oxide [393]. However, the control of morphology and structure (crystallinity, stoichiometry) at the nanoscale is of paramount interest to deliver a unique properties in technology application [394]. Seeing that, sensor performance is directly related to the granularity, porosity and the ratio of surface area to volume of the sensing materials, it has been recognized that sensitivity of semiconductor metal oxide and conducting polymers are more improved, especially at nano level, and of course, in terms of the size of the combining nano fillers. The sensitivity increases as the grain size decrease [395].

In this work, the combination of materials such as WO_3 and graphene in form of nanoparticle and at nanoscale to conducting polymers is been investigated and presented, to however provide a good opportunity and greatly increase the response of theses material based sensor. Whereby, the different catalytic properties of the individual materials are explored and utilised to produce a highly electrocatalytic and stable sensor.

2.11. Sensor and sensor devices

A sensor is a sophisticated device that are commonly used to detects a change in a physical stimulus and turns it into a signal which can be measured or convey by an instrument in a definite way. Sensors offer many benefit information and are used in everyday objects, such as traffic monitoring, touch-sensitive elevator buttons, lamps which dim or brighten by touching the base. Numerous applications of sensors include aerospace, air traffic control, medicine, manufacturing and robotics. Consequently, information on the physical, chemical and biological environment can be provided by sensor. Physical sensors are usually used in the aquatic environment. They evaluate parameters such as turbidity, transparency, depth/pressure and temperature that regulate the transfer or flux of mass or energy inside and into a specific area. These parameters often regulate a wide range of chemical and biological processes that occur within the environment. And can vary from simple handheld devices to complex remote float based systems used for real-time data on conditions [396]. Biological sensors functions in living organism and can monitor living cells that are sensitive and detectable. It measures the presence, movement and number of organisms, providing important information on the health and safety of the environment. Biosensors measure and characterize organic materials. In this respect biological response is converted to electrical signals where information is recovered. These sensors include enzyme sensors and DNA analysis systems while chemical sensors measure and transform chemical information of a chemical compound. Thus, chemical and biological sensors have a thoughtful control in the areas of personal safety, medical diagnosis, public security, agriculture and detection of environmental toxins, semiconductor processing, automotive and aerospace industries.

Electrochemical sensors are among the largest group of chemical sensors, having been widely used in a chemical and biomedical sensing element where they can form an entire or fundamental part of the system. They are devices that extract information about sample from measurement of some electrical parameter that are with basic components comprising of a working electrode, a counter electrode and usually a reference electrode. Electrochemical sensors is principally categorized according to the measured parameter and ultimately depends on the analyte, nature of the sample, sensitivity and selectivity requirements, and are generally linked by Ohm's Law, namely; conductometric, potentiometric and voltammetric sensors. A typical electrochemical sensor is illustrated in **Figure 27**. There is interaction between the analyte and the polymer interface in a secured mechanism to generate an electrical signal through the chosen transducer which is amplified and monitored with a computer to produce a measurable analytical signal that can appear inform of current, potential or impedance. In addition, the ability to change the properties of the sensor parameters is probable. Some parameters such as sensing material or temperature can be altered during operation in order to get a better selectivity and sensitivity. A current form of signal will be measured at a fixed potential or potential difference across the electrochemical cell, scanning from one set value to another. Thus, cell current is recorded as a function of the applied potential, and the rate of flow of electrons is proportional to the concentration of the analyte. Different material such as polymers, nanocomposites of polymers or nanoparticles can also be used as working electrode when modified, so as to get more enhancements in sensitivity or sometime reduce the problem of fouling.

Electrochemical sensors are electroanalytical devices that are obligated in their reputation and success to the discipline of electrochemistry, in which a strong scientific base is being provided, intentionally to give information about the chemical environment and the growing need for consistent sources of information that guarantees their future, and they are not exempted in the engineering facet of any sensor research [397-399]. As compared to the classical method, electrochemical sensors are simple in their set up, the electronic equipment necessary for operation are as well easy. An electrode is used as the transducer, and at such, has been able to meet up with cost, size and power requirement of on-site environmental monitoring, with high sensitivity and selectivity of sensing system [400]. Sensor signals are obtained by in situ measurement of chemical composition and provide real time information for process control. Electrochemical sensors have therefore reached the stage of exploratory use in industries and environmental application. A particular interest is in environmental monitoring, where there is an urgent need for low-cost sensor system for detecting various pollutants at trace level [401-402]. Over the years researchers have started to apply novel approaches in sensor devices. The latest development is in the fabrication of composite including nanocomposite of polymers and other material as well as nanotubes, graphene or inorganic compounds, because of their extraordinary structure and properties. In sensors of different kinds, conducting polymers are used as the active, catalytic or sensing layers. The biocompatibility of several conducting polymers provide opportunity for the application of various types of sensors and biosensors, in light weight batteries, solar cells, electrochromic devices, molecular electronic devices and sensors to mention a few [403]. The various categories of the electrochemical sensors are listed and briefly discussed.

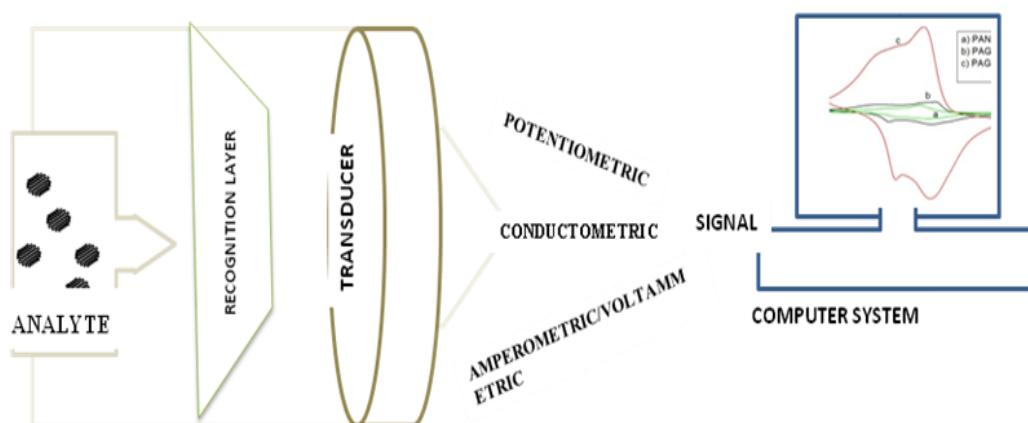


Figure 27. Schematic representation of electrochemical sensor.

2.11.1. Chemiresistor or conductometric sensors

This is based on inflection of resistivity of the selective material whereas resistivity is the reciprocal of conductivity .i.e. measures resistance (in ohms) or conductance. In a typical chemiresistor, the conductivity of a material can be changed upon contact with chemical species when clamped between two contact electrodes at which the resistivity of the entire device can be measured, and this is commonly use in gas sensing. While in conductometric, the chemically interactive layer is at the top of an electrode and immersed in the solution of electrolyte, a suitable counter electrode is then provided to complete the electrical circuit. This are typically found in various biosensors where the selectivity of the response comes from some biological interaction [404-405].

2.11.2. Potentiometric sensor

This is a type of chemical sensor that may be used to determine the analytical information of some component of the analyte in gas phase or solution. It measure the difference in potential between the working electrode and the reference electrode (in volts) when no current is flowing [406-408]. A Redox reaction, $Ox + Ze = Red$ usually takes place at an electrode surface

(cathode) and can be define as half-cell reaction. At thermodynamic equilibrium, the Nernst equation is applicable and can be expressed as:

$$E = E^{\circ} + \frac{RT}{ZF} \ln \left(\frac{a_{\text{ox}}}{a_{\text{red}}} \right) \quad \text{Equation 1}$$

Where E and E° are the measured electrode potential and the electrode potential at standard state, respectively, a_{ox} and a_{red} , are Ox (reactant) and (product) in this case, respectively. Z is the number of electron transferred, F represent the faraday constant, R the gas constant, and T the operating temperature in the absolute scale. Two half-cell reactions usually take place simultaneously in an electrochemical cell. So for sensing purposes, only one of the two half-cell reaction should involve the specie of interest, and other half –cell reaction is preferably reversible and no interference. As indicated in the equation, a linear relation exists between the measured potential E and the natural logarithm of the ratio of the activities of the reactant and product. If the number of the electron transferred Z , is one, at ambient temperature (25 °C or 298 K) the slope is approximately 60 mV/ decade. The slope value governs the sensitivity of the potentiometric sensor. Potentiometric sensors are classified based on electrodes, whether inert or active electrodes. An inert electrode (e.g. noble metals such as platinum and gold, graphite, and glassy carbon) merely provides the surface for the electron or provides a catalytic surface for the reaction but does not participate in the half-cell reaction. However, the active electrode is either an ion donor or acceptor in the reaction. Generally, three types of active electrode are available: the metal/metal ion, the metal/insoluble salt or oxide, and the metal/metal chelate electrodes. To complete the circuitry for the potentiometric sensor, a reference electrode is usually used in which a non-interference half-cell reaction occurs. Silver–silver chloride (Ag/AgCl) and calomel electrodes are the most commonly used

reference electrodes. Calomel consists of Hg/HgCl and is less desirable for biomedical systems in terms of toxicity [408].

2.11.3. Amperometric/Voltammetric sensors

This can be used in the detection of ions in a solution based on electric current or changes in electric current (in amperes). In single amperometric detection, single-potential, or direct current (DC), amperometry is involved. An extension of single-potential amperometry is pulsed amperometry (PAD), most commonly used for analyte that tend to foul electrodes.

Oxidation or reduction of electroactive specie occurs as result of the applied potential (between a reference and a working electrode) which serves as the driving force for the electron transfer reaction. The rate of the electron transfer reaction can be determined by the direct measure of the resulting current and which is proportional to the target analyte concentration [409]. The key consideration of an amperometric sensor is that it operates at a fixed potential. However, a voltammetric sensor can operate in other modes such as linear or cyclic voltammetric modes. Consequently, the respective current potential response for each mode will be different. Usually, voltammetric sensors examine the concentration effect of the detecting species on the current-potential characteristics of the reduction or oxidation reaction involved, the mass transfer rate of the detecting species in the reaction onto the electrode surface and the kinetics of the faradaic as well as the charge transfer reaction at the electrode surface that is directly affecting the current potential characteristics. This mass transfer can be attributed to; (a) an ionic migration as a result of an electric potential gradient, (b) diffusion under a chemical potential difference or concentration gradient and (c) a bulk transfer by natural or forced convection. In electrochemical cell, the electrode reaction kinetics and the mass transfer processes contribute to the rate of the faradaic process and this provides the basis for the

operation of the voltammetric sensor. However, assessment of the simultaneous mass transfer and kinetic mechanism is rather complicated. Thus, the system is usually operated under definitive hydrodynamic conditions. A situation where a voltammetric sensor operates with a small overpotential, the rate of faradaic reaction is also small; as a result, a high-precision instrument for the measurement is needed. An amperometric sensor is usually operated under limiting current or relatively small overpotential conditions. If operated under an imposed fixed electrode potential, then, the cell current can be correlated with the bulk concentration of the detecting species (the solute). This operating mode is commonly classified as amperometric in most sensor work, but it also is referred to as the *Chronosuperometric* method, since time is involved [410].

2.11.4. Electroanalytical techniques

Electroanalytical techniques such as, stripping voltammetry, differential pulse polarography, cyclic voltammetry square wave and chronoamperometry are not only examining traces concentration of an analyte, helpful information as regards the physical and chemical properties of the electroactive analyte are also provided. Among the aforementioned, the cyclic voltammetry and square wave voltammetry are two commonly and widely used techniques.

2.11.4.1. Voltammetry

Voltammetry is a class of electrochemical method used in analytical chemistry and various industrial processes whereby, information about an analyte is obtained by measuring the current against the potential [411]. The development of voltammetry can be dated back to 1922 by Jaroslav Heyrovsky through the discovery of polarography. An experiment was performed by Heyrovsky in which information about the nature of a specie was obtained in a solution

through reduction at the mercury drop by measuring current while the potential is been changed. In 1925, an automatic instrument called polarograph, which can photographically record current – potential ($I-E$) curves was developed by Heyrovsky and Shikata [412]. This earns them an award of 1959 Noble prize received by Jaroslav Heyrovsky. A number of difficulties were later experience by this early voltammetric method resulting in less ideal for routine analytical use. Advances were later made in the 60s and 70s in all areas of voltammetry which includes theory, methodology and instrumentation, thereby enhancing the sensitivity and expanding the range of analytical methods. The possibility of this advancement has also facilitated a speedy commercial development of an instrument that is quite inexpensive [413]. In a voltammetric technique, the common characteristic involves the application of a potential (E) to an electrode and the monitoring of the resulting current (I) flowing through the electrochemical cell. The applied potential in many cases is varied or the current monitored over a period of time (T). Thus, Voltammetric techniques can be described as some function of E , I and T [414]. Therefore voltammetry can be generally defined as the investigation of three dimensional space relating to potential (E), current (I) and time (T) [415]. At least two electrodes are required to conduct an experiment in voltammetry. The working electrode (WE), reference electrode (RE) and usually a counter electrode (CE) are the types of electrodes commonly used in voltammetric technique [399].

2.11.4.2. Instrumentation

The basic component of a modern electroanalytical technique for voltammetry comprises of the following; a potentiometer, a computer and the electrochemical cell. The types of the electrodes are, working, reference and counter electrodes. **Figure 28** showed a typical conventional three electrode cell showing the working electrode (glassy carbon in the centre),

auxiliary electrode (Pt-disk electrode-left side), and reference electrode (Ag/AgCl-right side), potentiometer and a computer for a voltammetry analysis in an electrochemical set up.

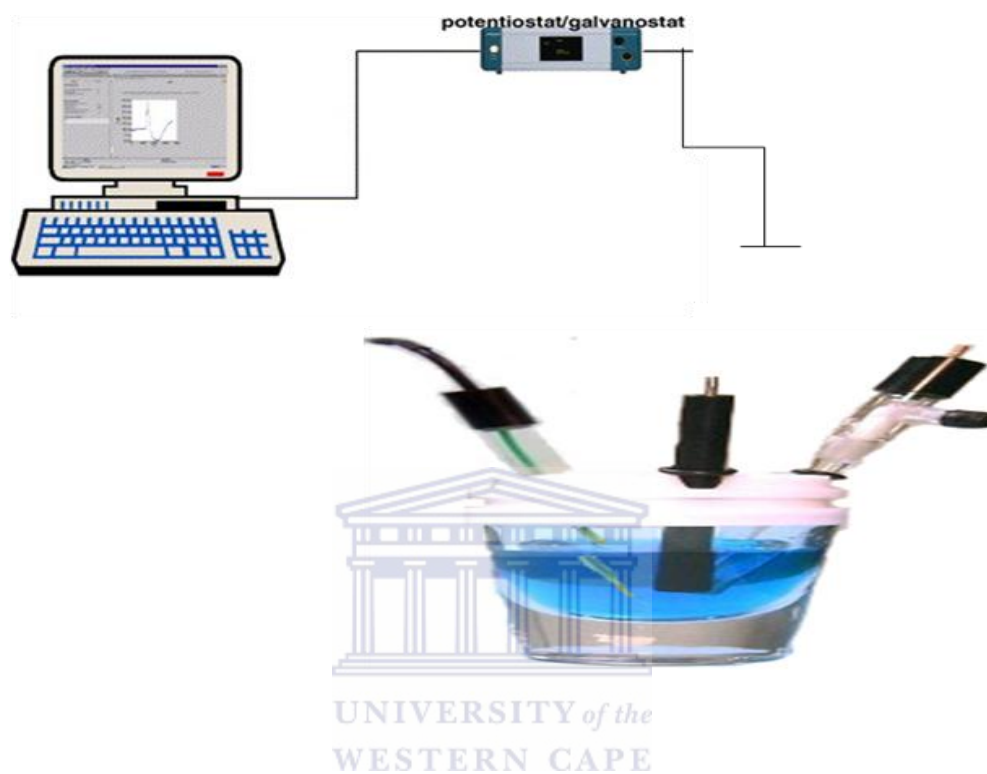


Figure 28. A typical conventional set up in electrochemical cell.

2.11.4.2.1. The potentiostat

The working principle of a potentiostat actually depends on its connection to the electrochemical cell. Thus, according to the typical illustration which is the common one, it controls the potential of the counter electrode (CE) against the working electrode (WE) so that the potential difference between the reference electrodes (RE) is distinct, and agrees with the value specified by the user. Therefore in potentiostatic/galvanostatic mode, the current flow between the working electrode and the current is controlled. The potential difference between the reference electrode and working, and the current flowing between the current and working electrode are constantly monitored [399].

2.11.4.2.2. Electrochemical cell and electrodes

A typical electrochemical cell may consist of the following, a sample dissolve in a solvent, or an ionic electrolyte and obviously, three or sometimes two electrodes. They can come in different shapes, sizes and material (e.g. glass, teflon, polyethylene etc.). The choice of cell also depends on the amount of sample, the technique, and the analytical data to be achieved. A glass cell with a close fitting that have ports of electrodes and a purging line is commonly used. The arrangement of the electrode should also be considered. More often, the reference electrode is placed as close as possible to the working electrode, and sometimes there may be need to place the reference in a separate compartment to avoid contamination.

2.11.4.2.3. Electrodes

Generally, an electrode provides the interface across which a charge can be transferred or where the effect of the charge can be felt e.g. the working electrode (WE), which is where the

reaction of interest takes place. So the electrode is an utmost important part of the system. The shape, size and style of modification on the surface, all depends on the application process.

2.11.4.2.4. The reference electrode (RE)

The reference electrode is an electrode with a steady and recognizable electrode potential. It is used as point of reference to control and measure the potential of the other electrodes. The saturated calomel electrodes (SCE), silver/silver chloride (Ag/AgCl) electrode are the most commonly used reference electrode for aqueous solutions.

2.11.4.2.5. Counter electrode (CE)

The counter electrode (also known as auxiliary electrode) is usually made of an inert material of platinum (Pt) or metallic foil, gold (Au), graphite or sometimes glassy carbon may be used. Counter electrode does not usually take part in the electrochemical reaction, but the total surface act as source of electron so that current can flow between the working electrode and counter electrode which make it not to be isolated from the reaction. The surface area must however be higher than that of the working electrode so that it will not be a limiting factor in the kinetics of the process under investigation [415].

2.11.4.2.6. Working electrode (WE)

The working electrode is where the reaction or transfer of interest is taking place. At an appropriate potential, oxidation or reduction of a substance on the surface of the working electrode will bring about a mass transport of a new material along with current been produced. The commonly used materials for working electrodes are glassy carbon (GC), platinum (Pt),

gold (Au). Others include small mercury drop and film electrodes. The size and shape also varies and depends on application. The quality of an ideal working electrode includes a wide potential range, low resistance as well as a surface that is reproducible [415].

2.11.4.3. Cyclic voltammetry

The cyclic voltammetry is the most extensively used technique for acquiring qualitative information about electrochemical reactions, as a result of its ability to rapidly provide considerable information on the thermodynamics of redox processes and the kinetics of heterogeneous electron-transfer reactions as well as the coupled chemical reactions or adsorption processes. The cyclic voltammetry is frequently the first experiment performed in an electroanalytical study, especially proffering a rapid location of redox potentials of the electroactive species and suitable assessment of the consequences of the media upon the redox process. However, voltammetry could also be linear mode of operation [416], if it involves an increase in the imposed potential linearly at constant scanning rate from an initial potential to a definite upper potential limit (i.e. normally referred to as potential window). The current potential curve usually shows a peak at a potential where the oxidation or reduced reaction occurs whilst the height of the peak current could be used for the quantification of the concentration of the oxidation or reduction species. In linear sweep voltammetry (LSV), illustrated in **Figure 29**, fixed potential range is employed much like potential step measurements; the voltage is scanned from a lower limit (V_1) to an upper limit (V_2) as shown below. And the voltammogram recorded depend on a number of factors including, the electron transfer reaction(s) rate, the voltage scan rate and the chemical reactivity of the electroactive species [417].

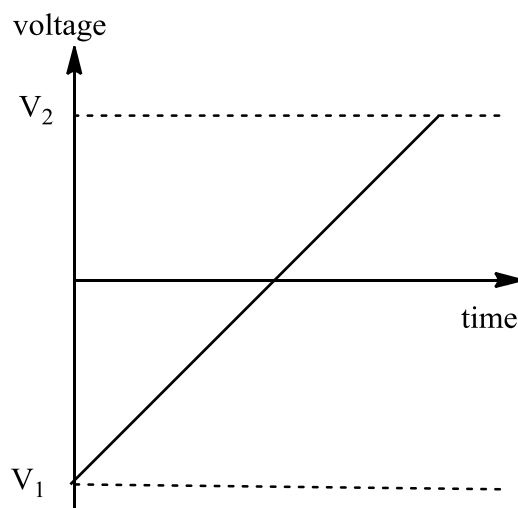


Figure 29. Illustration of a typical linear sweep voltammetry.

The cyclic voltammetry is similar to linear but the electrode potential returns to initial value at a fixed scanning rate, and the peak being generated normally corresponds to the oxidation and reduction reactions, i.e. condition at which the peak value is related to the oxidation and reduction reaction. In this case the voltage is swept between two values at a fixed rate, when the voltage reaches V_2 the scan is reversed and the voltage is swept back to V_1 . This is shown in **Figure 30**.

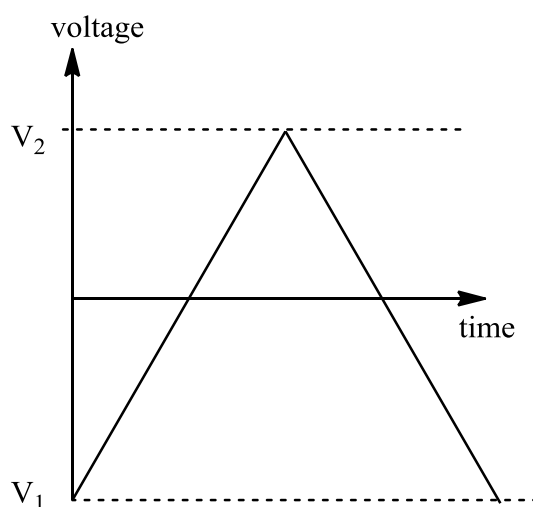


Figure 30. Illustration of a typical cyclic sweep voltammetry.

In a typical cyclic voltammetry, a solution component is electrolyzed (oxidised or reduced) by placing the solution in contact with an electrode surface and then making that surface sufficiently positive or negative in voltage to force electron transfer. In simple analysis, the surface is started at a particular voltage with respect to a reference half-cell such as calomel or Ag/AgCl, the electrode voltage then changes to a higher or lower voltage at a linear rate and finally changed back to the original value at the same linear rate [418]. When the surface becomes sufficiently negative or positive, a solution species might gain electrons from the surface or transfer electrons to the surface [418] resulting in a measurable current in the electrode circuitry. However, some important information can also be investigated from the parameters, this include whether the electrochemical process displayed by the sample is reversible, irreversible or quasi –reversible, and also give close information on how fast the electron process is, relative to other processes such as diffusion. For example, if the electron transfer is fast relative to the diffusion of electroactive species from the bulk solution at the surface of the electrode, the reaction is said to be electrochemically reversible, and the peak separation (ΔE_p) is given by equation;

$$\Delta E = E_{p,a} - E_{p,c} = \frac{2.303RT}{nF} \quad \text{Equation 2}$$

Where ΔE_p is the peak separation (V), $E_{p,a}$ is the anodic peak potential (V), $E_{p,c}$ is the cathodic peak potential (V), n represent the number of electrons and F the Faraday constant (96 486 C mol⁻¹), R is the gas constant (8.314 J mol⁻¹ K⁻¹) and T is the absolute temperature of the system (298 K). Therefore, number of electrons (n) involved in the electrochemical process can be estimated from the above equation [418].

Therefore, for a redox couple that is reversible, the cyclic voltammograms has been studied to have the following defined characteristics;

The expression; $\Delta E = E_{p,a} - E_{p,c} = \frac{59}{n} \text{mV}$ Equation 3 [419],

determines the voltage separation between the current peaks.

The ratio of the peak currents is always equal to one:

$$\frac{I_{p,a}}{I_{p,c}} = 1$$
Equation 4 [419]

The formal potential $E^{o'}$ for a reversible redox couple is easily determined as the average of the two peak potentials:

$$E^{o'} = \frac{(E_{p,a} + E_{p,c})}{2}$$
Equation 5 [419]

The peak currents are usually proportional to the square root of the scan rate

$$(I_p \text{ is proportional to } v^{1/2})$$
Equation 6

Quantitative information regarding analyte concentration, that specifies the anodic peak current, ($I_{p,a}$) and cathodic peak current ($I_{p,c}$) in terms of analyte concentration, C . and while the scan rate (mV s^{-1}) of the process is been varied, (i.e. how rapidly the electroactive specie is diffusing through the solution to and from the surface of the working electrode), can be obtained from the voltammograms using Randles- Sevcik equation:

$$I_p = -0.4463nF\left(\frac{nF}{RT}\right)^{1/2} \Gamma^* D^{1/2} v^{1/2} A \quad \text{Equation 7}$$

Where, n is number of electrons appearing in the half-reaction for the redox couple, v is the rate at which potential is swept, F is the Faradays constant (96485 C mol^{-1}), A , the electrode area (cm^2), R represent the universal gas constant ($8.314 \text{ J mol}^{-1} \text{ K}^{-1}$), T is the absolute temperature (K), D is the diffusion coefficient analyte ($\text{cm}^2 \text{ sec}^{-1}$) and Γ^* represents the surface concentration of the adsorbed species on the modified electrode [420].

If temperature is assumed to be 25°C (298.15 K), the equation can be written as:

$$I_p = 2.69 \times 10^5 n^{3/2} A D^{1/2} v^{1/2} C_o \quad \text{Equation 8}$$

An illustration of a cyclic voltammetry (CV) for the reduction of 5 mM ferricyanide in 0.1 M KCl at glassy carbon electrode, scan rate; 100 mV s^{-1} is shown in **Figure 31**. The peak shape of the oxidative and the reverse reductive current versus electrode potential is typical of an electrode reaction in which the rate is governed by diffusion of the electroactive species to a planar electrode surface. ($I_{p,a}$ and $I_{p,c}$) are the anodic and cathodic peak respectively.

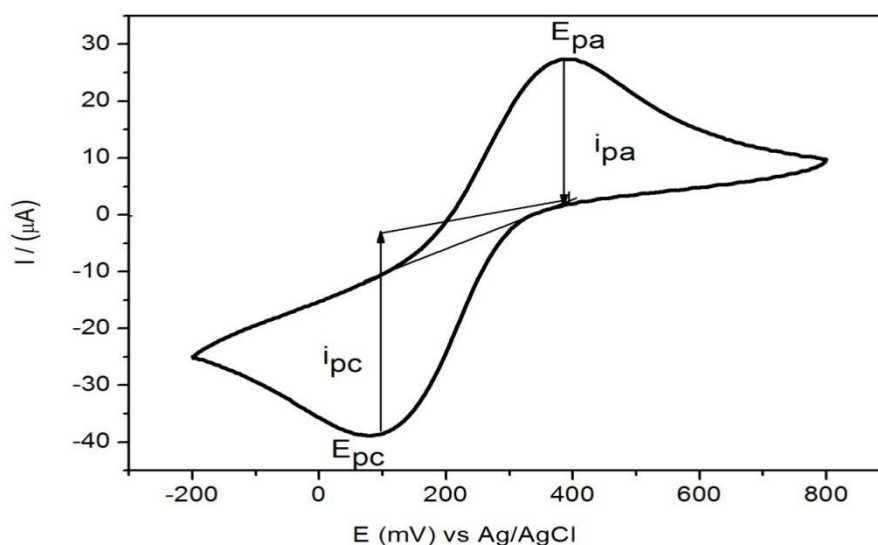


Figure 31. A typical illustration of cyclic voltammogram for a reversible reaction.

Though, some voltammograms performed at different scan rates can lead to preparation of quite a number of linear plots whose slopes could give further information about the redox properties of the sample under investigation. For instance, when the peak current is plotted against the square root of the scan rate, the slope of the linear plot can be used to estimate the diffusion coefficient according to the Randles-Sevcik equation shown above. At this instance, the log of peak current versus the log of scan rate gives a linear plot whose slope distinguishes between diffusion controlled peaks, adsorption peaks or even a mixture of the two. For diffusion peak, a plot of the $\text{Log } i_p$ versus $\text{log } v$ is linear with a slope of 0.5 and a slope of 1 for an adsorption peak. Intermediate values of the slope are sometimes observed, and suggested to be a “mixed” diffusion-adsorption peak [421].

A situation where the process involved a chemically modified electrode, the sample to be investigated is deposited on the surface of the electrode and the surface concentration of the adsorbed material can then be estimated by the use of the Brown-Anson model equation;

$$I_p = \frac{n^2 F^2 \Gamma^* A \nu}{4RT}$$

Equation 9

Where I_p , n , F , A , R , ν , T and Γ^* (the surface concentration of the adsorbed species of the electrode modifier) are all expressed in the equations above. It is important to note that, in a sensor operation, some parameter such as potential scanning rate, operating temperature and diffusivity of the reactant are very necessary. The peak current may be used to quantify the concentration of the reactant of interest provided, that the effect of concentration on the diffusivity is negligible [422].



2.11.4.4. Square wave voltammetry (SWV)

A square wave voltammetry is a further improvement of staircase voltammetry (staircase voltammetry is a derivative of linear sweep voltammetry). In square wave voltammetry, a square wave is placed over the potential staircase sweep, where the forward pulse of the square wave concurs with the staircase step. The net current (I_d), obtained by taking the difference between the forward and reverse current ($I_f - I_r$) is usually plotted as a function of potential and centres on the potential of the oxidation/reduction process of the species. **Figure 32** shows the SWV containing the forward, reverse and net currents. It can be observed that the net current showed a very large and more pronounced peak difference compared to the forward and reverse because it is the difference between the two. The peak height is directly proportional to the concentration of the electroactive species and can measure as low as 10^{-8} M. The square wave voltammetry has several advantages, but the major advantage is its high speed in which a complete voltammogram can be recorded within a couple of seconds, this speed coupled with computer control and signal average, allows for experiment to be performed repetitively and increase the signal-to-noise ratio. Others include excellent sensitivity and the rejection of background current. Its usage includes the study of electroactive kinetics with regards to catalytic homogeneous chemical reaction and determination of some species at trace level [423]. **Figure 32** showed a typical SWV of PANI film on glassy carbon electrode showing the forward, reverse and difference current

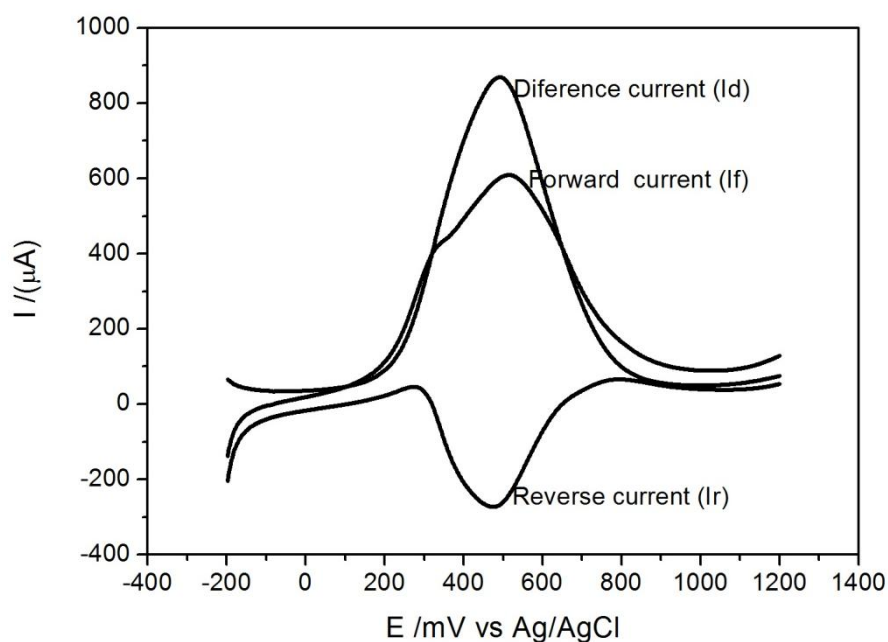


Figure 32. A typical SWV containing the forward, reverse and difference currents.

2.11.4.5. Electrocatalysis

Electrocatalysis can be defined as a process whereby, an electrocatalyst participate as a catalyst in electrochemical reaction. The electrocatalyst can be a specific form of catalyst that function at the surface of the electrode or may be the surface of the electrode itself [424]. Thus, catalyst materials modify and increase the rate of chemical reaction without being consumed in the process. The process can be heterogeneous, which involve chemical reaction occurring at the surface of the electrode and electron transfer usually takes place at the interface, leading to a new product formation (in catalytic electrosynthesis), or homogeneous reaction which is a sequence of reactions that involve a catalyst in the same phase as the reactants. However, a homogeneous catalyst is most commonly co-dissolved in a solvent with the reactants (coordinating complex or enzymes) [425-426]. The ability to catalyse some reaction is one of the most outstanding properties of conducting polymers. The kinetics of electrode processes of some solution specie is able to be improved by a thin layer of a conducting polymer, deposited onto the surface of a substrate electrode. These electrocatalytic processes, proceeding at a

conducting polymer electrode is presently yielding application in various fields of electrochemistry [426].

Three processes are considered to be happening during the electrocatalytic conversion of solution species at conducting polymer modified electrode. Firstly, heterogeneous electrons transfer between the electrode and a conducting polymer layer, and electron transfer within the polymer film. This process is normally accompanied by the movement of charge compensating anions and solvent molecules within the conducting polymer film, and possibly changes the conformational structure of the polymer. However, many factors determine the rate of this process and which include, electric conductivity of polymer layer, electron self-exchange rate between the chains/or clusters of polymer, and anion movement within polymer films also seems to be greatly significant. Secondly, the diffusion of solution species to the reaction zone, where the electrocatalytic conversion occurs. Unlike simple electrode reaction, this process can be more complicated in cases where the electrocatalytic conversion occurs within the polymer film. In that case, the diffusion of species within the film, in addition to the possible electrostatic interaction of this specie with the polymer film should be taken into account.

In the third process, a chemical (heterogeneous) reaction takes place between solution species and conducting polymer. Consequently, the kinetic behaviour and voltammetric responses are difficult to interpret, and some simplify model has been considered for this to a great extent. This includes experimental technique (e.g., spectroelectrochemistry) that has been able to yield valuable information on the subject [427-428]. In which case, various catalytic surfaces have been successfully employed for facilitating the detection of environmentally relevant analyte, with otherwise slow electron transfer kinetics [429]. Zhang *et al.* [430] and Xi *et al.* [431], have showed a glassy carbon electrodes, covered with electropolymerized layer of PANI, to exhibit electrocatalytic properties towards the oxidation of ascorbic acid. Liu *et al.* [432],

concluded that the electrocatalytic reaction occurs within the composite film rather than just at the outside, and observed the reversible inhibition by the reaction product oxidised coenzyme.

In this work, Electrocatalysis method engaged, the transfer of electrons between the analyte and electrode surface. In this regard, the catalyst on the modified electrode becomes oxidised in the electrolyte and then interacts with the analyte which are mostly in their reduced state. There is electron process taking place which leads to the oxidation of the analyte and simultaneous reduction of the catalyst. The schematic illustration is shown in **Figure 33**

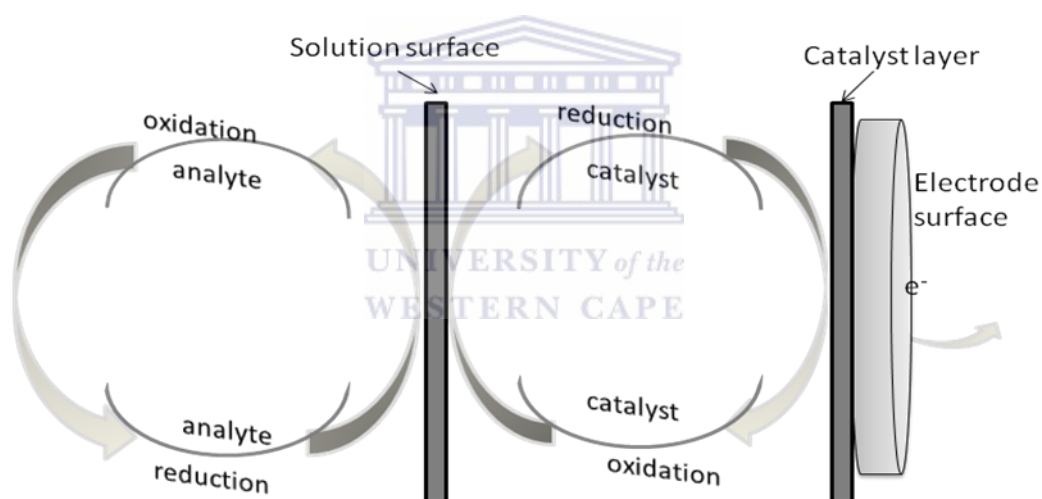


Figure 33. Schematic diagram of electrocatalytic process on the surface of a modified electrode.

2.11.4.6. Chemically modified electrode

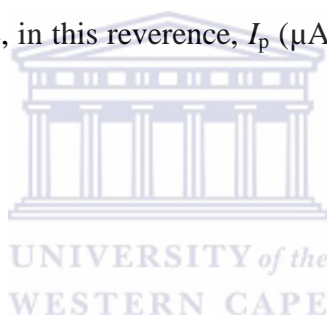
Chemically modified electrode (CMEs) involves an approach to electrode system design that finds application in electrochemical investigation, which includes the relationship of

heterogeneous electron transfer and chemical reactivity of electrode surface chemistry, electron and electrostatic phenomena at electrode surface, as well as ionic transport phenomena in polymers. The distinguishing feature of a chemically modified electrode is that it can allow a thin film of selected conducting material to be bounded on its surface for the purpose of improving the chemical, electrochemical, optical, electrical, transfer of electron and other desirable properties of the film in a rational chemically designed manner [433]. Therefore, the significant drive for modifying electrode surface is electrocatalysis of the electrode reaction of an analytical desired substrate. It is often observed that redox reaction of an analyte on a naked electrode surface using voltammetry techniques such as cyclic voltammetry or square wave voltammetry are slow, so that oxidation or reduction occurs at a potential that is greatly higher than positive or negative, respectively, than the expected thermodynamic potential. Such situation can be sorted by accelerating the desired reaction with an immobilized mediator catalyst. The mediator is attached on the surface of the electrode to function as facilitator for the charge transfer between the analyte and electrode (as illustrated in **Figure 33**). The oxidised form of the mediator catalyst is rapidly reduced, and then, its reduced form reacts with the analyte specie in solution. It can thus be indicated that the electron transfer occurred between the mediator and the electrode and not between electrode and the analyte, directly. From the illustrated equation below, a mediator can be represented by M and the analyte, A, [434].



Therefore, three features can be ascribed to a mediated electrocatalysis; firstly, the catalysed reaction occurs near the formal potential of the mediator catalyst couple (oxidised and reduced form) unless a catalyst-analyte adduct is formed, in which case reaction occurs at the potential for adduct. Secondly, the formal potential of the mediator catalyst and that of the analyte must be alike, as this decrease the reduced plus analyte reaction energy, thus, the choice is also associated with a maintained and agreeably fast reaction rate. And finally, for a successful catalysed reaction of analyte to occur, the reaction must be at less negative or positive potential for reduction or oxidation, respectively, than required for the naked electrode reaction of analyte [435-436]. Therefore, under this condition, a surface concentration of an electrochemical material can be determined by applying the following equation below, with respect to surface confined specie, in this reverence, I_p (μA) is directly proportional to the scan rate, v (mV s^{-1})

$$\Gamma = \frac{Q}{nFA} \quad \text{Equation 12}$$



$$I_p = \frac{n^2 F^2 A \Gamma v}{4RT} \quad \text{Equation 13}$$

Chemically modified electrodes can be obtained by various methods which include, attaching molecules on the electrode surface through adsorption, covalent binding, self-assembled monolayer etc. [437], by immobilising multimolecular layers films on electrode (mainly polymer) and by designing heterogeneous, and spatially defined layered microstructure onto electrode surface or within the bulk of the electrode materials [438-439]. CMEs have been widely employed in various process including, electrocatalysis, surface analysis [440], electrosynthesis [441], molecular electronics [442] etc.

2.11.5. Electrochemical impedance spectroscopy (EIS)

Electrochemical impedance spectroscopy can however be described as a technique that can be used to investigate the mechanism of individual contributions of components under investigation in electrochemical reaction. Through EIS, the dielectric and transport properties of materials, the properties of porous electrode were able to be explored as well as the passive surfaces [443-444]. This special technique was reviewed by Macdonald to have been founded by a scientist, named Oliver Heaviside [445], who defined electrochemical impedance spectroscopy as being an excellent, non-destructive, accurate and rapid in situ technique for examining processes occurring at electrode, and can then give information about a process in progress [446]. The exclusive control of the technique can also be attributed to; ability to readily interpret results due to its linear system theory. All impedance information can be gathered by linear electrical perturbation/response techniques even if measured at an infinite frequency range or at high experimental efficiency, and the validity of the data is willingly determined using integral transform techniques that are independent of the physical process involved [447]. Impedance spectroscopy is different from other electrochemical techniques, in that, application is either by potentiostatic or potentiodynamic method, a small perturbing potential across a cell or sample that changes in a cyclic sinusoidal manner (hence impedance is termed alternating current (AC) and current is then generated due to the overpotential (η) caused by the displacement of the potential from the value at equilibrium. The term alternating current, is a measure of the ability of a circuit to resist the flow of an electrical current, defined by ohm's law as the ratio between voltage (E) and the current (I) [409, 448].

$$R = \frac{E}{I}$$

Equation 14

In EIS experiment, a small perturbation (sinusoidal potential AC wave form of 5-10 mV) is applied on the DC potential to generate a response from the equilibrium position. The response which is generally sinusoidal is measured in terms of the AC impedance or the impedance, Z , of the system, which permits analysis of the electrode process in relation to diffusion, kinetics, double layer, coupled homogenous reaction, etc. [449]. The ratio of the applied voltage (E) over measured current (I) is the impedance of the system ($Z = E/I$). As an AC potential is applied to the cell, there is every possibility for a phase shift by an angle (ϕ) between the applied AC potential waveform and the AC current response, as a result, the impedance can be represented using a vector diagram [Figure 34], displaying the in-phase and out-of-phase impedances, the total impedance, and the phase angle ϕ .

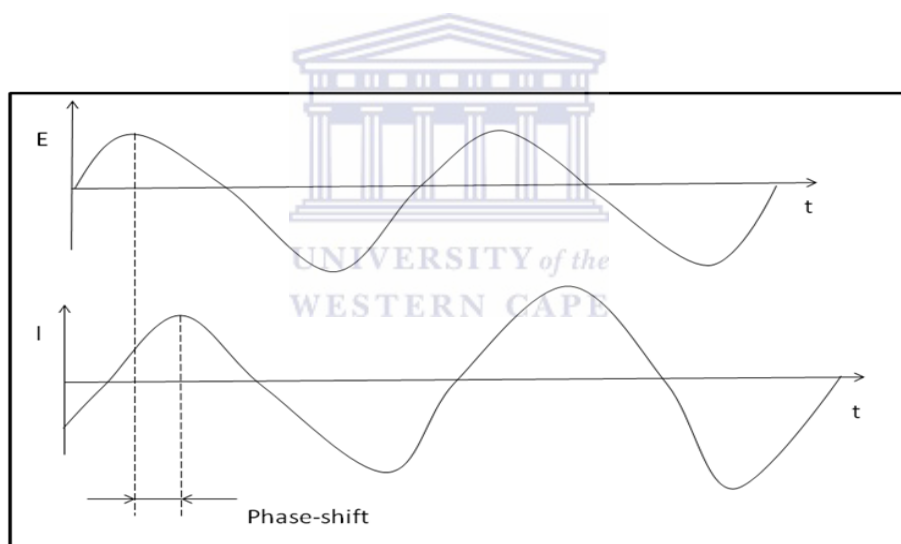


Figure 34. Illustration of a sinusoidal current response to potential perturbation as a function of time in a linear system

The excitation signal, expressed as a function time, has the form

$$E_t = E_o \sin(\omega t)$$

Equation 15

Where E_t is the potential at a time t , E_o is the amplitude of the signal, ω is the radial frequency.

The relationship between radial frequency ω (expressed in radian/second) and frequency f (expressed in hertz) is:

$$\omega = 2\pi f \quad \text{Equation 16}$$

In a linear system, the response signal I_t , is shifted in phase (ϕ) and has a different amplitude, I_o .

$$I_t = I_o \sin(\omega t + \Phi) \quad \text{Equation 17}$$

Using ohm's law, an analogous expression allows the impedance of the system to be calculated by substituting equation 3 and 4, and then we have:

$$Z = \frac{E_t}{I_t} = \frac{E_o \sin(\omega t)}{I_o \sin(\omega t + \phi)} = Z_o \frac{\sin(\omega t)}{\sin(\omega t + \phi)} \quad \text{Equation 18}$$

Because of complex number of terminology that is involved when analysing impedance spectra, the in-phase and out-of-phase impedances are often referred to as real and imaginary impedances. The complex impedance (Z) is made up of a resistive or real part Z' , attributable to resistors (in phase with the applied voltage), and a reactive or imaginary part Z'' , attributable to the contributions of capacitors (out of phase with the applied voltage by $+\pi/2$) and /or inductors (out of phase with the applied voltage by $-\pi/2$). This is related to the resistance (R), reactance (X) and capacitance (C) according to the equation:

$$Z = Z' + jZ'' = R - jX; \quad X = 1 / \omega C \quad j = \sqrt{-1}, \quad \text{Equation 19}$$

Where R represent the resistance (measured in Ω), X the reactance, C the capacitance measured in Farads, F), and ω is the applied angular frequency (radian/s): $\omega = 2 \pi f$ and f is the frequency in hertz (Hz) [448].

Represented by the term Z' and Z'' by the equation:

$$Z = Z' - j Z'' \text{ where } j = \sqrt{-1} \quad \text{Equation 20}$$

The expression Z is defined by the term, j , which determines the contribution of Z'' to Z , often represented as complex impedance. From impedance experimental data, the expression Z is composed of a real and an imaginary part, therefore if the real part plotted on the x-axis versus the imaginary part plotted on the y-axis of a chart, a ‘Nyquist plot’ (Z' versus Z'') is the result. However, it should be noted that the imaginary part which is y-axis is almost always capacitive and it is usually negative and each point on the Nyquist plot is the impedance at one frequency. Also, the impedance can be represented as a vector (arrow) of length $|Z|$ on the Nyquist Plot [450]. The angle between this vector and the X-axis, commonly called the “phase angle”, is ϕ ($= \arg Z$). A typical Nyquist plot is shown in the **Figure 35**, for the real impedance (x-axis) and the imaginary impedance (y-axis) with low frequency data on the right side of the plot and higher frequency on the left side.

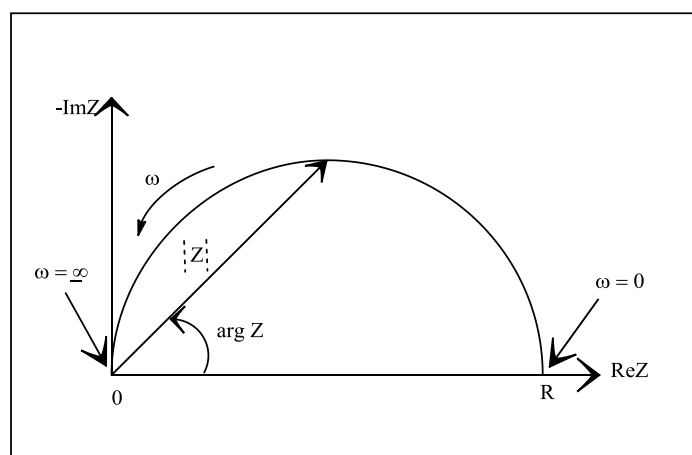


Figure 35. A typical Nyquist plot showing some kinetics.

2.11.5.1. Bode plot

Another popular presentation method for impedance is the Bode plot [450], where the impedance is plotted with log frequency on the X-axis and both the absolute values of the impedance ($|Z| = Z_0$) and the phase-shift on the Y-axis. Unlike the Nyquist plot, the frequency information f and ϕ that helps to ascertain the different constituents' phases of the system more easily can be achieved. However, in those frequency region where a resistive behaviour is dominant, a horizontal line is observed for the $\log Z - \log f$ representation and a ϕ close to 0° is measured [450]. In addition, capacitive behaviour within a frequency region is described by a straight line with a slope of -1 in the $\log Z - \log f$ plots and a ϕ around 90° , whereas diffusion-controlled phenomena (Warburg Impedance) would give a straight line with a slope of $-1/2$ and a ϕ of 45° [451]. **Figure 36** showed a typical Bode plot with one time constant for the equivalent electric circuit of **Figure 37**.

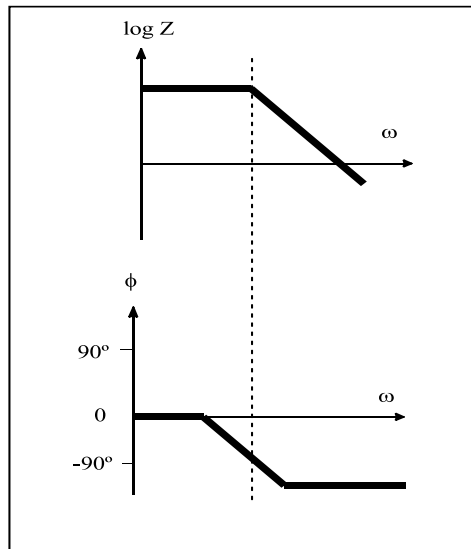


Figure 36. Bode plot with one time constant.



2.11.5.2. Equivalent electrical circuit

Experimental impedance data of an electrochemical cell can easily be fitted to the impedance of an equivalent circuit, the equivalent electrical circuit (EEC) usually considered as the main technique used to analyse EIS data [452] (also called Randle equivalent circuit) and mainly comprising of different element such as resistor, capacitor and an inductor joined in series or in parallel. In such circuits, a resistance ideally describes as a conductive path, such as that generated by the bulk conductivity of the system or the charge-transfer step due to an electrode reaction, whereas a capacitance is generally described as space-charge-polarization regions within the system as well as modification of an electrode surface due to adsorption processes or polymer-layer deposition [453]. Self-made fitting programs can normally be used to construct a quantitative fitting by adopting the proper electrical circuit. In many cases, however, the obtained parameters do not have physical equivalents; therefore, it is difficult to extract information about the electrode reaction mechanism. For example, an inductance arc is often observed in the impedance spectra, but the source for this element in the electrode system remains unclear [450]. Moreover, for a given impedance spectra, there may be several electrical circuits, all of which can provide a good fit and sometimes making it difficult to select the proper equivalent electric circuit model for the electrode system [452, 454].

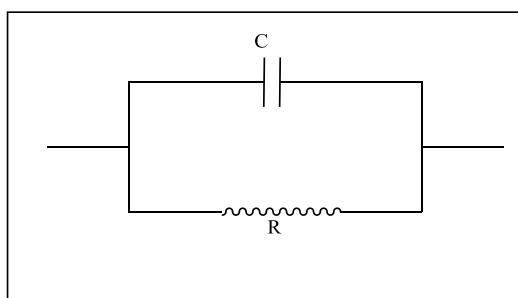


Figure 37. A typical simple equivalent electrical circuit.

A typical electrical circuit element however, comprises of the following parameters which include the following: Solution resistance (R_s), the charge transfer resistance (R_{ct}), Warburg impedance (Z_w) while contribution to the capacitance could be, as a capacitor (C) and constant phase element (CPE) [452, 455]. Table 2 showed the common circuit elements, the equation for their current versus voltage relationship, and the impedance that should be noted.

Table 2. Common circuit elements

Component	Current vs Voltage	Impedance
Resistor	$E = IR$	$Z = R$
Inductor	$E = L di/dt$	$Z = j\omega L$
capacitor	$I = C dE/dt$	$Z = 1/j\omega C$



The following should however be noted about an electrical circuit:

The impedance of a resistor does not depend on the frequency and has no imaginary component. The current through a resistor stays in phase with the voltage across the resistor with only a real impedance component [452]. Also, the impedance of an inductor increases as the frequency increases and inductor has only an imaginary impedance component [452]. As a result, the current through an inductor is phase shifted -90 degree with respect to the voltage. The impedance versus frequency behaviour of a capacitor is opposed to that of an inductor which results in the capacitor's impedance decreasing as the frequency is increased. Capacitors also have only an imaginary impedance component[452]. The current through a capacitor is

phase shifted 90 degree [452] with respect to the voltage. The following parameters are then briefly discussed:

2.11.5.2.1. Solution resistance (R_s)

The solution resistance is the resistance between the working electrode and the reference electrode. This is indicated as a small offset on the real impedance axis. It is measured at high frequency intercept near the origin of the Nyquist plot. The resistance of an ionic solution depends on the ionic concentration and type of ions the electrolyte is made up, temperature and the geometry of the area of the current.

2.11.5.2.2. Charge transfer resistance (R_{ct})

This is the resistance associated with the charge transfer mechanisms for electrode reactions. It is the resistance to electron transfer at the electrode interface. It is deduced from the kinetically controlled electrochemical reaction at low over-potential. The net current (I_{net}) from the oxidation and reduction reactions is then represented by the equation below.

$$I_{net} = I_o \left(\exp\left(\alpha \frac{nF}{RT} \eta\right) - \exp\left(- (1-\alpha) \frac{nF}{RT} \eta\right) \right) \quad \text{Equation 21 [415, 452].}$$

The equation is called Butler-Volmer equation [456]. It is applicable when the polarisation depends only on the charge transfer kinetics. The solution can be stirred to minimise the diffusion layer thickness which can help reduce concentration polarization. When $(n F \eta / RT)$ is well below unity, according to the Buttler-Volmer equation [456], this could be inform of equation 22.

$$I = I_o \frac{nF\eta}{RT} A \quad \text{Equation 22}$$

And also in terms of over-potential (η) and concentration terms for oxidised, reduced and equilibrium states for a one electron redox process thus,

$$\eta = \frac{RT}{F} \left[C_o \frac{(0,t)}{C_o^*} - C_R \frac{(0,t)}{C_R^*} + \frac{I}{I_o} \right] \quad \text{Equation 23 [452].}$$

However, for a small over-potential and in equilibrium system, the expression for the charge transfer resistance for an n electron process could be represented as below

$$R_{ct} = \frac{RT}{nFI_o} \quad \text{Equation 24}$$



From this equation the exchange current density (I_o) can be calculated when R_{ct} is known. The charge transfer resistance is approximated from the diameter of the semicircular region on the real impedance axis of the Nyquist plot. When the chemical system is kinetically sluggish, the R_{ct} will be very large and may display a limited frequency region where mass transfer is a significant factor. But the semicircular region does not form when we have a kinetically facile system and mass transfer always playing the role [452].

2.11.5.2.3. Warburg impedance

The Warburg impedance is associated with diffusion. And it depends on the frequency of the potential perturbation. When the frequency is high, a small Warburg impedance is observed since the diffusion reactant does not move fast enough, whereas, at low frequencies the reactant

have to diffuse farther so as to increase the Warburg impedance. The equation for the "infinite" Warburg impedance is represented as;

$$Z_w = \sigma (\omega)^{-1/2} (1-j) \quad \text{Equation 25}$$

The Warburg impedance usually appear as a diagonal line with a slope of 45° on a Nyquist plot, while on a Bode plot, the Warburg impedance exhibit a phase shift of 45°

The Warburg coefficient, σ , in equation 25 is defined as

$$\sigma = \frac{RT}{n^2 F^2 A \sqrt{2}} \left(\frac{1}{C^* \circ \sqrt{D_o}} + \frac{1}{C^* R \sqrt{D_R}} \right) \quad \text{Equation 26}$$

Where ω is radial frequency, D_o and D_R represents the diffusion coefficient of the oxidant and of the reductant respectively, A is the surface area of the electrode and n is the number of electrons involved. However, if the diffusion layer is bounded i.e., not infinite as discussed above, then, the impedance at lower frequency will no longer obeys the equation above, rather, a form of equation below come into play;

$$Z_o = \sigma \omega^{-1/2} (1-j) \tanh\left(\delta \left(\frac{j\omega}{D}\right)^{-1/2}\right) \quad \text{Equation 27}$$

Where δ represents the Nernst diffusion layer thickness and D represents some of average value of the diffusion coefficients of the diffusing species [457].

2.11.5.2.4. Coating capacitance

A capacitor is formed when two conducting plates are separated by a non-conducting media, called the dielectric [456]. The value of the capacitance depends on the size of the plates, distance between the plates as well as the properties of the dielectric [456]. The relationship is referred to as;

$$C = \frac{\epsilon_0 \epsilon_r A}{d} \quad \text{Equation 28}$$

Where ϵ_0 is the permittivity of free space, ϵ_r is dielectric constant (relative electrical permittivity), A = surface of one plate and d , distances between two plates. Permittivity of free space is a physical constant, but the dielectric constant depends on the material.

2.11.5.2.5. Constant phase element (CPE)

Constant phase is used when there is deviation in capacitors. In some EIS experiment, capacitors does not behave ideally, in such situation, the constant phase element is used, and the impedance can be expressed as:

$$Z = (1/Y_0) (j \omega)^{-\alpha} \quad \text{Equation 29}$$

Where, $Y_0 = C$ which is the capacitance, α is an exponent that equals 1 for a capacitor.

However, for a constant phase element, the exponent α is less than one. When $\alpha = 0.5$, a 45° line is produced on the complex plane graph and could be used for an infinite length of Warburg element. During circuit fitting, the CPE is defined by two values, i.e., the capacitance, C , and the CPE exponent, α , which has a value between 0.5 and 1 for a non-ideal capacitor. If n

equals 1, the equation is identical to that of a capacitor and smaller values can be related to surface roughness and in-homogeneities, which leads to frequency dispersion.

Table 3 showed the common equivalent circuit model, the elements used are listed and equation for both admittance and impedance are given for each element.

Table 3. Equivalent circuit model and dependent variables as fit parameter.

Equivalent element	Admittance	Impedance
R	$1/R$	R
C	$j/\omega C$	$1/j \omega C$
L	$1/j \omega L$	$j\omega L$
W (infinite Warburg)	$Y_o \sqrt{(j\omega)}$	$\frac{1}{Y_o} \sqrt{(j\omega)}$
O (finite Warburg)	$Y_o \sqrt{(j\omega)} \coth(B \sqrt{(j\omega)})$	$\text{Tanh}(B \sqrt{(j\omega)}) / Y_o \sqrt{(j\omega)}$
Q (CPE)	$Y_o (j\omega)^\alpha$	$1/Y_o (j\omega)^\alpha$

2.11.5.2.6. EIS characterisation of a polymer thin film

The numerous processes that take place simultaneously during recharge of polymer layer have made it quite complex, and as such various numbers of models are used describing the impedance spectra for some particular layer. An ideal Nyquist plot for a polymer coated metal electrode in an electrolyte solution and in a purely charge-transfer control system is shown where the charge transfer resistance can be derived from the diameter of the semicircle. The mass transfer in EIS is limited to diffusion (concentration gradient) by the steady state

condition. **Figure 38** shows an equivalent circuit (a) and sample of Nyquist plot of a polymer membrane coated electrode indicating the kinetically controlled (higher frequency) and the mass controlled (low frequency) parts of the plot.

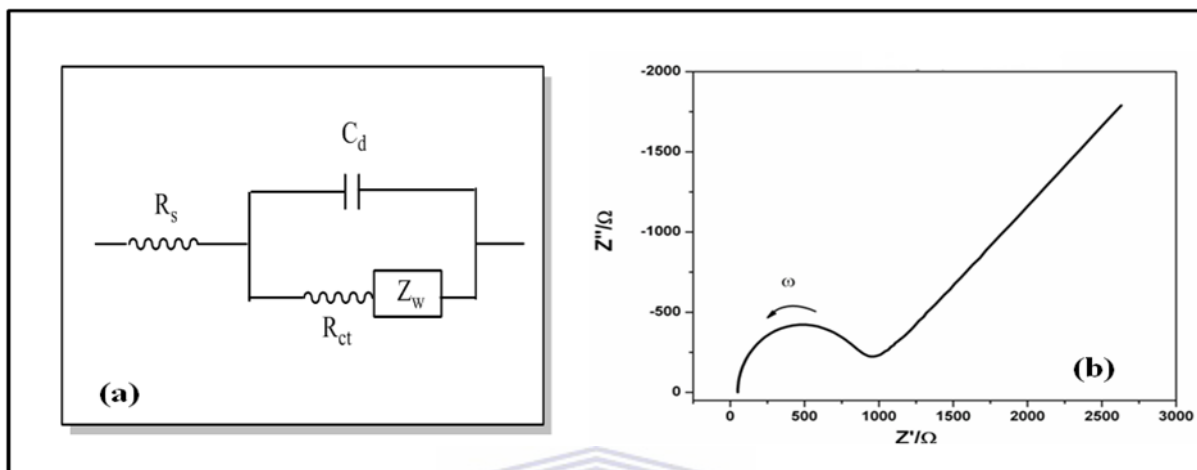


Figure 38. A typical equivalent circuit (a) and Nyquist plot of a polymer membrane (b).

2.11.5.2.7. Impedance modelling using equivalent electrical circuit

The following discussion is on a typical modelling method for EIS based on the impedance theory and reaction mechanism that has been used to interpret and predict EIS characteristics of multi-step reactions. The approach reported has been successfully used in metal corrosion by Péter *et al.* [458], in electrocatalytic reaction. Hsing, *et al.* [459] and Boukamp *et al.* [460], successfully interpreted the behaviour of low frequency reaction-initiated inductive in a solid-state/oxygen-electrode. They showed that the faradaic impedance of electrode reaction can be expressed as a function of the state variables and kinetic parameters as long as the reaction mechanism can be identified, which is a major advantage of this method for data interpretation, as every parameter in the impedance expression has a clear physical significant related to the reaction mechanism. However, in some electrode material, where the values of the kinetic

parameters are not usually available, the experimental impedance modelling approach is combined with equivalent circuit method to solve the problem [450]. **Figure 39** showed a model proposed for the transport process in polyaniline, and the charge transfer kinetics of the ions and solvent at the polymer/electrode/electrolyte interface. The C_L in the circuit model represents the combination of the double layer capacitance from the carbon substrate and pseudo-capacitance (CF) from PANI, which was related to the faradaic process of its redox transition. The concentration of aniline in the 1 M H_2SO_4 solution used for polymerisation was as low as 10 mM. Such a PANI-deposited carbon electrode is denoted as a PC electrode. If the minimum PANI loading is considered, the specific mass of PC electrodes was assumed to be 2.9 mg cm^{-2} [452].

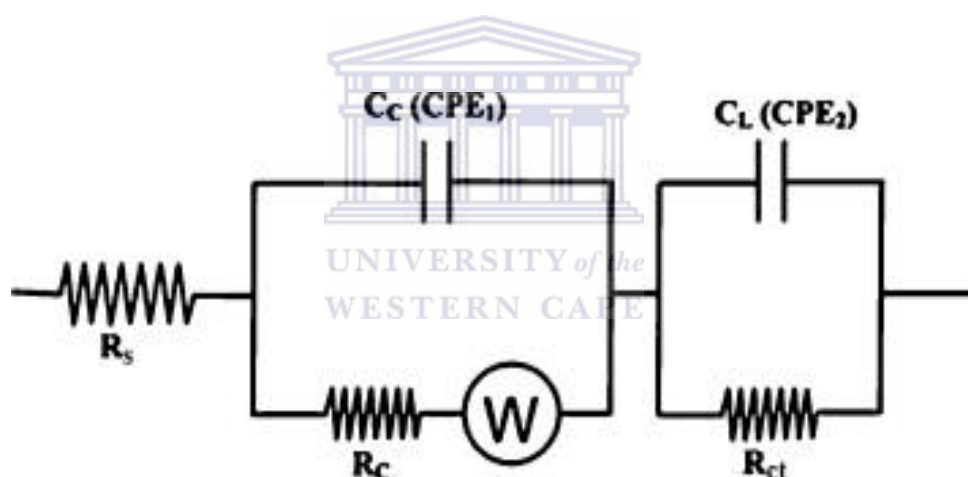


Figure 39. Equivalent circuit for simulating the impedance spectra of bare carbon electrode (BC) and polyaniline carbon (PC) electrodes. Reprinted Diagram from [461] and [452].

The combination of EIS with a commonly used technique like cyclic voltammetry has proven to provide a useful understanding of the properties of conducting polymer based nanocomposite and thus to develop such nanomaterials for specific applications [452, 462].

Other spectroscopic techniques used in this work are Fourier transmittance infrared spectroscopy (FT-IR) and ultra violet visible spectroscopy (UV Vis spectroscopy). Morphological techniques include Raman spectroscopy, atomic force microscopy (AFM), X-ray diffraction (XRD) high resolution transmission electron microscopy (HR-TEM) and high resolution scanning electron microscopy (HR-SEM). These are briefly discussed.



2.11.6. Microscopy and Spectroscopy techniques

2.11.6.1. Ultraviolet-visible (UV-vis) spectroscopy

This is a spectroscopic technique that is referred to as, absorption spectroscopy or reflectance spectroscopy in the UV visible spectral region. It uses light in the visible and adjacent (near-UV and near-infrared (NIR) ranges. It is also referred to as electronic spectroscopy, which implies the involvement of high energy photons in the distribution of the electrons within the molecules, and changes takes place during excitation. In UV-visible spectroscopy, the absorption in the visible range directly affects the perceived colour of the materials involved; consequently, the material as well as the current can be monitored. The colour is associated with the maximum wavelength of the absorption band, λ_{\max} , together with absorbance at individual wavelengths. The optical absorbance of the material, Abs, defined as the logarithmic ratio of the radiation that falls on a material, to the radiation been transmitted through a material [463-465], can be expressed as:

$$Abs = \log_{10} \frac{T \text{ with no sample}}{T \text{ with sample}} \quad \text{Equation 30}$$

Where, T represents the transmittance of light passing through the cell with and without sample. This in essence, gives the amount of electroactive material as converted by the current. Quantitative information of solution of many molecules (metal ion and highly conjugated compounds) absorbing at ultraviolet or visible light is determined. In this case, the absorbance of a solution increase as the attenuation of the beam increases. Therefore, according to the Beer's Law [466], the absorption is directly proportional to b , which is the path length, and c , which is the concentration of the absorbing species, and can be represented as;

$$A = \epsilon bc,$$

Equation 31

Where ϵ is a constant of proportionality, called the absorbtivity, the equation can be re-written as:

$$Abs = \epsilon C_0 l$$

Equation 32

Where the absorbance is determined at fixed wavelength λ , ϵ is the extinction coefficient (cited at the same value of λ), and l is the optical path length. If the magnitude of the extinction coefficient at λ is known, then the amount of analyte (C_0) can be quantified simply by determining the optical absorbance and inserting the values into equation 31 [465]. Different molecules absorb radiation at different wavelength as such, an absorption spectrum will show a number of absorption bands corresponding to structural group within the molecule. So there is a possibility of identifying a certain analyte, using UV-vis spectroscopy. UV-vis spectroscopy is a complementary technique to fluorescence spectroscopy, as electronic transition in fluorescence is from excited state to the ground state, while absorption measures transition from the ground state to excited state [465]. A typical UV-visible spectrum of graphene oxide is shown in the **Figure 40** below.

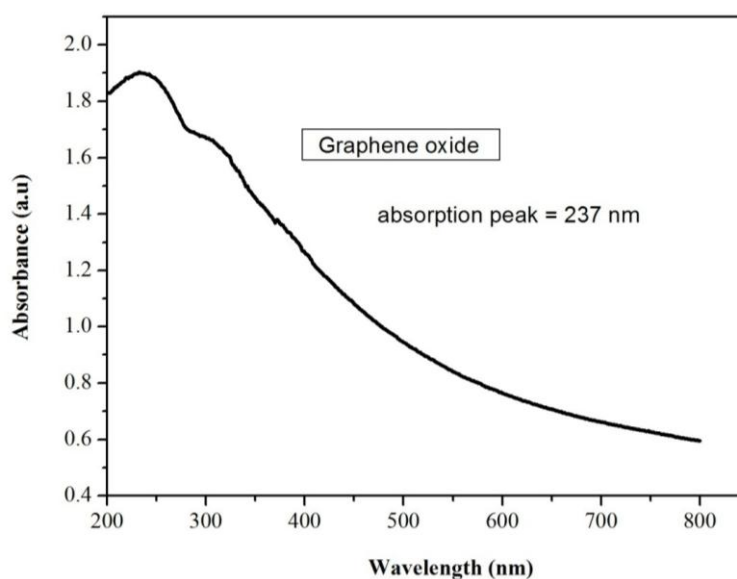


Figure 40. UV-vis spectrum of graphene oxide.

2.11.6.2. Fourier transforms infrared spectroscopy (FT-IR)

Infrared spectroscopy is an important technique that provides easy way to identify the presence of certain functional groups in a molecule. Also, the unique collection of absorption bands can be used to confirm the identity of a pure compound or to sense the presence of specific impurities [467]. In infrared spectroscopy, IR radiation is passed through a sample where some of the radiation is absorbed by the sample and some of it is passed through (transmittance). The resulting spectrum represents the molecular absorption and transmission, producing a molecular fingerprint of the sample. Similar to a fingerprint, two unique molecular structures cannot produce the same infrared spectrum. As a result, infrared spectroscopy can result in a positive identification (qualitative analysis) of every diverse kind of material. Additionally, the size of the peaks in the spectrum is a direct indication of the amount of material present. This makes infrared spectroscopy a useful technique for several types of analysis in terms of identifying an unknown materials, determining the quality or consistency of a sample and the amount of component in a mixture [468]. **Figure 41** is a typical FT-IR spectrum of graphene oxide showing absorption peaks of some functional group.

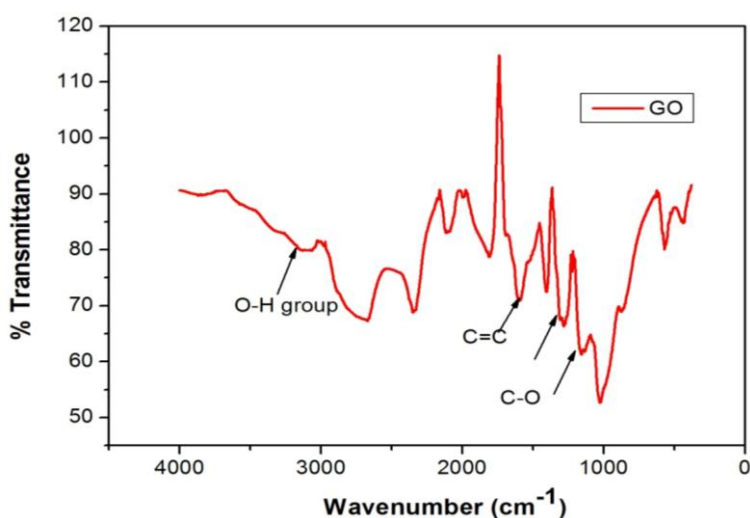


Figure 41. FT-IR Spectra of Graphene oxide.

2.11.6.3. Raman spectroscopy

Raman spectroscopy is a spectroscopic technique that can be used to observe, rotational, vibrational and other low-frequency modes in a system [469]. The technique is based on inelastic scattering of monochromatic light, generally from a laser in the visible, near infrared range, or near ultraviolet range. The interaction of the laser light with molecular vibration, phonons or other excitation in the system results in the Raman shifted photon. This Raman shifted photon could either be higher or lower in energy; it however depends upon the vibrational state of the molecule under study. The shift in wavelength of the inelastically scattered radiation provides the chemical and structural information [470]. Typically, a sample is illuminated with a laser beam and this produces a light spot that is collected with a lens and made to pass through a monochromator. Wavelengths nearer to the laser line owing to elastic Rayleigh scattering are filtered out while the rest of the collected light is dispersed onto detector. Theoretically, when light impinges upon a molecule and interacts with the electron cloud and the bond of the molecule, a spontaneous raman effect will occur in form of light scattering and the molecule is then excited by a photon from the ground state to a virtual energy state. At this stage, the molecule relaxes and emits a photon in return to a different rotational or vibrational state. The energy difference between the states leads to a shift in the emitted photon's frequency away from the excitation wavelength.

However, raman effect is a light scattering phenomenon where excitation of molecule is to a virtual energy level not absorption as with fluorescence where excitation is to a discrete energy level. The emitted photon's shift actually depends on the energy of the vibrational state as regards the molecule under study as earlier mentioned. The photon will shift to a lower frequency if the final vibration state of the molecule is more energetic than the initial state, creating a balance in energy of the system. This shift in frequency is designated as a Stokes shift, and anti-Stokes, if it is reversed. The observed Raman shift of the Stokes and anti-Stokes

features are a direct measure of the vibrational energies of the molecule [469]. However, during raman effect, about 99.999% of all incident photons in spontaneous raman undergo elastic rayleigh scattering while only 0.001% of the incident light produces inelastic raman signal, rendering the spontaneous raman scattering very weak. As such, measures are made by introducing the use of instruments such as tunable filters, laser stop aperture and double or triple spectrometric systems so as to reduce rayleigh scattering and produce a high-quality and raman spectral [469]. Raman shifts are typically in wavenumbers with a unit of inverse length. To convert between spectral wavelength and wavenumbers of shift in the raman spectrum, then expression in equation 33 can be used.

$$\Delta w = \left(\frac{1}{\lambda_o} - \frac{1}{\lambda_1} \right) \quad \text{Equation 33 [471]}$$

Where ΔW is the raman shift expressed in wavenumber, λ_o is the excitation wavelength and λ_1 is the raman spectrum wavelength. The unit commonly use for expressing wavenumber in raman spectra is the inverse of centimetre (cm^{-1}), and wavelength is often expressed as nanometre, therefore, the equation can be scaled for unit conversion, thus, [471].

$$\Delta W (\text{cm}^{-1}) = \left(\frac{1}{\lambda_o (\text{nm})} - \frac{-1}{\lambda_1 (\text{nm})} \right) \times \frac{(10^7 \text{ nm})}{(\text{cm})} \quad \text{Equation 34}$$

A typical example of a raman spectrum is shown in **Figure 42** revealing the characteristics absorption peaks of G band D band of graphene.

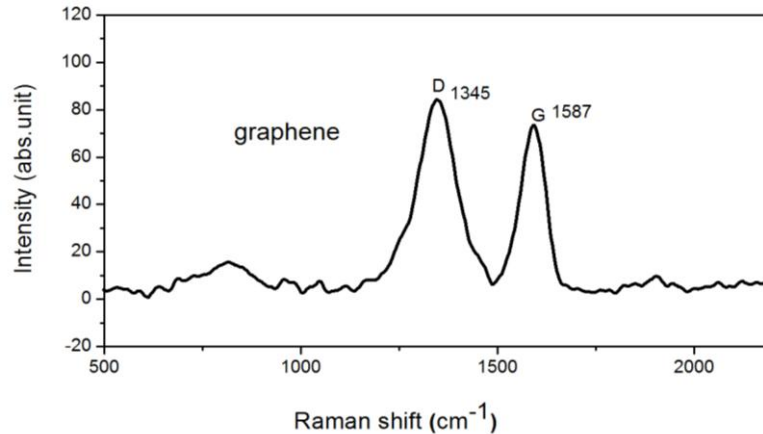


Figure 42. Raman spectrum of graphene.

2.11.6.4. Atomic force microscopy (AFM)

Atomic force microscopy is a type of scanning probe microscopy that is of high resolution and one of the leading tools for imaging. It can measure as well as manipulate matter at the nanoscale [472-473]. The AFM operates by physical interaction of a cantilever sharp tip with the specimen surface. As the cantilever scan the sample surface, forces between the tip and sample leads to a deflection of the cantilever according to hook's law, which is then measured by using a laser spot reflected from the top of surface of the cantilever into an array of photodiode or with some other methods such as capacitive sensing or piezoresistive AFM cantilever [474]. The measurement of the sample is made in three dimension, x, y, and z, which resulted into three-dimensional images of sample surfaces. The type of force measured in AFM however, depends on the situation, and the various types of forces with the inclusion of mechanical contact force, are:, capillary forces, chemical bonding, electrostatic forces, magnetic forces van der waals forces etc. Also, care must be taken during scanning so as to avoid damage of the tip of the cantilever; this may occur if the tip collides with the surface of the sample. Therefore, a feedback mechanism is generally used to adjust the tip-to-sample distance in other to maintain a constant force between the two [475]. A typical AFM usually operates in a number of modes, and the type of mode depends on the kind of application. The

possible imaging modes are then divided into static which is also called contact mode and a variety of dynamic, called non-contact or tapping mode [475]. A sample of an atomic force microscope with a controlling computer is shown in **Figure 43**, while an example of AFM topography image of a graphene on SiO₂ substrate with the profile is shown in **Figure 44**.



Figure 43. Atomic force microscope with a controlling computer.

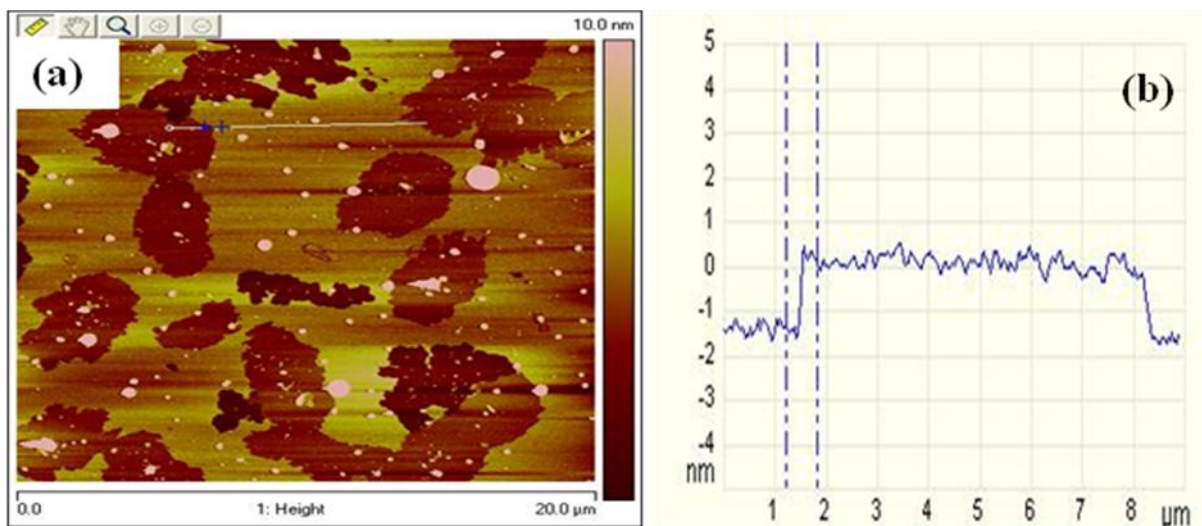


Figure 44. AFM topography image of graphene on a SiO₂ substrate.

2.11.6.5. X-ray diffraction (XRD)

X-ray diffraction is a non-destructive analytical technique which can yield the unique fingerprint of bragg reflections associated with a crystal structure. It is reflected such that, the angle of reflection is equal to the angle of incidence, and this is referred to as diffraction which can be described by Bragg's law [476].

$$2d\sin\theta = n\lambda$$

Equation 35

At this satisfaction, a constructive interferences of the diffraction X-ray beams occurred and a detector scanning picked up the bragg's reflection at this angle. It is the position of these reflection that give information about the inter-layer spacing of atoms in the crystal structure [476]. Therefore, a phenomenon, whereby, x-ray crystallographic method is used to determine the atomic and molecular structure of a crystal, in which the crystalline atoms caused a beam of x-rays to diffract into many specific directions (term referred to as reflection) with a wavelength similar to the distance between the atomic or molecular structure of interest, is called X-ray diffraction. As such, two-dimensional images taken at different rotations are converted into a three-dimensional model of density of the electrons within the crystal while measuring the angle and intensities of the diffraction beam. The mean position of the atom in the crystal can be determined, in addition to their chemical bonds, theirs disorder and various other information can also be gathered through the electron density. However, Poor resolution (fuzziness) or even errors may result if the crystals are too minimal, or not consistent enough in their internal makeup [477]. The following information is expected of a very effective and reliable x-ray diffraction pattern:

The ability to measure the average spacing between layers or rows of atoms

It must be able to determine the orientation of a single crystal of grain

The crystal structure of unknown crystal can be found with x-ray diffraction.

Measurements of the size, shape and internal stress of small crystalline regions of a sample must be possible [478]. **Figure 45** showed x-ray diffraction pattern of graphene oxide and graphite.

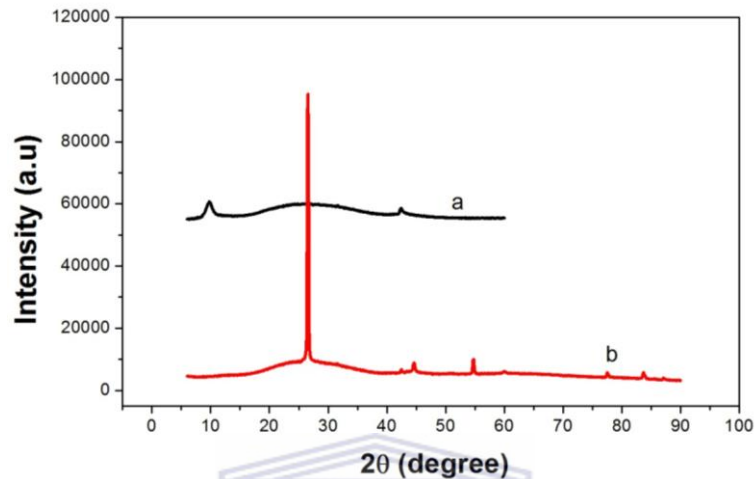
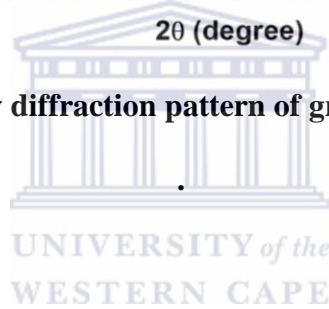


Figure 45. Presentation of x-ray diffraction pattern of graphene oxide and graphite.



2.11.6.6. High Resolution Transmission Electron Microscopy (HR-TEM)

High resolution transmission electron microscope is an imaging mode of the transmission electron microscope that allows for direct imaging of the atomic structure of a sample. The properties of material such as semiconductors, metals, nanoparticles and sp^2 -bonded carbon (e.g. graphene) can be conveniently studied by using HR-TEM [479]. Imaging in HR-TEM is based on phase contrast with a scale (presently around 0.5 angstroms) enough to resolve individual atoms of a crystal and its defects. The process of contrast of a HR-TEM image occurred from the interference in the image plane of the electron wave with itself, a large part of the structure information of the sample which is contained in the phase of the electron wave is then recorded using the amplitude in the image plane. However, the phase contrast mode of

operation is prone to some limitation, as image in phase contrast is influenced by aberration (e.g. defocus) of the imaging lenses in the microscope, which may not allow an instinctive interpretation. Also, problem may arise from the high magnification imaging which requires a high electron dose therefore, specimens need to be comparatively beam insensitive so as to avoid any damage of specimen, however, compounds with a high thermal stability and especially high melting inorganic material can be investigated at atomic resolution. Analysis in HRTEM requires very thin specimen, because, the thinner the better for the technique normally smaller than 50 nm, depending on acceleration voltage used [480]. HRTEM is more applicable and useful in the distribution and structure of defects, interfaces and grain boundaries in samples, nano-crystalline features in amorphous films, small particle analysis in heterogeneous catalysts, sub-micron morphological and device features and in thermodynamic decompositions, diffusion and phase transformations [481-482].

Jiang *et al.* [483] has employed high-resolution transmission electron microscopy (HRTEM) to examine nanodefects at shear bands (main microstructural effect of plastic deformation in amorphous alloys) in both the tensile and compressive regions, and the results have been used to elucidate the mechanism of mechanically-induced nanocrystallisation. They have been able to conclude from the difference in crystallization at shear bands in compression versus tension, that the effect of the adiabatic heating on nanocrystallisation at shear bands is much less significant than enhancement of atomic mobility by deformation. HRTEM has been employed by Yuk *et al.* [484] and reported that direct atomic-resolution imaging allowed visualized critical steps in the process. Site-selective coalescence, surface faceting as well as structural reshaping after coalescence can also be achieved [484]. A typical representation of HRTEM instrument and sample of an image of graphene from the instrument is shown in **Figure 46** below.

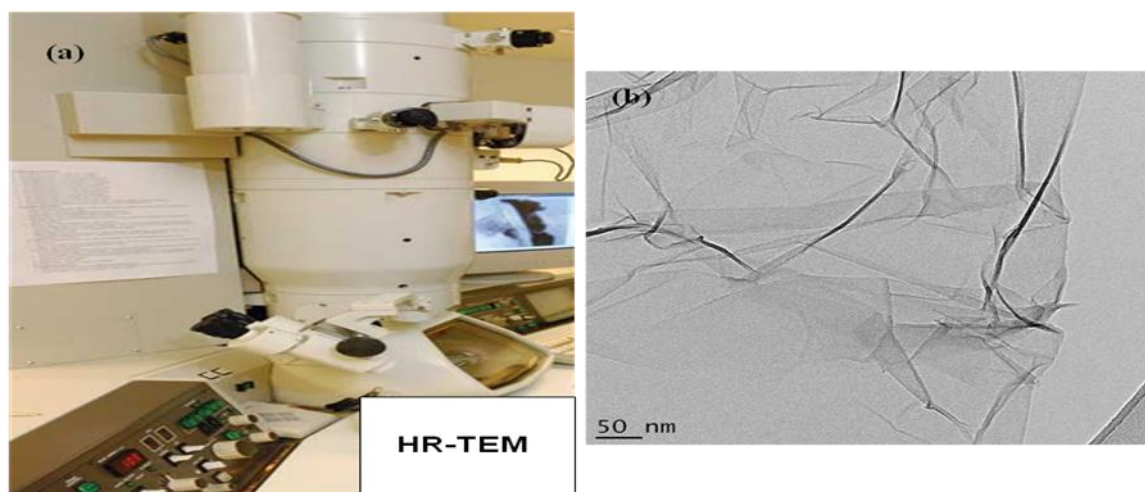


Figure 46. A typical HRTEM (a) and an example of image (b).

2.11.6.7. High resolution scanning electron microscope (HR-SEM)

A scanning electron microscope is a powerful type of electron microscopic techniques in the examination of materials. Images of a sample are produced in HR-SEM when samples are scanned with a focused beam of electron, the electrons then interact with atoms of the sample which resulted in the production of various signals that can be detected and that contain information about the surface topography of the sample and composition. Usually, the electron beams scan in a raster scan pattern and position is combined with the detected signal to produce an image. High modification of images can also be obtained, with a good depth of field as well as analyse individual crystals or other feature. A high-resolution SEM image has been reported to show detail down to about 20 to 25 Angstroms, or even higher [485]. When used in conjunction with the closely-related technique of energy-dispersive x-ray microanalysis (EDX, EDS, and EDAX), the composition of individual crystals or features can be determined. The magnification of the image is the ratio of the size of the screen to the size of the area

scanned on the specimen, for example, if the screen is 300 mm across and the scanned area is 3 mm across on the specimen, then the magnification is x100, also if the scanned area is 0.3 mm across on the specimen, the magnification is x1000 which serves as a higher magnification. **Figure 47** showed a typical MEB-FEG Low voltage and high resolution scanning electron microscope: Hitachi S-4700 (cold FEG) – EDS – back scattered electrons detector. LEO 1530 (Schottky source) – EDS – CL and EBIC at ambient and cryogenic temperature for high resolution imaging and high spatial resolution elemental analysis and an image sample of graphene that was taken [485].

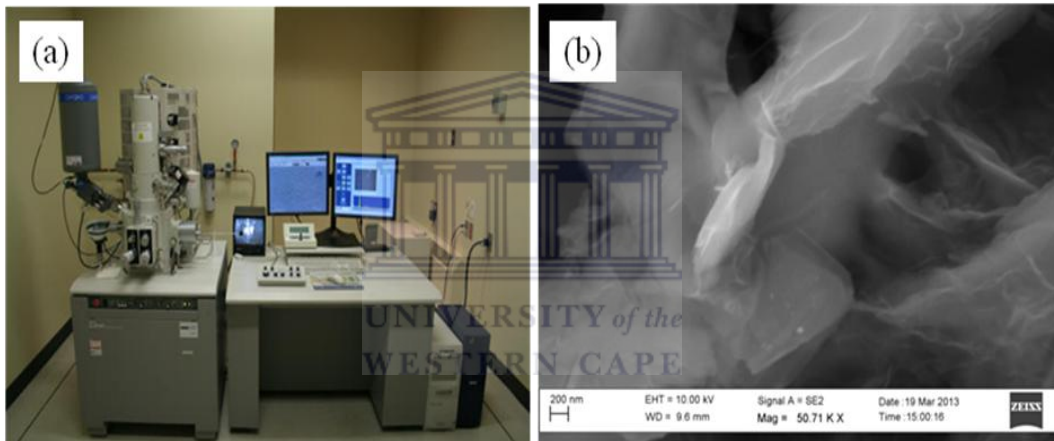


Figure 47. A typical HRSEM (a) and an example of image (b).

CHAPTER THREE

MATERIALS AND METHODS

Introduction

This chapter gives information on materials and different experimental procedures employed for the chemical and electrochemical preparation of graphene oxide, graphene, polyaniline, graphene-polyaniline modified electrode and fabrication of electrochemical sensor based on graphenated –polyaniline doped tungsten oxide.

3.1 Reagents

Natural graphite powder (microcrystal grade, 99.9995%) (Metal base) UCP -1 –M grade, ultra “F” purity purchased from Alfa Aesar was used for graphite oxide preparation Analytical grade aniline (99%) was obtained from Aldrich Chemical, Gillingham, England and purified twice by distillation under reduced pressure and kept in a refrigerator prior to use. Ammonium peroxydisulfate (APS), phenanthrene (PHE), anthracene (ANT), pyrene (PYR) (99%), hydrochloric acid (HCl, 37%), hydrogen peroxide (H₂O₂, 35 wt% water solution), sulphuric acid (H₂SO₄), sodium nitrite (NaNO₂), potassium permanganate (KMnO₄), lithium perchlorate (LiClO₄) and tungstic acid (H₂WO₄) were obtained from Sigma-Aldrich. All chemicals used in this study were analytical reagent grade and used without further purification. 1 M HCl and acetonitrile were used as the supporting electrolytes. Deionised water (18.2 mΩ) purified by a milli-QTM system (Millipore) was used for sample preparations. Analytical grade argon, purchased from Afrox Company, South Africa, was used in cause of analysis. Polishing pads obtained from Buehler, IL, USA and Alumina micro powder (1.0, 0.3 and 0.05 μm alumina slurries) were used for polishing the glassy carbon electrode (GCE).

3.2. Measurements and instrumentations

Cyclic voltammetric (CV) and square wave voltammetric measurements were carried out using a BAS 100W integrated, automated electrochemical workstation from BioAnalytical Systems (BAS) Technicol, Stockport, UK. A conventional three-electrode system consisting of glassy carbon (0.071 cm^2), Ag/AgCl (saturated NaCl) and platinum wire as working, reference and counter electrodes were used respectively. The platinum wire was cleaned by burning through flame and reference electrode was cleaned by rinsing with distilled water. The experiments were carried out at controlled room temperature ($25 \text{ }^\circ\text{C}$). The infrared spectra of graphite, graphite oxide and graphene and the composites were evaluated using Fourier Transform InfraRed spectrometer (FT-IR, Perkin Elmer Spectrum 100), the structural properties were also evaluated through X-ray diffraction (XRD, Phillips X-ray diffractometer with Cu-K α radiation). A tapping-mode atomic force microscope (AFM) (Veeco Nanoman V) was employed to evaluate the morphology of graphite oxide and graphene, with special emphasis on estimating its thickness. The silicon tip [antimony (n) doped] had a curvature radius of 2.5–3.5 μM , a force constant of 1–5 N m^{-1} and a resonance frequency of 60–100 kHz. The samples for AFM were prepared by drop coating the graphene/water (5 μL) dispersion onto a silicon wafer. Transmission electron microscopy images were taken on a Tecnai F20 HRTEM and the scanning electron microscopy images were taken using LEO 1450 HRSEM 30KV instrument equipped with EDX and WDS. The Raman spectra were recorded on a Dilor XY Raman spectrometer with a Coherent Innova 300 Argon laser with a 514.5 nm laser excitation. Electrochemical impedance spectra (EIS) measurements were performed using VoltaLab PGL 402 from Radiometer Analytical (Lyon, France) in a solution containing 1 M HCl. UV-Vis spectra measurements were recorded over a range of 200–900 nm using 3 cm^3 quartz cuvettes with Nicolette Evolution 100 Spectrometer (Thermo Electron Corporation, UK).

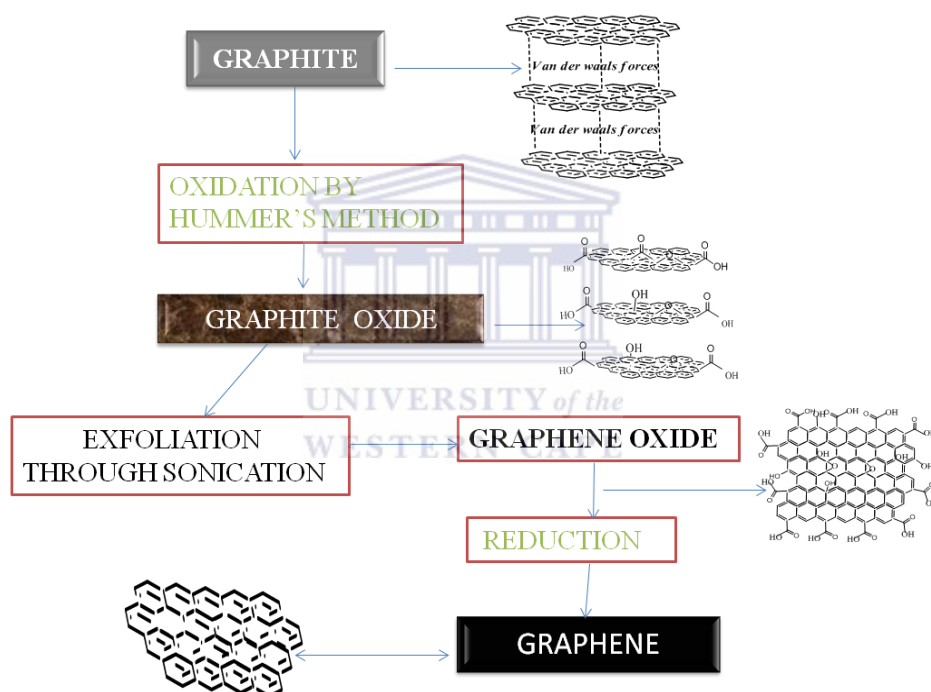
3.3 Preparation of materials

3.3.1. Synthesis of graphite oxide

Graphite oxide was synthesised chemically from graphite powder by the modified Hummers method [346, 486]. In a typical synthesis, concentrated sulphuric acid (50 mL) was gradually added to a 500 mL volumetric flask containing mixture of powdered graphite flakes (2.0 g) and sodium nitrate (1.0 g) at room temperature. The solution was then cooled to 0 °C in ice bath, while vigorous agitation was maintained; potassium permanganate (7.0 g) was added to the suspension for duration of about 30 min. The rate of addition was carefully controlled to prevent the temperature of the suspension from exceeding 20 °C. The ice bath was then removed, and the suspension brought to room temperature, where it was maintained for 30 min. The temperature was then raised to 35 °C in a water bath, and then stirred with a Teflon coated magnetic stirring bar for 12 h. As the reaction progressed, the slurry gradually thickened with diminishing effervescence. The mixture was then cooled in ice bath, followed by addition of excess deionised water to the mixture and treated with hydrogen peroxide (30%) until gas evolution ceased, to reduce the residual permanganate and manganese dioxide to colourless soluble manganese sulphate. The resultant brownish yellow suspension was filtered off, thoroughly washed several times with warm deionised water/ conc. HCl mixed solvent (9:1 volume ratio) in order to remove all sulphate ions, followed by distilled water until neutral pH of the filtrate. The precipitate was then dried under reduced pressure at 60.°C for 24 h to obtain graphite oxide.

3.3.2. Preparation of graphene

From the prepared graphite oxide, 100 mg powder was dispersed in 100 mL of deionised water to be exfoliated into graphene oxide (GO) sheets by ultrasonication for 1 h and to form a stable aqueous dispersion. 200 mg of sodium borohydride (NaBH_4) was added to the dispersion under magnetic stirring, and the mixture was continuously stirred at 125 °C for 3 h. Finally a black precipitated solid was obtained and isolated by filtration then dried under vacuum at 60 °C to obtain graphene (GR) [335]. Scheme 2 showed the illustration to the preparation of graphene from graphite. The sample of the prepared graphite oxide and graphene is shown in **Figure 48**.



Scheme 2. Schematic illustration to the synthesis of graphene.

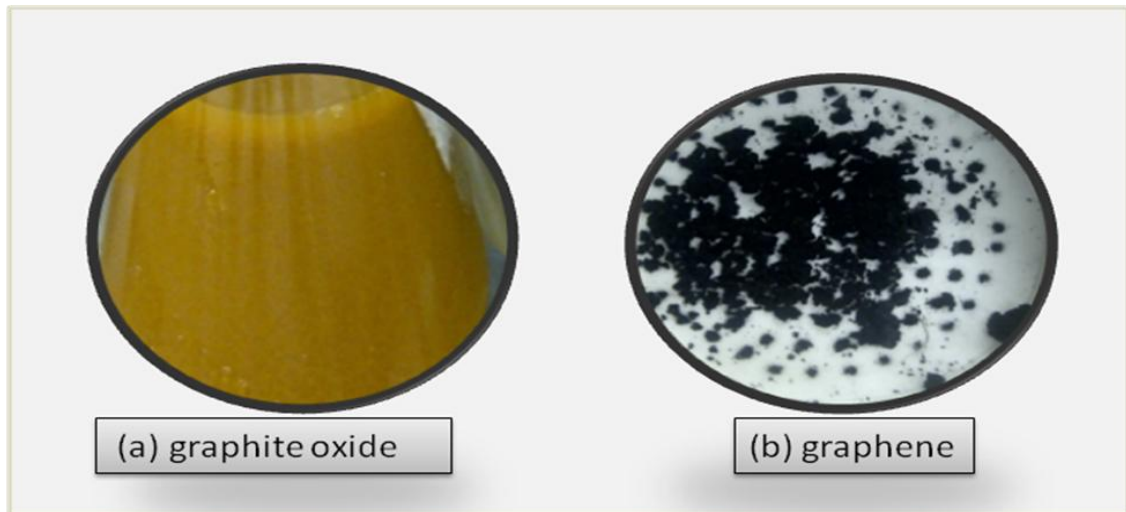
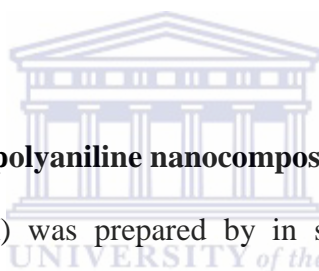


Figure 48. Sample of synthesised solution of (a) graphite oxide and (b) reduced graphene oxide (graphene).



3.3.3. Preparation of polyaniline by chemical polymerisation

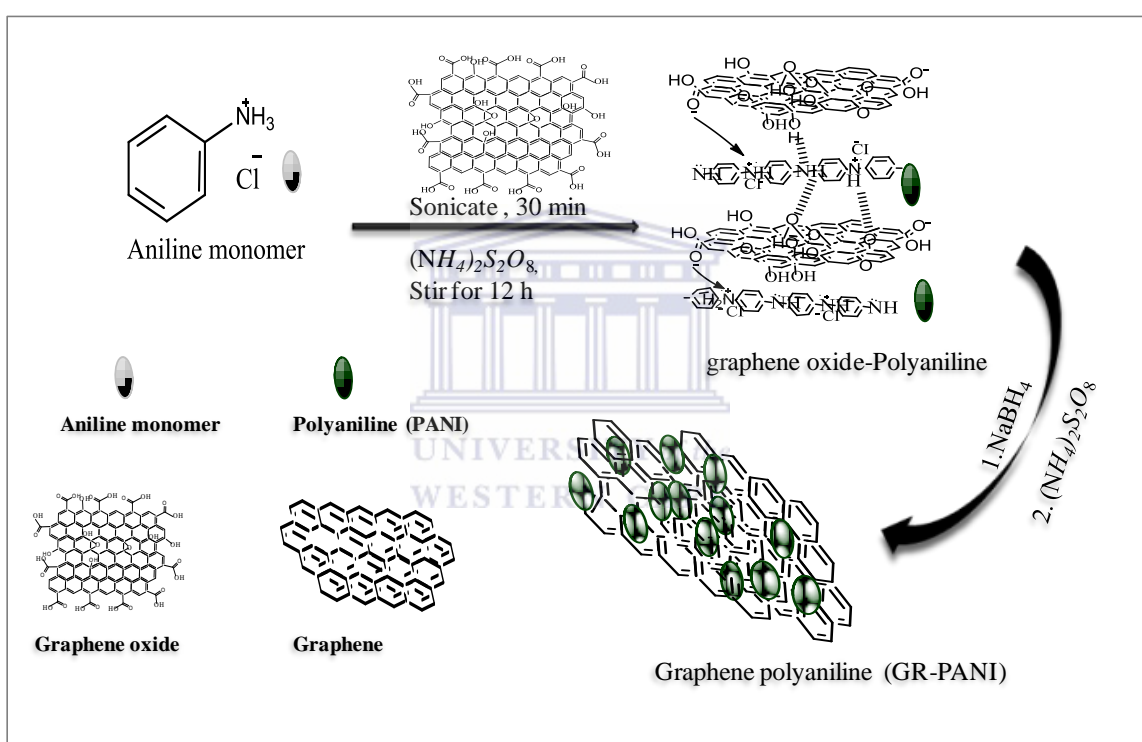
Aniline was first distilled under vacuum to remove impurities. The purified aniline (0.2 M) was dissolved in 10 mL of 1 M HCl aqueous solution. While maintaining vigorous stirring at room temperature, ammonium peroxydisulfate (APS 0.05 M) in 10 mL of 1 M HCl aqueous solution was rapidly poured into the aniline solution. Polymerisation was observed after 5 min when the characteristic green colour of polyaniline emeraldine salt appeared [487]. The mixture was allowed to stir at room temperature overnight, after which the precipitated polymer was collected by filtration and repetitively washed with water, ethanol, and hexane until the filtrate became colourless. Polyaniline sample was collected after having been dried under vacuum at 60 °C [217, 225, 488].



3.3.4. Preparation of graphene-polyaniline nanocomposite (GR-PANI)

Graphene-polyaniline (GR-PANI) was prepared by in situ polymerisation of aniline in a suspension of graphene oxide through the chemical oxidation of aniline with APS in an acidic medium according to the literature [489]. In a typical preparation, 0.2 M solution of purified aniline in aqueous 1 M HCl was added to the aqueous dispersion of graphene oxide [GO: Aniline ratio = 2:1]. The solution was further sonicated for 30 min. Another solution of 0.05 M Ammonium peroxydisulfate in aqueous 1 M HCl was rapidly added to the mixture under vigorous stirring at room temperature. A green colour change appeared after about 5 min indicating the polymerisation of aniline. The solution was left to stir at room temperature overnight, after which the resulting mixture was filtered, washed with water, ethanol and hexane until filtrate became colourless. The resulting mixture was then reduced in sodium borohydride (NaBH₄) [3]. Typically, the prepared sample was dispersed in distilled water [1 mg mL⁻¹] and sonicated for 1 h to form a stable aqueous dispersion. NaBH₄ was added to the

dispersion under magnetic stirring, and the mixture was continuously stirred at 125 °C for 3 h. The reduced precipitated solid was obtained and isolated by filtration, then re-dispersed in 1 M aqueous HCl containing ammonium peroxydisulfate (APS), and stirred at room temperature overnight for reoxidation and reprotonation to occur so as to recover the polyaniline (PANI) crystallinity. The resulting graphene–polyaniline nanocomposite was collected by filtration and dried in vacuum at 60 °C [24, 488, 490].



Scheme 3. Schematic illustration of chemical synthesis of graphene-polyaniline nanocomposite via in situ polymerisation.

3.3.5. Preparation of the graphene polyaniline modified electrode

The bare glassy carbon electrode (GCE) was polished with 1.0, 0.3 and 0.05 μM alumina powder rinsed with distilled water followed by ultrasonication with ethanol, and deionised water, respectively, and dried at room temperature prior to modification. The GR-PANI nanocomposite (1 mg) was dispersed in ethanol (1 mL) and ultrasonicated for 30 min to get homogenous suspension. Then, 5 μL of the suspension was drop coated onto the surface of the freshly polished glassy carbon electrode (GCE) and dried at room temperature, resulting in graphene-polyaniline modified electrode (GR-PANI|GCE) [489]. Graphene modified electrode was also prepared in the absence of polyaniline for comparison of results.

3.3.6. Preparation of polyaniline-tungsten oxide-graphene film (PANI|WO₃|GR)

3.3.6.1. Optimisation of the PANI film

Experiment was carried out to determine the potential scan rate that will be suitable for the electrosynthesis of the PANI film before the inclusion of the Graphene and WO₃ in the film. According to the method adopted [16]. PANI films were grown at 20, 50, 100 and 200 mV s^{-1} on a glassy carbon electrode (GCE). The cyclic Voltammetric polymerisation was carried out in a 10 mL cell solution containing 0.1 M aniline and 1M HCl at constant potential scan rates of 20, 50, 100 and 200 mV s^{-1} , and potential window, from -200 to +1200 mV with reference to Ag/AgCl electrode. Electropolymerisation was stopped after 10 cycles, after which the PANI|GCE was placed in 1 M HCl solution for cyclic voltammetry at 5, 10, 15, 20, 30, 40 and 50 mV s^{-1} . The cyclic voltammogram of these PANI films at different scan rates were then analysed and compared. The potential sweep rate of 50 mV s^{-1} was chosen after considering the polymerisation current and electrochemical behaviour of the PANI|GCE films. This was used

as one of the experimental conditions in the preparation of the polyaniline-tungsten-oxide-graphene (PANI|WO₃|GR) films for the target nanocomposite.

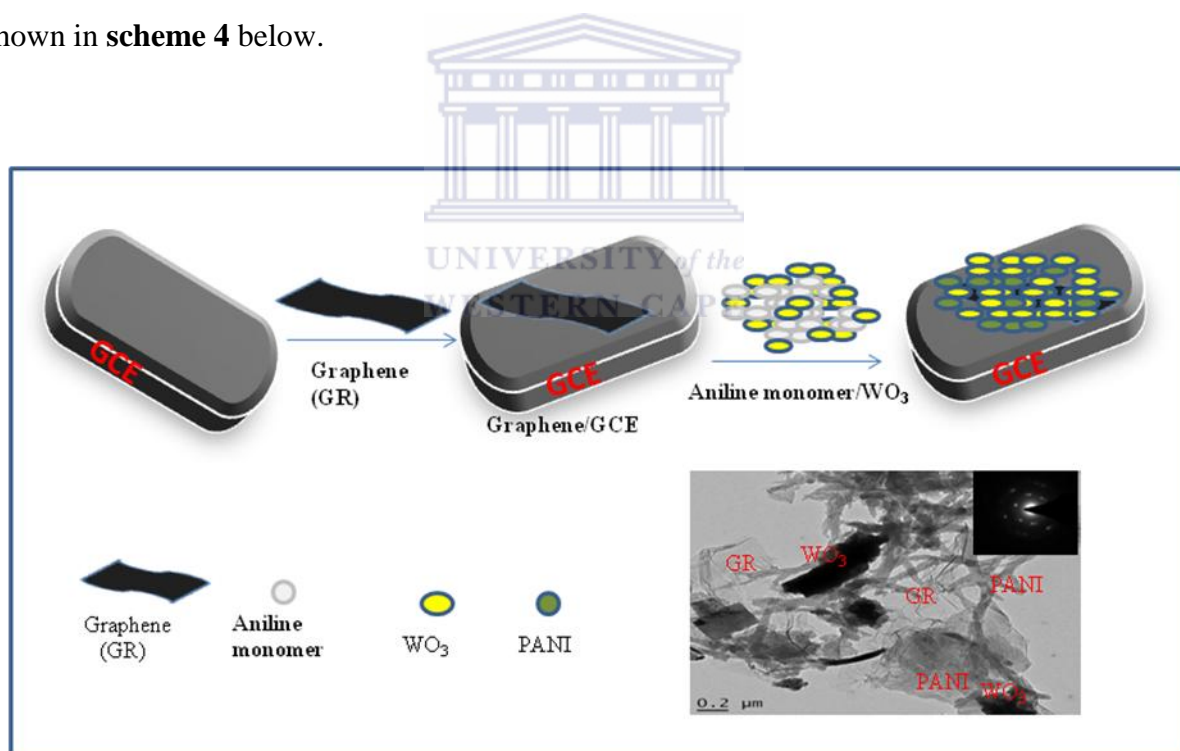
3.3.6.2. Optimisation of hydrogen peroxide

The addition of hydrogen peroxide (H₂O₂ 30%) to the solution of Tungstic acid is essentially attributed to the formation of peroxy-precursor in the deposition solution. The peroxy tungstate formed is assumed to undergo electrochemical reduction and gives rise to tungsten oxide (WO₃) on the substrate as earlier reported that the deposition of WO₃ from peroxy-tungstate is more favourable on the substrate and serves as stabilizer as well as complex reagent in preventing aggregation of tungsten oxide whereby forming homogenous solution [491]. However, excess hydrogen peroxide has been reviewed to have effect on the deposition of PANI by restraining the electrodeposition of PANI on the substrate [492]. It is then become necessary to optimise the addition of the peroxide in other for a suitable deposition of polyaniline. After optimisation of H₂O₂ at different concentration (0.05, 0.08, 0.1 and 0.15 M.), 0.08 M was found suitable for the deposition of PANI.

3.3.6.3. Preparation of polyaniline-tungsten oxide-graphene film

Prior to modification, the bare GCE was polished with 1.0, 0.3 and 0.05 μM, alumina powder, rinsed with distilled water followed by ultrasonication with ethanol, and deionised water, respectively, and dried at room temperature. Graphene (1 mg) was dispersed in ethanol (1 mL) and ultrasonicated for 30 min to get homogenous suspension. Then, 5 μL of the suspension was drop coated onto the surface of the freshly polished and dried glassy carbon electrode (GCE) and dried at room temperature, resulting in graphene modified electrode (GR-GCE). According to the procedure [492], prior to electrodeposition, deposition solution was prepared, consisting of Tungstic acid (0.2 M), HCl (1 M), H₂O₂ (0.08 M). The solution was stirred at 60 °C for 1 h, after which aniline (0.1 M) was introduced into the solution, and resulting solution was then

electrodeposited on the graphene modified electrode. The cyclic voltammetry electrodeposition was carried out by scanning the potential from -600 to + 1000 mV at a potential scan rate of 50 mV s⁻¹. After 10 voltammetry cycles, the polyaniline-tungsten oxide-graphene (PANI|WO₃|GR) electrode formed was then removed, gently rinsed with distilled water to remove any loosely adsorbed aniline and ready for further characterisation and application. Polyaniline-tungsten oxide (PANI|WO₃) composite film was prepared at the same condition in the absence of graphene to get PANI|WO₃ electrode. Electropolymerisation of aniline on the glassy carbon electrode was also carried out in a solution of 0.1 M aniline and 1 M HCl at a scanning potential of between -600 mV and +1000 mV, potential scan rate of 50 mV s⁻¹ as PANI|GCE according to literature [493-496]. The schematic illustration of the synthesis is shown in **scheme 4** below.



Scheme 4. Schematic diagram of the deposition of PANI|WO₃ film on graphene modified electrode.

3.4. Characterisation of graphene-polyaniline (GR-PANI) modified electrode and Polyaniline-tungsten oxide-graphene (PANI|WO₃|GR) nanocomposite

3.4.1. Electrochemical characterisation

3.4.1.1. Cyclic voltammetry (CV)

Electrochemical measurement and behaviour of graphene, graphene-polyaniline (GR-PANI) and polyaniline-tungsten oxide-graphene (PANI|WO₃|GR) modified electrodes prepared were studied in 1 M HCl solution over a potential range of -200 to + 1200 mV for (GR-PANI) and -600 to + 1000 mV for (PANI|WO₃|GR) at different scan rates.

3.4.1.2. Electrochemical impedance spectroscopy (EIS)

Electrochemical impedance spectroscopy (EIS) of the GR-PANI and PANI|WO₃|GR modified electrodes were performed in a solution containing 1 M HCl solution. The results are then plotted in the form of Nyquist plots at perturbation amplitude of 10 mV and within a frequency range of 100 kHz to 0.1 Hz for each of the electrodes, respectively.

3.5. Morphological characterisation

The morphology of graphene, graphene-polyaniline (GR-PANI) and polyaniline-tungsten oxide-graphene (PANI|WO₃|GR) was characterised on FT-IR, XRD, HR-SEM, HR-TEM, RAMAN, AFM and UV-Vis spectroscopy as described in section 3.2.

3.6. Application of the GR-PANI modified electrode as sensor on anthracene

The anthracene stock solution of 0.005 M was prepared by dissolving 0.044 g in 20 cm³ of acetonitrile to attain solubility and later made up to 50 cm³ with distilled water. Aliquots solution (in μL) was spiked from the stock solution into the cell and used for sensor

development. The cell consisted of graphene-polyaniline (GR-PANI) modified glassy carbon electrode as the working electrode, platinum counter electrode and Ag/AgCl (3 M NaCl) reference electrode. A 5 mL solution of acetonitrile (acetonitrile: water = 80:20) containing 0.1 M LiClO₄ was used as the working electrolyte. Cyclic voltammetry and square wave voltammetry was performed over the potential range of -200 mV and +1400 mV to study the modified electrode and electrocatalytic oxidation of the anthracene.

3.7. Application of polyaniline–tungsten oxide-graphene nanocomposite as polyaromatic hydrocarbon nanosensor

3.7.1. Choice of electrolyte

The choice of suitable solvent for dissolution of polyaromatic hydrocarbon is necessary because of their hydrophobic nature in water hence, acetonitrile was chosen as a suitable solvent because of its relatively high dielectric constant, and reported ability to dissolve most PAHs [435]. Acetonitrile, as a common and general choice of electrolyte in the quantification of polyaromatic hydrocarbon is however, a non-aqueous electrolyte and non-conducting, and usually require the support of an electrolyte that can enhance the conductivity and migration of current. Also, Polyaromatic hydrocarbons (PAHs) are in aqueous form in the aquatic environment (wastewater). It is therefore in our interest to use an electrolyte that is aqueous, more conducting and that can also allow the detection of PAHs in the aqueous environment. In this work, the choice of aqueous HCl as the working electrolyte in the quantification and determination of polyaromatic hydrocarbon goes along with the fact that, HCl is a strong electrolyte due to its ability to ionize completely in water; it is more electrically conducting and has affinity for the electroactive species [497].

3.7.2. Preparation and determination of PAHs

A stock solution of 1.0×10^{-5} M of anthracene, phenanthrene and pyrene were prepared by dissolving 8.7×10^{-5} g and 1.0×10^{-4} g of anthracene, phenanthrene and pyrene respectively in 50 mL of acetonitrile /water (80:20 v/v) [498]. Further dilution of the stock solution was done to get 1.0×10^{-6} mM of each of the initial stock solution and from these stock solutions, aliquot solution (in μL) were spiked into the supporting electrolyte. For the electrocatalytic oxidation of the PAHs, 5 mL solution of 1 M HCl was placed in the electrochemical cell consisting of the PANI|WO₃|GR nanocomposite modified glassy carbon as the working electrode, platinum counter electrode and Ag/AgCl (3 M NaCl) reference electrode. The solution was degassed with argon for 10 min before the experiment. Cyclic voltammetry and square wave voltammetry characterisation of the modified electrodes were carried out at scan rate of 30 mV s^{-1} , initial potential of 0 mV to final potential 2000 mV, and response in the absence and presence of PAHs were monitored. Solution was stirred for 5 min after each addition of aliquots (in μL) of PAHs and increase in the catalytic current as well as the potential at which oxidation occurred was then monitored after every addition of each analyte [499].

3.7.2. Interferences, stability and reproducibility studies

Reproducibility and stability studies of the modified electrodes were investigated in the presence of each the analyte of interest by performing cyclic voltammetry experiments 6 times with each of the modified electrodes. Changes in sensitivity were monitored to ascertain the reproducibility of electrochemical sensors. Also, some substances that are assumed to interfere with the detection of the PAHs were also investigated by the developed electrochemical sensors. Substances such as Mn^{2+} , Fe^{2+} , K^+ , Mg^{2+} , NO_3^- and Cl^- were taken into account [144, 500-501]. Mixture of the selected substances was prepared and mixed with a similar

concentration of each of the different PAHs at a ratio of 1:1, and the cyclic voltammetry measurement was carried out on the resulting mixtures.



CHAPTER FOUR

RESULTS AND DISCUSSION-PART 1

Summary

This part presents results and discussion on the chemical synthesis of graphite oxide and graphene. Morphology and structural characterisation of the prepared materials were studied using techniques such as AFM, HR-TEM, SEM, XRD, RAMAN and UV-vis spectroscopy.

4.1. Introduction

The hummer's method of preparing graphene is one of the most successful approaches to getting graphene and has proven to be one route to a fairly large amount and effectively low cost graphene [346, 502]. The method involves treatment of graphite with potassium permanganate, sulphuric acid, sodium nitrite and hydrogen peroxide which produced brownish colour graphite oxide (GO) that is hydrophilic in nature due to the presence of the functional groups generated during oxidation. As such, a stable colloidal suspension of thin sheets of GO can be formed in water which later brings about a stable dispersion of very thin sheet of graphene oxide by exfoliation process through ultrasonication [331]. However, the GO synthesised is insulating nature and there is need for further processing so as to be used as a conductive nanomaterials, as such the conductivity of GO can be restored by chemical reduction with a reducing agent in producing a very thin sheets of graphene. Sodium borohydride was then added as a reducing agent which enables the homogeneously dispersed graphene oxide sheets to turn from brownish yellow to black aggregate and precipitated sheet, confirming the reduction of graphene oxide to graphene, mechanism illustration is shown in the **Figure 49** below [335, 503].

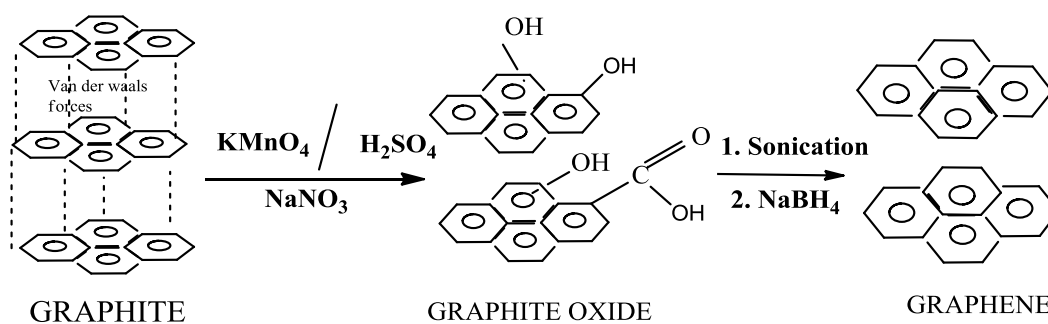


Figure 49. Schematic representation of the mechanisms in the preparation of graphene.

4.2. Characterisation of graphite oxide and graphene

4.2.1. Scanning electron microscopy (SEM)

The formation of the graphite oxide and graphene was confirmed by scanning electron microscopy (SEM) analysis. **Figure 50a** showed a well exfoliated folding sheets of graphene oxide (GO) and closely associated, compared to an agglomerated particles with aggregated and overlapped of thin, crumpled, wrinkled graphene sheets and closely associated with each other, forming a disordered solid, shown in **Figure 50b** according to literature [266]. The EDX analysis is shown in **Figure 51**, revealing the elemental composition of graphene oxide to consist of carbon with a weight percentage of 51.46%, followed by a weight percentage of 44.81% of oxygen. The presence of sulfur element with a weight percentage of 3.74% may be attributed to contaminant from sulfuric acid used during washing.

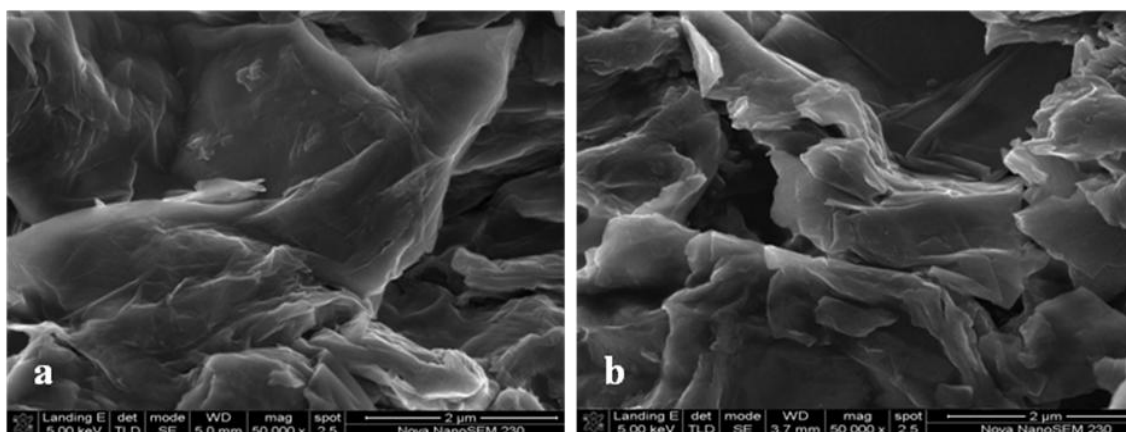


Figure 50. SEM images of (a) graphene oxide (GO) and (b) graphene (GR).

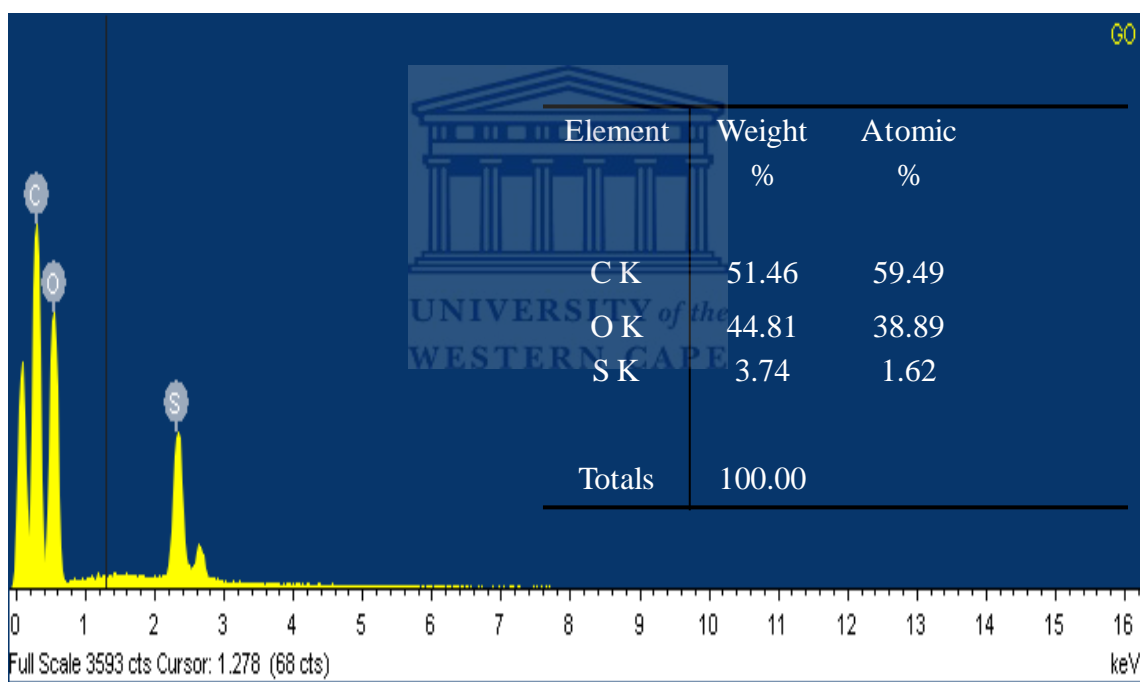


Figure 51. Energy dispersive X-ray spectrum of graphene oxide.

4.2.2. High resolution transmission electron microscopy (HRTEM)

The graphene oxide and graphene prepared were investigated using high resolution transmission microscopy (HRTEM). Typical HRTEM images can be observed from **Figure 52a and Figure 52b**. GO showed a transparent wrinkled surfaces of silky sheets and an entangled folding edges can also be observed. A thin, flat and well transparent sheet can be observed for graphene, with the selected area electron diffraction (SAED) pattern confirming crystalline character of the structure., but different from GO and comparable to literature [300]. **Figure 53** revealed the elemental composition of graphene acquired from HR-TEM analysis of graphene, dominated with more of carbon and less percentage of oxygen that may be from impurities or from oxygen functional group of graphene oxide that are left inform of impurities after redution. Other noticeable elements such as sodium and chlorine are as a result of impurieties during washing.

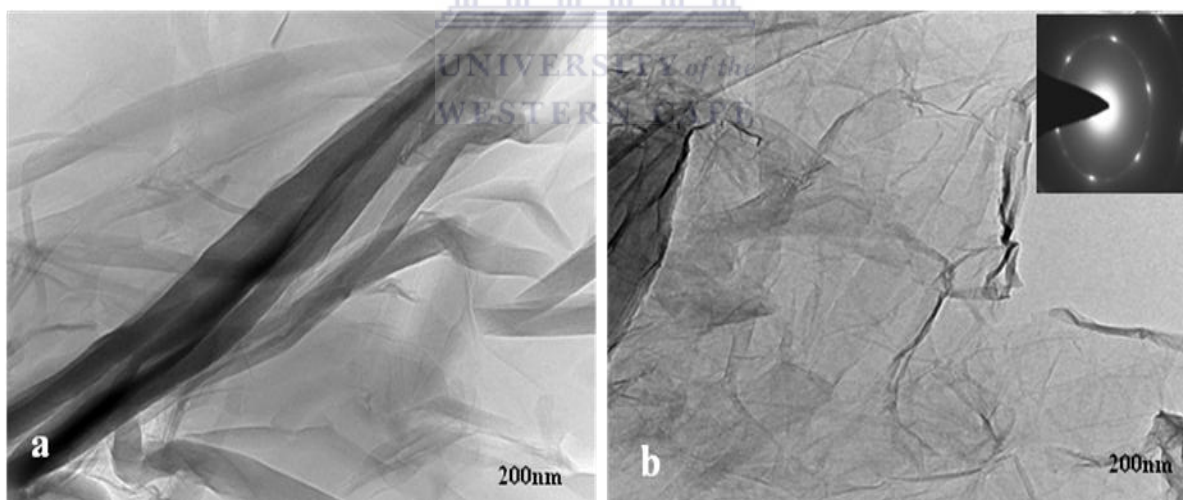


Figure 52. HRTEM images of (a) graphene oxide and (b) graphene.

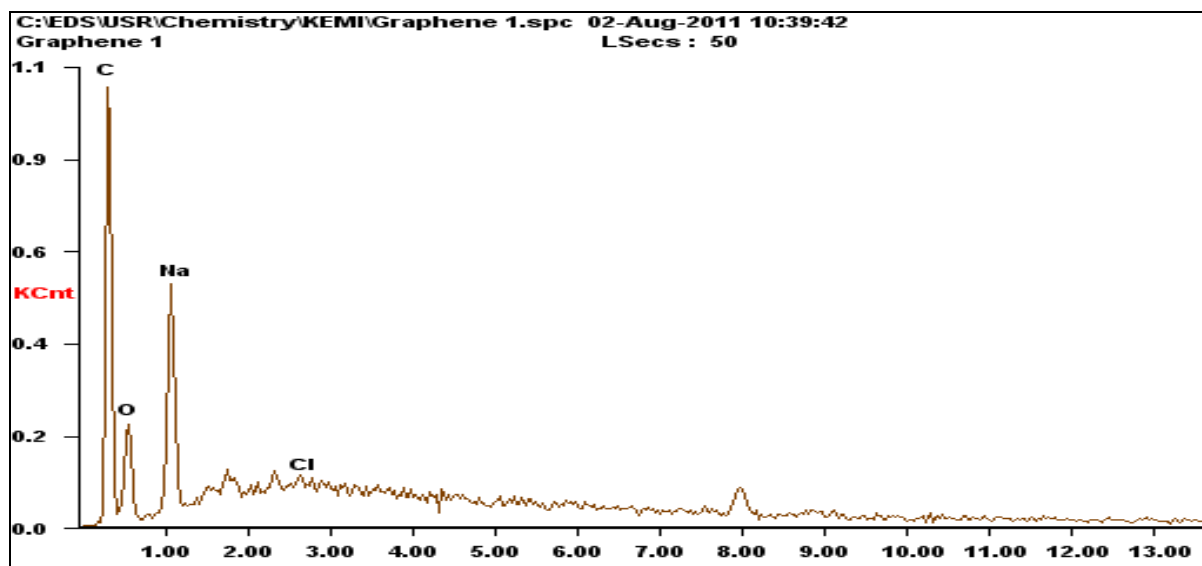


Figure 53. Energy dispersive X-ray spectrum of graphene.

4.2.3. Fourier Transform Infra-Red (FT-IR)

The Fourier Transform Infra-Red (FT-IR) spectra of graphite, graphene oxide (GO) and graphene is showed in **Figure 54**. No distinct peaks can be detected in graphite (a). Graphene oxide (GO), however showed collections of peaks corresponding to the following functional groups: C=O (1735 cm^{-1}), aromatic C=O (1602 cm^{-1}), carboxyl C-O (1416 cm^{-1}), epoxy C-O (1265 cm^{-1}), alkoxy C-O (1047 cm^{-1}), hydroxyl O-H (3390 cm^{-1}) [504-505]. The appearance of the collection of the functional peaks gave an indication that the original extended conjugated orbital system of the graphite powder were destroyed during the oxidation process and oxygen containing functional groups has been inserted into the carbon skeleton according to literature [506]. After reduction with sodium borohydride (NaBH_4), bulk of the oxygen functional groups was eliminated, confirming the reduction of graphene oxide by chemical reduction to graphene and in agreement with those reported by Chen *et al.* [319].

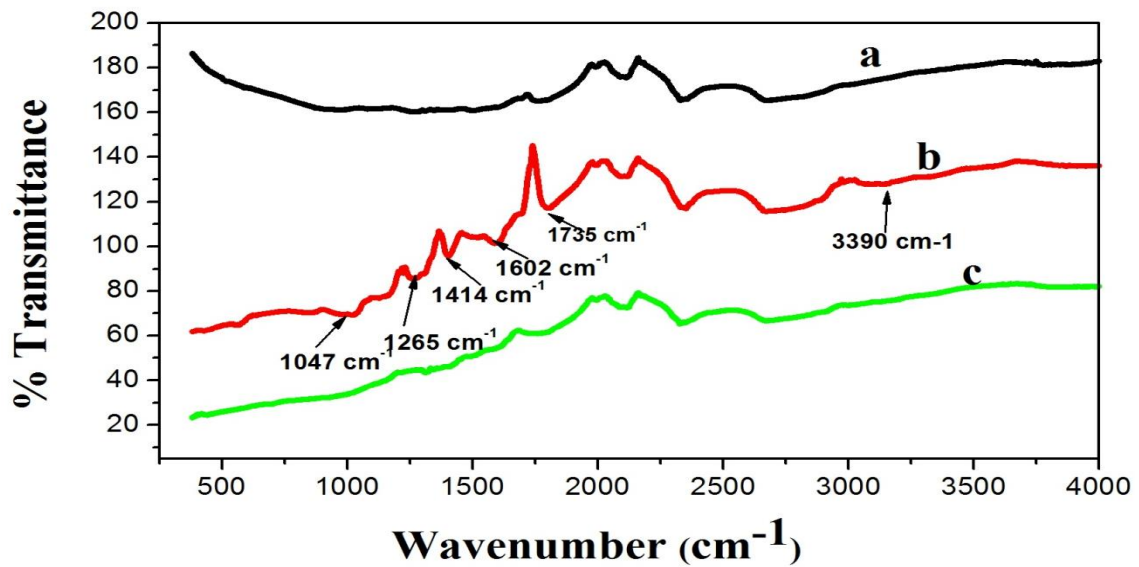


Figure 54. FTIR spectra of (a) graphite, (b) graphene oxide and (c) graphene.

4.2.4. Atomic force microscopy (AFM)

The level of exfoliation of graphene was characterised by using atomic force microscopy (AFM) as showed in **Figure 55**. The AFM topography image of graphene, in which several graphene sheets were randomly deposited on the silicon substrate revealed slightly rough surface which can be attributed to the existence of some functional groups after reduction. The cross sectional view across the plain area of the sheet gave an estimated height of 1.4 nm which is consistent with that reported by Chandre *et al.* [336]

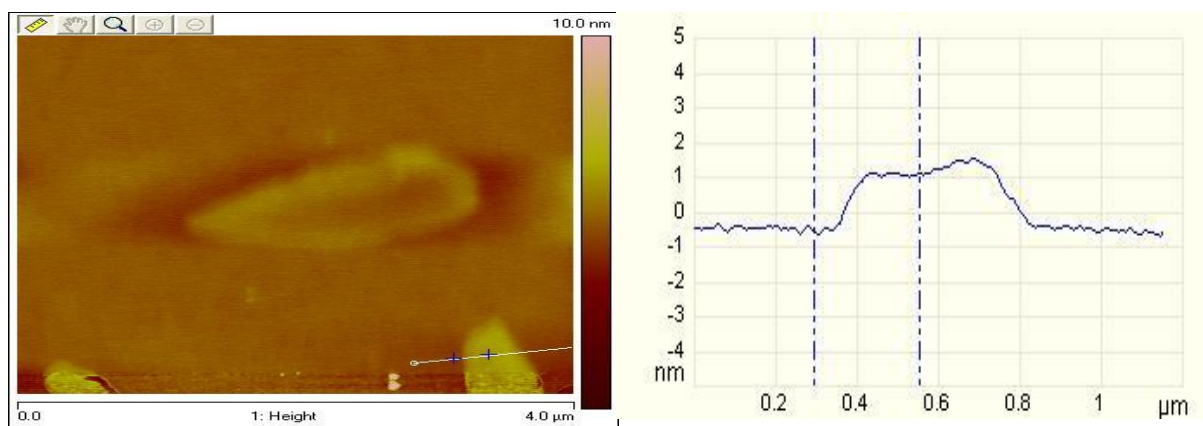


Figure 55. AFM image of graphene sheets with height profile.

4.2.5. X-ray diffraction (XRD)

X-ray diffraction pattern of graphite, graphene oxide and graphene is presented in **Figure 56**. The interlayer distance of graphite exhibits a strong peak (002) at 26.55° which can be attributed to van der Waals layer of carbon atoms tightly packed together. After oxidation, it becomes expanded as result of the displacement of the carbon atoms and the presence of the oxygen containing functional groups and water (H_2O) molecule [507]. The (002) peak disappears and an additional peak corresponding to diffraction peak of graphene oxide (001) is observed at 9.65° . At reduction, the interlayer distance returns showing the disappearance of the diffraction peak of graphite oxide, and replaced by a broadened diffraction peak at 23.81° that is lowered in intensity compared to graphite and graphene oxide as earlier confirmed [507]. This suggested that most of the oxygen functional groups have been removed and there is restoration of the conjugated sp^2 carbon graphene network which is also confirmed by the changes in FT-IR.

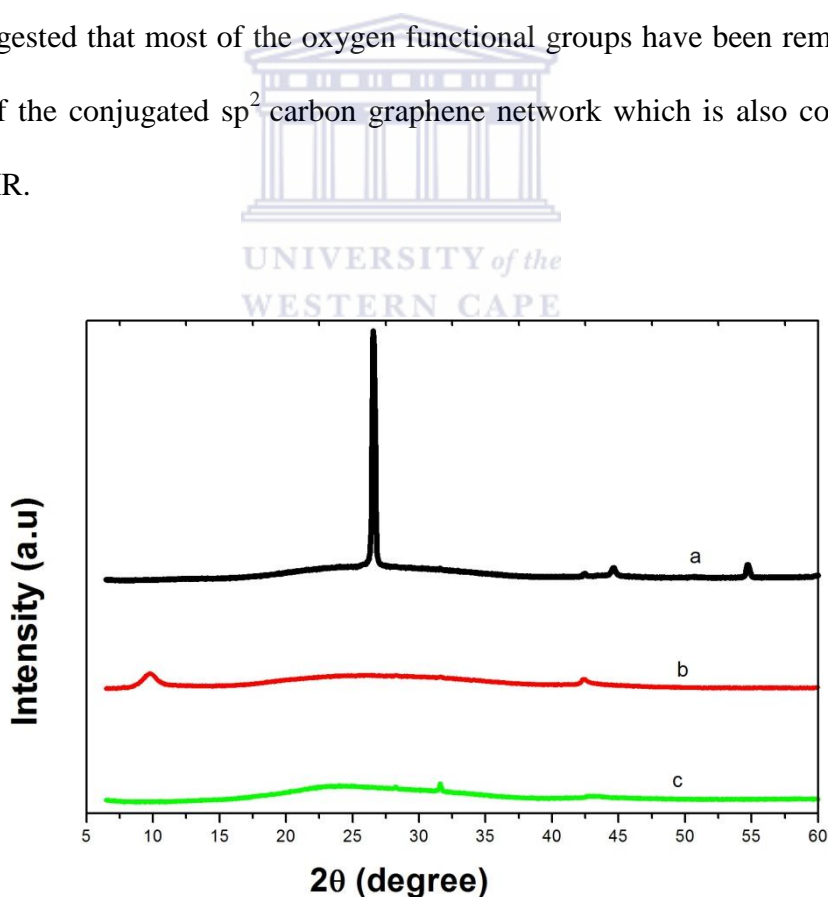


Figure 56. XRD pattern of (a) graphite, (b) graphene oxide and (c) graphene.

4.2.6. Raman spectroscopy

Raman spectroscopy is generally used to determine the transformation in the structural pattern during the chemical synthesis of the graphite oxide to graphene and also to identify the number of layers of graphene [508]. In the raman spectral shown in **Figure 57**, graphene (a) showed three peaks, G-mode at 1583 cm^{-1} due to stretching of the C-C bonding in the in-plane vibration of graphitic materials and typical of sp^2 carbon system, D- mode appeared at around 1345 cm^{-1} , usually caused by disordered structure in sp^2 – hybridised carbon systems as earlier studied [509]. Graphene oxide (GO) showed a G-mode shift at 1604 cm^{-1} (b) compared to graphene. The oxidation of graphite brings about the intensity ratio of I_D/I_G of D band and G band of graphite oxide to be 0.973 as result of the oxygen functional groups in the sp^3 graphitic structure. According to Ferrari *et al.* [510], after reduction, the intensity ratio I_D/I_G increased to 1.073 confirming the formation of graphene and with indication that a new structure has been formed in the sp^2 [509]. The appearance of a peak at the 2D band in the region of 2861 cm^{-1} in the graphene spectrum which constitutes the third peak shown by graphene, is typical of all sp^2 carbon system and determines the number of layer of graphene. The 2D peaks revealed a noteworthy change in shape compared to graphite oxide and also showed an intense and shaper peak compared to multi-layer graphene which is broad and wide according to literature [338]. This confirmed the reduction of graphite oxide to graphene as earlier confirmed by Stankovich *et al.* [299].

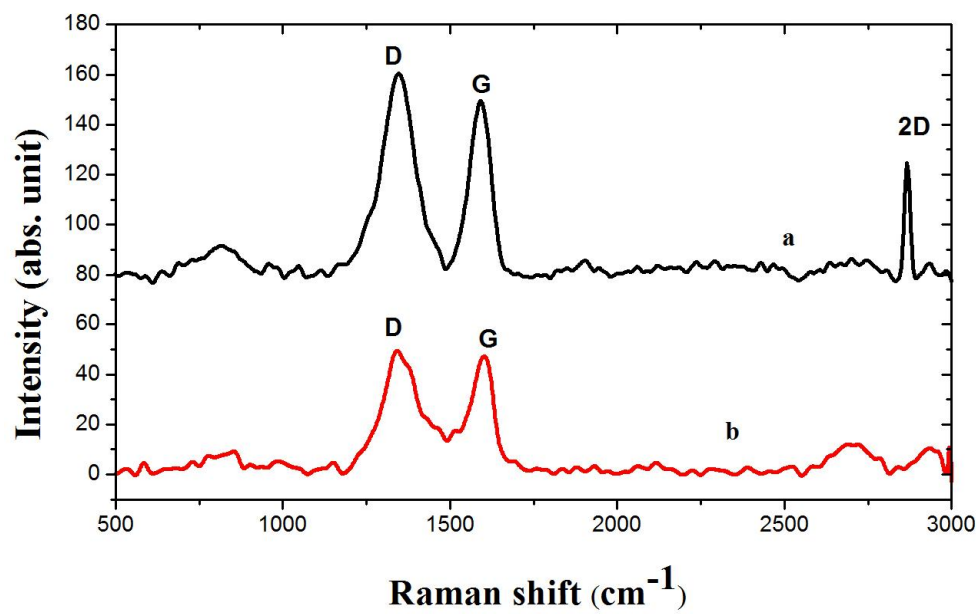
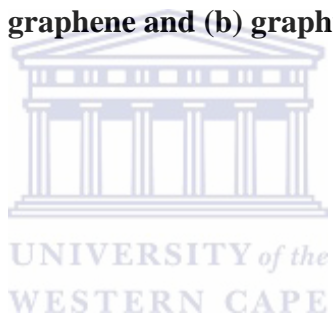


Figure 57. Raman spectra of (a) graphene and (b) graphite oxide.



4.2.7. UV –Vis spectroscopy

Figure 58 showed the UV visible spectral of (a) graphene oxide (GO) and (b) graphene. A maximum absorption peak at around 237 nm can be observed for GO in the UV visible spectra, which corresponds to the π - π^* transition of aromatic C-C bonds. After reduction, the peak, red shifted to 270 nm. This can be attributed to the fact that, the removal of the functional groups from GO, has restored back the electronic configuration within the graphene sheets after the reduction reaction [299].

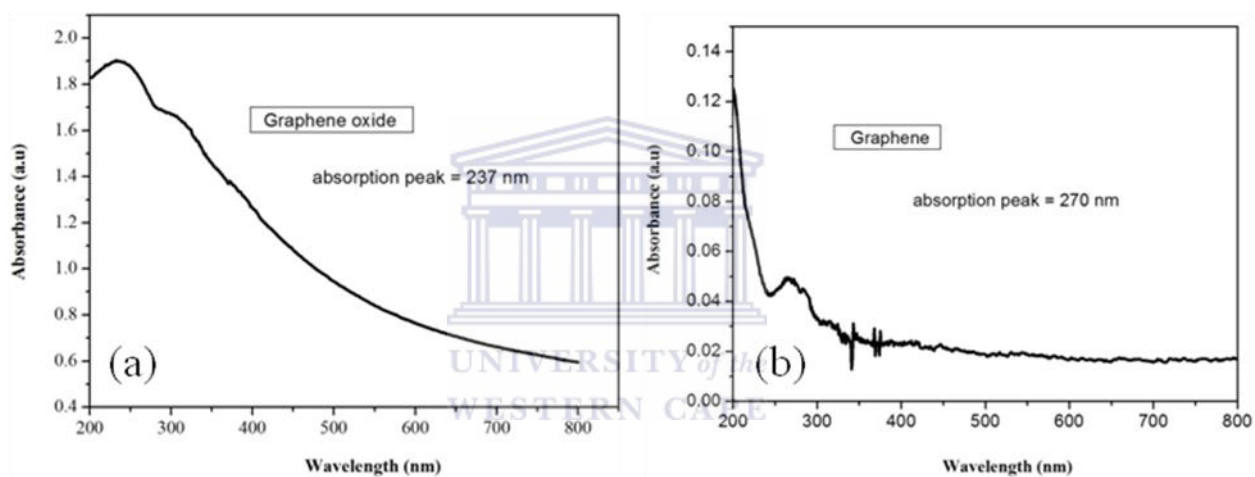


Figure 58. UV- visible spectra of (a) graphene oxide and (b) graphene.

CHAPTER FIVE

RESULTS AND DISCUSSION-part 2

Summary

The result and discussion on in situ polymerisation of graphene-polyaniline (GR-PANI) modified electrode, morphology and structural characterisation is presented. Electrochemical analysis by means of cyclic voltammetry, square wave voltammetry and catalytic effect of the prepared modified electrode on anthracene is discussed.

5.1. Introduction

It is well known and proven from studies that polyaniline is one of the promising conducting polymers, due to its electrochemical activity, low cost and environmental stability. However, its processibility can be improved by forming composite with nanofillers such as graphene, which has also proven to be gifted with unique properties such as high surface area and thermal conductivity. Graphene-polyaniline composite was prepared using in situ polymerisation method. The graphene not only serves as nucleating site for polyaniline, but has also provided a large surface to volume for a well dispersed polyaniline matrices in the composite. The morphological characterisation revealed a well intercalated polyaniline matrix with the graphitic layers of graphene in the composite, which has also resulted in a noticeable enhancement in current density compared to polyaniline. Electrolytic activity of the composite is then investigated. The author showed for the first time, the catalytic effect of graphene-polyaniline modified electrode on anthracene oxidation.

5.2. Characterisation of graphene-polyaniline (GR-PANI) nanocomposite

5.2.1. Cyclic voltammetry

The cyclic voltammetric response of the prepared GR-PANI|GCE nanocomposite was carried out in 1 M HCl electrolyte within a potential window of -200 to +1200 mV versus Ag/AgCl. From the cyclic voltammograms, there is a difference in the electrochemical surface activity of the electrodes. The electrochemical activities of the different electrodes are presented in **Figure 59 a – d**. No peak was observed at the bare electrode, on modification with graphene, a pair of redox peaks was observed which is typical for carbon materials as result of transition between quinone/hydroquinone **Figure 59a** [511]. On the other hand, from the PANI composite film modified on bare electrode (PANI|GCE), peaks with 2 redox couples ($I_{p,a(1)}$, $I_{p,c(1)}$), ($I_{p,a(2)}$, $I_{p,c(2)}$) were observed, which indicates the behaviour of polyaniline corresponding to redox transition of leucomeraldine form (semiconductor) and polaronic emeraldine form (conducting) and faradaic transformation of emeraldine/Penigraniline (**Figure 59 b**) [512]. The graphene-polyaniline composite film modified electrode (GR-PANI|GCE) showed a well-defined redox peaks and more enhancement in the magnitude of the current compared to PANI|GCE and bare GCE. Also noted is a shift in potential compared to PANI|GCE and an increase in peak current as the scan rate sweeps from 10 to 50 and 100 mV s^{-1} . This can be attributed to the confinement of the composite on the electrode and also showing the electroactive property of the GR-PANI|GCE composite (**Figure 59 c - d**). Comparing the CV of PANI|GCE in **Figure 59b** which has current density and peak to peak separation $\Delta E_{p(1)}$ and $\Delta E_{p(2)}$ of 184 and 137 mV respectively, GR-PANI|GCE exhibited a more enhancement in anodic peak current and decrease in peak to peak separation $\Delta E_{p(1)}$ and $\Delta E_{p(2)}$ of 83 and 51mV respectively (difference of 101 and 86 mV respectively, compared to PANI), and this can be viewed from the CV parameters in **Table 4** and **Table 5** below. A high surface area as well as good conductivity

possessed by GR-PANI|GCE can be attributed to the catalytic properties of graphene as a result of its higher surface-to-volume ratio which allows accessibility surface to polymer matrix [24, 299], hence a more enhancement compared to PANI. **Table 4** and **Table 5** represent parameters obtained from the cyclic voltammograms of GR-PANI and PANI modified electrodes.

Table 4. CV peak parameters of GR-PANI and PANI modified electrodes.

Electrode	I_{pa1} (μA)	I_{pa2} (μA)	I_{pc1} (μA)	I_{pc2} (μA)	I_{pa}/I_{pc1}	I_{pa}/I_{pc2}
PANI GCE	112.85	150.58	-84.37	-178.92	1.33	0.84
GR PANI GCE	1651.50	2116.30	-1442.60	-2099.20	1.15	1.0

Table 5. CV peak parameters of GR-PANI and PANI modified electrodes.

Electrode	E_{pa1} (mV)	E_{pa2} (mV)	E_{pc1} (mV)	E_{pc2} (mV)	ΔE_{p1}	ΔE_{p2}
PANI GCE	322	556	138	473	184	137
GR-PANI GCE	296	564	159	513	83	51

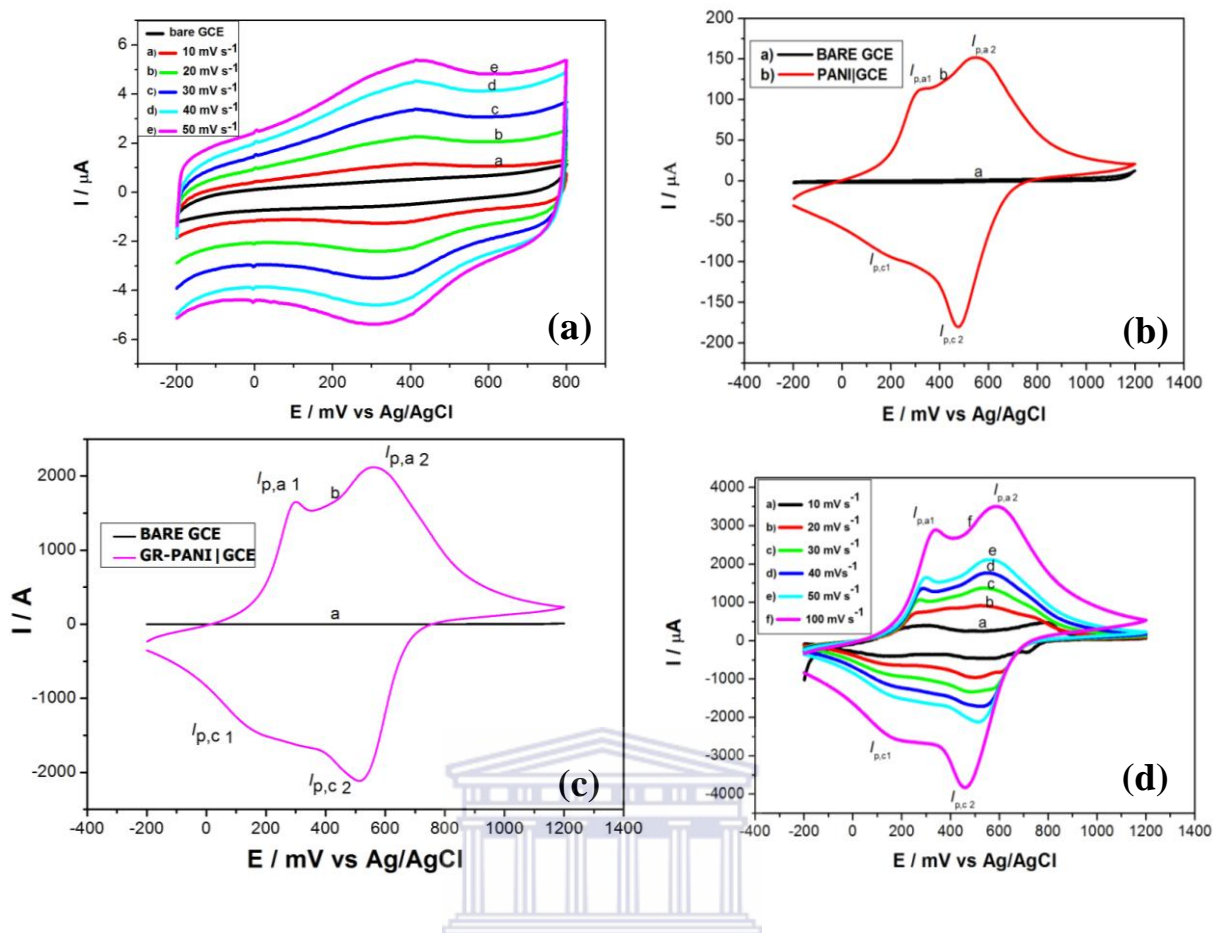


Figure 59. Cyclic voltammograms of (a) modified graphene|GCE (potential window -200 to +800 mV) , (b) PANI|GCE, (c) GR-PANI|GCE and (d) GR-PANI|GCE at different scan rate in 1 M HCl. Potential window: -200 to +1200 mV.

5.2.2. Scan rate dependence of the modified electrode

Scan rate dependence of the modified electrode in 1 M HCl solution was investigated. Figure 59 showed the scan rate dependence of the anodic peak current of the graphene-polyaniline composite film on the electrode (GR-PANI|GCE). **Figure 60a** and **Figure 60b** show the plot of the anodic current $I_{p,a1}$ (a) and $I_{p,a2}$ (b) versus scan rate respectively. This revealed that the peak current is directly proportional to the scan rate for each of the redox peaks. **Figure 60a**, gave a linear equation of $I_{p,a1} = 2.0461 \times 10^{-4} + 2.7413 \times 10^{-5} x$ with a correlation coefficient, $r^2 = 0.9980$. while the linear equation of $I_{p,a2} = 3.0782 \times 10^{-4} + 3.3360 \times 10^{-5} x$ is shown in

Figure 60b, correlation coefficient, $r^2 = 0.9930$ and the slope for each of the redox peaks are non-zero intercept. This behaviour according to literature is in agreement with that of a thin film adsorbed electroactive species undergoing Nernstian reaction [16, 513]. The surface concentration Γ^* (mol cm^{-2}) of the adsorbed electroactive species can be estimated from the equation [514]. Consequently, the slope of the linear $I_{p,a}$ vs v of the first redox peak has been shown to be a one electron process involving polyleucoemeraldine/ polyleucoemeraldine radical cation, according to literature [514-515].

$$\frac{I_{p,a}}{v} = \frac{n^2 F^2 A \Gamma_{\text{PAG}}^*}{4RT} \quad \text{Equation 36}$$

From the equation, n is the number of electron transferred ($n= 1$), F is the faraday constant (96500 C mol^{-1}), $\Gamma_{\text{GR-PANI}}^*$ represent the surface concentration of the graphene-polyaniline composite film (mol cm^{-2}), A is the surface area of the electrode (0.071 cm^2), v is the scan rate (mV s^{-1}), R is the gas constant ($8.314 \text{ J mol}^{-1} \text{ K}^{-1}$) and T is the operating absolute temperature of the system ($25 \text{ }^\circ\text{C}$ T in 298 K). The surface concentration of GR-PANI film $\Gamma_{\text{GR-PANI}}^*$ for the one electron transfer evaluated from the slope of the plot ($I_{p,a 1}$ vs v) is $3.073 \times 10^{-9} \text{ mol cm}^{-2}$.

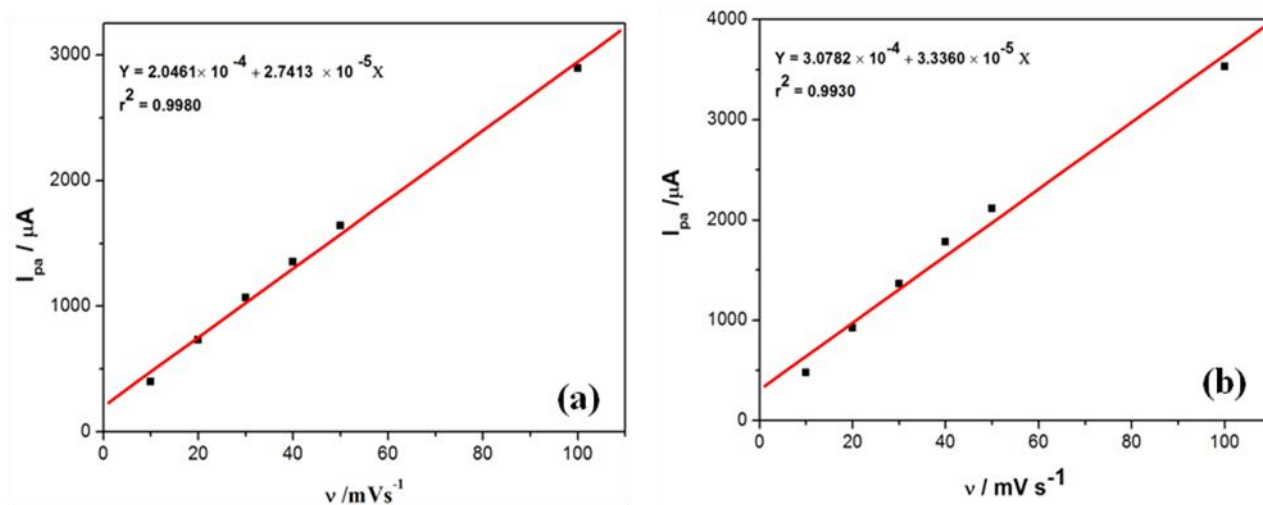


Figure 60. Plot of scan rate dependence curves of anodic peak current $I_{p,a 1}$ (a) and $I_{p,a 2}$ (b)



5.3. Morphology and spectroscopic characterisation

5.3.1. Electrochemical Impedance Spectroscopy (EIS) of GR-PANI|GCE

Electrochemical impedance spectra (EIS) were used to investigate the performance of the modified electrodes being an effective method of probing the features of a surface modified electrode [516-518]. The measurement was performed in a cell containing 10 mL of 1 M HCl aqueous solution with a frequency range of 100 kHz to 0.1 Hz of which the amplitude of the alternating voltage was 10 mV as shown in **Figure 61**. The y-axis represents the negative number of the imaginary part of the measured impedance while the x-axis represents the real part of the measured impedance. The diagram (Nyquist plots- real part of the impedance Z' vs. imaginary part Z'') represents the charge transfer kinetics of the modified electrodes in which R_s is the ohmic (internal or solution) resistance [517]. CPE is the capacitance phase element for the semiconductor || electrolyte interface, W (Warburg impedance) represent the mass transfer

element while the R_{ct} is the charge - transfer resistance across the interface [519]. For a reaction that is reversible, the Nyquist plot usually exhibits two regions: One, a semicircle at a high frequency region which corresponds to electron charge transfer process, thus, the electron-transfer resistance value can be measured directly, and two, a straight line of the plot at a lower frequency region representing the diffusion-limited transport of the redox species from the electrolyte to the electrode interface. As shown in the **Figure 61**, the Nyquist plot displayed significant differences in the diameter of the Nyquist semicircle upon the stepwise modification of the electrodes showing the capability of electron transfer of the different electrodes. The charge transfer resistance (R_{ct}) value for bare GCE was 51200 Ω . On modification with polyaniline -graphene (GR-PANI), a decrease in R_{ct} value 7360 Ω was exhibited, indicating its high conductivity and more facile to electron transfer compared to PANI with R_{ct} value of 27680 Ω . The charge transfer resistance (R_{ct}) values calculated after fitting the EIS data to the Randle's equivalent circuit diagram in Figure 60 (inset) can be observed in table 6. The value confirmed that graphene decreased the resistance of PANI by about 20 Ω suggesting the suitability of graphenated PANI as a good conducting platform for electrocatalysis.

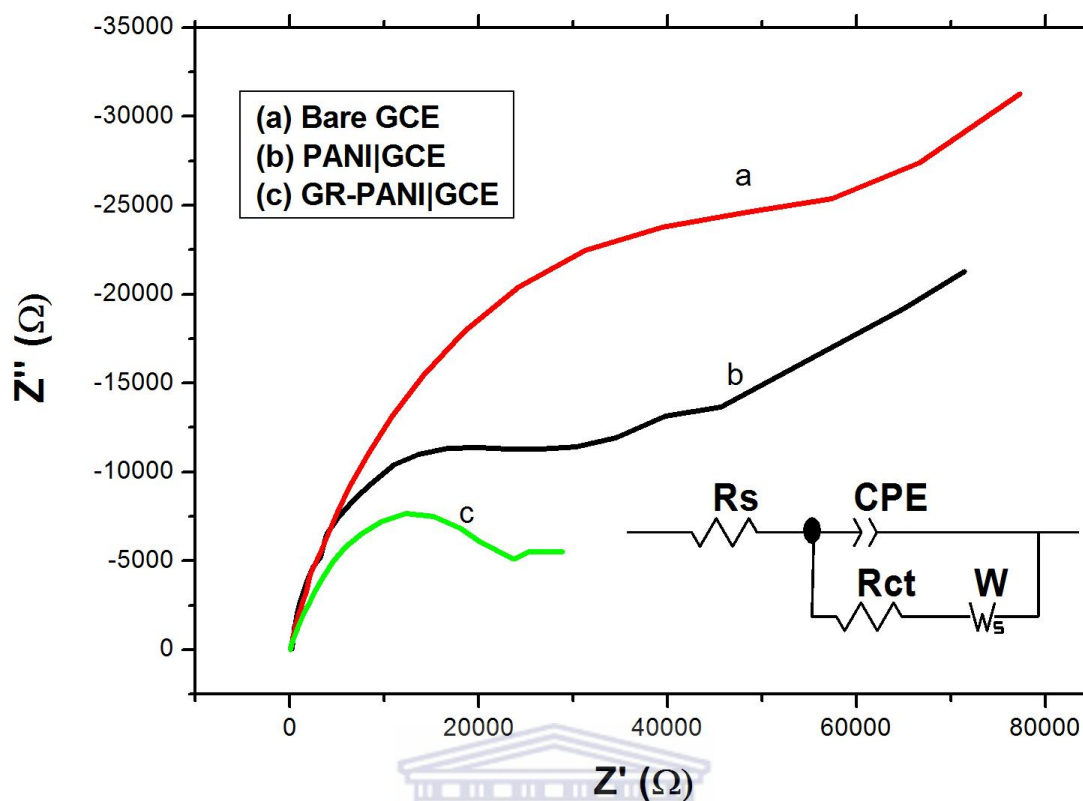


Figure 61. Nyquist plots of the EIS measurement of (a) GCE, (b) PANI|GCE and (c) GR-PANI|GCE in 1 M HCl. Inset is the Randle's equivalent circuit for fitting.

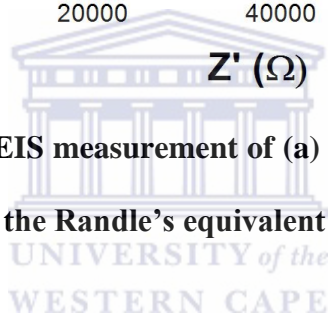


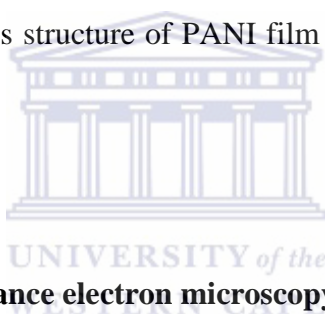
Table 6. Impedance data obtained from the Randle equivalent circuit fitting from Figure

61

Electrode	R_s (Ω)	R_{ct} (Ω)	CPE (nF)	Z_w ($k \Omega s^{1/2}$)
Bare GCE	52.34	51200	346.2	30.07
PANI GCE	209.3	27680	309.0	23.63
GR-PANI GCE	13.37	7360	821	11.33

5.3 2. Scanning electron microscopy (SEM)

Scanning electron microscope (SEM) analysis was carried out on the prepared nanocomposite. SEM images of the prepared nanocomposite are shown in **Figure 62**. From **Figure 62a** and **Figure 62b**, a well exfoliated graphene oxide sheets, compared to an agglomerated sheet with aggregated and overlapped thin, crumpled, wrinkled graphene sheets closely associated with each other and forming a disordered solid can be observed for graphite oxide and graphene, respectively, consisted with previous report [24]. The prepared nanocomposite showed a different morphology in structure compared to both graphite oxide and graphene. A fibrous PANI can be observed to mainly intercalate between the graphene sheets as shown in **Figure 62c** and showing some porosity in the composite formed which is consistent with previous report [490] compared to a porous structure of PANI film formed in the absence of graphene, observed in **Figure 62d**.



5.3 3. High resolution transmittance electron microscopy (HR-TEM)

HR-TEM images of the composite can be observed from **Figure 63**. **Figure 63a** and **Figure 63b** showed the HR-TEM images of graphene oxide and graphene. Large sheets entangled in layers with each other like a silky veils and a flat transparent thin layer sheets can be observed, respectively. However, the nanocomposite formed showed a completely different morphology from pure PANI and graphene. **Figure 63d** showed polyaniline intercalating in- between and the surface of the graphene sheet, which could however be attributed to the well dispersive interaction of the two materials. The in situ polymerisation method of synthesis has greatly contributed to the nanocomposite formed, which has however, exhibited a higher conductivity than pure polyaniline. **Figure 63c** showed a Pure PANI with uniform fibrillar structures of

hundreds of nanometres and a diameter of 50 nm according to literature [490, 520] and different from the composite.

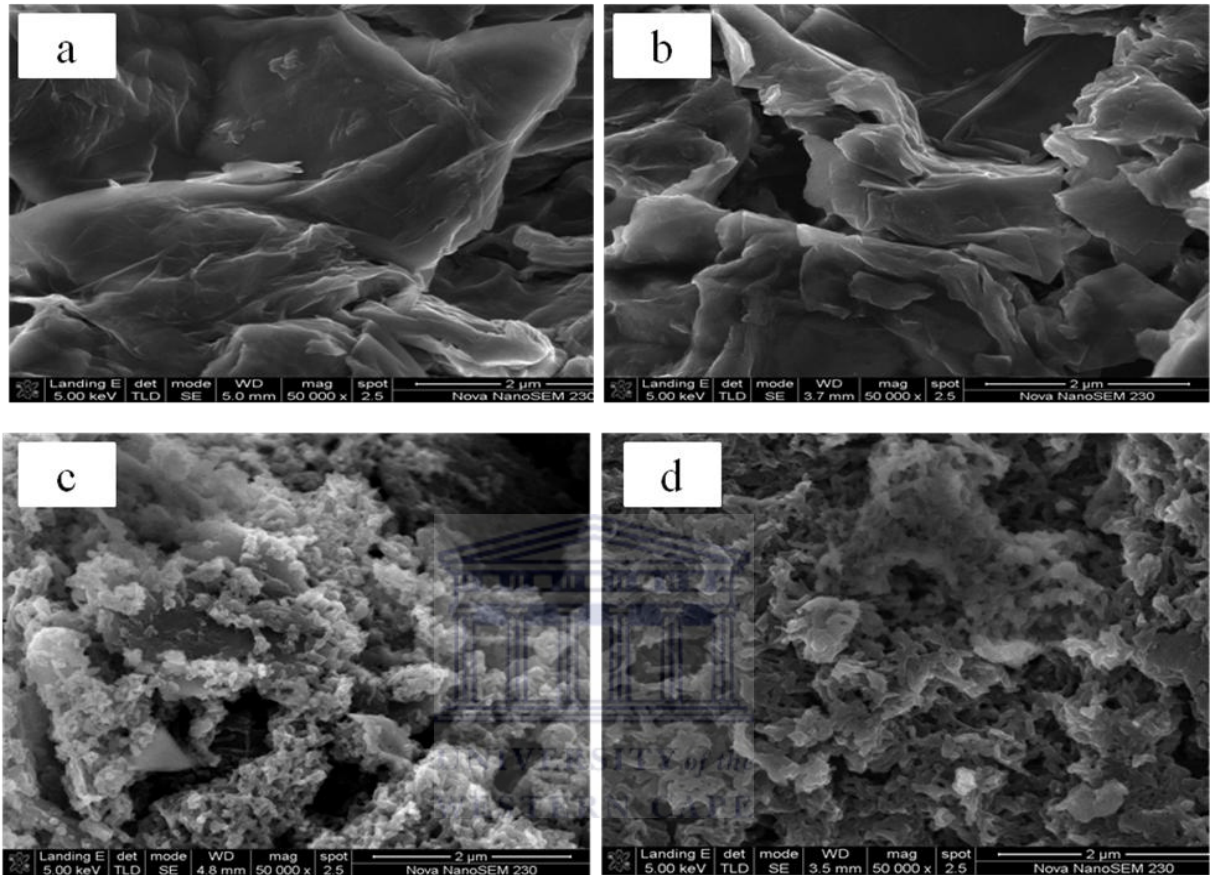


Figure 62. SEM images of (a) GO, (b) GR, (c) GR-PANI and (d) PANI.

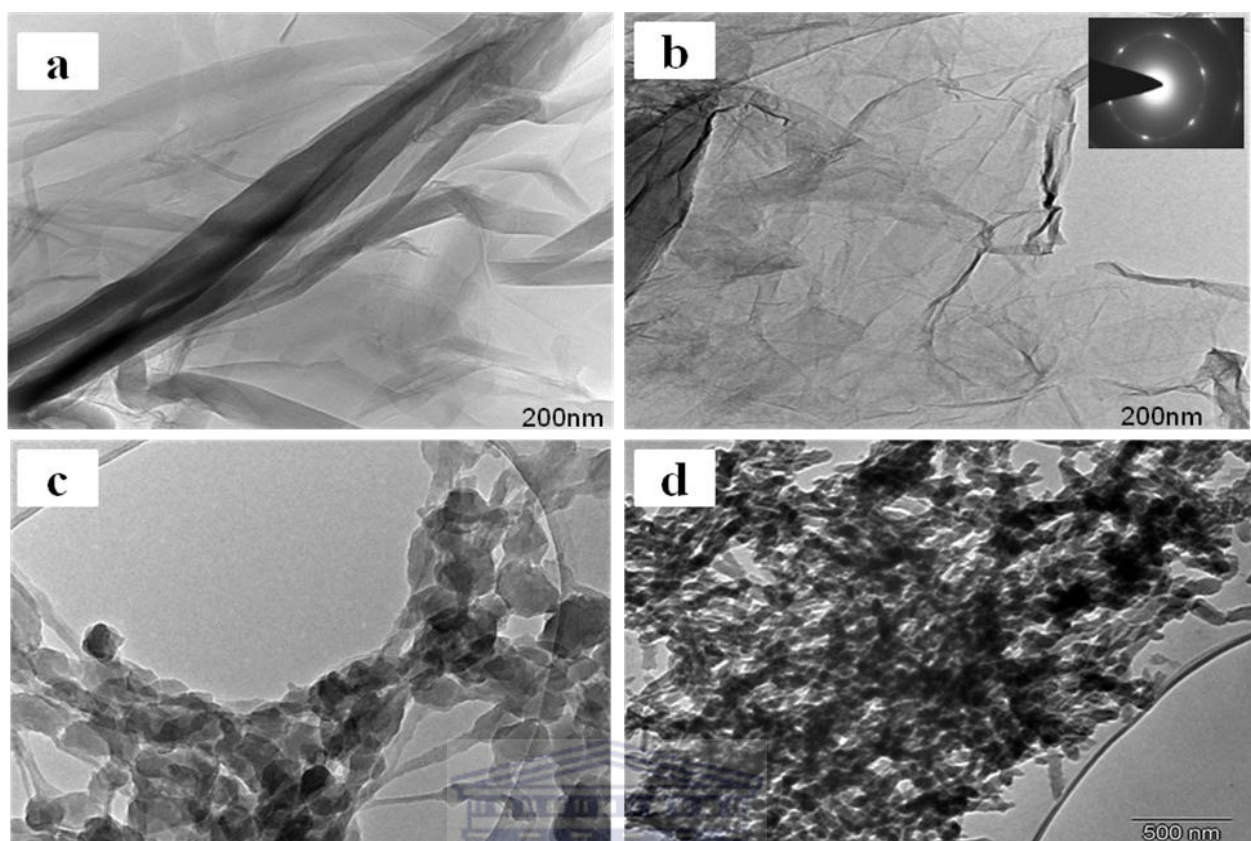


Figure 63. HRTEM pictures of (a) GO, (b) GR, (c) PANI and (d) and GR-PANI.

5.3 4. Fourier transmission infrared (FT-IR)

Figure 64 showed the FTIR spectra of (a) GR, (b) GR-PANI nanocomposite, (c) PANI and (d) GO. The appearance of the absorption peaks on the graphene oxide sheet can be confirmed by the collections of functional groups corresponding to: C=O (1735 cm^{-1}), aromatic C=O ($1,602\text{ cm}^{-1}$), carboxyl C-O ($1,416\text{ cm}^{-1}$), epoxy C-O ($1,265\text{ cm}^{-1}$), alkoxy C-O (1047 cm^{-1}), hydroxyl O-H (3390 cm^{-1}). This is in agreement to the reported data [319, 521]. However this absorption bands are decreased tremendously in graphene sheets after reduction. Observation from the PANI film showed all the characterisation peaks of PANI in its emeraldine form, 1568 and 1476 cm^{-1} which can be assigned to the stretching vibration of quinone and benzene rings, respectively. The peaks at 1290 and 1233 cm^{-1} correspond to the C-N stretching vibration. The

in-plane bending and the out-plane bending of C-H stretching is reflected in 1111 and 791 cm^{-1} peak, respectively [522]. GR-PANI composite films clearly revealed the presence of the interaction of graphene and PANI in the composite with less intense in the characteristic bands of PANI and also almost similar in comparison with graphene. This is an indication that PANI is well adsorbed and intercalated on to the graphene surface. This is consistent with TEM, SEM and XRD investigation of the nanocomposite.

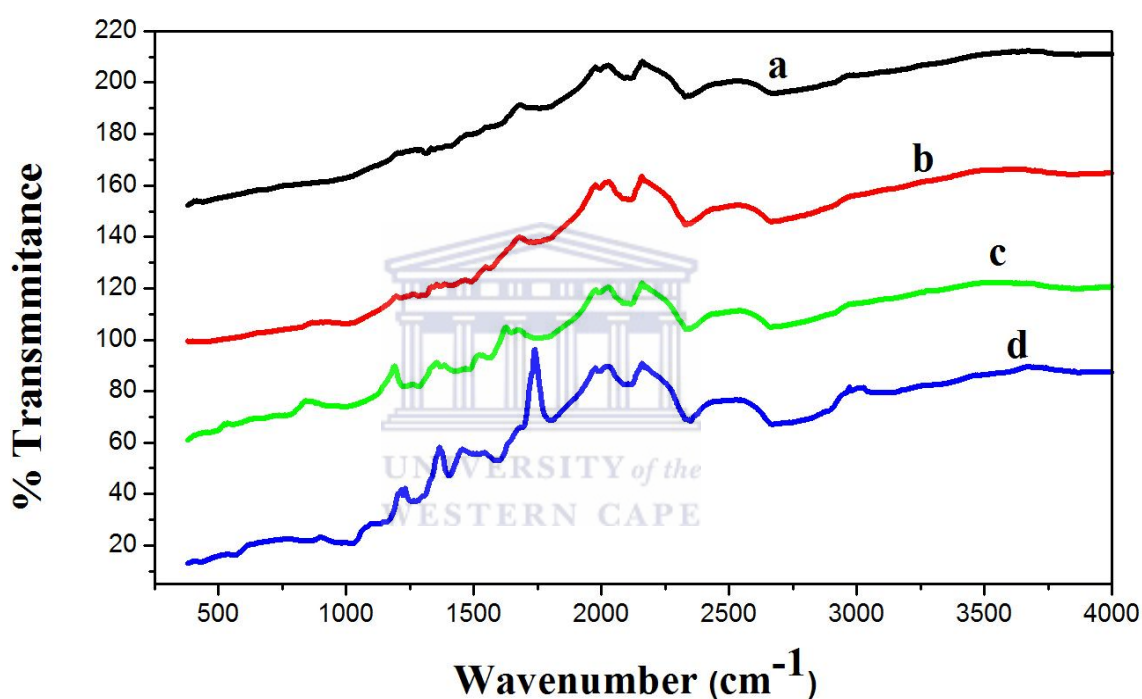


Figure 64. FTIR spectra of (a) GR, (b) GR-PANI, (c) PANI and (d) GO.

5.3.5. X-ray diffraction (XRD)

The XRD patterns of (a) GR, (b) PANI and (c) GR-PANI composite are presented in **Figure 65**. Graphene showed diffraction broad peaks at 24.2° (002) and 43.6° (100) with some crystalline features of graphitic-like structure. The broad nature can be attributed to the loosely stacked sheets in graphene, but different from graphite according to literature [523-524]. PANI revealed a slightly broad peak at around 25.4° and another low intensity peak at 12.7° which are referred to as the corresponding peaks of crystal planes of pure PANI in its emeraldine salt form [525]. The graphene-polyaniline nanocomposite revealed broadened peaks that are similar in comparison to both graphene and PANI, showing the interaction and merged peaks of both PANI and graphene in the composite [24] This is consistent with the morphology of SEM and TEM studies of the composite.

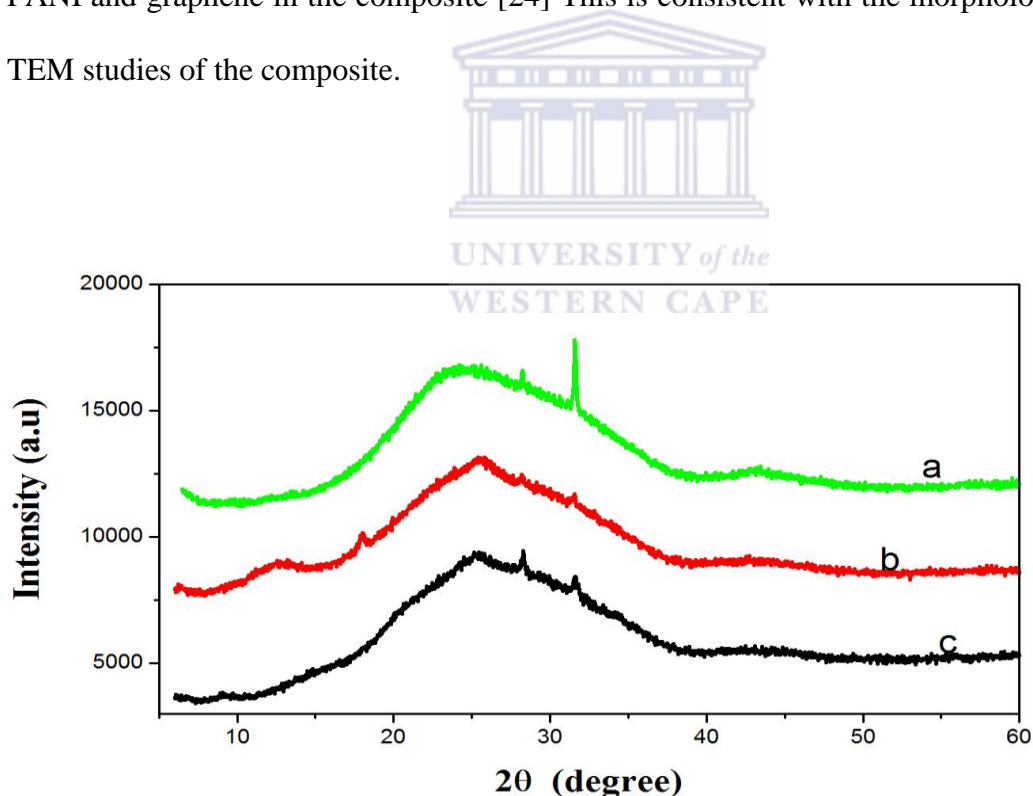
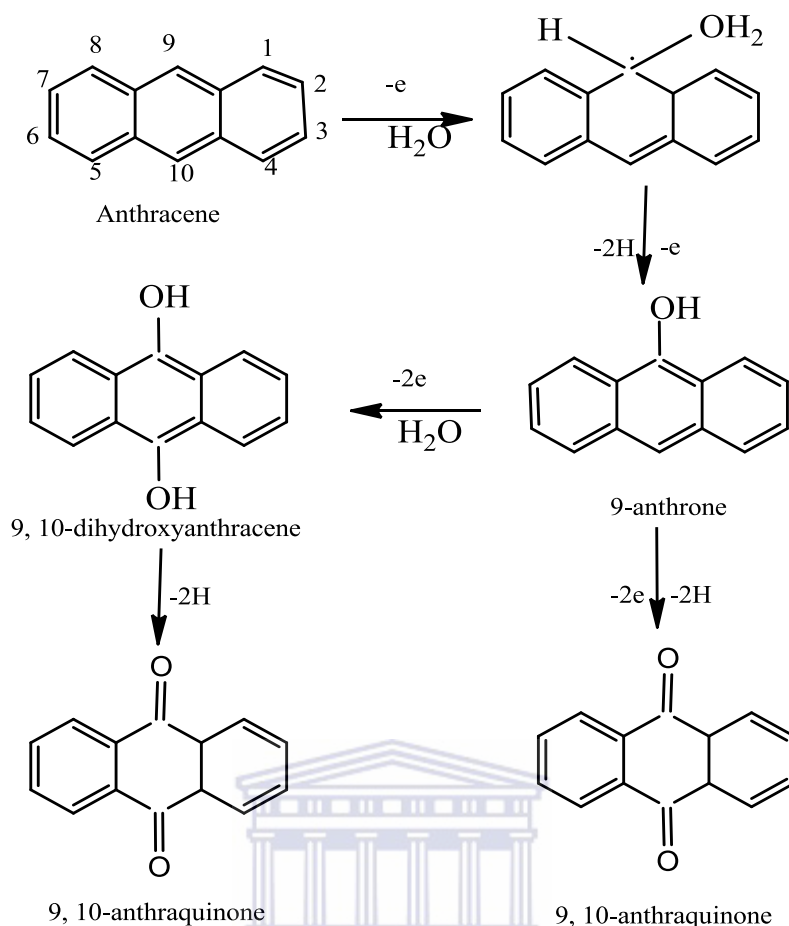


Figure 65. XRD patterns of GR (a), PANI (b) and GR-PANI nanocomposite (c).

5.4. Response of modified electrode to anthracene

Analysis on the electrocatalytic response of the modified electrode to different concentration of anthracene was studied in acetonitrile/water with 0.1 M LiClO₄ as the supporting electrolyte. A potential window of -200 to +1400 mV with reference to Ag/AgCl electrode and scan rate of 50 mV s⁻¹ were used as the working conditions. An anodic peak at around 1101 mV was observed which can be ascribed to clear oxidation of anthracene and without a cathodic peak. A new product (anthraquinone) is suggested to have been rapidly formed as a result of the irreversible behaviour of the response, according to literature [526]. Oxidation of PAHs through electrochemical method of degradation is usually initiated with direct electron transfer from adsorbed PAH to the electrode, cation radicals are then generated which undergo subsequent reactions [527-528]. Thus, the oxidation of anthracene in acetonitrile containing small amount of water involves one electron reaction that appears to be the initial step [529], followed by steps of radical cation that can lead to formation of the final the product (9, 10-anthraquinone) [527-528]. However it is also important to note that a small amount of water in acetonitrile plays a crucial role in the oxidation of anthracene which actually favours the production of the final product [529]. A possible mechanism involved in the oxidation of anthracene is shown in the **scheme 5** below.



Scheme 5. Possible products expected from the oxidation of anthracene.

5.4.1. Electrochemical Application of the modified GR-PANI electrode for anthracene

Detection

5.4.1.1. Electrochemical behaviour of the modified electrodes

The electrochemical behaviour of the modified electrode was investigated on the bare electrode and on the individual modified electrodes. **Figure 66** showed the cyclic voltammograms of bare GCE (a) and GR-PANI|GCE in acetonitrile/water (80:20 v/v) with 0.1 M LiClO₄ as the working electrolyte. However, the choice of acetonitrile/water in the mixture of (80:20 v/v) as previously mentioned can be associated with the ability of a suitable solvent like acetonitrile to dissolve PAHs and introduction of a little quantity of water to the electrolyte, as most PAHs are

found in wastewater, which is also consistent with previous literature [529-530]. A scan rate of 50 mV s^{-1} and potential window of -200 to $+1400 \text{ mV}$ was also used. The Voltammograms revealed the behaviour of the bare electrode and modified electrode in acetonitrile/water (80:20 v/v) with 0.1 M LiClO_4 before application to anthracene.

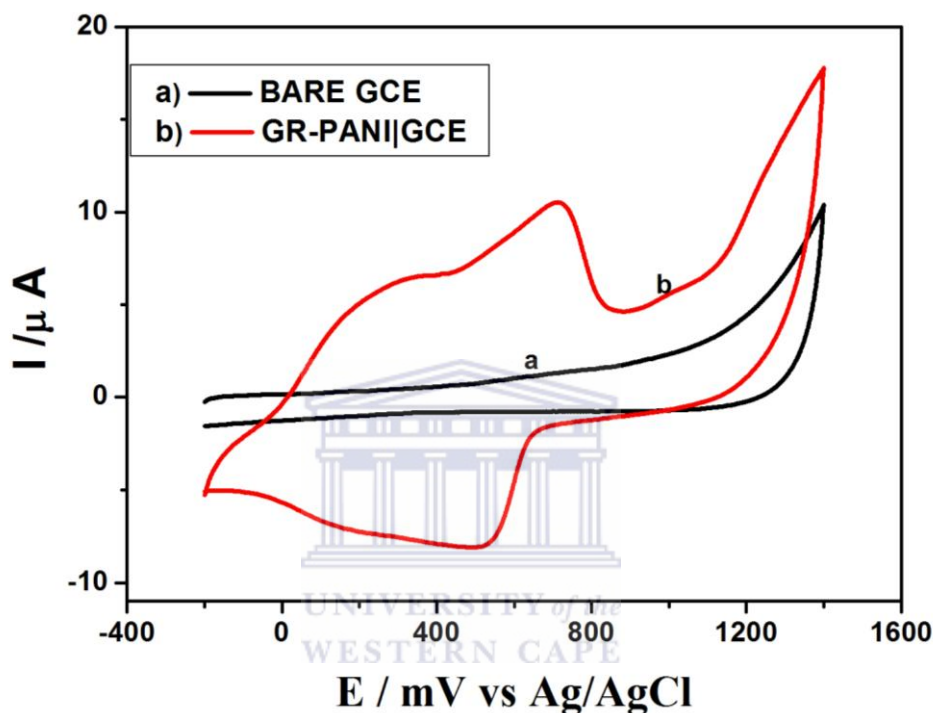


Figure 66. Cyclic voltammograms of GR-PANI|GCE in acetonitrile/water (80:20 v/v) with 0.1 M LiClO_4 at scan rate of 50 mV s^{-1} .

Figure 67 showed the electrochemical behaviour of the different modified electrodes. PANI|GCE, GR-PANI|GCE and bare GCE in acetonitrile/water with 0.1 M LiClO_4 as the supporting electrolyte at a scan rate of 50 mV s^{-1} and potential window of $-200 - +1400 \text{ mV}$ evaluated by the electro oxidation of anthracene 100 μM ($1.0 \times 10^{-4} \text{ M}$) dissolved in the above solution. Another visible anodic peak current can be observed at positive potential around 1101 mV upon the addition of 100 μM ($1.0 \times 10^{-4} \text{ M}$) of anthracene which indicates that the

oxidation of anthracene has occurred **Figure 67a**. The modified electrode with GR-PANI exhibited a higher catalytic property by showing a more enhancement in the anodic peak at the oxidation of anthracene, compared to the response of PANI|GCE. No visible peak was observed for bare GCE in **Figure 67b**.

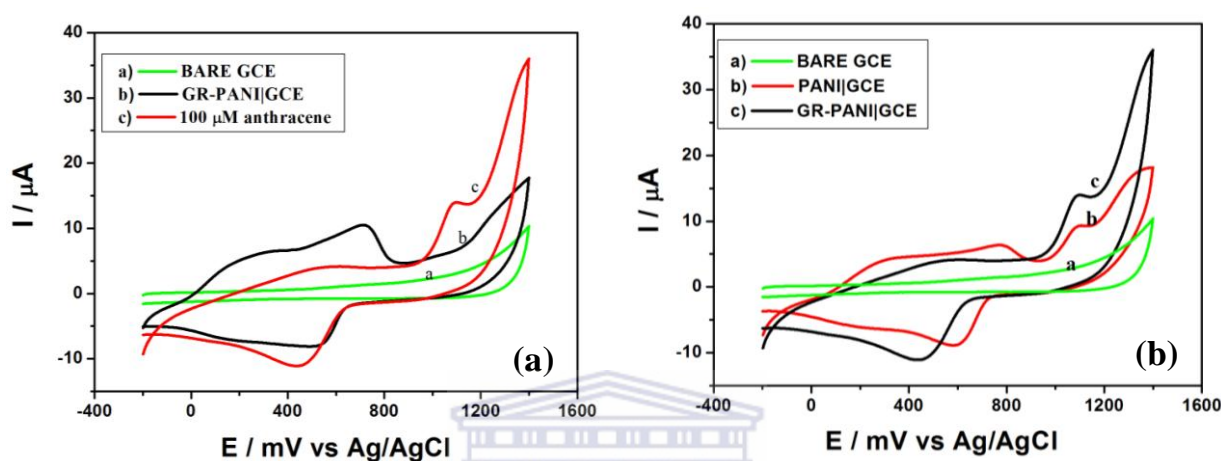


Figure 67. Cyclic voltammograms of bare GCE before modification, after modification and response of modified electrode at addition of 100 μM (1.0×10^{-4} M) of anthracene in acetonitrile/water containing 0.1 M LiClO_4 (a) and GR-PANI|GCE, PANI|GCE and bare GCE in the presence of 100 μM (1.0×10^{-4} M) of anthracene (b) at scan rate of 50 mV s^{-1} and potential window of -200 to +1400 mV.

5.4.1.2. Effect of scan rate

The effect of scan rate on the anodic peak current was also investigated in acetonitrile/water (80:20 v/v) with 0.1 M LiClO_4 , between the working potential windows of -200 mV and +1400 mV at the addition of 1.0×10^{-4} M anthracene. As the scan rate increases, there is also an increase in the oxidation peak. **Figure 68a** showed the cyclic voltammograms of GR-PANI|GCE at different scan rate in the presence of constant concentration of anthracene. The plot of the anodic peak current for anthracene which increases linearly with the square root of

the scan rate over the range of 20 – 250 mV s^{-1} is shown in **Figure 68b**. This gave a linear regression of $I_{p,a} (\mu\text{A}) = -2.0966 \times 10^{-6} + 2.0847 \times 10^{-6} v^{1/2} (\text{mV s}^{-1})^{1/2}$ and has a correlation coefficient, $r^2 = 0.990$. This suggested a diffusion controlled electrochemistry [235, 530-531] which indicated that the process was limited by the rate of diffusion of anthracene from the solution to the surface of the electrode [530]. It could also be observed that the peak potentials shifted positively with increase in scan rate denoting the irreversible behaviour of the system [530].

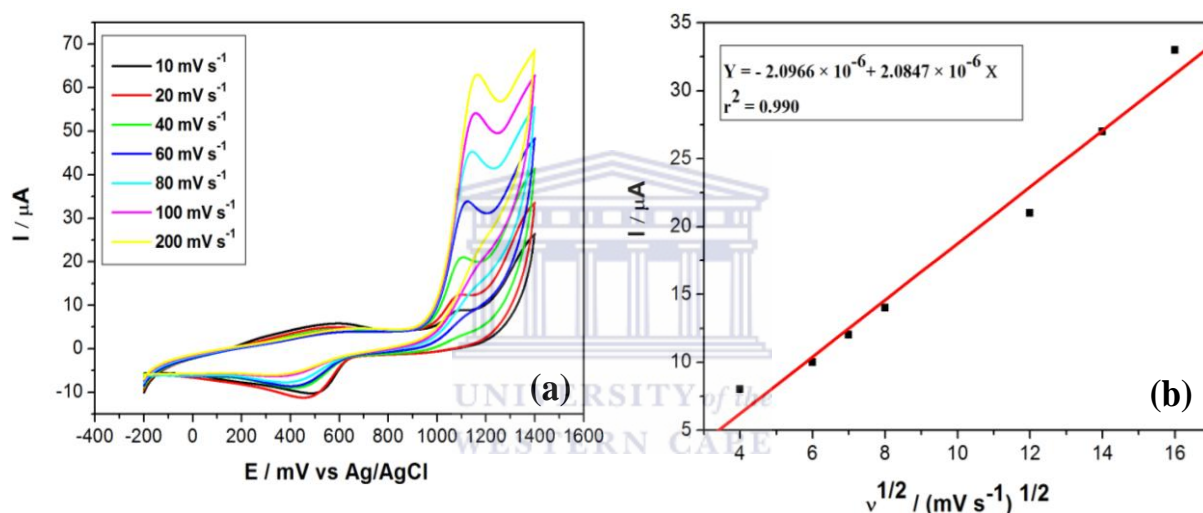


Figure 68. Cyclic voltammograms of (a) GR-PANI|GCE in acetonitrile/water (80:20 v/v) with 0.1 M LiClO_4 , in the presence of 1.0×10^{-4} M anthracene and (b) a plot of the scan rate dependence of its anodic peak currents.

5.4.1.3. Analytical application of the modified electrode

The electrocatalytic oxidation of anthracene is studied using the GR-PANI modified electrode. The cyclic voltammetric and square wave voltammetric analysis of the modified electrode and the electrocatalytic property to anthracene in acetonitrile/water (80:20 v/v) with 0.1 M LiClO_4 , between the working potential windows of -200 to +1400 mV and scan rate of 50 mV s^{-1} is illustrated. The oxidation peak which can be observed at 1101 mV and shifting positively,

increases at every addition of different concentrations of anthracene (20 – 1000 μM) which is shown from **Figure 69a**. However, another observation is the electrochemistry of the two anodic peak current attributing to the peaks of platform around 200 and 800 mV which merges to form a broad peak and decreases as the concentrations of anthracene increases due to the catalytic electrochemistry of the GR-PANI sensor. Addition at low concentrations of anthracene is shown in **Figure 69b**. Plot of the calibration curve based on the anodic peak current against concentrations was found to be satisfactorily linear ($r^2 = 0.9954$) as can be observed in **Figure.69c**. The correlation coefficient ($r^2 = 0.9990$) with respect to lower concentrations is shown in **Figure 69d**.



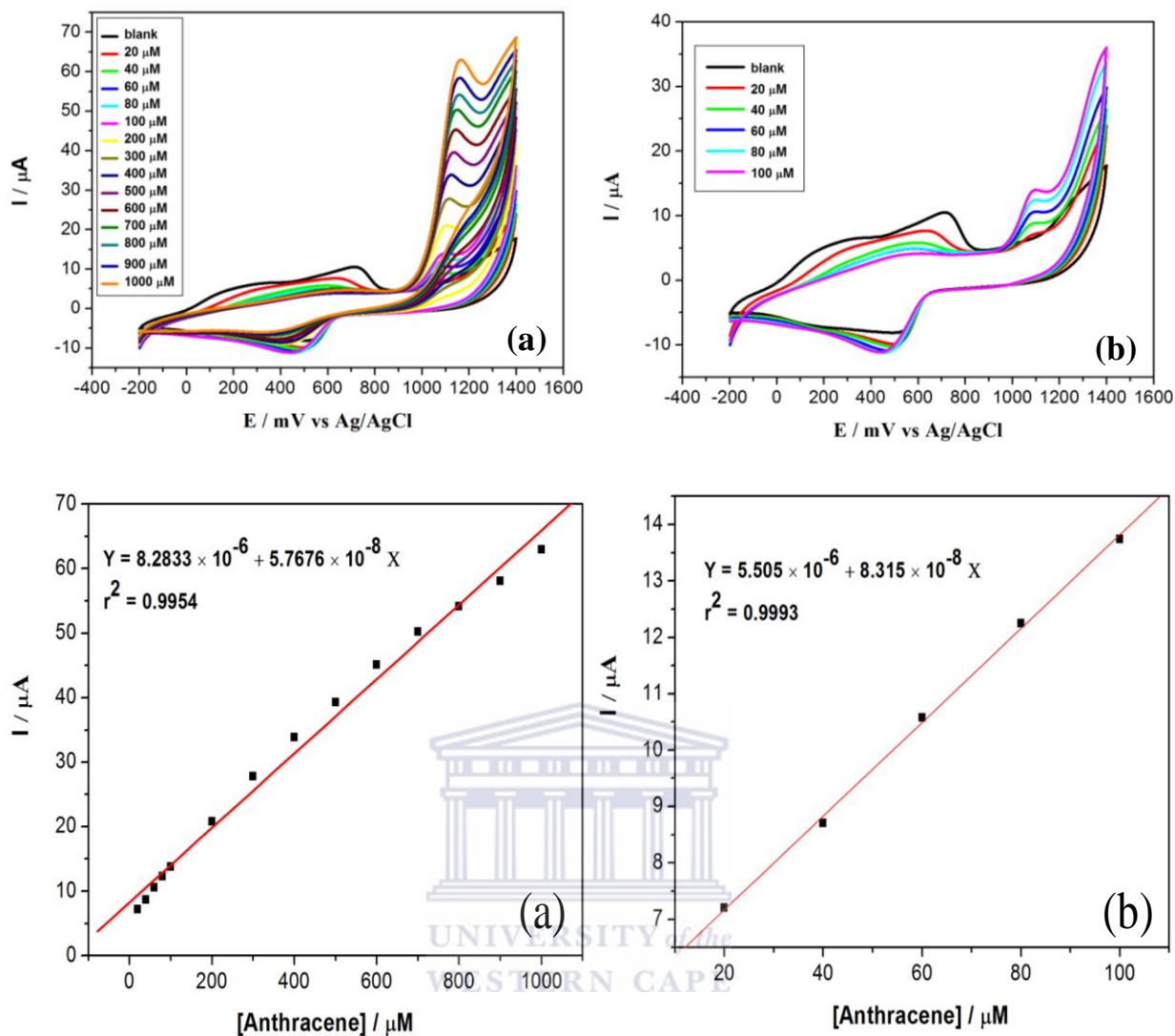


Figure 69. Cyclic voltammograms of (a) modified GR-PANI|GCE upon the addition of different concentrations (20 – 1000 μM) of anthracene (at high concentrations), (b) at lower concentrations, (c) plot of calibration curve for GR-PANI|GCE anthracene sensor at high concentrations and (d) at low concentrations.

A similar result is observed from the square wave voltammograms which confirmed the oxidation of anthracene at GR-PANI film modified electrode upon every addition of different concentrations of anthracene (20 –1000 μM) at 50 mV s^{-1} in 0.1 M $\text{LiClO}_4/\text{acetonitrile}/\text{water}$ (80:20 v/v) as shown in **Figure 70**. An increase in the anodic peak current occurred at different

addition of anthracene which can be observed in **Figure 70a**. A plot of the calibration curve of the anodic peak as a function of the concentrations using SWV is shown in **Figure 70b**. The response at lower concentrations of anthracene and calibration plot with respect to lower concentrations which gave a correlation coefficient ($r^2 = 0.9950$) is shown in **Figure 70c** and **Figure 70d**. The dynamic linear range of the anodic peak and anthracene concentrations based on the SWV measurement at lower concentrations was over the range of 2.0×10^{-5} to 1.0×10^{-3} M. A detection limit of 4.39×10^{-7} M was obtained.

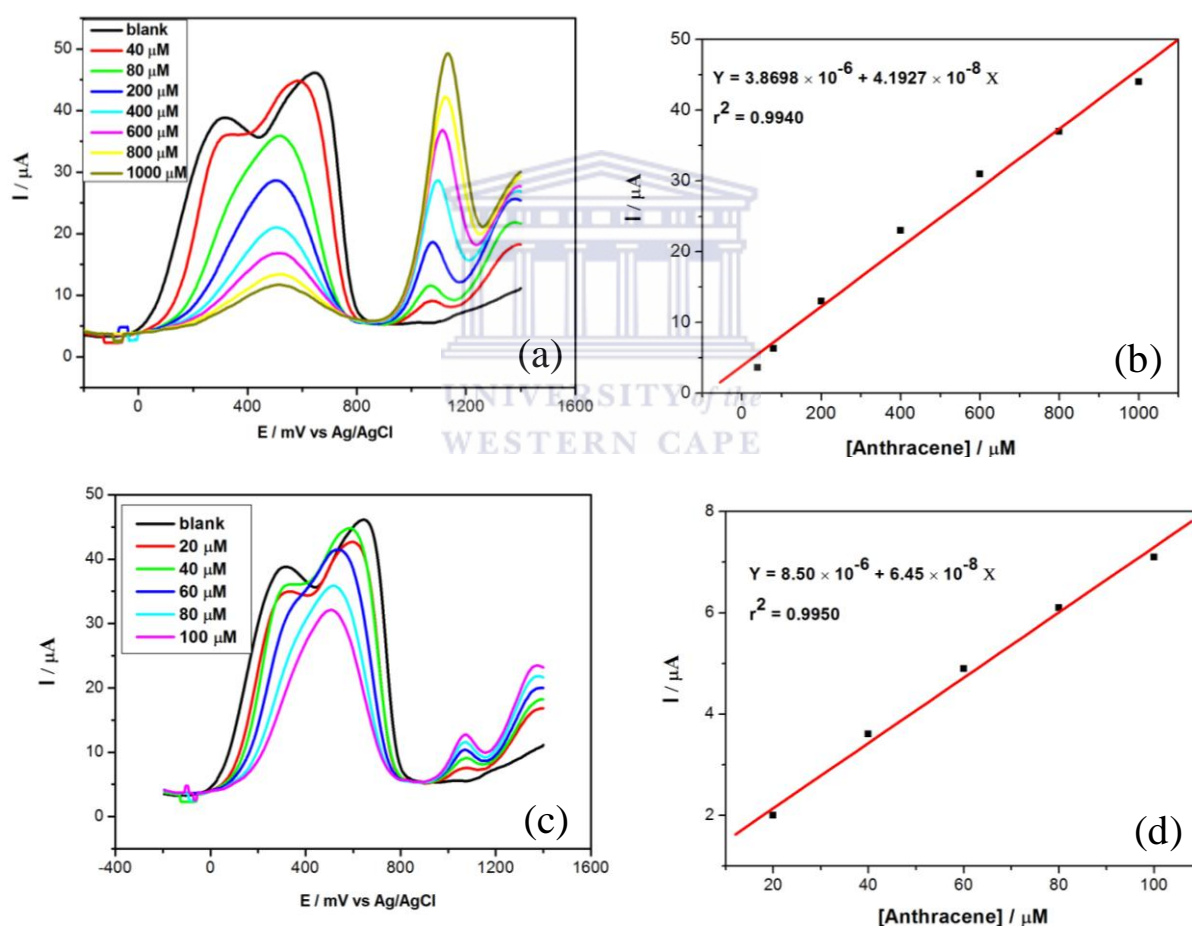


Figure 70. Square Wave Voltammograms of (a) modified GR-PANI|GCE upon the addition of different concentrations of anthracene (high concentrations), (b) plot of calibration curve of the anodic peak current versus concentrations, (c) addition at lower concentrations and (d) plot of calibration curve at lower concentrations of anthracene.

5.5. Reproducibility, Stability and Interference Studies

A stability and reproducibility study was carried out to test the performance of the prepared electrodes. Investigation by cyclic voltammetric analysis repeatedly for 6 successive measurement ($n = 6$) in 1 M HCl towards the anthracene oxidation (1.0×10^{-4} M) gave 1.5%, relative to standard deviation indicating reproducibility. After monitoring for 3 weeks at interval of four (4) days in order to check for the storage ability in which it has been stored in the refrigerator at 4 °C, 88.86% of its initial response was recovered, there has been 11.14% decrease in the peak current. The following ions: Mn^{2+} , Cl^- , SO_4^{2-} and NO_3^- were not observed to interfere at 1.0×10^{-4} M of the anthracene concentration when tested for interferences. The validated results can then conclude that the modified electrode has stability and reproducibility for anthracene detection.



CHAPTER SIX

RESULT AND DISCUSSION-part 3

Summary

The chapter presents results and discussion on the electrochemical synthesis and application of the nanocomposite (PANI/WO₃/GR), PAHs determination on nanocomposite (PANI/WO₃/GR). Morphology, spectroscopic and electrochemical characterisation of the nanocomposite is discussed.

6.1. Introduction

A great deal of interest has recently been focused on the utilization of metal oxide as nanofillers to form nanocomposite. However, Metal oxide semiconductor such as tungsten oxide among several others, have shown good conductivity and electronic properties. Conversely, polyaniline has also been regarded as a promising semiconducting polymer due to its unique properties which include ease of processing, electrical and mechanical properties. The nanocomposite of conducting polyaniline doped with tungsten oxide has presented effective electrode materials in many electrochemical devices as a result of the interaction of the two components. Also several studies have been reported on the excellent performance of graphene doped tungsten oxide nanocomposite or graphene- conducting polyaniline composites.

In the present study, polyaniline nanocomposite doped tungsten oxide and graphene nanosheets are introduced. The interaction of the three components has shown considerable impact in the nanocomposite formed. Morphology and spectroscopic investigation has been carried out and

electrocatalytic activity has been extensively studied. The nanocomposite has proved to be a good electrocatalyst for the oxidation of polyaromatic hydrocarbons.

6.2. Spectroscopic and morphological characterisation

6.2.1. UV-visible spectroscopy

The UV-vis spectral of PANI, PANI|WO₃, PANI|WO₃|GR and GR in DMF is presented in **Figure 71**. **Figure 71a** showed the spectrum of GR demonstrating absorption at 270 nm. The spectrum of PANI showed absorption bands at 326 nm which corresponds to the benzenoid Π - Π^* transition and at the 620 nm due to Π - Π^* transition of quinone-imines group of a typical polyaniline [532-533]. PANI|WO₃ showed an appearance of an absorption peak at 452 nm which can be attributed to the presence of tungsten oxide (WO₃), and a characteristic peak of PANI film around 300 nm attributing to the benzenoid Π - Π^* transition. The spectrum of PANI|WO₃|GR revealed absorptions at about the same region as that of PANI but more broadened and slightly shifting towards higher wavelength, (633nm) which can be attributed to the merging with the absorption of WO₃. However, PANI|WO₃ composite film has been studied to exhibit UV-vis transmission spectra similar to PANI especially at positive potentials [534]. Also GR in the PANI|WO₃|GR composite appeared to be merged with the benzenoid Π - Π^* transition and with increase in intensity of the peak and a slight shift to lower wavelength of 294 nm. However the broadening of the WO₃ band and appearance of merged band of GR in the composite of PANI|WO₃|GR film revealed the presence and interaction of the individual particles in the composite **Figure 71b**.

The band gap energy for the different modified composite on the electrodes, based on the UV-vis spectra in Figure 71 was calculated, using the formula:

$$\text{Band Gap Energy } (E) = hc/\lambda$$

Equation 37

Where h is the plank constant (6.66×10^{-34} Joules second), C is the speed of light (3.0×10^8 meters) and λ is the wavelength maximum absorbance of a specific composite (nm). From the calculated data in Table 7, it can be observed that PANI|WO₃|GR composite has the lowest band gap energy value (1.9 eV), this is an indication that graphene has great influence on the PANI|WO₃ film, thereby reducing the bang gap energy and thus being higher in conductivity. However, in agreement with the general characteristics of the activity of different types of nanomaterial in which the band gap energy of an insulator is usually large (> 4 eV), semiconductor (< 3 eV), PANI|WO₃|GR has also showed the activity of being a better semiconductor than PANI|WO₃ and PANI.

Table 7. Band gap energy values calculated from the UV-vis spectra

Electrode	λ (nm)	E (eV)
PANI GCE	602	2.014
PANI WO ₃ GCE	452	2.763
PANI WO ₃ GR GCE	633	1.973

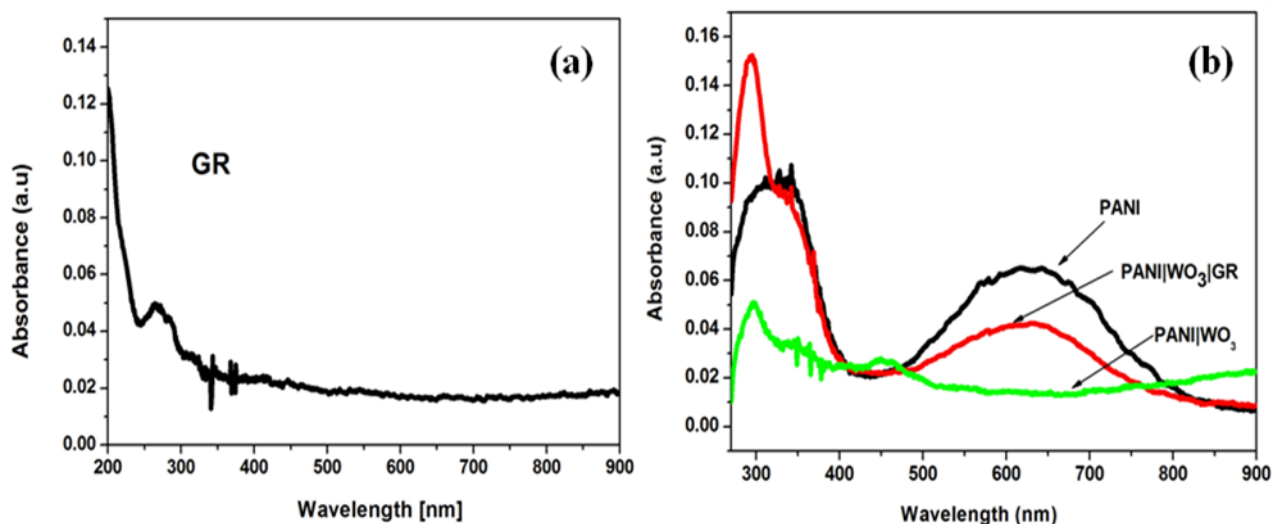


Figure 71. UV Vis absorption spectra of (a) GR and (b) PANI, PANI|WO₃|GR and PANI|WO₃.

6.2.2. High resolution scanning electron spectroscopy

The typical morphologies of the resulting PANI, WO₃, PANI|WO₃, GR and PANI|WO₃|GR films were observed by HR-SEM, as exhibited in **Figure 72 a - f**. A porous fibrillar and rod like irregular structure can be observed for PANI (a). WO₃ display fused white and large particles (b). The microstructure of PANI|WO₃ film showed smaller granules of WO₃ with rough porous surface of aggregates within the PANI film (c). An overlapped thin, crumpled and wrinkle sheets closely associated together can be observed for GR (d). However, the composite film of PANI|WO₃|GR revealed a porous surface of micro aggregate of WO₃ and PANI enveloped and absorbed on the thin film of the graphene sheet with a large surface area which may have the tendency of enhancing the electron transport and catalytic activity of the PANI|WO₃|GR nanocomposite (e). The EDX analysis revealed the composition of the individual elements in the synthesised nanocomposite (f). Investigating the elemental composition acquired from HR-SEM analysis of the nanocomposite, **Figure 73** showed the elemental compositions, revealing the three elements to be present in the composite. However,

other elemental signals such as chlorine may have been formed from contamination during preparation.



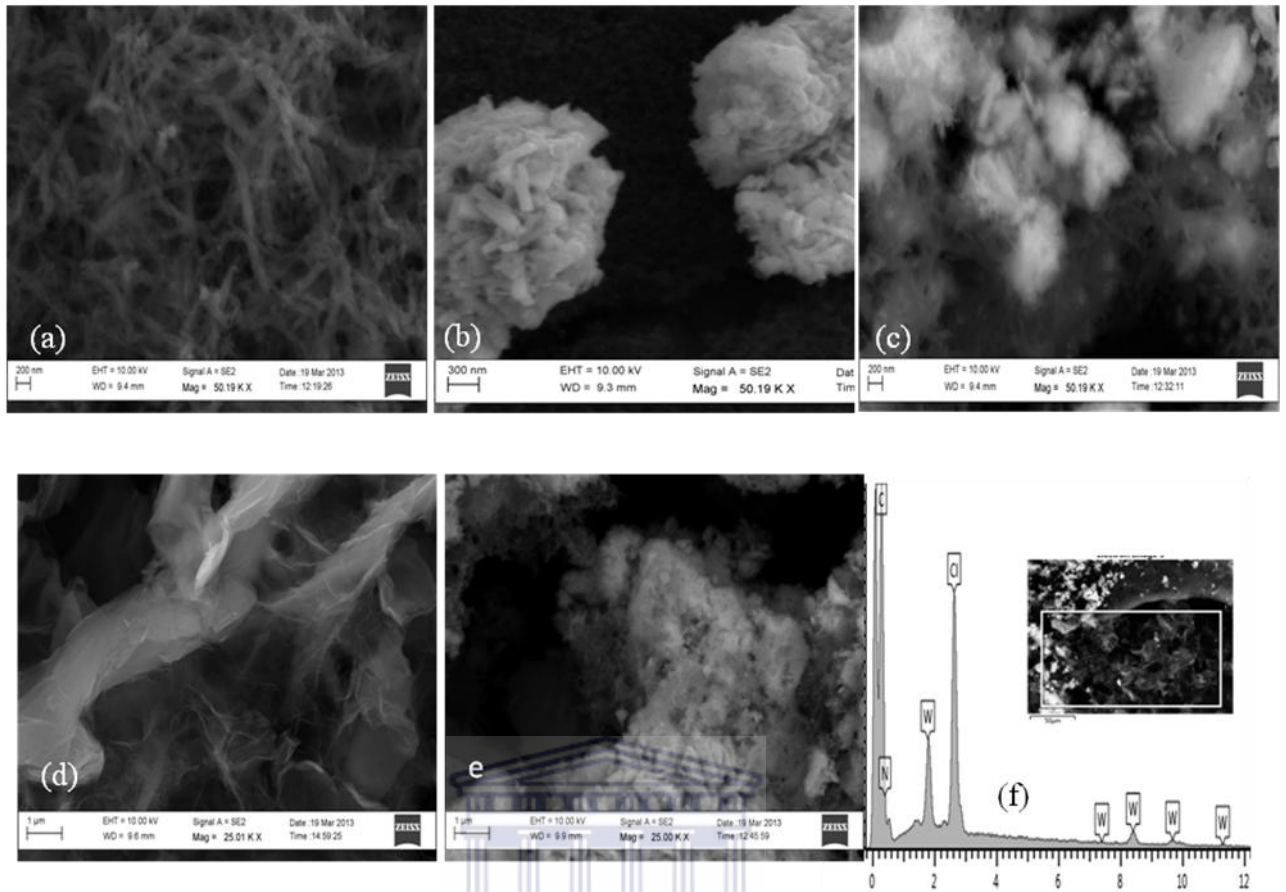


Figure 72. HRSEM images of (a) PANI, (b) WO_3 , (c) PANI| WO_3 , (d) GR, (e) PANI| WO_3 |GR and EDX result of the elemental analysis of nanocomposite formed (f).

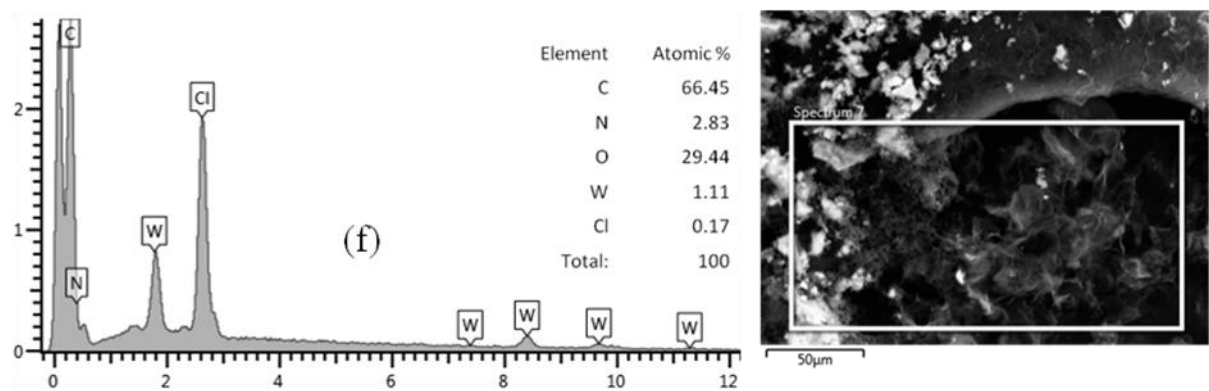


Figure 73. Electron dispersive X-ray results of the elemental composition of PANI| WO_3 |GR nanocomposite.

6.2.3. High resolution transmission electron microscopy (HRTEM)

The structure and composition of the composite was further performed using high resolution transmission electron microscopy (HRTEM). **Figure 74a – d** represents the HRTEM images of GR, PANI, PANI|WO₃ and PANI|WO₃|GR nanocomposite. A flat transparent layer thin sheet can be observed for GR (a), with the selected area electron diffraction (SAED) pattern showing some crystallinity. The appearance of long rod like shapes of flakes of nanofibrous structure can be observed for PANI (b). The PANI|WO₃ film shows compact of WO₃ particles clearly shown on the surface of PANI nanofibers possibly due to agglomeration of the nanoparticle (c). The resulting composite in (d) revealed the distribution of nanoparticle of WO₃ and PANI nanofibers in between the surface and edges of the thin sheets of graphene with selected area electron diffraction (SAED) pattern exposing the crystallinity of the carbon material which is confirmed by SEM images. The STEM image (e) of the PANI|WO₃|GR and the corresponding elemental acquisition from the EDX analysis (f) is also presented in **Figure 75**. The elemental composition of the nanocomposite showed to consist of carbon, nitrogen, and tungsten that were involved in the preparation of the composite. The presence of element like copper may be from the copper grid used while chlorine could be from contamination during sample preparation.

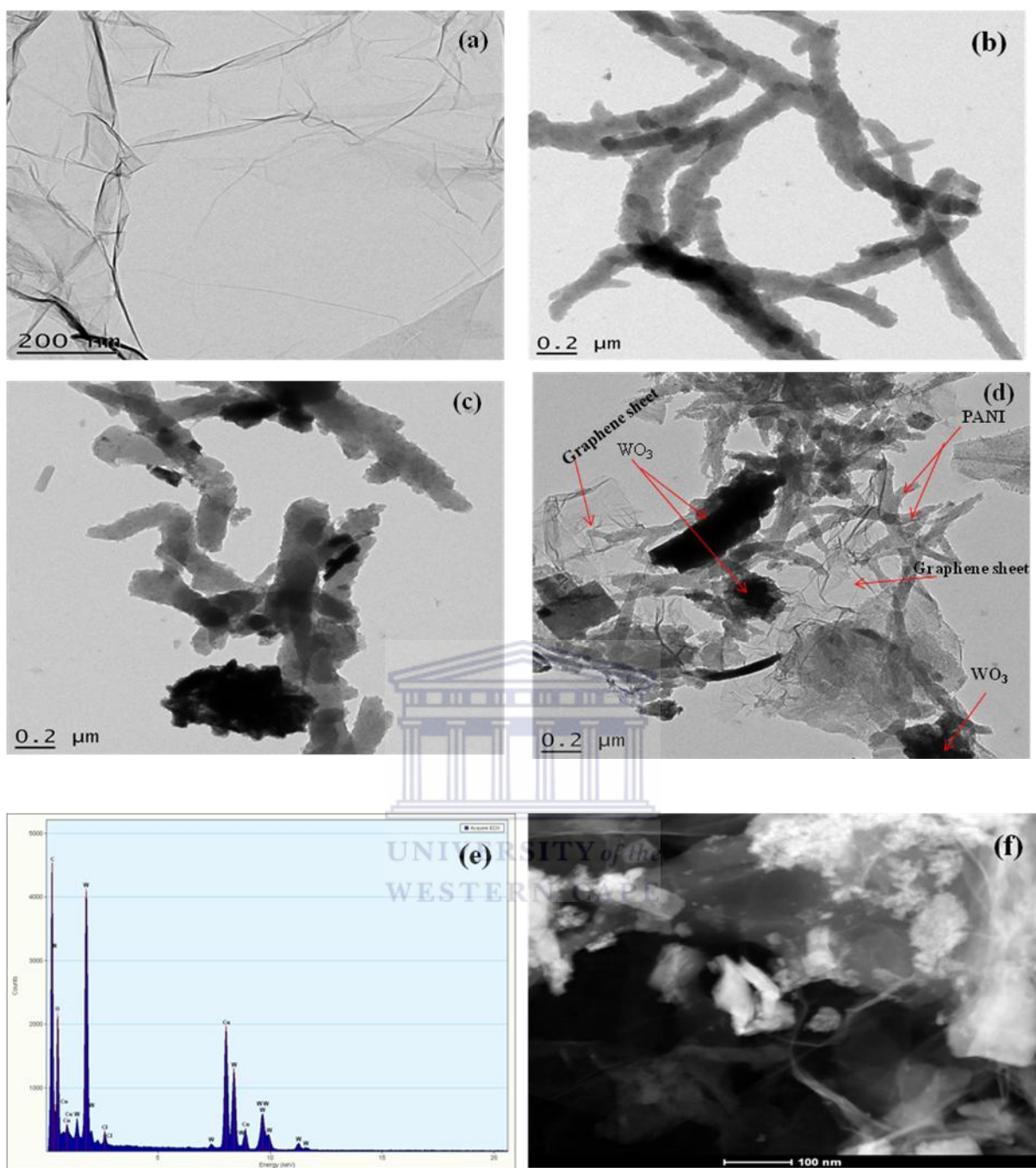


Figure 74. HRTEM images of (a) GR, (b) PANI, (c) PANI|WO₃, (d) PANI|WO₃|GR nanocomposite, (e) EDX analysis and (f) STEM image of nanocomposite.

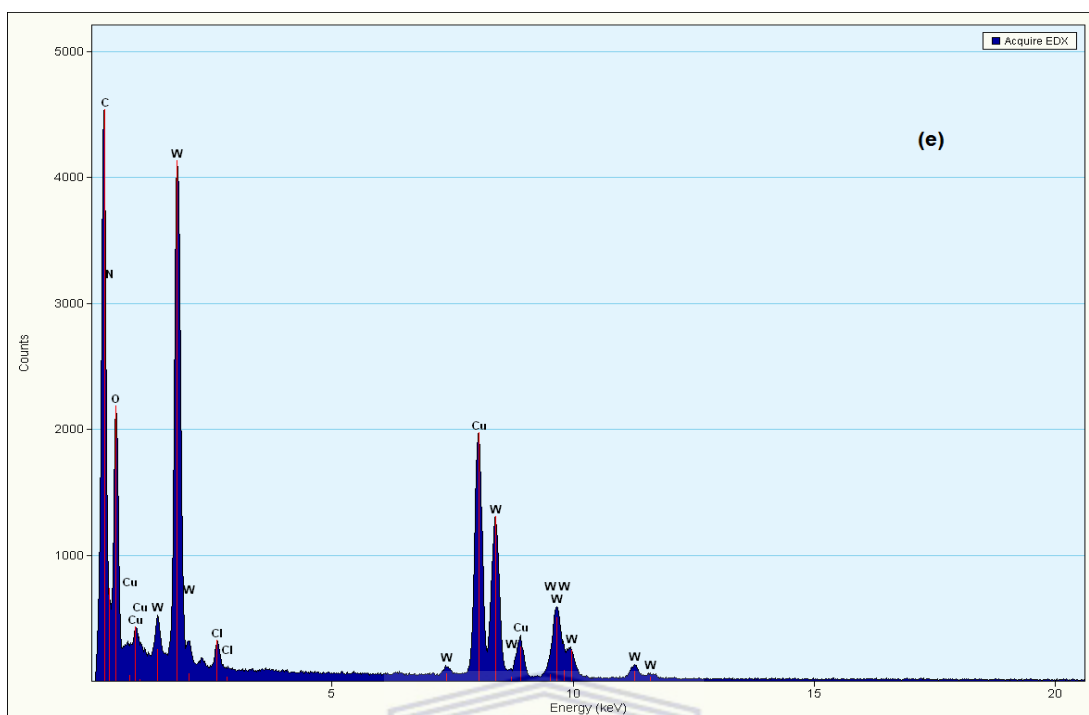
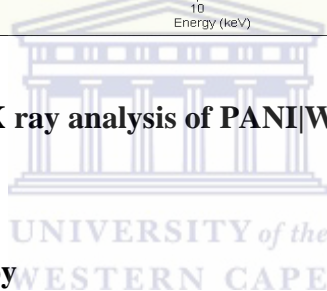


Figure 75. Electron dispersive X ray analysis of PANI|WO₃|GR.



6.2.4. Raman micro spectroscopy

Raman spectral of PANI, PANI|WO₃ and PANI|WO₃|GR films are shown in **Figure 76**. In the spectra, **Figure 76a** showed characteristics bands of PANI that can be associated with the following vibrational peaks, 371 cm⁻¹ and 475 cm⁻¹ (out of plane deformation of the benzene rings), 575 cm⁻¹ (out of plane C-H stretching), 951 cm⁻¹ and 828 cm⁻¹ (benzene and imine deformation), 1156 cm⁻¹ (C-H in plane bending), 1253 cm⁻¹ (C-H stretching of benzene, quinone and Polaroid forms), 1332 cm⁻¹ (C-N⁺ stretching), 1433 cm⁻¹ and 1582 cm⁻¹ (C-C stretching quinone). PANI|WO₃ in **Figure 76b** showed some overlap vibrational peaks of WO₃ with PANI and an appearance of a pronounced peak at 475 cm⁻¹. (Out of plane deformation of W-O-W mode) and 942 cm⁻¹ (W=O terminal mode of surface grains) [535] and has also been confirmed by Balazi *et al.* [536]. Collection of strong and weak peaks between 600 cm⁻¹ and

800 cm^{-1} , also corresponding to stretching vibration of WO_3 in the PANI/ WO_3 film can be observed from the spectra [394]. Vibrational peaks of WO_3 and PANI can be identified in PANI/ WO_3 /GR film, **Figure 76c** of the spectra. The corresponding D and G mode of graphene showed a prominent peak at 1344 and 1587 respectively in the spectra, a slight shift in the D band from 1344 cm^{-1} to 1329 cm^{-1} can be observed for graphene in PANI/ WO_3 /GR film, which is also confirmed from literature [537]. **Figure 77** showed the Raman spectrum for graphene.

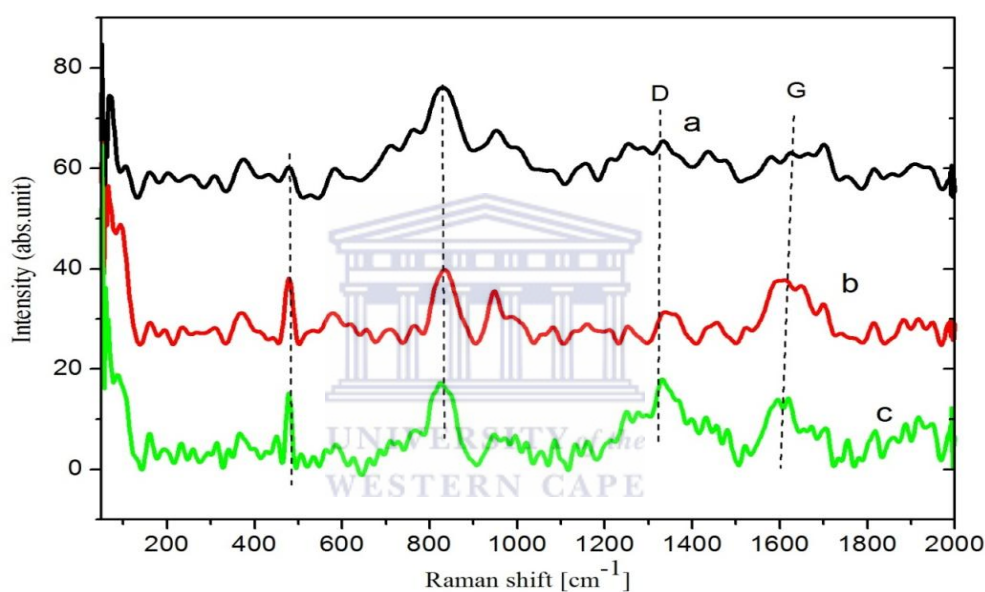


Figure 76. Raman spectra of (a) PANI, (b) PANI/ WO_3 and (c) PANI/ WO_3 /GR films.

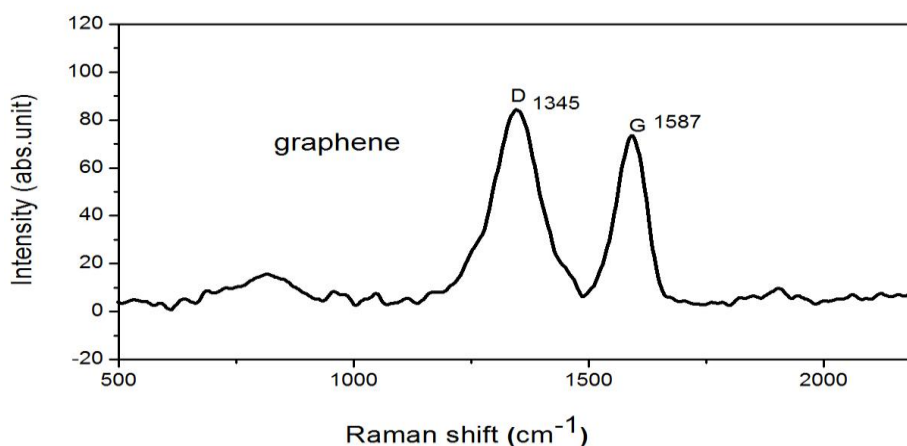


Figure 77. Raman spectrum of graphene (GR).

6.3. Voltammetric interrogation of the modified film on glassy carbon electrode.

CV studies were conducted to optimise the synthesis conditions and subsequently, the interrogation of the electrochemistry of the modified electrode.

6.3.1. Results of the optimised parameters

6.3.1.1. Characterisation of the PANI electrode for optimisation

Figure 78 showed the cyclic voltammograms of electrochemically synthesised polyaniline (PANI) at 50 mV s^{-1} in a solution containing 0.1 M aniline, 1 M HCl , and at window potential of -200 to $+1200 \text{ mV}$. The polyaniline film was grown on 0.071 cm^2 glassy carbon electrode. The PANI film exhibited a high magnitude in current with three redox peaks. The three anodic and cathodic redox peaks in the CVs showed the existence and behaviour of a typical synthesis of polyaniline on the surface of electrode and which confirms its three different forms: Leucomeraldine, Emeraldine and Penigraniline. The redox peaks A/A' and C/C' indicate the conversion of leucomeraldine to emeraldine and emeraldine to Penigraniline respectively. The middle redox peaks B/B' could be referred to as the dimers or benzoquinone / hydroquinone couple of the polymeric chains. The first redox (A/A') peaks which is assigned

leucomeraldine/leucomeraldine radical cation, the second one, (B/B') is assigned emeraldine radical cation/emeraldine and the third (C/C') also assigned pernigraniline radical cation/pernigraniline have been similarly reported by Iwuoha *et al.* [515]. The magnitude of the redox peaks was also observed to increase as a result of repeated potential scans revealing that deposition is actually taking place at the surface of the glassy carbon electrode and confirming the conductivity of the polymer [235]. However, the same PANI film was also grown at 100 mV s^{-1} and 200 mV s^{-1} .

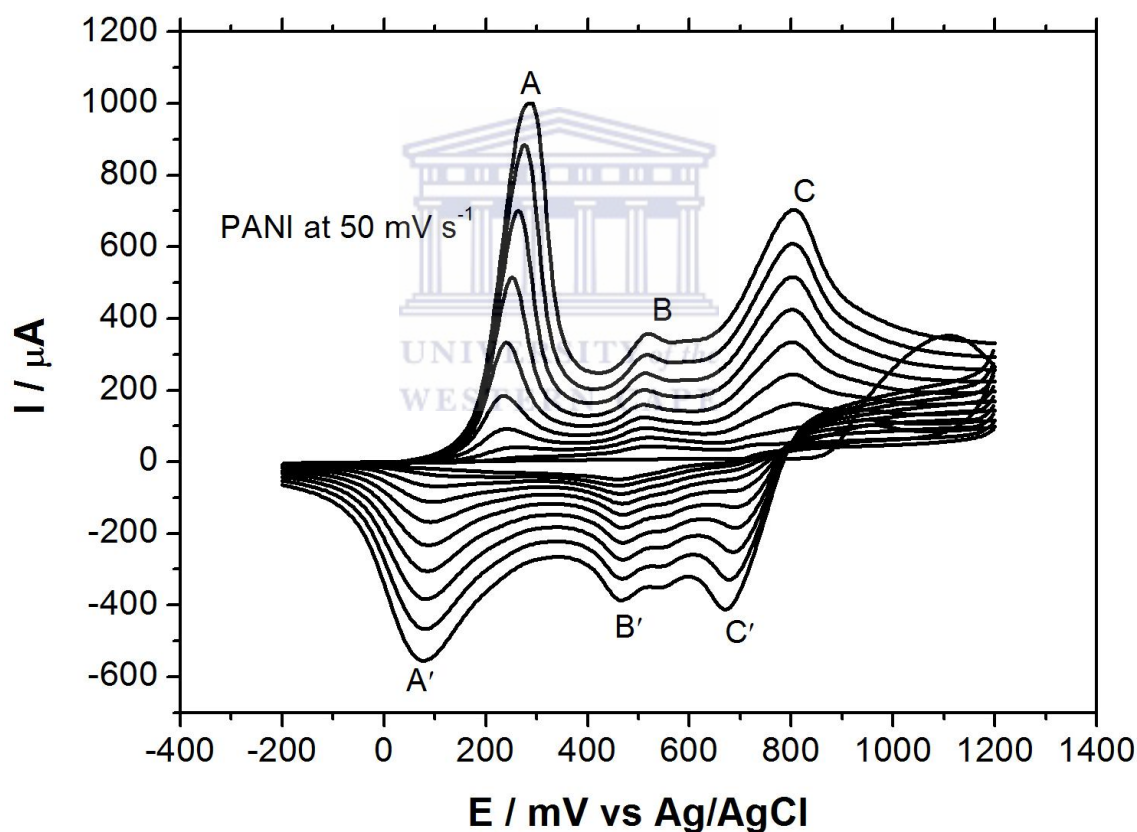


Figure 78. Cyclic voltammograms for electropolymerisation of polyaniline in 1 M HCl at scan rate of 50 mV s^{-1} and window potential of -200 to +1200 mV.

The cyclic voltammograms for the characterisation of the PANI|GCE electrode in 1 M HCl is presented in **Figure 79**. The multi scan voltammograms showed both anodic peak potentials and the corresponding peak currents to vary as the scan rate varies which conforms to the reported study that the polymer is electroactive and conducting, and that the diffusion of the electrons takes place along the polymer chain [16, 235, 515]. The peaks $I_{p,a1}/I_{p,c1}$ and peaks $I_{p,a2}/I_{p,c2}$ are assigned the polyleucoemeraldine radical cation/polyleucoemeraldine and polyemeraldine/polyemeraldine radical cation respectively. It can also be observed that the $I_{p,a1}$ and $I_{p,c2}$ peaks increases and even more prominent as the scan rate increases, exhibiting the characteristics of a reversible electrochemistry system.

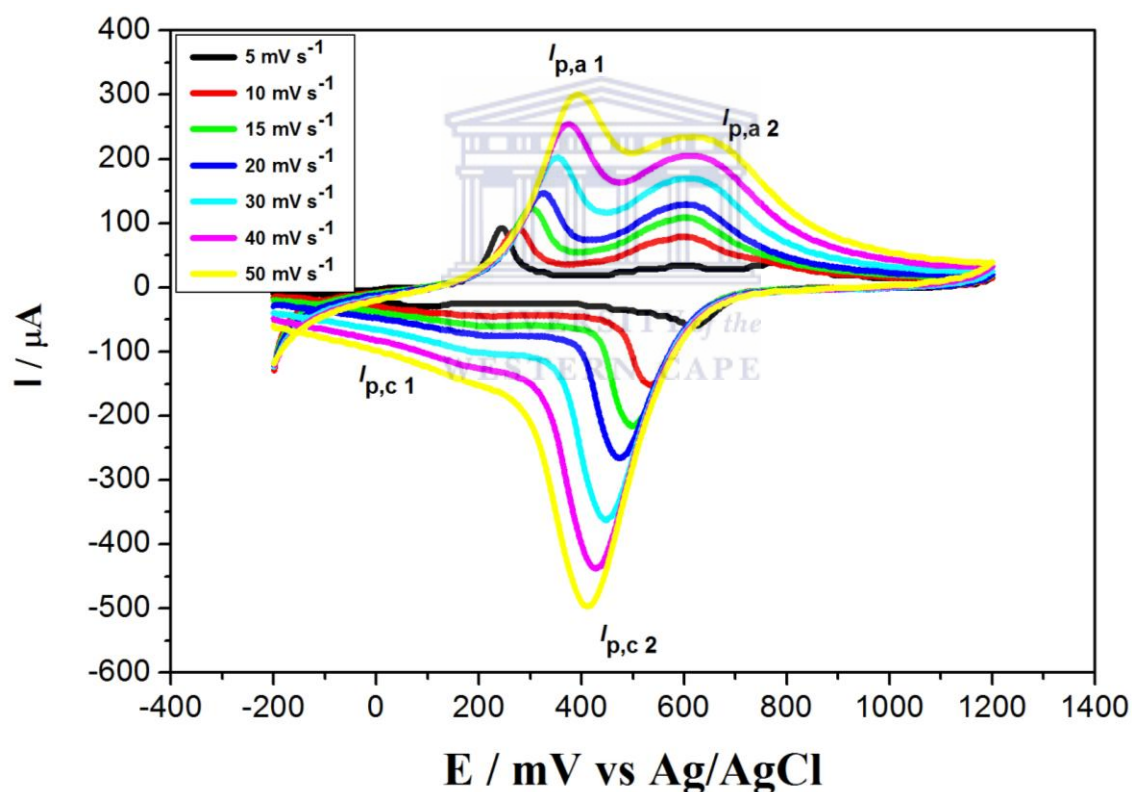


Figure 79. Cyclic voltammograms of PANI|GC electrode in 1 M HCl at different scan rate.

Figure 80 showed the cyclic voltammograms of the different electropolymerisation of PANI electrodes at scan rate of 50, 100 and 200 mV s^{-1} in 1 M HCl at potential window of -200 to +1200 mV. The cyclic voltammograms observed for PANI at 50 mV s^{-1} and from the ΔE_p ($E_{p,a1} - E_{p,c2}$) calculated for each of the scan rates, only PANI electropolymerised at 50 mV s^{-1} exhibit ΔE_p value less than 65 mV (14 mV). This indicates that the polymer film showed a fast and reversible electrochemistry under the experimental condition, compared to the other scan rates and this has also been previously reported by Iwuoha *et al.*[515]. It can also be observed that the $I_{p,a1}$ and $I_{p,c2}$ peaks increases and even more prominent for 50 mV s^{-1} than for the other scan rates. This reveals the characteristics of a reversible electrochemistry system. The mentioned studies therefore guided the choice of 50 mV s^{-1} as the scan rate for the electrosynthesis.



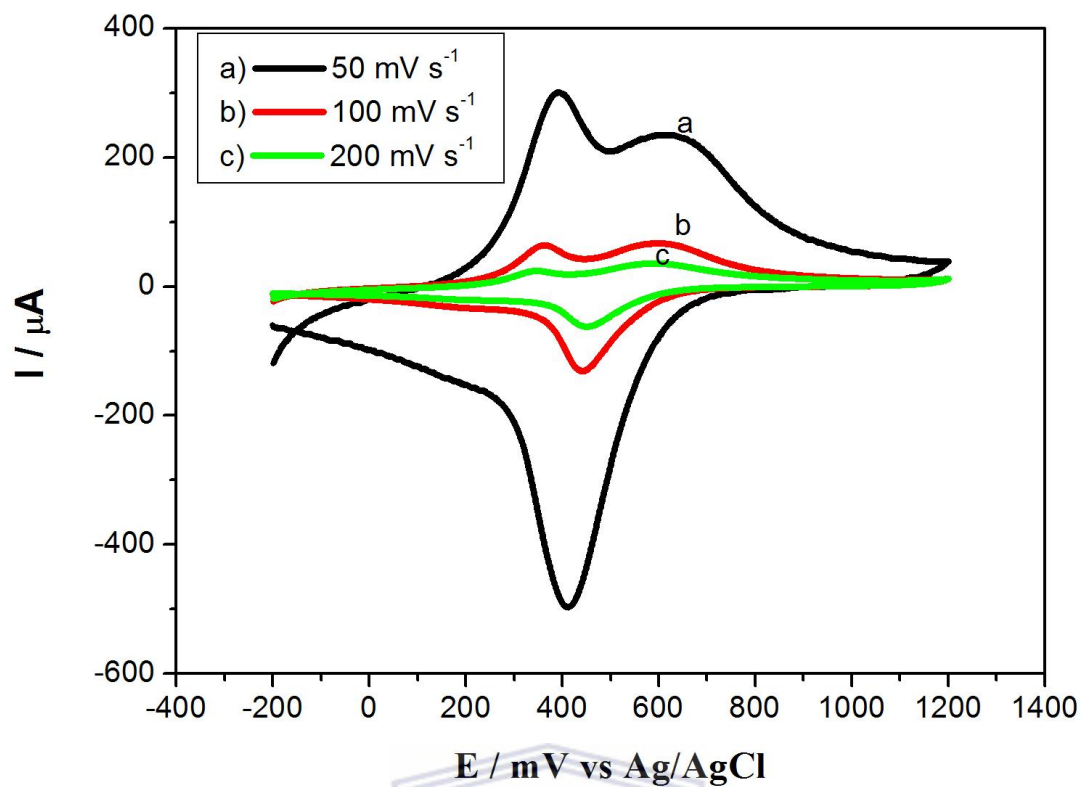


Figure 80. Cyclic voltammograms for the electropolymerisation of PANI film at (a) 50 mV s^{-1} , (b) 100 mV s^{-1} and (c) 200 mV s^{-1} in 1 M HCl.

6.3.1.2. Optimisation of hydrogen peroxide concentration for WO₃ synthesis

CV studies were also conducted to optimise the synthesis conditions and subsequent interrogation of the concentrations of hydrogen peroxide.

The choice of concentration of hydrogen peroxide (H₂O₂) used for the preparation of tungsten oxide was determined after considering the various concentrations 0.05, 0.08, 0.1 and 0.15 M during electrosynthesis of polyaniline. The addition of hydrogen peroxide in the deposition solution essentially allow the formation of peroxy-tungstate in the presence of tungsten acid which serves as a precursor and assumed to undergo electrochemical reduction during electrodeposition, giving rise to tungsten oxide (WO₃) on the substrate of the electrode. Studies has also reported formation of WO₃ from peroxy-tungstate through electrochemical deposition to be more favourable [492, 538]. In addition, H₂O₂ has been reported to play a good role as a stabilizer and complex reagent for the formation of homogenous solution in other to prevent the aggregation of the WO₃ [539]. However, presence of H₂O₂ in the solution can also affect the electrochemical deposition or growth of PANI on the substrate by either restraining the growth of PANI-related redox peak, when in excess according to literature [492] or cause the deprotonation of PANI, whereby acting as an oxidant [540]. **Figure 81a** showed the cyclic voltammograms of different concentrations of H₂O₂ during Electropolymerisation of PANI|WO₃ film in 1 M HCl at 50 mV s⁻¹. An increase in PANI-related peak can be observed as the concentration of H₂O₂ increases from 0.05, 0.1, 0.08 and 0.15 M, but concentration at 0.08 M showed more enhancements in redox peaks which could also be attributed to deprotonation of the half oxidised emeraldine salt form to fully oxidised pernigraniline according to literature [540]. The cyclic voltammograms of PANI and PANI|WO₃ in the presence of 0.08 M concentration of H₂O₂ can be observed from **Figure 81b**.

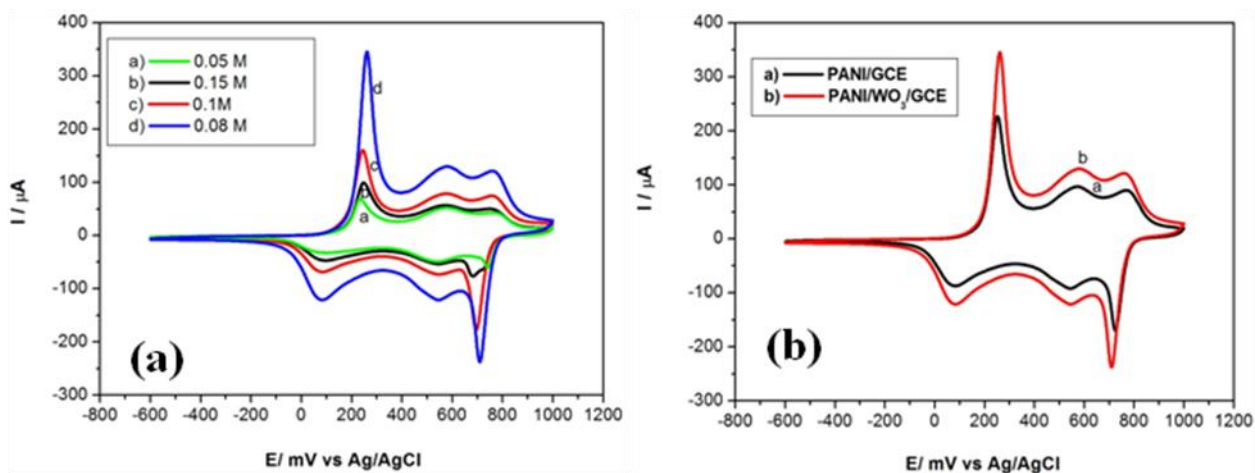


Figure 81. Cyclic voltammograms of PANI| WO_3 in the presence of different concentrations of H_2O_2 (a) and at 0.08 M of H_2O_2 overlay with PANI (b).



6.4. Electrochemical Characterisation of PANI|WO₃|GR electrode

The behaviour of PANI, PANI|WO₃ and PANI|WO₃|GR films grown on the glassy carbon electrode at scan rate of 50 mV s⁻¹ and potential window of -600 mV to + 1000 mV, are shown in **Figure 82**. The cyclic voltammograms revealed that the polymerisation current increases as the number of Voltammetric cycles increases, confirming that the polymer is conducting. Moreover the redox peaks (A/A', B/B' and C/C',) also appeared and their peak heights increased with increase of number of potential scans suggesting that the film is electroactive. The three anodic and cathodic redox peaks in the CVs showed the existence and behaviour of a typical synthesis of polyaniline on the surface of electrode and which confirms its three different forms: Leucomeraldine, Emeraldine and Penigraniline. The redox peaks A/A' and C/C' indicate the conversion of leucomeraldine to emeraldine and emeraldine to Penigraniline respectively. The middle redox peak B/B' could be referred to as the dimers or benzoquinone / hydroquinone couple of the polymeric chains but with a lesser amount of intensity [512]. **Figure 82a – c** showed the cyclic voltammograms of PANI, PANI|WO₃ and PANI|WO₃|GR films on a glassy carbon electrode respectively. Three anodic and cathodic corresponding peaks can be observed with increase in the peak currents as the potential scan increases. The three redox peaks has been assigned accordingly [515]. From the obtained data in table 8, the anodic peak current ($I_{p,a}$) from each of the three redox couples A/A' B/B' and C/C' can be observed to increase with the cathodic peak potential ($I_{p,c}$), shifting anodically for each of the electrodes, PANI|WO₃|GR possessed the highest peak current compared to PANI|WO₃ and PANI electrode. And the $I_{p,a}/I_{p,c}$ ratio is 'unity' for all the couples from the experimental data. It can also be observed that the $I_{p,a}/I_{p,c}$ ratio drops within the range of 0.5 and 0.7 for C/C' in each of the electrode. This change can be attributed to the efficiency of the polymer when in the form

of leucomeraldine radical cation or pernigraniline radical cation according to literature thus revealing some charge transportation [515].

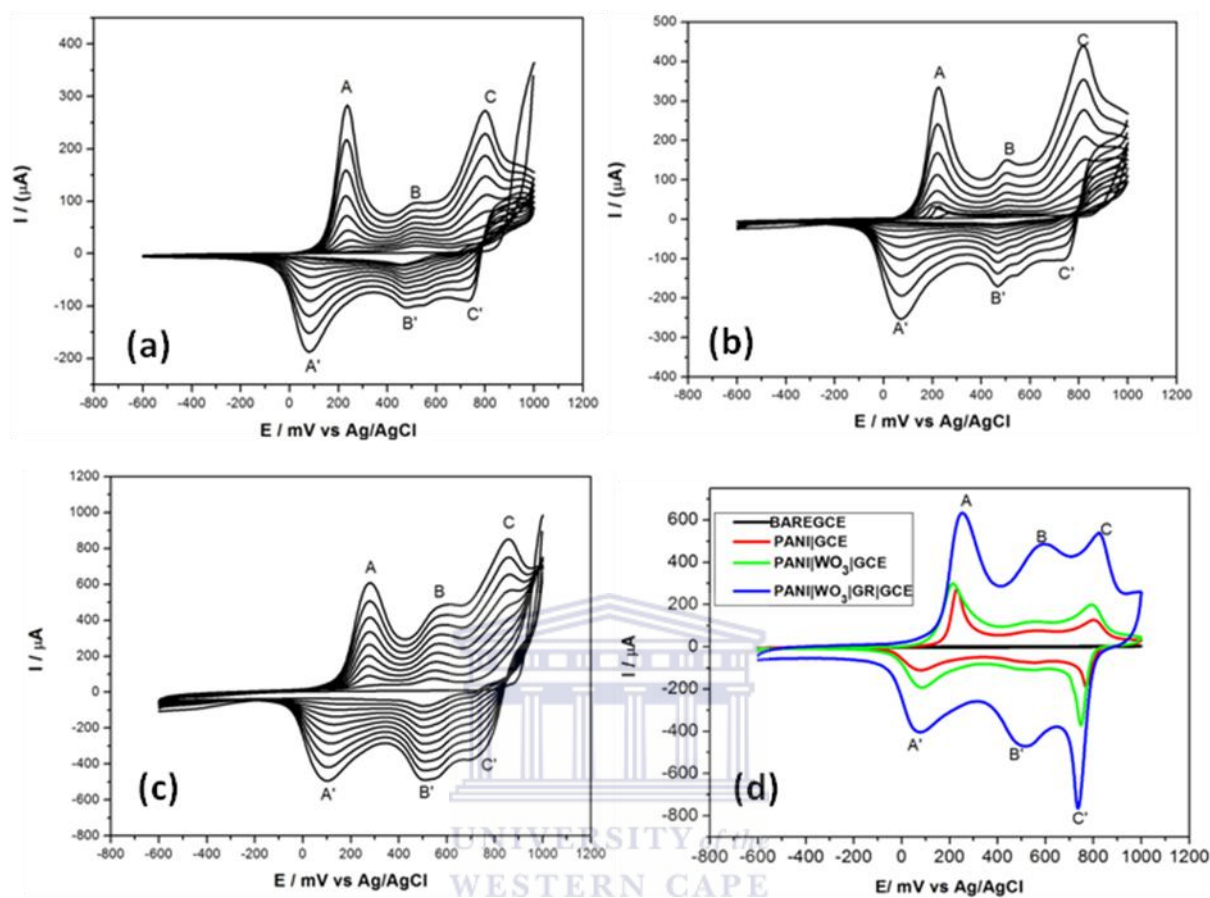


Figure 82. Cyclic voltammograms for the electrodeposition of (a) PANI, (b) PANI|WO₃ and (c) PANI|WO₃|GR films on a glassy electrode in a solution of 1 M HCl, at potential window of -600 mV to + 1000 mV and overlay of bare GCE, PANI|GCE, PANI|WO₃|GCE and PANI|WO₃|GR|GCE in a solution of 1 M HCl at scan rate of 50 mV s⁻¹.

Table 8. Obtained data of cyclic voltammetric analysis from Figure 81

Electrode	Redox couple	E_{pa} (mV)	E_{pc} (mV)	I_{pa} (μ A)	I_{pc} (μ A)	I_{pa}/I_{pc}	$E^{o'}$ (mV)
PANI WO ₃ GR	A/A'	253	75	634.13	406.51	1.5	166.5
	B/B'	598	521	488.02	468.00	1.04	559.5
	C/C'	823	733	538.03	-760.05	0.71	778
PANI WO ₃	A/A'	211	86	301.60	192.60	1.5	148.5
	B/B'	543	533	119.20	107.13	1.1	538
	C/C'	792	747	200.39	-369.77	0.5	769.5
PANI	A/A'	230	79	272.44	108.09	2.4	154.9
	B/B'	548	548	76.96	74.71	1.0	548
	C/C'	802	767	126.50	-184.94	0.6	786

For the electrodeposition of PANI|WO₃, **Figure 82b**, the response is similar to pure PANI film, except for the oxidation of the monomer occurring at a slightly lower potential and an enhancement in the peak current. The response in PANI|WO₃ film could be attributed to the WO₃ particles agglomeration observed in HRSEM, which can likely reduce the expectation in the effective surface area of the film when incorporated with PANI. The response in PANI|WO₃ film in the presence of graphene modified glassy electrode is shown in **Figure 82c**. The three anodic peaks are more prominent and higher than in **Figure 82a** and **Figure 82b**, also the cathodic peaks shifted more positively, The remarkable increase in peak current of PANI|WO₃|GR film can be associated to the exceptional properties of graphene which include its high catalytic property and large surface area. Also, the distribution of the polymer matrix

and interfacial adhesion due to bonding between PANI|WO₃ and the graphene thin layer which can be confirmed by the morphology analysis from HRTEM. The voltammograms in **Figure 82d** obviously revealed the difference in the peak enhancement for the different electrodes with PANI|WO₃|GR film having a more prominent in peaks.



6.4.1. Cyclic voltammetry of PANI|WO₃|GR electrode in HCl

Figure 83 showed the cyclic voltammetric response of the prepared PANI|WO₃|GR electrode in 1M HCl as the working electrolyte to the effect of scan rate. The peak current increases as the scan rate are increased. And plot of the anodic peak current as a function of potential scan rate of peak A showed linearity with a correlation coefficient (r^2) = 0.9891 which showed that the nanocomposite is confined on the surface of the electrode and electroactively conducting (b). The plot of log of peak current against log of scan rate gave a slope of 1, which revealed a surface-adsorbed electrochemistry.

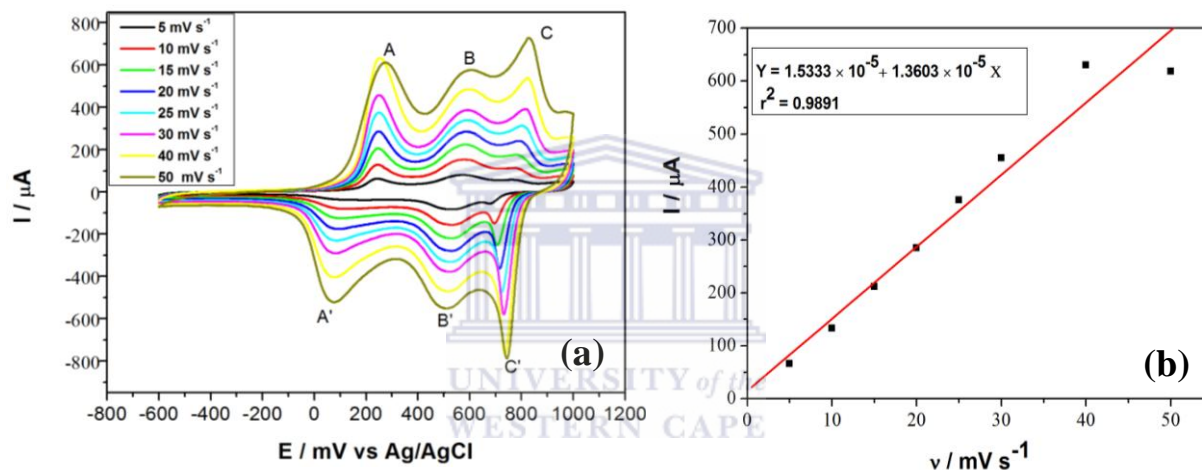


Figure 83. Cyclic Voltammograms of (a) PANI|WO₃|GR electrode at different scan rates (5, 10, 15, 20, 25, 30, 40 and 50 mV s^{-1}) in 1 M HCl and (b) a plot of scan rate dependence anodic peak current.

6.5. Electrochemical Impedance Spectroscopy (EIS) of PANI|WO₃|GR|GCE

Electrochemical impedance spectra (EIS) were used to investigate the performance of the modified electrodes being an effective method of probing the features of a surface modified electrode. [516-518]. The measurement was performed in 1M HCl aqueous solution with a frequency range of 100 kHz to 0.1 Hz of which the amplitude of the alternative voltage was 10 mV as shown in the **Figure 84**. The y-axis represents the negative number of the imaginary part of the measured impedance while the x-axis represents the real part of the measured impedance. The diagram (Nyquist plots- real part of the impedance Z' vs. imaginary part Z'') represents the charge transfer kinetics of the modified electrodes in which R_s is the ohmic internal or solution resistance, CPE is the capacitance phase element for the semiconductor || electrolyte interface, W (Warburg impedance) represent the mass transfer element while the R_{ct} is the charge – transfer resistance across the interface [541].

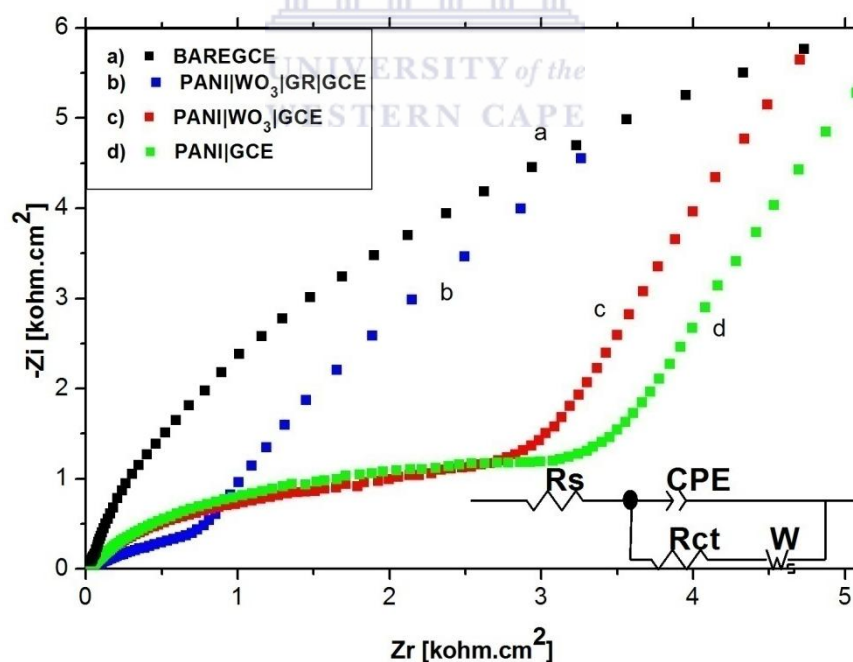


Figure 84. Nyquist plot of the EIS measurement of (a) bare GCE, (b) PANI|WO₃|GR|GCE, (c) PANI|WO₃|GCE and (d) PANI| GCE in the presence of 1 M aqueous solution of HCl. Inset is Randles equivalent circuit Nyquist plots obtained.

Table 9. Values for the fitted parameter of Randles equivalent circuit Nyquist plots from Figure 84

Electrode	R_s (Ω)	R_{ct} (Ω)	CPE	Z_w
Bare GCE	28.53	9.637×10^3	0.91044	0.41358
PANI WO ₃ GCE	28.22	2.831×10^3	0.66312	0.72029
PANI GCE	22.73	3.371×10^3	0.66489	0.72734
PANI WO ₃ GR GCE	24.29	1.433×10^3	0.40447	0.85483

The different charge transfer resistance results of the modified electrodes can be observed from above parameters in table 9 and from the Nyquist plot illustration in **Figure 84**. Bare GCE gave an R_{ct} value of 9.637×10^3 (Ω), exhibiting a line path length in the lower frequency similar to the characteristics of a diffusion process. On modification with PANI film, the R_{ct} value of the modified electrode reduces, as well as when modified with PANI|WO₃ film with values of 3.371×10^3 Ω and 2.831×10^3 Ω respectively. They both exhibited a large semicircle and a straight line in the lower frequency region, indicating a sign of modification and charge resistance transfer but high diffusion system. The R_{ct} of PANI|WO₃|GR GCE is 1.433×10^3 Ω which is much lesser than that of both PANI and PANI|WO₃ indicating that the GR modified electrode in the presence of PANI and WO₃ has high interfacial charge–transfer resistance i.e. facile to electron transfer and indicating high conductivity than PANI|GCE and PANI|WO₃|GCE which was consistent with cyclic voltammetry results. More so, graphene has the ability of creating a nucleating site for polyaniline. Also, the coating of the surface of polyaniline with tungsten oxide could possibly contribute to the synergic effect and more

interaction in the components which thus created more enhancements, conductivity and catalytic effect of the PANI|WO₃|GR|GCE.

6.6. Electrochemical Application of the modified PANI|WO₃|GR electrode on some polyaromatic hydrocarbons (PAHs)

Electrochemical method typically involves the flow of electric current across an electrode in aqueous media to generate redox reaction. However, during oxidation of polyaromatic hydrocarbons in aqueous solution, oxidation can occur by transfer of oxygen atom and electron anodically. An intermediate reactive species such as hydroxyl radicals are generated from water and actually assisted in the oxidation of the organic pollutants [12, 138, 519]. The hydroxyl radical can readily react with the organic molecules from adsorbed PAHs to the electrode and then undergo subsequent reactions [528, 542]. According to reported studies by Panizza *et al.* [138], formation of quinone is usually observed during oxidation of polyaromatic hydrocarbon. Thus the primary degradation products among others include anthraquinone from anthracene, phenanthrenequinone from phenanthrene and pyrenequinone from pyrene.

6.6.1. Electrocatalytic oxidation of phenanthrene

Analysis on the electrocatalytic oxidation of phenanthrene was monitored using the modified electrodes in aqueous acid (1 M HCl) as the supporting electrolyte, potential window of +0 to +2000 mV and scan rate of 30 mV s⁻¹. The cyclic voltammogram of PANI|WO₃|GR|GCE before addition (a) and after addition of 5.0 x 10⁻³ nM of phenanthrene (b) is shown in **Figure 85**. The behaviour of the different electrodes, PANI|GCE, PANI|WO₃|GCE and PANI|WO₃|GR|GCE to oxidation of phenanthrene (5.0 x 10⁻³ nM) dissolved in the above solution is shown in **Figure 86**. PANI|WO₃|GR electrode exhibited a high increase in the anodic peak current revealing a catalytic property compared to the PANI|WO₃ and PANI modified electrodes. This may be attributed to the large surface area and good conductivity of

PANI|WO₃|GR modified electrode as result of the incorporation of graphene nanofiller which have a high catalytic effect [543]. Phenanthrene actually exhibited a remarkable enhancement in anodic current compared to the other electrodes.

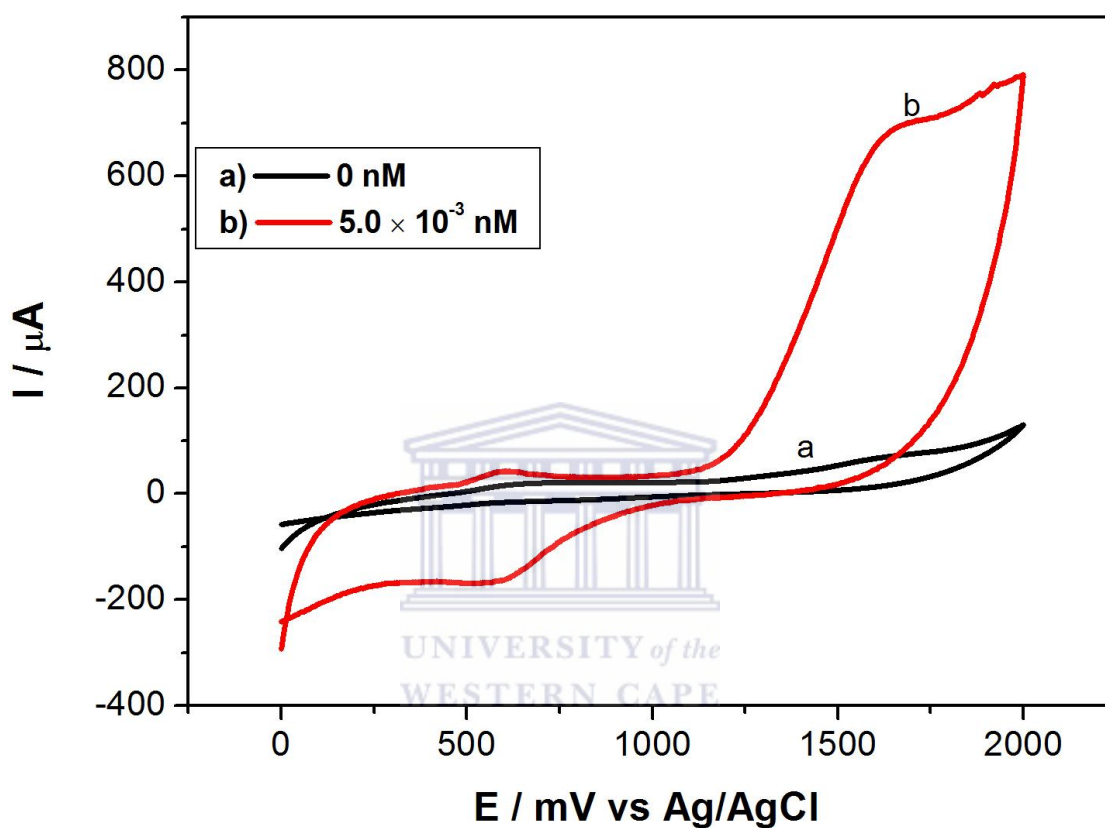
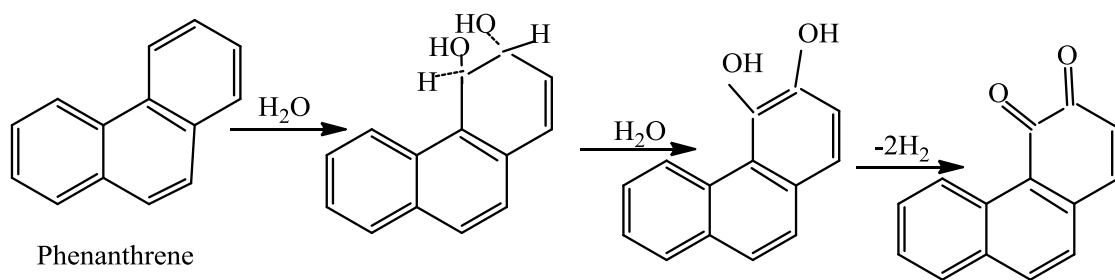


Figure 85. Cyclic voltammograms of (a) PANI|WO₃|GR|GCE before addition and (b) after addition of 5.0×10^{-3} nM of phenanthrene analyte in 1 M HCl at scan rate of 30 mV s^{-1} and potential window of +0 mV to +2000 mV.



Scheme 6. Schematic diagram showing Pathway to degradation of phenanthrene [124]

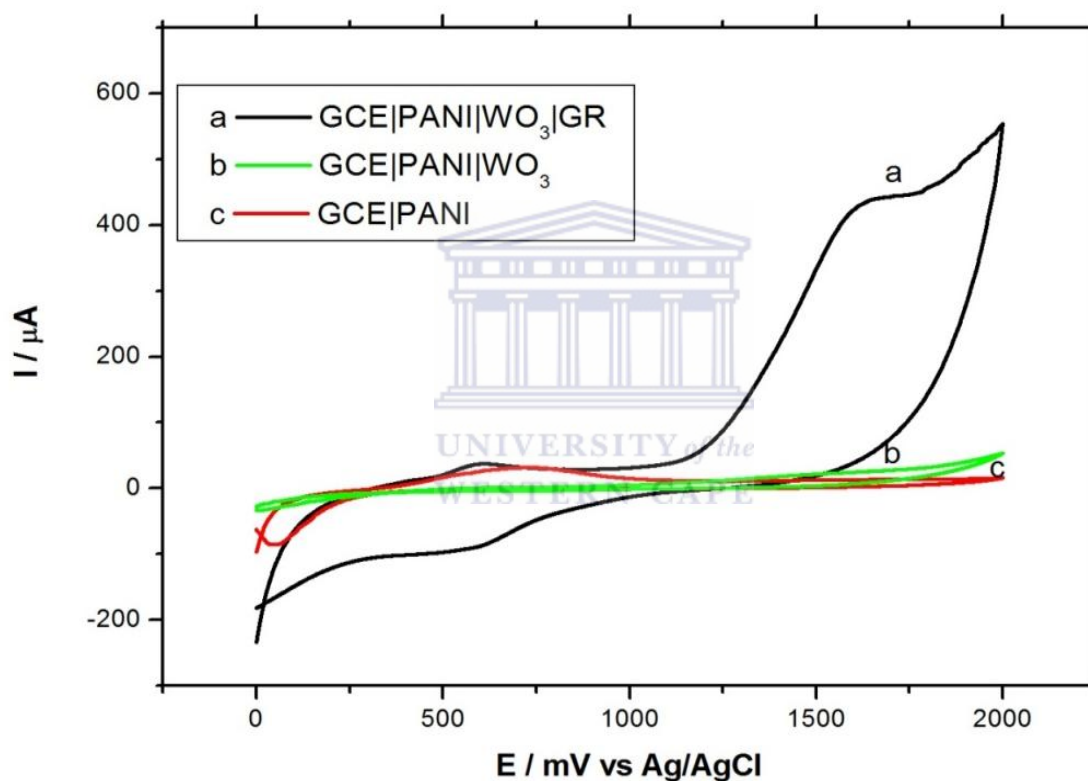


Figure 86. Cyclic Voltammograms of 5.0×10^{-3} nM of phenanthrene at PANI|WO₃|GR|GCE (a), PANI|WO₃|GCE (b) and PANI|GCE (c) in 1 M HCl at a scan rate of 30 mV s^{-1} .

6.6.1.2. Effect of scan rate

Effect of scan rate was investigated on the response of 5.0×10^{-3} nM phenanthrene at PANI|WO₃|GR modified electrode in 1 M HCl. **Figure 87** showed the cyclic voltammograms

of modified electrode at different scan rate upon the addition of 5.0×10^{-3} nM phenanthrene. The plot of the anodic peak current versus the square root of scan rate over the range of 10 and 200 mV s^{-1} increased linearly with the liner equation of $I_{p,a} = 1.3 \times 10^{-3} + 7.01 \times 10^{-4} \times v^{1/2} (\text{mV s}^{-1})^{1/2}$ and a correlation coefficient (r^2) = 0.999 (b). Hence, revealing that the electrochemistry process was limited by the rate of diffusion of phenanthrene from the solution to the surface of the electrode. Also observed is the oxidation peak potential shifting to more positive potential confirming the peak currents were diffusion-controlled. [235].

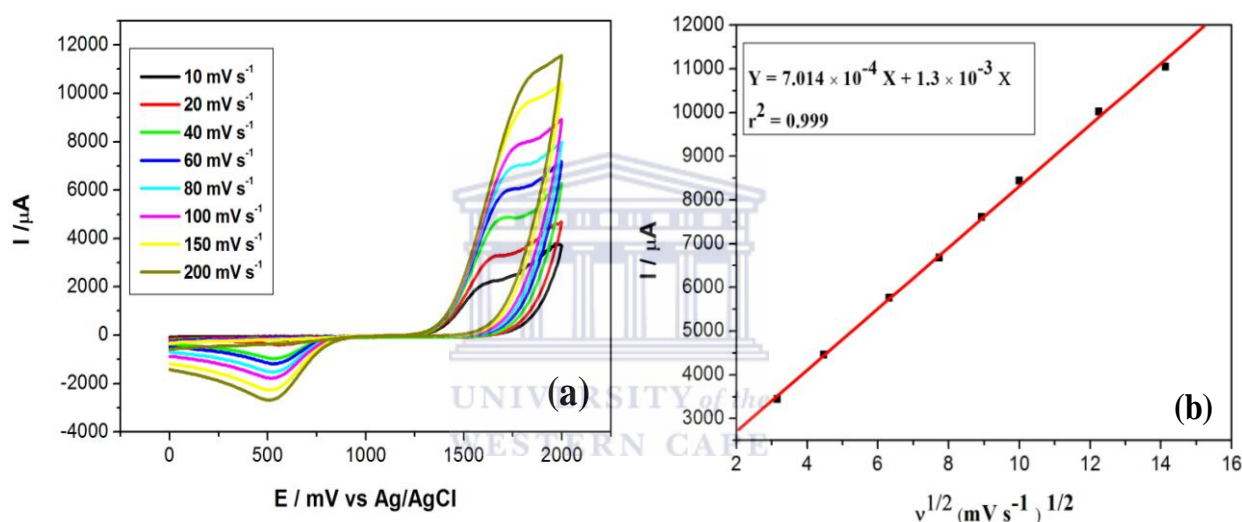


Figure 87. Cyclic Voltammograms of PANI|WO₃|GR GCE upon the addition of 5.0×10^{-3} nM of phenanthrene in 1 M HCl at different scan rates (a) and a plot of scan rate dependence of its anodic peak current (b).

6.6.1.3. Cyclic voltammetric response at different concentration of phenanthrene.

Cyclic voltammetric response of electrocatalytic oxidation of different concentration of phenanthrene at the PANI|WO₃|GR modified electrode in 1 M HCl can be observed in **Figure 88a**. An increase in the anodic peak current occurs at every addition of phenanthrene indicating the oxidation of phenanthrene and also confirming the catalytic behaviour of the modified

electrode. A plot of the anodic current versus concentration showed the linearity ranging from 1.0×10^{-3} to 6.0×10^{-3} nM with a correlation coefficient of 0.9806. The limit of detection was determined to be 1.23×10^{-4} nM (0.123 pM) as observed in **Figure 88b**. This established that the modified electrode have a good electroactive activity towards the degradation of phenanthrene.

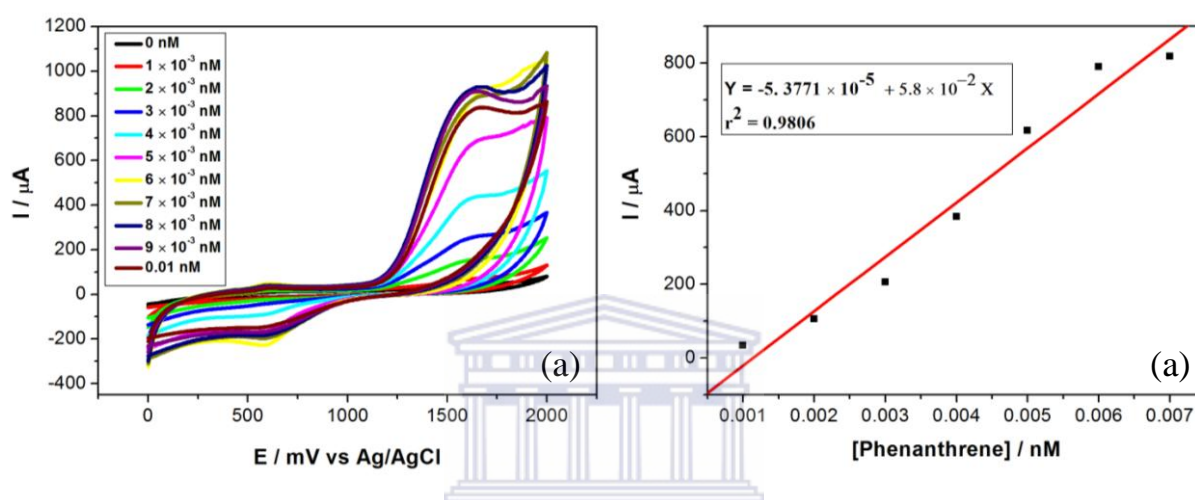


Figure 88. Cyclic Voltammograms of PANI|WO₃|GR GCE in 1 M HCl, in the presence of phenanthrene at 30 mV s⁻¹ (a) and a calibration plot for PANI|WO₃|GR/GCE phenanthrene sensor versus concentrations of phenanthrene (b).

A similar behaviour can be confirmed from the square wave voltammograms. There is increase in the anodic peak current upon successive addition of phenanthrene which can be observed from **Figure 89a**. The response at lower concentrations and the calibration plot of the anodic peak current versus concentrations with respect to the lower concentrations can be observed from **Figure 89b** and **Figure 89c**.

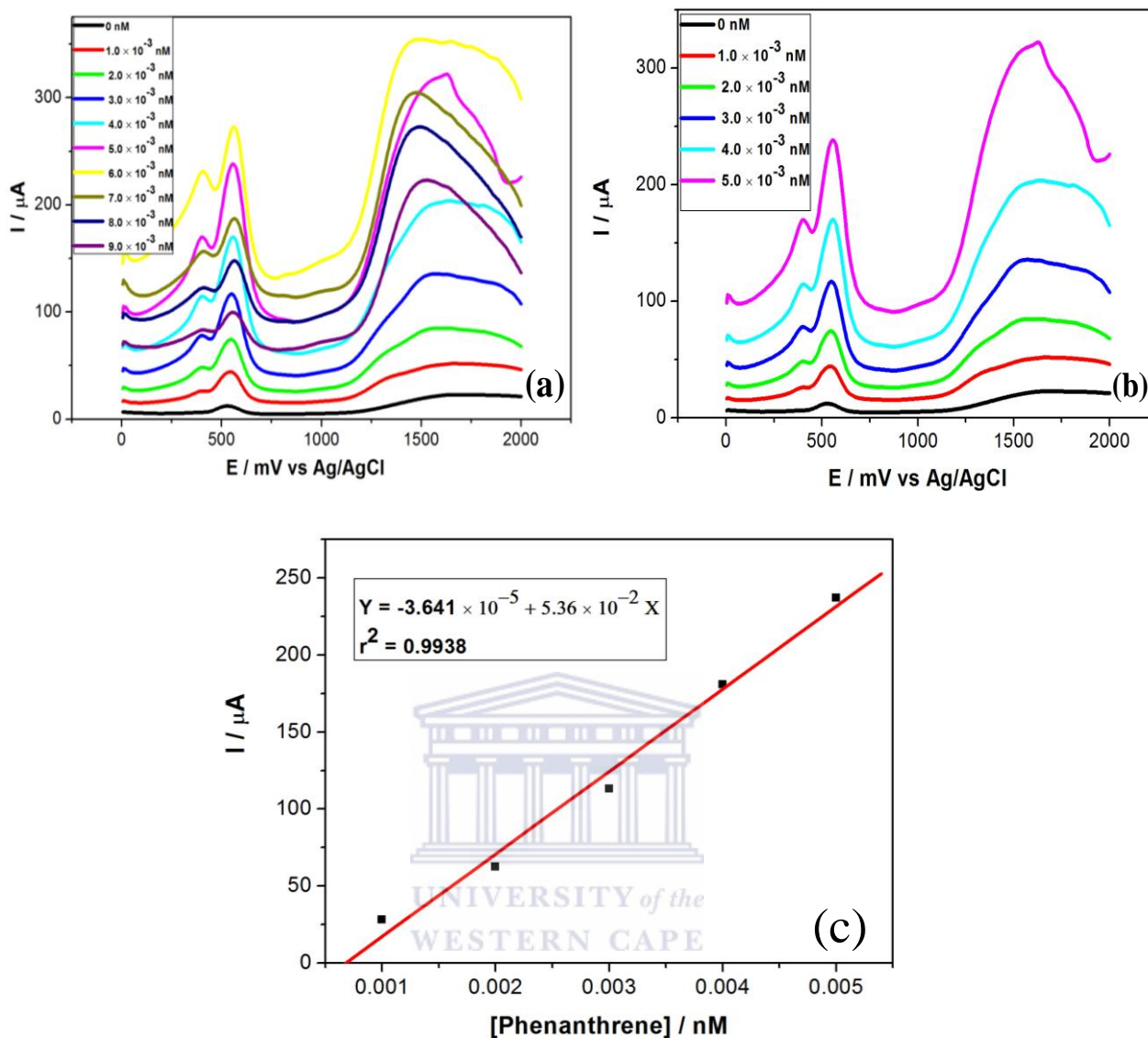


Figure 89. Square wave voltammograms of (a) PANI|WO₃|GR electrode at every successive addition of phenanthrene in 1 M HCl at a scan rate of 30 mV s⁻¹, (b) response at lower concentrations and (c) and a calibration plot for PANI|WO₃|GR|GCE phenanthrene sensor versus concentrations of phenanthrene.

6.6.2. Reproducibility stability and interference studies

The reproducibility study of PANI|WO₃|GR nanocomposite modified electrode was studied in the presence of 5.0 × 10⁻³ nM phenanthrene in 1 M HCl. The cyclic voltammetry were

repeatedly performed and monitored, a relative deviation of 5.1 % from 6 successive measurements ($n = 6$) was conferred from the fabricated electrode, showing its reproducibility. The storage stability of the modified electrode was also examined with 5.0×10^{-3} nM phenanthrene and the oxidation current was been monitored after 3 days for 2 weeks using CV. About 15.69% decrease was observed in the peak current and was able to retain 84.31% of phenanthrene initial sensitivity at 4 °C. Further investigation was made to check for possible interferences using some inorganic ions which may probably present in water samples. The following ion: Mn^{2+} , Cl^- , SO_4^{2-} and NO_3^- were not observed at 5.0×10^{-3} nM of the phenanthrene concentration. The validated results can then conclude that the modified electrode has stability and reproducibility for phenanthrene.



6.6.3. Electrochemical responses of the PANI|WO₃|GR|GCE anthracene sensor

The cyclic voltammetric response of the PANI|WO₃|GR|GCE anthracene sensor was also investigated in the presence anthracene. The PANI|WO₃|GR GCE sensor is observed in the presence and absence of 5.0×10^{-3} nM anthracene. Analysis took place in 1 M HCl, scan rate of 30 mV s^{-1} and potential window of +0 to +2000 mV. The cyclic voltammograms revealed the catalytic property of the nanocomposite exhibited in the presence of anthracene and showing to be more sensitive to the analyte, an increase in the intensity of the anodic peak current indicated that oxidation of anthracene has taken place as can be observed in **Figure 90**.

Figure 91 showed the anodic response of the different electrodes in the presence of 5.0×10^{-3} nM anthracene at 30 mV s^{-1} in 1 M HCl. With more enhancements in the anodic peak for PANI|WO₃|GR|GCE due to its high catalytic property compared to PANI|WO₃|GCE and PANI|GCE.

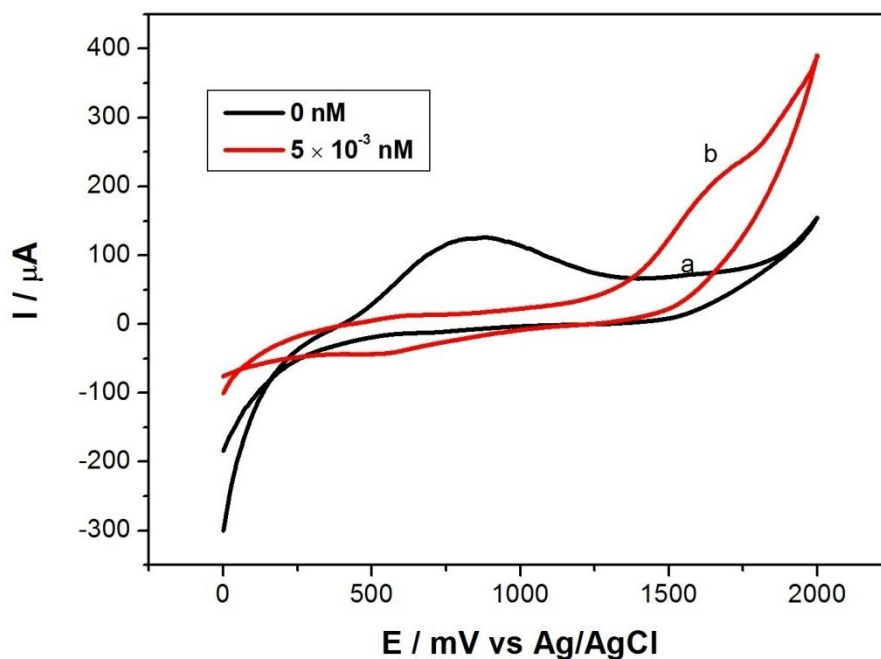
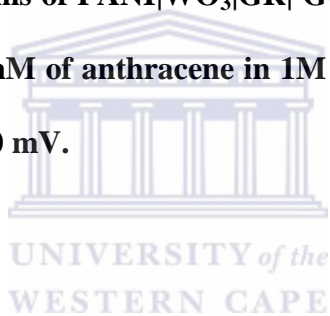


Figure 90. Cyclic voltammograms of PANI|WO₃|GR| GCE in 1 M HCl (a) before and (b) after the addition of 5.0×10^{-3} nM of anthracene in 1M HCl at scan rate of 30 mV s^{-1} and potential window of +0 to +2000 mV.



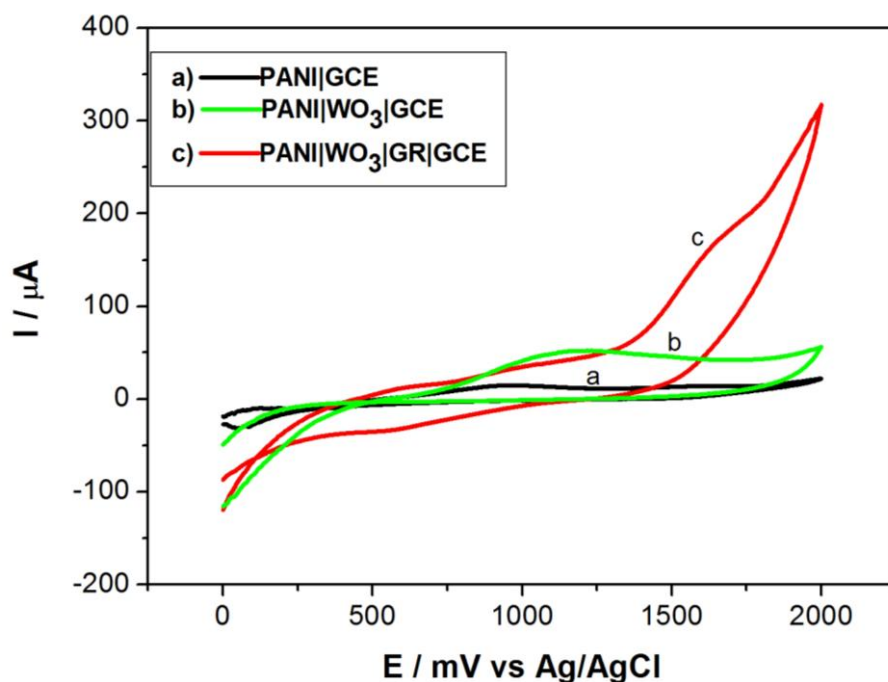


Figure 91. Cyclic Voltammograms of 5.0×10^{-3} nM of anthracene at PANI|GCE (a), PANI|WO₃|GCE (b) and PANI|WO₃|GR|GCE (c) in 1 M HCl at a scan rate of 30 mV s^{-1} .

6.6.3.1 Effect of scan rate

Investigating the effect of scan rate on the response of 5.0×10^{-3} nM anthracene at PANI|WO₃|GR modified electrode in 1 M HCl, showed there is an increase in anodic peak current as the scan rate increases. **Figure 92** showed the cyclic voltammograms of PANI|WO₃|GR|GCE upon the addition of 5.0×10^{-3} nM anthracene at different scan rate. The anodic peak of anthracene increased linearly with the square root of scan rate ($v^{1/2}$) over the range of 10 to 250 mV s^{-1} with a linear regression of $I_{p,a} = -3.5194 \times 10^{-4} + 1.8887 \times 10^{-4} \times v^{1/2} (\text{mV s}^{-1})^{1/2}$ and a correlation coefficient of 0.994, which is shown in **Figure 93**. Also observed, is the oxidation peak potential shifting more positive. This indicated that electrochemistry of the process was limited by rate of diffusion of anthracene from the solution to the surface of the electrode and the peak current is diffusion controlled

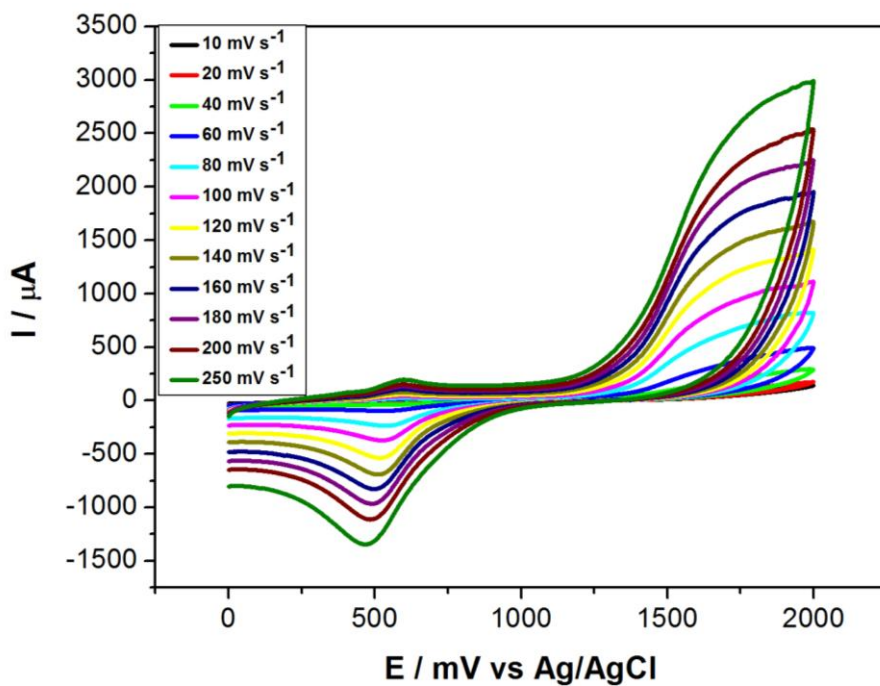


Figure 92. Scan rate dependence cyclic voltammograms of PANI|WO₃|GR|GCE sensor in 1 M HCl containing 5.0 × 10⁻³ nM anthracene.

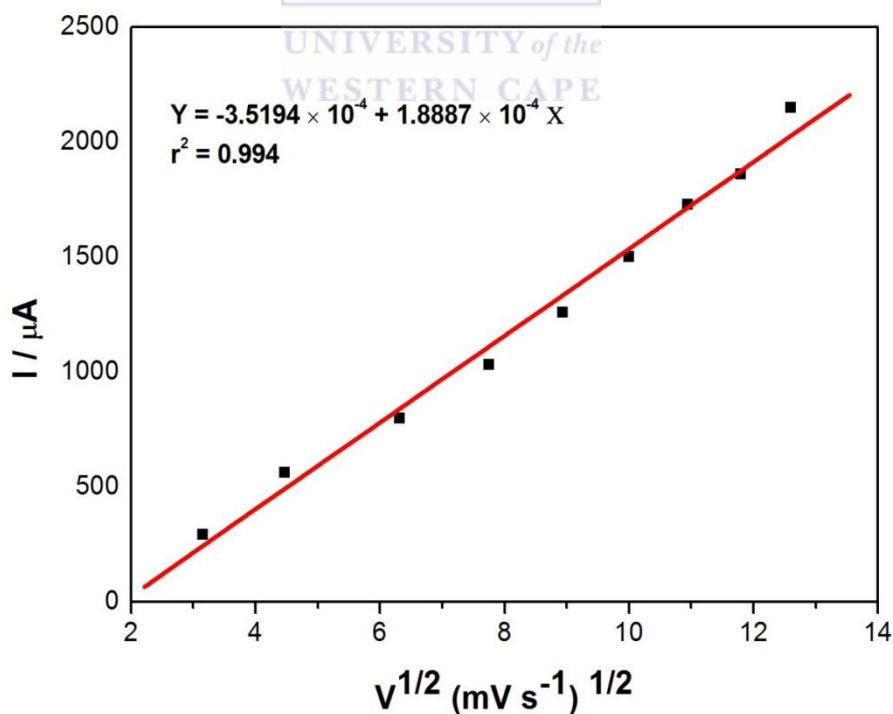
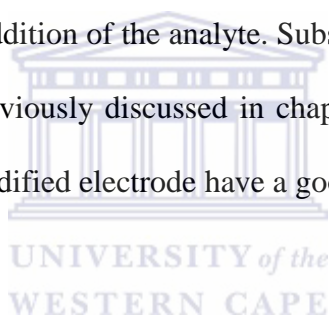


Figure 93. A plot of scan rate dependence of its anodic peak current.

6.6.3.2. Cyclic voltammetry response at different concentration of anthracene.

Cyclic voltammetric response of electrocatalytic oxidation of different concentrations of anthracene at the PANI|WO₃|GR modified electrode in 1 M HCl can be observed in **Figure 94**. An increase in the anodic peak current occurs at every addition of anthracene indicating the oxidation of anthracene and also confirming the catalytic behaviour of the modified electrode. A calibration plot for the PANI|WO₃|GR sensor anthracene is shown in **Figure 95**, with a linear relationship between the anodic current and anthracene concentrations attained over the range of 1.0×10^{-3} to 0.01 nM (1.0 pM to 10.0 pM) and a correlation coefficient of 0.9953. The limit of detection (LOD) which was determined by spiking of different concentrations of anthracene into the cell containing 5mL solution of 1 M HCl, response in the anodic peak current was monitored at every addition of the analyte. Subsequently, the limit of detection was calculated and determined as previously discussed in chapter 3, to be 0.136 pM (1.36×10^{-4} nM). This established that the modified electrode have a good electroactive activity towards the degradation of anthracene.



The square wave voltammograms of the response is shown in **Figure 96**. There is increase in the anodic peak current at every addition of concentrations of anthracene. **Figure 97** showed the square wave voltammograms at lower concentration of anthracene and the calibration plot at lower concentrations shown in **Figure 98**.

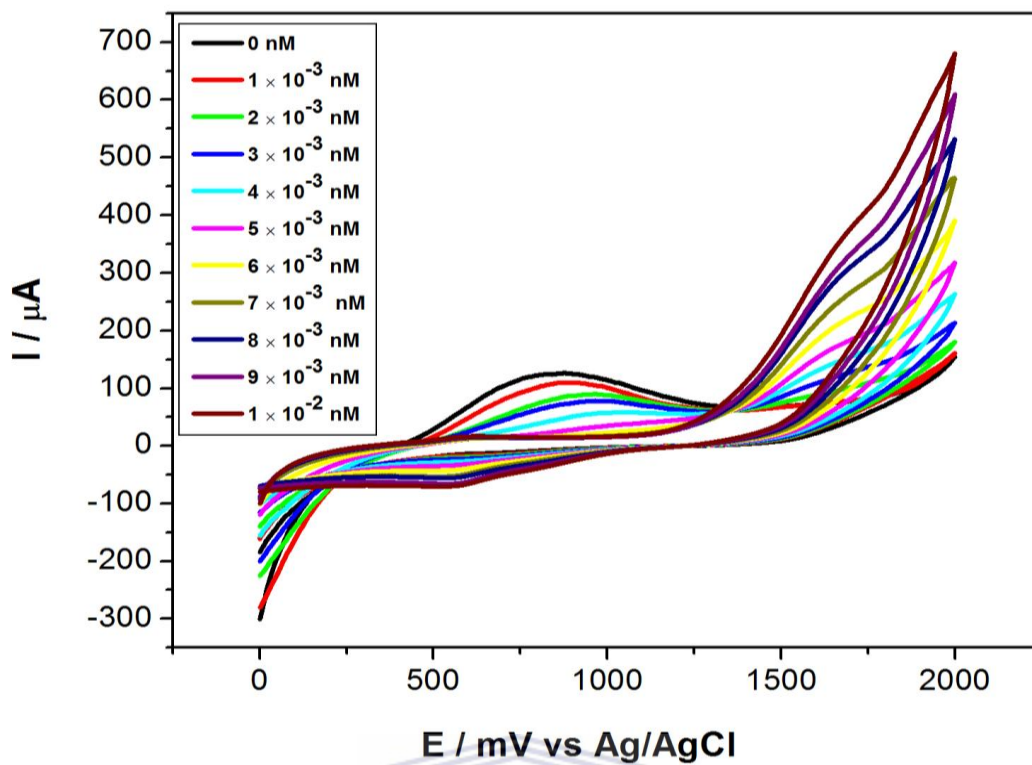


Figure 94. Cyclic voltammograms of the PANI|WO₃|GR|GCE in 1 M HCl in the presence of different concentrations of anthracene at scan rate of 30 mV s⁻¹ and potential window of +0 to +2000 mV.

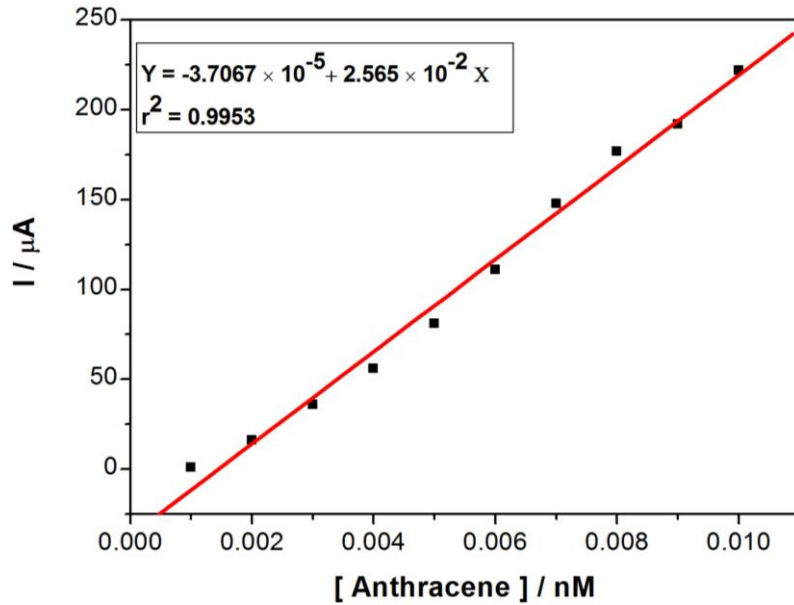


Figure 95. Calibration plot for PANI|WO₃|GR|GCE anthracene sensor versus different concentrations of anthracene.

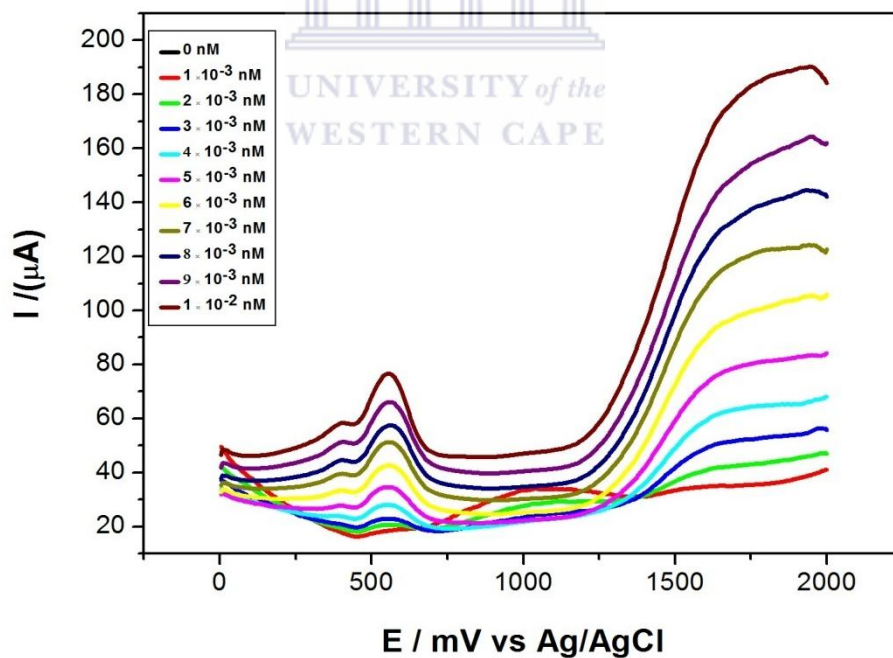


Figure 96. Square wave voltammograms of the PANI|WO₃|GR|GCE in 1 M HCl at every addition of concentrations of anthracene at scan rate of 30 mV s⁻¹ and potential window of +0 to +2000 mV.

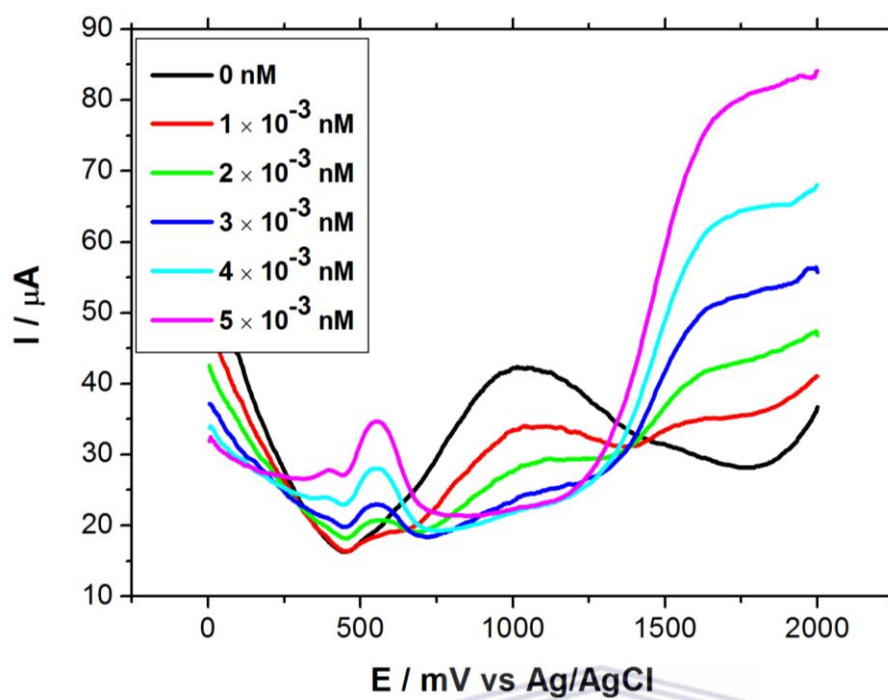
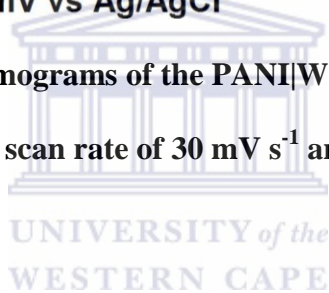


Figure 97. Square wave voltammograms of the PANI|WO₃|GR|GCE in 1 M HCl at lower concentrations of anthracene at scan rate of 30 mV s⁻¹ and potential window of +0 to +2000 mV.



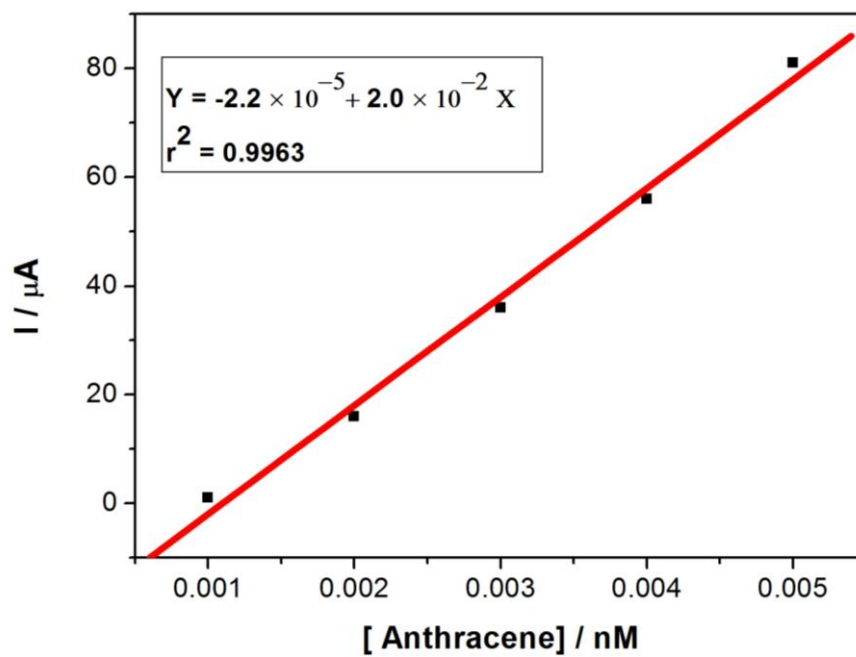
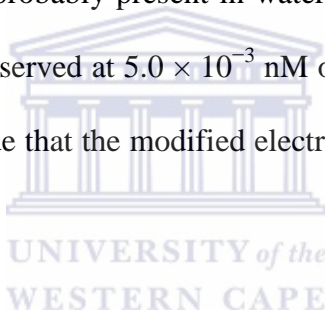


Figure 98. Calibration plot for PANI|WO₃|GR|GCE anthracene sensor at lower concentrations.



6.6.4. Reproducibility, stability and interference studies

Reproducibility studies of the PANI|WO₃|GR nanocomposite modified electrode also investigated in the presence of 5.0×10^{-3} nM of anthracene in 1 M HCl. The relative standard deviation of the monitored modified electrode in the anthracene solution gave 5.8 % from 6 successive measurements ($n = 6$) confirming that the result is reproducibility. The storage stability of the modified electrode was also examined with 5.0×10^{-3} nM anthracene and the oxidation current was been monitored after 3 days for 2 weeks using CV. About 17.72% decrease was observed in the peak current and was able to retain 82.28% of anthracene initial sensitivity at 4 °C. Further investigation was made to check for possible interferences using some inorganic ions which may probably present in water samples. The following ion: Mn²⁺, Cl⁻, SO₄²⁻ and NO₃⁻ were not observed at 5.0×10^{-3} nM of the anthracene concentration. The validated results can then conclude that the modified electrode has stability and reproducibility for anthracene.



6.6.5. Electrocatalytic oxidation of pyrene (PYR)

The response of the PANI|WO₃|GR|GCE sensor was also investigated on pyrene. The PANI|WO₃|GR| GCE sensor observed in the presence and absence of 5.0×10^{-3} nM pyrene is shown in **Figure 99**. Analysis took place in 1 M HCl and at scan rate of 30 mV s^{-1} and window potential of + 0 mV to + 2000 mV. The cyclic voltammograms revealed the catalytic property of the nanocomposite exhibited in the presence of pyrene, revealing high intensity in anodic peak current at addition of pyrene which indicated that oxidation of pyrene has taken place.

The response of the different electrodes in the presence of 5.0×10^{-3} nM pyrene at 30 mV s^{-1} in 1 M HCl is shown in **Figure 100**, and revealing more enhancements in the anodic peak for PANI|WO₃|GR|GCE due to its catalytic property compared to PANI|WO₃|GCE and PANI|GCE.

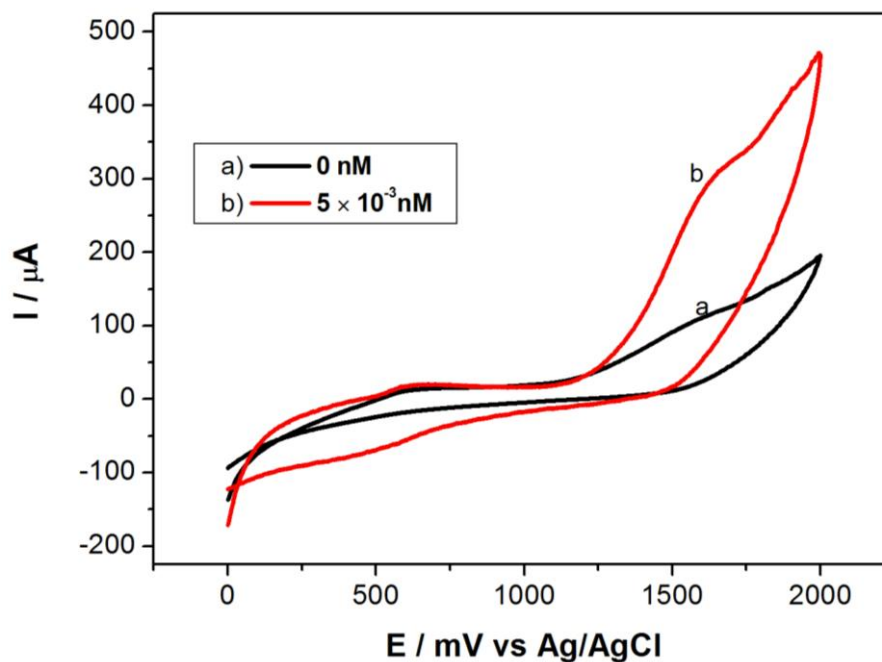


Figure 99. Cyclic voltammograms of PANI|WO₃|GR|GCE in 1 M HCl before (a) and after the addition of 5.0 × 10⁻³ nM pyrene (b).

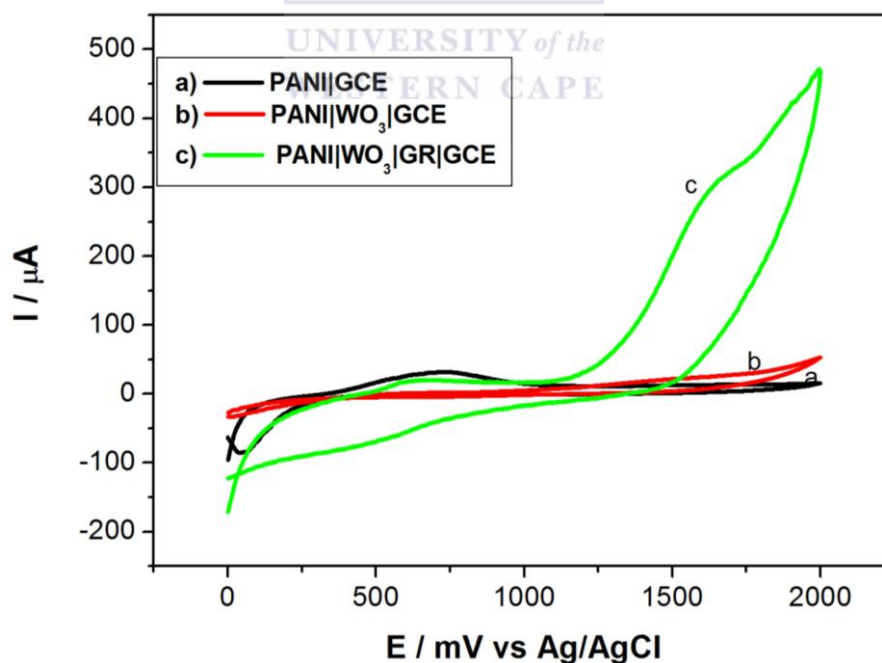


Figure 100. Cyclic Voltammograms of 5.0 × 10⁻³ nM of pyrene at PANI|GCE (a), PANI|WO₃|GCE (b) and PANI|WO₃|GR|GCE (c) in 1 M HCl at a scan rate of 30 mV s⁻¹ and potential window of +0 to +2000 mV.

6.6.5.1. Effect of scan rate

The effect of scan rate on the response of 5.0×10^{-3} nM pyrene at PANI|WO₃|GR modified electrode was also investigated in 1 M HCl. It showed there is an increase in anodic peak current as the scan rate increases. **Figure 101** showed the cyclic voltammograms of PANI|WO₃|GR|GCE upon the addition of 5.0×10^{-3} nM pyrene at different scan rate. In **Figure 102**, the anodic peak current of pyrene increases linearly with the square root of scan rate ($v^{1/2}$) over the range of 10 to 120 mV s⁻¹ with a linear regression of $I_{p,a} = -1.314 \times 10^{-4} + 8.854 \times 10^{-5} \times v^{1/2}$ (mV s⁻¹)^{1/2} and a correlation coefficient of 0.992. Also observed is the oxidation peak potential shifting more positive. This indicated that electrochemistry of the process was limited by rate of diffusion of anthracene from the solution to the surface of the electrode and the peak current is diffusion controlled.

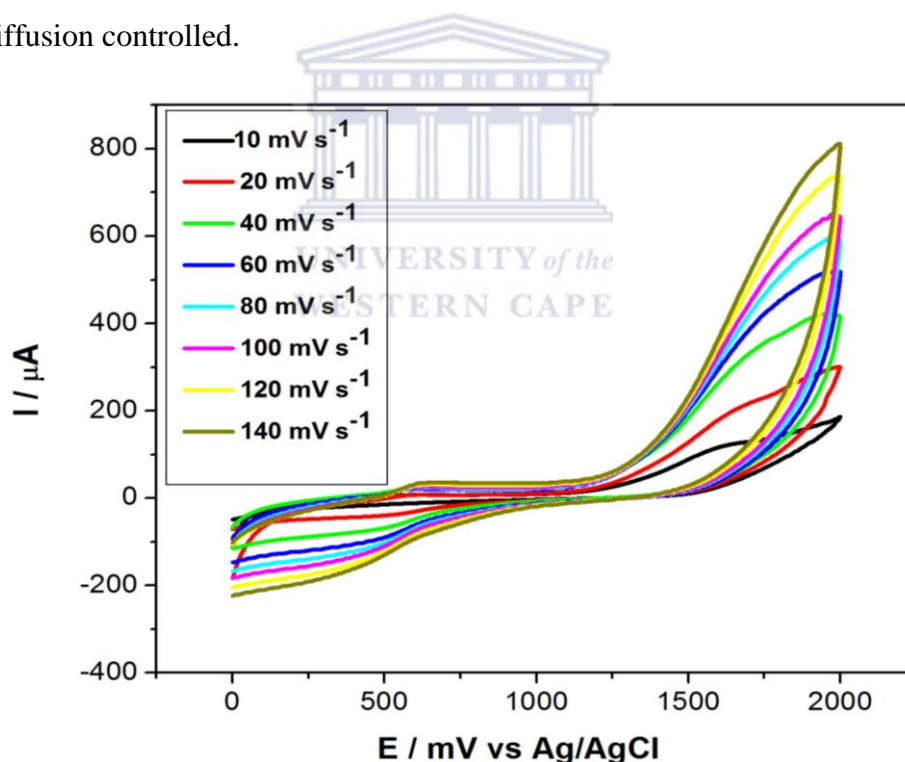


Figure 101. Scan rate dependent cyclic voltammograms of PANI|WO₃|GR|GCE sensor in 1 M HCl containing 5.0×10^{-3} nM pyrene.

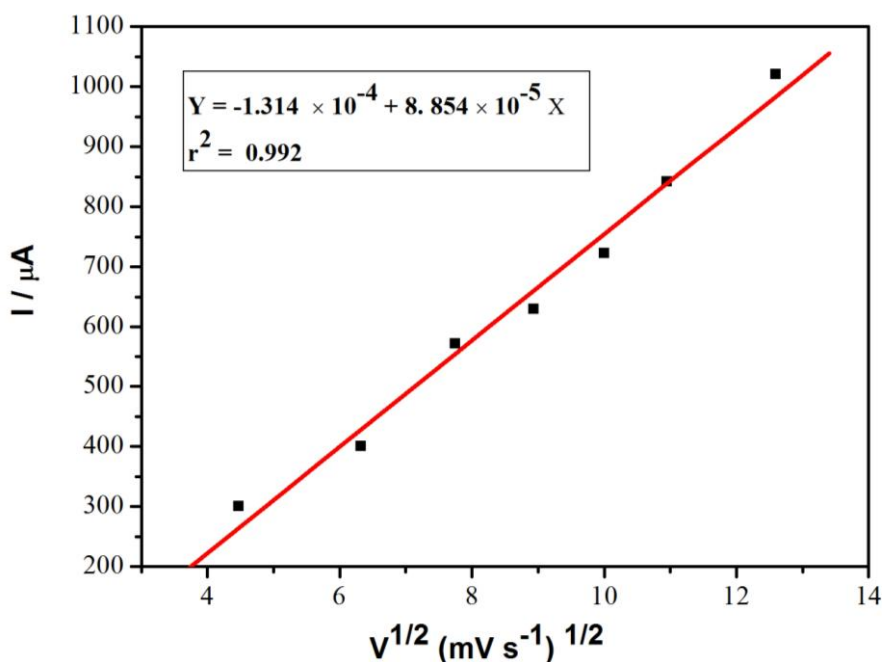


Figure 102. A plot of the scan rate dependence of its anodic peak currents.

6.7.5.2. Cyclic voltammetry response of different concentrations of pyrene.

The cyclic voltammetric response of electrocatalytic oxidation of pyrene at different concentrations in 1 M HCl is shown in **Figure 103**. An increase in the anodic peak current occurs at every addition of pyrene. A calibration plot for the PANI|WO₃|GR sensor pyrene is shown in **Figure 104** with a linear relationship between the anodic current and pyrene concentration attained over the range of 1.0×10^3 to 0.01 nM and a correlation coefficient of 0.9959. The limit of detection (LOD) was determined to be 0.132 pM (1.32×10^{-4} nM).

Square wave voltammograms of the PANI|WO₃|GR sensor pyrene was also observed to show an increase in anodic peak current with different pyrene concentration. **Figure 105** and **Figure 106** showed the square wave voltammograms at every concentrations of pyrene and at lower concentrations, respectively. **Figure 107** showed the calibration plot at lower concentrations of pyrene.

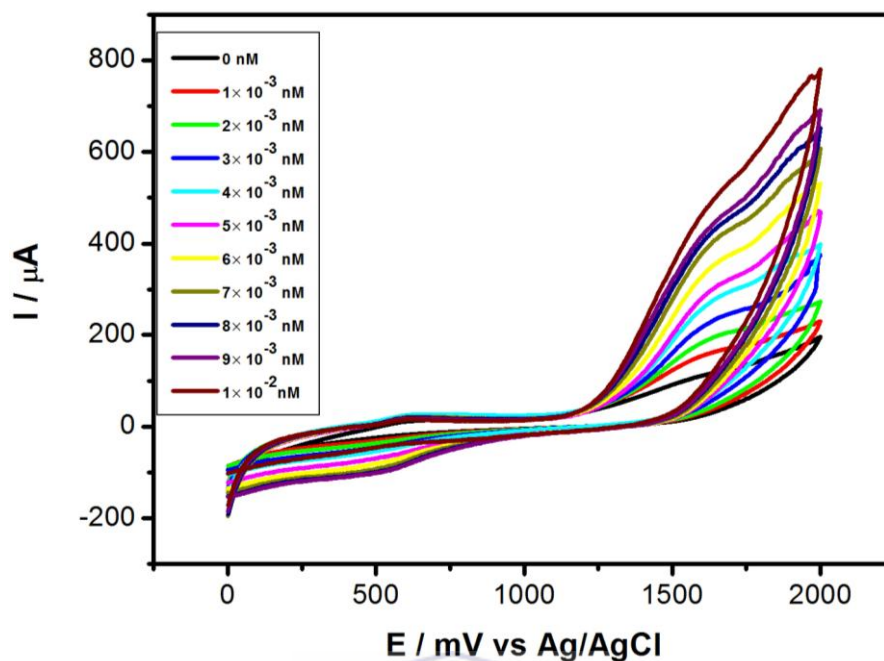


Figure 103. Cyclic voltammograms of the PANI|WO₃|GR|GCE in 1 M HCl at increasing concentrations of pyrene at scan rate of 30 mV s⁻¹.

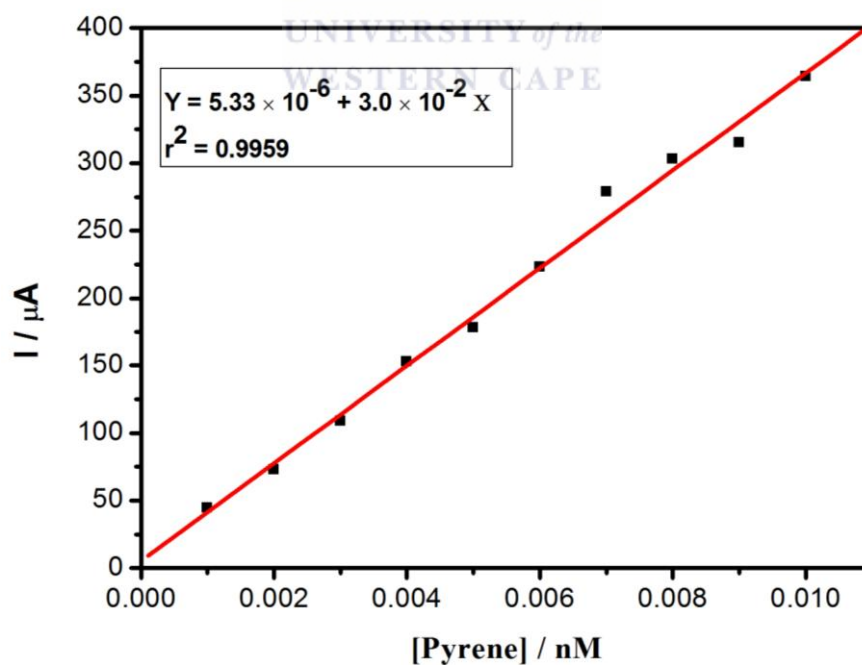


Figure 104. Calibration plot for PANI|WO₃|GR|GCE pyrene sensor at different concentrations.

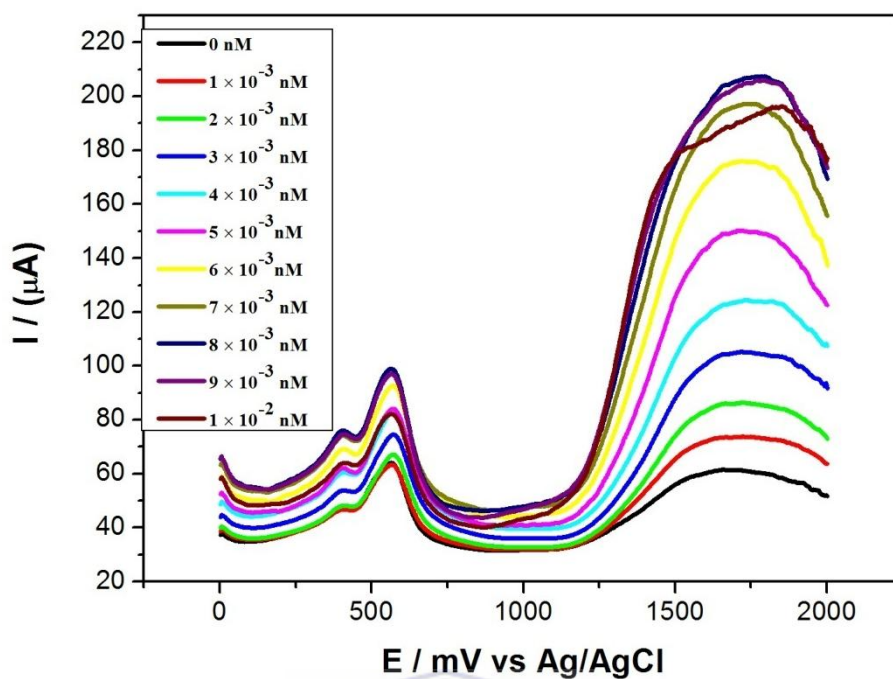
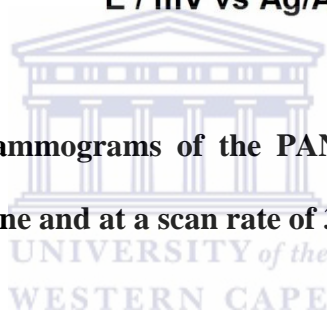


Figure 105. Square wave voltammograms of the PANI|WO₃|GR|GCE in 1 M HCl at different concentrations of pyrene and at a scan rate of 30 mV s⁻¹.



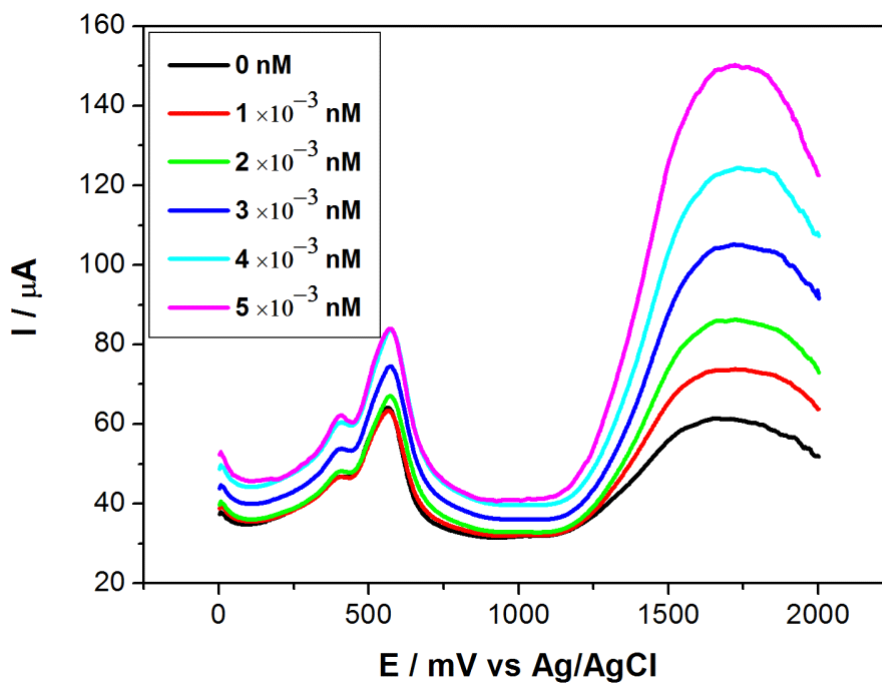


Figure 106. Square wave voltammograms of the PANI|WO₃|GR|GCE in 1 M HCl at lower concentrations of pyrene at scan rate of 30 mV s⁻¹.

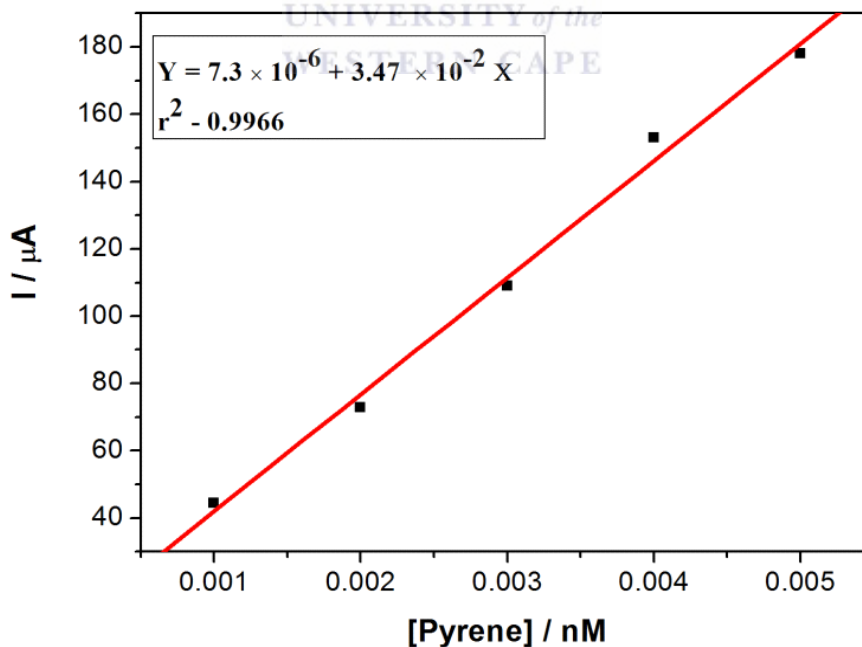
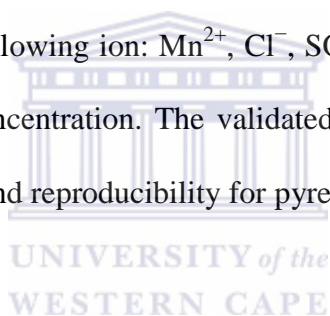


Figure 107. Calibration plot at lower concentrations of pyrene.

6.6.6. Reproducibility, stability and interference studies.

Reproducibility of the PANI|WO₃|GR modified electrode was investigated towards the Pyrene oxidation in the presence of 5.0×10^{-3} nM pyrene in 1 M HCl solution. CV analysis were repeatedly performed and monitored in a solution of 1 M HCl containing 5.0×10^{-3} nM pyrene. The sensitivity remained the same with a relative standard deviation of 5.5 % for 6 successive measurement (n = 6) on the fabricated electrode, indicating its reproducibility. The storage stability of the modified electrode was also examined with 5.0×10^{-3} nM pyrene and the oxidation current was been monitored after 3 days for 2 weeks using CV during which the sensor was able to retain 82.79% of its initial sensitivity at 4 °C. Further investigation was made to check for possible interferences using some inorganic ions which may probably present in water samples. The following ion: Mn²⁺, Cl⁻, SO₄²⁻ and NO₃⁻ were not observed at 5.0×10^{-3} nM of the pyrene concentration. The validated results can then conclude that the modified electrode has stability and reproducibility for pyrene.



CHAPTER SEVEN

CONCLUSION AND RECOMMENDATION

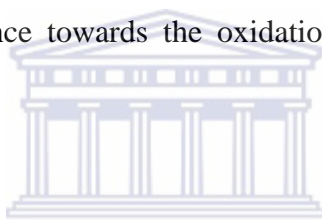
7.1. Conclusion

The aims of the thesis towards the development of an electrochemical sensor for the detection and quantification of polyaromatic hydrocarbons have been successfully achieved. The novel sensor has been based on conducting polyaniline doped with tungsten oxide and graphene nanocomposite, synthesised using electrodeposition method and evaluated. The motivation and objective of this work has however been outlined in chapter one.

Chapter four of the study discussed the chemical preparation and characterisation of graphite oxide and graphene which was confirmed through the characterisation techniques. A thin sheet of graphene with a thickness of 1.4 nm was identified by AFM, and used for subsequent experiments.

Furthermore, a discussion on the preparation, characterisation and catalytic properties of graphene-polyaniline modified glassy carbon electrode, prepared chemically, using in situ polymerisation method has been outlined in chapter five. The modified electrode revealed its catalytic properties for the first time, towards the oxidation of anthracene, in acetonitrile, as the working electrolyte. The dynamic linear range of the anodic peak and anthracene concentration based on the SWV measurement at lower concentration was over the range of 2.0×10^{-5} to 1.0×10^{-3} M and a detection limit of 4.39×10^{-7} M was obtained.

The conducting polyaniline-tungsten oxide-graphene (PANI|WO₃|GR) nanocomposite, as a novel sensor platform has been developed for the first time in this study and discussed in chapter six. The morphology, spectroscopic and electrochemical characterisation of the nanocomposite materials were studied using a variety of characterisation techniques such as SEM, TEM, FT-IR, AFM, RAMAN, UV-vis spectroscopy and EIS including cyclic and square wave voltammetry techniques. The characterisation techniques confirmed the successful preparation of the materials and nanocomposites. The electrochemical measurement studied in aqueous acid revealed the electrochemical properties of the prepared nanocomposites. A more enhanced and well defined redox peaks can be observed for PANI|WO₃|GR|GCE compared to PANI|WO₃|GCE and PANI|GCE. The prepared PANI|WO₃|GR sensor showed a profound and highly electrocatalytic performance towards the oxidation of phenanthrene, anthracene and pyrene.



Application of the sensor in aqueous solution on the detection of phenanthrene gave a dynamic linear range and detection limit of 1.0 to 6.0 pM and 0.123 pM, respectively. On anthracene, a dynamic linear range of 1.0 to 10.0 pM was attained with a limit of detection (LOD) of 0.136 pM, while for pyrene; the dynamic linear range was attained over the range of 1.0 to 10.0 pM. The limit of detection (LOD) was determined to be 0.132 pM (1.32×10^{-4} nM). The prepared PANI|WO₃|GR sensor has exhibited an excellent sensitivity, long term storage stability and good reproducibility as observed from the Table below, showing obtained values for the different polymer systems. The results indicated that the sensor catalyst has huge benefit for the electro-oxidation of PAHs and has shown an excellent sensitivity to the detection of the various PAHs.

Table 10. The relative sensitivities, LOD, low concentration linear range obtainable for the different polymer systems.

PAHs	DLR (pM)	RSD (%)	Stability (%)	LOD (pM)
Phenanthrene	1.0 to 6.0	5.1	84.31	0.123
Pyrene	1.0 to 10.0	5.5	82.28	0.132
Anthracene	1.0 to 10.0	5.8	82.78	0.136

The successful constructed platform has displayed a well and excellent reproducibility in the cyclic measurements and in sensitivity to PAHs, providing a lower detection limits for PAHs. The possible reason can be attributed to the combination of the advantages of the metal oxide and graphene which has provided a highly efficient catalytic property on the nanocomposite, improving the sensitivity and determination of PAHs at lower detection limit. This work has provided a platform for developing a highly sensitive and selective electrochemical sensor for PAHs and has opened up a promising route to an environmentally friendly method for the degradation of PAHs with minimal energy requirement.

7.2. Future work and Recommendation

The following further investigations are recommended as a future work to the research activities.

The proposed method of preparation through electrodeposition has proven to be efficient. However, chemical method of preparation of the nanocomposite is recommended and which is actually one of the ultimate objectives of the study.

The developed sensor system based on tungsten oxide and polyaniline in this thesis represent only a sample of the respective groups of semiconductors. Further study on metal oxide and derivatives of polyaniline or other conducting polymers should be explored for their potential use as electrocatalytic sensor devices.

The development of the sensor devices using gold, platinum and carbon disc or printed electrodes should be explored in other to produce more specific and sensitive sensor devices. Also, more electrocatalysis of other persistent organic pollutants can be studied on this graphenated polyaniline nanocomposite.

References

1. Ashbolt, N. J. Microbial contamination of drinking water and disease outcomes in developing regions. *Toxicology* **2004**, 198, 229-238.
2. Gambaro, A.; Manodori, L.; Moret, I.; Capodaglio, G.; Cescon, P. Determination of polychlorobiphenyls and polycyclic aromatic hydrocarbons in the atmospheric aerosol of the Venice Lagoon. *Analytical and bioanalytical chemistry* **2004**, 378, 1806-1814.
3. Manjavacas, A.; Marchesin, F.; Thongrattanasiri, S.; Koval, P.; Nordlander, P.; Sánchez-Portal, D.; García de Abajo, F. J. Tunable Molecular Plasmons in Polycyclic Aromatic Hydrocarbons. *ACS Nano* **2013**, 7, 3635-3643.
4. Wenzl, T.; Simon, R.; Anklam, E.; Kleiner, J. Analytical methods for polycyclic aromatic hydrocarbons (PAHs) in food and the environment needed for new food legislation in the European Union. *TrAC Trends in Analytical Chemistry* **2006**, 25, 716-725.
5. Xu, J.; Yu, Y.; Wang, P.; Guo, W.; Dai, S.; Sun, H. Polycyclic aromatic hydrocarbons in the surface sediments from Yellow River, China. *Chemosphere* **2007**, 67, 1408-1414.
6. Plaza-Bolaños, P.; Frenich, A. G.; Vidal, J. L. M. Polycyclic aromatic hydrocarbons in food and beverages. Analytical methods and trends. *Journal of Chromatography A* **2010**, 1217, 6303-6326.
7. Jiao, L.; Zheng, G. J.; Minh, T. B.; Richardson, B.; Chen, L.; Zhang, Y.; Yeung, L. W.; Lam, J. C.; Yang, X.; Lam, P. K. Persistent toxic substances in remote lake and coastal sediments from Svalbard, Norwegian Arctic: levels, sources and fluxes. *Environmental Pollution* **2009**, 157, 1342-1351.

8. Flowers, L.; Rieth, S.; Cogliano, V.; Foureman, G.; Hertzberg, R.; Hofmann, E.; Murphy, D.; Nesnow, S.; Schoeny, R. Health assessment of polycyclic aromatic hydrocarbon mixtures: current practices and future directions. *Polycyclic Aromatic Compounds* **2002**, 22, 811-821.
9. Environmental Protection Agency. (EPA/623/R/002S),. USA, **2002**.
10. Busetti, F.; Heitz, A.; Cuomo, M.; Badoer, S.; Traverso, P. Determination of sixteen polycyclic aromatic hydrocarbons in aqueous and solid samples from an Italian wastewater treatment plant. *Journal of Chromatography A* **2006**, 1102, 104-115.
11. Gao, Y.; Ling, W.; Wong, M. H. Plant-accelerated dissipation of phenanthrene and pyrene from water in the presence of a nonionic-surfactant. *Chemosphere* **2006**, 63, 1560-1567.
12. Martínez-Huitle, C. A.; Ferro, S. Electrochemical oxidation of organic pollutants for the wastewater treatment: direct and indirect processes. *Chemical Society Reviews* **2006**, 35, 1324-1340.
13. Jara, C. C.; Martínez-Huitle, C. A.; Torres-Palma, R. A. Distribution of nitrogen ions generated in the electrochemical oxidation of nitrogen containing organic compounds. *Portugaliae Electrochimica Acta* **2009**, 27, 203-213.
14. Andrade, L. S.; Ruotolo, L. A. M.; Rocha-Filho, R. C.; Bocchi, N.; Biaggio, S. R.; Iniesta, J.; García-García, V.; Montiel, V. On the performance of Fe and Fe, F doped Ti-Pt/PbO₂ electrodes in the electrooxidation of the Blue Reactive 19 dye in simulated textile wastewater. *Chemosphere* **2007**, 66, 2035-2043.
15. Aquino, J. M.; Pereira, G. F.; Rocha-Filho, R. C.; Bocchi, N.; Biaggio, S. R. Electrochemical degradation of a real textile effluent using boron-doped diamond or β-PbO₂ as anode. *Journal of hazardous materials* **2011**, 192, 1275-1282.

16. Iwuoha, E. I.; Saenz de Villaverde, D.; Garcia, N. P.; Smyth, M. R.; Pingarron, J. M. Reactivities of organic phase biosensors. 2. The amperometric behaviour of horseradish peroxidase immobilised on a platinum electrode modified with an electrosynthetic polyaniline film. *Biosensors and Bioelectronics* **1997**, *12*, 749-761.
17. Janáky, C.; Visy, C. Conducting polymer-based hybrid assemblies for electrochemical sensing: a materials science perspective. *Analytical and bioanalytical chemistry* **2013**, 1-23.
18. Zhang, X.; Zhao, D.; Feng, L.; Jia, L.; Wang, S. Electrochemical sensor for procaine based on a glassy carbon electrode modified with poly-amidosulfonic acid and multi-walled carbon nanotubes. *Microchimica Acta* **2010**, *169*, 153-159.
19. Akinyeye, R.; Michira, I.; Sekota, M.; Al-Ahmed, A.; Baker, P.; Iwuoha, E. Electrochemical interrogation and sensor applications of nanostructured polypyrroles. *Electroanalysis* **2006**, *18*, 2441-2450.
20. Akinyeye, R. O.; Michira, I.; Sekota, M.; Ahmed, A. A.; Tito, D.; Baker, P. G. L.; Brett, C. M. A.; Kalaji, M.; Iwuoha, E. Electrochemical synthesis and characterization of 1, 2-naphthaquinone-4-Sulfonic acid doped polypyrrole. *Electroanalysis* **2007**, *19*, 303-309.
21. Li, Q.; Kim, N. H.; Yoo, G.-H.; Lee, J. H. Positive temperature coefficient characteristic and structure of graphite nanofibers reinforced high density polyethylene/carbon black nanocomposites. *Composites Part B: Engineering* **2009**, *40*, 218-224.
22. Jeevananda, T.; Kim, N. H.; Lee, J. H.; Basavarajaiah, S.; Urs, D.; Ranganathaiah, C. Investigation of multi-walled carbon nanotube-reinforced high-density polyethylene/carbon black nanocomposites using electrical, DSC and positron lifetime spectroscopy techniques. *Polymer International* **2009**, *58*, 775-780.

23. Renukappa, N. M.; Samuel, R. D. S.; Rajan, J. S.; Lee, J. H. Dielectric properties of carbon black: SBR composites. *Journal of Materials Science: Materials in Electronics* **2009**, 20, 648-656.
24. Wang, G.; Zhuo, S.; Xing, W. Graphene/polyaniline nanocomposite as counter electrode of dye-sensitized solar cells. *Materials Letters* **2012**, 69, 27-29.
25. Geim, A. K.; MacDonald, A. H. Graphene: Exploring carbon flatland. *Physics Today* **2007**, 60, 35.
26. Si, Y.; Samulski, E. T. Synthesis of water soluble graphene. *Nano Letters* **2008**, 8, 1679-1682.
27. Dreyer, D. R.; Park, S.; Bielawski, C. W.; Ruoff, R. S. The chemistry of graphene oxide. *Chemical Society Reviews* **2010**, 39, 228-240.
28. Wang, G.; Shen, X.; Wang, B.; Yao, J.; Park, J. Synthesis and characterisation of hydrophilic and organophilic graphene nanosheets. *Carbon* **2009**, 47, 1359-1364.
29. Wang, G.; Yang, J.; Park, J.; Gou, X.; Wang, B.; Liu, H.; Yao, J. Facile synthesis and characterization of graphene nanosheets. *The Journal of Physical Chemistry C* **2008**, 112, 8192-8195.
30. Li, X.; Wang, X.; Zhang, L.; Lee, S.; Dai, H. Chemically derived, ultrasmooth graphene nanoribbon semiconductors. *Science* **2008**, 319, 1229-1232.
31. Blake, P.; Brimicombe, P. D.; Nair, R. R.; Booth, T. J.; Jiang, D.; Schedin, F.; Ponomarenko, L. A.; Morozov, S. V.; Gleeson, H. F.; Hill, E. W. Graphene-based liquid crystal device. *Nano Letters* **2008**, 8, 1704-1708.
32. Allen, M. J.; Tung, V. C.; Kaner, R. B. Honeycomb carbon: a review of graphene. *Chemical Reviews* **2009**, 110, 132-145.
33. WHO. Guidelines of drinking-water Quality. *Geneva* **2008**, (3rd edition).

34. USEPA. Guidelines for carcinogen risk assessment. *Washington DC: Risk Assessment Forum EPA/630/P-03/001F*. **2008**.
35. Olivella, M. A. Isolation and analysis of polycyclic aromatic hydrocarbons from natural water using accelerated solvent extraction followed by gas chromatography–mass spectrometry. *Talanta* **2006**, 69, 267-275.
36. Flotron, V.; Houessou, J.; Bosio, A.; Delteil, C.; Bermond, A.; Camel, V. Rapid determination of polycyclic aromatic hydrocarbons in sewage sludges using microwave-assisted solvent extraction: comparison with other extraction methods. *Journal of Chromatography A* **2003**, 999, 175-184.
37. Cai, S.-S.; Syage, J. A.; Hanold, K. A.; Balogh, M. P. Ultra performance liquid chromatography– atmospheric pressure photoionization-tandem mass spectrometry for high-sensitivity and high-throughput analysis of US Environmental Protection Agency 16 priority pollutants polynuclear aromatic hydrocarbons. *Analytical Chemistry* **2009**, 81, 2123-2128.
38. Wang, W.-D.; Huang, Y.-M.; Shu, W.-Q.; Cao, J. Multiwalled carbon nanotubes as adsorbents of solid-phase extraction for determination of polycyclic aromatic hydrocarbons in environmental waters coupled with high-performance liquid chromatography. *Journal of Chromatography A* **2007**, 1173, 27-36.
39. Varlet, V.; Serot, T.; Monteau, F.; Bizec, B. L.; Prost, C. Determination of PAH profiles by GC–MS/MS in salmon processed by four cold-smoking techniques. *Food additives and contaminants* **2007**, 24, 744-757.
40. Corcoran, E.; Nellesmann, C.; Baker, E.; Bos, R.; Osborn, D.; Savelli, H. Sick water. *The central role of wastewater management in sustainable development. A rapid response assessment, United Nations Environment Programme. UN-HABITAT, GRID. Arendal* **2010**.

41. Water, U., 'Tackling a global crisis: International Year of Sanitation 2008, *Retrieved September, 3 2008*.
42. Watkins, K. Human Development Report 2006-Beyond scarcity: Power, poverty and the global water crisis **2009**.
43. Vörösmarty, C. J.; McIntyre, P.; Gessner, M. O.; Dudgeon, D.; Prusevich, A.; Green, P.; Glidden, S.; Bunn, S. E.; Sullivan, C. A.; Liermann, C. R. Global threats to human water security and river biodiversity. *Nature* **2010**, 467, 555-561.
44. Chang, I.-S.; Chung, C.-M.; Han, S.-H. Treatment of oily wastewater by ultrafiltration and ozone. *Desalination* **2001**, 133, 225-232.
45. Kim, S. D.; Cho, J.; Kim, I. S.; Vanderford, B. J.; Snyder, S. A. Occurrence and removal of pharmaceuticals and endocrine disruptors in South Korean surface, drinking, and waste waters. *Water Research* **2007**, 41, 1013-1021.
46. Assessment, M. E., Ecosystems and human well-being, Island Press Washington, DC, **2005** (unpublished).
47. Appelgren, B. 'Towards Sustainable Dryland Development in Africa: Integrating Groundwater and Land Management', *The Future of Drylands* (Springer), **2009** 199-208.
48. Pimentel, D.; Pimentel, M., 'Food, energy, and society. Boca Raton, Fla., CRC, London: Taylor & Francis [distributor] **2008**.
49. Fiedler, H. Persistent organic pollutants, Springer, **2003**
50. Gavrilescu, M. Fate of pesticides in the environment and its bioremediation. *Engineering in Life Sciences* **2005**, 5, 497-526.
51. Judson, R.; Richard, A.; Dix, D. J.; Houck, K.; Martin, M.; Kavlock, R.; Dellarco, V.; Henry, T.; Holderman, T.; Sayre, P. The toxicity data landscape for environmental chemicals. *Environmental health perspectives* **2009**, 117, 685.

52. Hagen, P. E.; Walls, M. P. The Stockholm Convention on persistent organic pollutants. *Natural Resources & Environment* **2005**, 19, 49-52.
53. Kelly, B. C.; Ikonou, M. G.; Blair, J. D.; Morin, A. E.; Gobas, F. A. Food web-specific biomagnification of persistent organic pollutants. *Science* **2007**, 317, 236-239.
54. Kelly, B. C.; Gobas, F. A. Bioaccumulation of persistent organic pollutants in lichen-caribou-wolf food chains of Canada's Central and Western Arctic. *Environmental science & technology* **2001**, 35, 325-334.
55. Fu, J.; Mai, B.; Sheng, G.; Zhang, G.; Wang, X.; Peng, P. a.; Xiao, X.; Ran, R.; Cheng, F.; Peng, X. Persistent organic pollutants in environment of the Pearl River Delta, China: an overview. *Chemosphere* **2003**, 52, 1411-1422.
56. Jacobs, M. N.; Covaci, A.; Schepens, P. Investigation of selected persistent organic pollutants in farmed Atlantic salmon (*Salmo salar*), salmon aquaculture feed, and fish oil components of the feed. *Environmental science & technology* **2002**, 36, 2797-2805.
57. Fiedler, H. National PCDD/PCDF release inventories under the Stockholm convention on persistent organic pollutants. *Chemosphere* **2007**, 67, S96-S108.
58. Novotny, P. Where we live, work, and play: the environmental justice movement and the struggle for a new environmentalism, Greenwood Publishing Group, **2000**
59. Grova. N; Laurent. C; Feidt. C; Rychen. G; Laurent. E; Lichtfouse. E. Gas chromatography-mass spectrometry study of polycyclic aromatic hydrocarbons in grass and milk from urban and rural farms. *Eur. J. Mass. Spectrom.* **2000**, 6, 457-460.
60. Countway, R. E.; Dickhut, R. M.; Canuel, E. A. Polycyclic aromatic hydrocarbon (PAH) distributions and associations with organic matter in surface waters of the York River, VA Estuary. *Organic Geochemistry* **2003**, 34, 209-224.
61. Dickhut, R. M.; Canuel, E. A.; Gustafson, K. E.; Liu, K.; Arzayus, K. M.; Walker, S. E.; Edgecombe, G.; Gaylor, M. O.; MacDonald, E. H. Automotive sources of

- carcinogenic polycyclic aromatic hydrocarbons associated with particulate matter in the Chesapeake Bay region. *Environmental science & technology* **2000**, 34, 4635-4640.
62. Lundstedt, S.; Haglund, P.; Öberg, L. Degradation and formation of polycyclic aromatic compounds during bioslurry treatment of an aged gasworks soil. *Environmental toxicology and chemistry* **2003**, 22, 1413-1420.
63. Evenset, A.; Christensen, G. N.; Carroll, J.; Zaborska, A.; Berger, U.; Herzke, D.; Gregor, D. Historical trends in persistent organic pollutants and metals recorded in sediment from Lake Ellasjoen, Bjornoya, . *Norwegian Arctic. Environ. Pollut.* **2007.**, 146, 196-205.
64. Djomo, J. E.; Dauta, A.; Ferrier, V.; Narbonne, J. F.; Monkiedje, A.; Njine, T.; Garrigues, P. Toxic effects of some major polyaromatic hydrocarbons found in crude oil and aquatic sediments on *scenedesmus subspicatus*. *Water Research* **2004**, 38, 1817-1821.
65. Geffard, O.; Geffard, A.; His, E.; Budzinski, H. Assessment of the bioavailability and toxicity of sediment-associated polycyclic aromatic hydrocarbons and heavy metals applied to *crassostrea gigas* embryos and larvae. *Marine Pollution Bulletin* **2003**, 46, 481-490.
66. Pagnout, C.; Rast, C.; Veber, A.-M.; Poupin, P.; Féraud, J.-F. Ecotoxicological assessment of PAHs and their dead-end metabolites after degradation by *mycobacterium* sp. strain SNP11. *Ecotoxicology and environmental safety* **2006**, 65, 151-158.
67. EPA, U. S. Environmental Protection Agency 2011. *Report No. EPA 430-R-11* **2011**, 5.
68. Tolosa, I.; de Mora, S.; Sheikholeslami, M. R.; Villeneuve, J.-P.; Bartocci, J.; Cattini, C. Aliphatic and aromatic hydrocarbons in coastal caspian sea sediments. *Marine Pollution Bulletin* **2004**, 48, 44-60.

69. Quantin, C.; Joner, E.; Portal, J.; Berthelin, J. PAH dissipation in a contaminated river sediment under oxic and anoxic conditions. *Environmental Pollution* **2005**, 134, 315-322.
70. Wang, X.-C.; Zhang, Y.-X.; Chen, R. F. Distribution and partitioning of polycyclic aromatic hydrocarbons (PAHs) in different size fractions in sediments from Boston Harbor, United States. *Marine Pollution Bulletin* **2001**, 42, 1139-1149.
71. Bixian, M.; Jiamo, F.; Gan, Z.; Zheng, L.; Yushun, M.; Guoying, S.; Xingmin, W. Polycyclic aromatic hydrocarbons in sediments from the Pearl river and estuary, China: spatial and temporal distribution and sources. *Applied Geochemistry* **2001**, 16, 1429-1445.
72. Yunker, M. B.; Macdonald, R. W. Alkane and PAH depositional history, sources and fluxes in sediments from the Fraser river basin and strait of Georgia, Canada. *Organic Geochemistry* **2003**, 34, 1429-1454.
73. Guo, W.; He, M.; Yang, Z.; Lin, C.; Quan, X.; Wang, H. Distribution of polycyclic aromatic hydrocarbons in water, suspended particulate matter and sediment from Daliao River watershed, China. *Chemosphere* **2007**, 68, 93-104.
74. Law, R. J.; Kelly, C.; Baker, K.; Jones, J.; McIntosh, A. D.; Moffat, C. F. Toxic equivalency factors for PAH and their applicability in shellfish pollution monitoring studies. *Journal of Environmental Monitoring* **2002**, 4, 383-388.
75. Johnsen, A. R.; Wick, L. Y.; Harms, H. Principles of microbial PAH-degradation in soil. *Environmental Pollution* **2005**, 133, 71-84.
76. Ntainjua, E.; Taylor, S. H. The catalytic total oxidation of Polycyclic Aromatic Hydrocarbons. *Topics in Catalysis* **2009**, 52, 528-541.
77. Srogi, K. Monitoring of environmental exposure to polycyclic aromatic hydrocarbons: a review. *Environmental Chemistry Letters* **2007**, 5, 169-195.

78. Yassaa, N.; Youcef Meklati, B.; Cecinato, A.; Marino, F. Particulate n-alkanes, n-alkanoic acids and polycyclic aromatic hydrocarbons in the atmosphere of Algiers City Area. *Atmospheric Environment* **2001**, 35, 1843-1851.
79. Koganti, A.; Singh, R.; Rozett, K.; Modi, N.; Goldstein, L. S.; Roy, T. A.; Zhang, F. J.; Harvey, R. G.; Weyand, E. H. 7H-benzo [c] fluorene: a major DNA adduct-forming component of coal tar. *Carcinogenesis* **2000**, 21, 1601-1609.
80. Koganti, A.; Singh, R.; Ma, B.-L.; Weyand, E. H. Comparative analysis of PAH: DNA adducts formed in lung of mice exposed to neat coal tar and soils contaminated with coal tar. *Environmental science & technology* **2001**, 35, 2704-2709.
81. Xie, M.; Wang, G.; Hu, S.; Han, Q.; Xu, Y.; Gao, Z. Aliphatic alkanes and polycyclic aromatic hydrocarbons in atmospheric PM 10 aerosols from Baoji, China: Implications for coal burning. *Atmospheric Research* **2009**, 93, 840-848.
82. Halek, F.; Nabi, G.; Kavousi, A. Polycyclic aromatic hydrocarbons study and toxic equivalency factor (TEFs) in Tehran, IRAN. *Environmental monitoring and assessment* **2008**, 143, 303-311.
83. Yajuan. Y; Huaicheng. G; Yong. L; Kai. H; Zhen. W; Xinye. Z. Mixed uncertainty analysis of polycyclic aromatic hydrocarbon inhalation and risk assessment in ambient air of Beijing. *Journal of Environmental Sciences* **2008**, 20, 505–512.
84. Smith, L. E.; Denissenko, M. F.; Bennett, W. P.; Li, H.; Amin, S.; Tang, M.-s.; Pfeifer, G. P. Targeting of lung cancer mutational hotspots by polycyclic aromatic hydrocarbons. *Journal of the National Cancer Institute* **2000**, 92, 803-811.
85. Z'graggen, K.; Warshaw, A. L.; Werner, J.; Graeme-Cook, F.; Jimenez, R. E.; Fernández-del Castillo, C. Promoting effect of a high-fat/high-protein diet in DMBA-induced ductal pancreatic cancer in rats. *Annals of surgery* **2001**, 233, 688.

86. Kizu, R.; Okamura, K.; Toriba, A.; Kakishima, H.; Mizokami, A.; Burnstein, K. L.; Hayakawa, K. A role of aryl hydrocarbon receptor in the antiandrogenic effects of polycyclic aromatic hydrocarbons in LNCaP human prostate carcinoma cells. *Archives of toxicology* **2003**, *77*, 335-343.
87. Wu, M.-T.; Lee, L.-H.; Ho, C.-K.; Wu, S.-C.; Lin, L.-Y.; Cheng, B.-H.; Liu, C.-L.; Yang, C.-Y.; Tsai, H.-T.; Wu, T.-N. Environmental exposure to cooking oil fumes and cervical intraepithelial neoplasm. *Environmental research* **2004**, *94*, 25-32.
88. Lee, C. H.; Yang, S. F.; Peng, C. Y.; Li, R. N.; Chen, Y. C.; Chan, T. F.; Tsai, E. M.; Kuo, F. C.; Huang, J. J.; Tsai, H. T. The precancerous effect of emitted cooking oil fumes on precursor lesions of cervical cancer. *International Journal of Cancer* **2010**, *127*, 932-941.
89. Chen, B.; Xuan, X.; Zhu, L.; Wang, J.; Gao, Y.; Yang, K.; Shen, X.; Lou, B. Distributions of polycyclic aromatic hydrocarbons in surface waters, sediments and soils of Hangzhou City, China. *Water Research* **2004**, *38*, 3558-3568.
90. Guo, W.; He, M.; Yang, Z.; Lin, C.; Quan, X.; Men, B. Distribution, partitioning and sources of polycyclic aromatic hydrocarbons in Daliao River water system in dry season, China. *Journal of hazardous materials* **2009**, *164*, 1379-1385.
91. Lee, B.-C.; Shimizu, Y.; Matsuda, T.; Matsui, S. Characterization of polycyclic aromatic hydrocarbons (PAHs) in different size fractions in deposited road particles (DRPs) from Lake Biwa area, Japan. *Environmental science & technology* **2005**, *39*, 7402-7409.
92. Viñas, L.; Angeles Franco, M.; Antonio Soriano, J.; José González, J.; Pon, J.; Albaigés, J. Sources and distribution of polycyclic aromatic hydrocarbons in sediments from the Spanish northern continental shelf. Assessment of spatial and temporal trends. *Environmental Pollution* **2010**, *158*, 1551-1560.

93. Pal, A.; Gin, K. Y.-H.; Lin, A. Y.-C.; Reinhard, M. Impacts of emerging organic contaminants on freshwater resources: review of recent occurrences, sources, fate and effects. *Science of the total environment* **2010**, 408, 6062-6069.
94. de Mora, S.; Tolosa, I.; Fowler, S. W.; Villeneuve, J.-P.; Cassi, R.; Cattini, C. Distribution of petroleum hydrocarbons and organochlorinated contaminants in marine biota and coastal sediments from the ropme sea area during 2005. *Marine Pollution Bulletin* **2010**, 60, 2323-2349.
95. Kennish, M. J. Environmental threats and environmental future of estuaries. *Environmental conservation* **2002**, 29, 78-107.
96. Van der Oost, R.; Beyer, J.; Vermeulen, N. P. Fish bioaccumulation and biomarkers in environmental risk assessment: a review. *Environmental Toxicology and Pharmacology* **2003**, 13, 57-149.
97. Rose, N. L.; Jones, V. J.; Noon, P. E.; Hodgson, D. A.; Flower, R. J.; Appleby, P. G. Long-range transport of pollutants to the Falkland Islands and Antarctica: evidence from lake sediment fly ash particle records. *Environmental science & technology* **2012**, 46, 9881-9889.
98. Soclo, H.; Garrigues, P.; Ewald, M. Origin of polycyclic aromatic hydrocarbons (PAHs) in coastal marine sediments: case studies in Cotonou (Benin) and Aquitaine (France) areas. *Marine Pollution Bulletin* **2000**, 40, 387-396.
99. Ravindra, K.; Wauters, E.; Tyagi, S. K.; Mor, S.; Van Grieken, R. Assessment of air quality after the implementation of compressed natural gas (CNG) as fuel in public transport in Delhi, India. *Environmental monitoring and assessment* **2006**, 115, 405-417.
100. Poster, D. L.; Schantz, M. M.; Sander, L. C.; Wise, S. A. Analysis of polycyclic aromatic hydrocarbons (PAHs) in environmental samples: a critical review of gas

- chromatographic (GC) methods. *Analytical and bioanalytical chemistry* **2006**, 386, 859-881.
101. Boehm, P.; Loreti, C.; Rosenstein, A.; Rury, P. A guide to polycyclic aromatic hydrocarbons for the non-specialist. *American Petroleum Institute Publication* **2002**, 4717, 36.
102. Dalsøren, S. B.; Endresen, Ø.; Isaksen, I. S.; Gravir, G.; Sjørgård, E. Environmental impacts of the expected increase in sea transportation, with a particular focus on oil and gas scenarios for Norway and northwest Russia. *Journal of Geophysical Research: Atmospheres (1984–2012)* **2007**, 112.
103. Stout, S. A.; Magar, V. S.; Uhler, R. M.; Ickes, J.; Abbott, J.; Brenner, R. Characterization of naturally-occurring and anthropogenic PAHs in urban sediments-wycoff/eagle harbor superfund site. *Environmental Forensics* **2001**, 2, 287-300.
104. Wang, Z.; Fingas, M. F. Development of oil hydrocarbon fingerprinting and identification techniques. *Marine Pollution Bulletin* **2003**, 47, 423-452.
105. Zakaria, M. P.; Takada, H.; Tsutsumi, S.; Ohno, K.; Yamada, J.; Kouno, E.; Kumata, H. Distribution of polycyclic aromatic hydrocarbons (PAHs) in rivers and estuaries in Malaysia: a widespread input of petrogenic PAHs. *Environmental science & technology* **2002**, 36, 1907-1918.
106. Liu, G.; Zhang, G.; Li, X.; Li, J.; Peng, X.; Qi, S. Sedimentary record of polycyclic aromatic hydrocarbons in a sediment core from the Pearl River Estuary, South China. *Marine Pollution Bulletin* **2005**, 51, 912-921.
107. Lima, A. L. C.; Eglinton, T. I.; Reddy, C. M. High-resolution record of pyrogenic polycyclic aromatic hydrocarbon deposition during the 20th century. *Environmental science & technology* **2003**, 37, 53-61.

108. Savinov, V. M.; Savinova, T. N.; Carroll, J.; Matishov, G. G.; Dahle, S.; Næs, K. Polycyclic aromatic hydrocarbons (PAHs) in sediments of the White Sea, Russia. *Marine Pollution Bulletin* **2000**, 40, 807-818.
109. Pereira, W. E.; Hostettler, F. D.; Luoma, S. N.; van Geen, A.; Fuller, C. C.; Anima, R. J. Sedimentary record of anthropogenic and biogenic polycyclic aromatic hydrocarbons in San Francisco Bay, California. *Marine Chemistry* **1999**, 64, 99-113.
110. Boitsov, S.; Jensen, H.; Klungsøyr, J. Geographical variations in hydrocarbon levels in sediments from Western Barents Sea. *Norwegian Journal of Geology* **2009**, 89, 91-100.
111. Wu, Y.; Zhang, J.; Mi, T.-z.; Li, B. Occurrence of alkanes and polycyclic aromatic hydrocarbons in the core sediments of the Yellow Sea. *Marine Chemistry* **2001**, 76, 1-15.
112. Douben, P. E. T. PAHs: an ecotoxicological perspective, Wiley. com, **2003**
113. Katz, D. R.; Cantwell, M. G.; Sullivan, J. C.; Perron, M. M.; Burgess, R. M.; Ho, K. T.; Charpentier, M. A. Factors regulating the accumulation and spatial distribution of the emerging contaminant triclosan in the sediments of an urbanized estuary: Greenwich Bay, Rhode Island, USA. *Science of the total environment* **2013**, 443, 123-133.
114. Fantozzi, L.; Manca, G.; Ammoscato, I.; Pirrone, N.; Sprovieri, F. The cycling and sea-air exchange of mercury in the waters of the Eastern Mediterranean during the 2010 MED-OCEANOR cruise campaign. *Science of the total environment* **2012**.
115. Qiu, Y.-W.; Zhang, G.; Liu, G.-Q.; Guo, L.-L.; Li, X.-D.; Wai, O. Polycyclic aromatic hydrocarbons (PAHs) in the water column and sediment core of Deep Bay, South China. *Estuarine, Coastal and Shelf Science* **2009**, 83, 60-66.
116. Mulder, H.; Breure, A.; Rulkens, W. Prediction of complete bioremediation periods for PAH soil pollutants in different physical states by mechanistic models. *Chemosphere* **2001**, 43, 1085-1094.

117. Iglesias-Groth, S.; Manchado, A.; Rebolo, R.; González Hernández, J.; García-Hernández, D.; Lambert, D. A search for interstellar anthracene towards the Perseus anomalous microwave emission region. *Monthly Notices of the Royal Astronomical Society* **2010**, 407, 2157-2165.
118. Dean, J. H.; Ward, E. C.; Murray, M. J.; Lauer, L. D.; House, R. V.; Stillman, W.; Hamilton, T. A.; Adams, D. O. Immunosuppression following 7, 12-dimethylbenz [a] anthracene exposure in B6C3F1 mice—II. Altered cell-mediated immunity and tumor resistance. *International journal of immunopharmacology* **1986**, 8, 189-198.
119. Gutman, I.; Stanković, S. Why is phenanthrene more stable than anthracene? *Macedonian Journal of Chemistry and Chemical Engineering* **2007**, 26, 111-114.
120. Wu, Q.; Cho, J.-G.; Yoo, K.-H.; Jeong, T.-S.; Park, J.-H.; Kim, S.-Y.; Kang, J.-H.; Chung, I.-S.; Choi, M.-S.; Lee, K.-T. A new phenanthrene derivative and two diarylheptanoids from the roots of *Brassica rapa* ssp. *campestris* inhibit the growth of cancer cell lines and LDL-oxidation. *Archives of pharmacal research* **2013**, 1-7.
121. Kanel, S.; Neppolian, B.; Choi, H.; Yang, J.-W. Heterogeneous catalytic oxidation of phenanthrene by hydrogen peroxide in soil slurry: Kinetics, mechanism, and implication. *Soil and Sediment Contamination* **2003**, 12, 101-117.
122. Liu, Z. Y.; Luo, Y. J. Research on oxidation of phenanthrene to phenanthrenequinone with TBHP. *Advanced Materials Research* **2013**, 690, 1256-1260.
123. USEPA. Polycyclic aromatic hydrocarbons (PAHs) United States Office of Solid Waste, . *Environmental Protection Agency, 2046-Washington, DC.* **2008**.
124. Moody, J. D.; Freeman, J. P.; Doerge, D. R.; Cerniglia, C. E. Degradation of phenanthrene and anthracene by cell suspensions of mycobacterium sp. strain PYR-1. *Applied and Environmental Microbiology* **2001**, 67, 1476-1483.

125. Zhu, J.; Lu, Y.; Chen, W. Single and joint toxic effects of cadmium and phenanthrene on enchytraeid *Fridericia bulbosa*. *European Journal of Soil Biology* **2008**, *44*, 260-265.
126. Gao, Y.; Zhu, L. Plant uptake, accumulation and translocation of phenanthrene and pyrene in soils. *Chemosphere* **2004**, *55*, 1169-1178.
127. Smith, C.; Perfetti, T.; Rumpel, M.; Rodgman, A.; Doolittle, D. "IARC group 2A Carcinogens" reported in cigarette mainstream smoke. *Food and Chemical Toxicology* **2000**, *38*, 371-383.
128. Eissen, M.; Hungerbühler, K.; Metzger, J. O.; Schmidt, E.; Schneidewind, U. 'Sustainable development and chemistry', *Kirk-Othmer Encyclopedia of Chemical Technology* (Wiley Online Library), **2004**.
129. Boonchan, S.; Britz, M. L.; Stanley, G. A. Degradation and mineralization of high-molecular-weight polycyclic aromatic hydrocarbons by defined fungal-bacterial cocultures. *Applied and Environmental Microbiology* **2000**, *66*, 1007-1019.
130. Wills, L. P.; Jung, D.; Koehn, K.; Zhu, S.; Willett, K. L.; Hinton, D. E.; Di Giulio, R. T. Comparative chronic liver toxicity of benzo [a] pyrene in two populations of the Atlantic killifish (*Fundulus heteroclitus*) with different exposure histories. *Environmental health perspectives* **2010**, *118*, 1376.
131. Nakamura, B. N.; Mohar, I.; Lawson, G. W.; Cortés, M. M.; Hoang, Y. D.; Ortiz, L.; Patel, R.; Rau, B. A.; McConnachie, L. A.; Kavanagh, T. J. Increased sensitivity to testicular toxicity of Transplacental benzo [a] pyrene exposure in male glutamate cysteine ligase Modifier subunit knockout (Gclm^{-/-}) mice. *Toxicological Sciences* **2012**, *126*, 227-241.
132. Germán-Hernández, M.; Pino, V.; Anderson, J. L.; Afonso, A. M. Use of ionic liquid aggregates of 1-hexadecyl-3-butyl imidazolium bromide in a focused-microwave

- assisted extraction method followed by high-performance liquid chromatography with ultraviolet and fluorescence detection to determine the 15+ 1 EU priority PAHs in toasted cereals (“gofios”). *Talanta* **2011**, 85, 1199-1206.
133. Zhao, W.-j.; Chen, X.-b.; Fang, L.; Li, C.-l.; Zhao, D.-y. Determination of light-medium-heavy polycyclic aromatic hydrocarbons in vegetable oils by solid-phase extraction and high-performance liquid chromatography with diode array and fluorescence detection. *Journal of Agricultural and Food Chemistry* **2013**, 61, 1804-1809.
134. Wang, X.-T.; Miao, Y.; Zhang, Y.; Li, Y.-C.; Wu, M.-H.; Yu, G. Polycyclic aromatic hydrocarbons (PAHs) in urban soils of the megacity Shanghai: Occurrence, source apportionment and potential human health risk. *Science of the total environment* **2013**, 447, 80-89.
135. Ieda, T.; Ochiai, N.; Miyawaki, T.; Ohura, T.; Horii, Y. Environmental analysis of chlorinated and brominated polycyclic aromatic hydrocarbons by comprehensive two-dimensional gas chromatography coupled to high-resolution time-of-flight mass spectrometry. *Journal of Chromatography A* **2011**, 1218, 3224-3232.
136. Ruan, X.; Yang, Z.; Xie, H.; Xiong, W.; Pan, Z.; Chen, L. Fast chemical fingerprinting analysis for biodiesel/diesel blends using commercial solid phase extraction (SPE) cartridge and gas chromatography-mass spectrometry (GC-MS). *Analytical Methods* **2013**, 5, 1205-1213.
137. Benhabib, M.; Chiesl, T. N.; Stockton, A. M.; Scherer, J. R.; Mathies, R. A. Multichannel capillary electrophoresis microdevice and instrumentation for in situ planetary analysis of organic molecules and biomarkers. *Analytical Chemistry* **2010**, 82, 2372-2379.

138. Panizza, M.; Bocca, C.; Cerisola, G. Electrochemical treatment of wastewater containing polyaromatic organic pollutants. *Water Research* **2000**, 34, 2601-2605.
139. Ricordel, C.; Miramon, C.; Hadjiev, D.; Darchen, A. Investigations of the mechanism and efficiency of bacteria abatement during electrocoagulation using aluminum electrode. *Desalination and Water Treatment* **2013**, 1-10.
140. Barek, J.; Cvačka, J.; Muck, A.; Quaiserova, V.; Zima, J. Electrochemical methods for monitoring of environmental carcinogens. *Fresenius' Journal of Analytical Chemistry* **2001**, 369, 556-562.
141. Chon, K.; Lee, Y.; Traber, J.; von Gunten, U., 'Quantification and characterization of dissolved organic nitrogen in wastewater effluents by electrodialysis treatment followed by size-exclusion chromatography with nitrogen detection, *Water Research* Elsevier **2013**.
142. Hammer, R.; VanBriesen, J. In fracking's wake: New rules are needed to protect our health and environment from contaminated wastewater. *Natural Resources Defense Council* **2012**, 11.
143. Dermentzis, K. Removal of nickel from electroplating rinse waters using electrostatic shielding electrodialysis/electrodeionization. *Journal of Hazardous Materials* **2010**, 173, 647-652.
144. Wang, J. Analytical electrochemistry Second edn., John Wiley & Sons, Inc., New York, NY 10158-0012, **2006** 31-32.
145. Tan, S. N.; Ge, L.; Tan, H. Y.; Loke, W. K.; Gao, J.; Wang, W. Paper-based enzyme immobilization for flow injection electrochemical biosensor integrated with reagent-loaded cartridge toward portable modular device. *Analytical Chemistry* **2012**, 84, 10071-10076.

146. Rudin, A.; Choi, P. *The Elements of Polymer Science & Engineering*, Access Online via Elsevier, **2012**
147. Van Krevelen, D. W.; Te Nijenhuis, K. *Properties of polymers: their correlation with chemical structure; their numerical estimation and prediction from additive group contributions*, Access Online via Elsevier, **2009**
148. Barron, A. E.; Zuckerman, R. N. Bioinspired polymeric materials: in-between proteins and plastics. *Current opinion in chemical biology* **1999**, 3, 681-687.
149. Kassim, A.; Ekarmul Mahmud, H.; Yee, L. M.; Hanipah, N. Electrochemical preparation and characterization of polypyrrole-polyethylene glycol conducting polymer composite films. *Pacific Journal of Science and Technology* **2006**, 7, 103-107.
150. Michel, S.; Zhang, X. Q.; Wissler, M.; Löwe, C.; Kovacs, G. A comparison between silicone and acrylic elastomers as dielectric materials in electroactive polymer actuators. *Polymer International* **2010**, 59, 391-399.
151. Hsieh, I.-F.; Sun, H.-J.; Fu, Q.; Lotz, B.; Cavicchi, K. A.; Cheng, S. Z. Phase structural formation and oscillation in polystyrene-block-polydimethylsiloxane thin films. *Soft Matter* **2012**, 8, 7937-7944.
152. Belgacem, M. N.; Gandini, A. *Monomers, polymers and composites from renewable resources*, Access Online via Elsevier, **2011**
153. Pandey, J. K.; Ahn, S.; Lee, C. S.; Mohanty, A. K.; Misra, M. Recent advances in the application of natural fiber based composites. *Macromolecular Materials and Engineering* **2010**, 295, 975-989.
154. Green, R. A.; Lovell, N. H.; Wallace, G. G.; Poole-Warren, L. A. Conducting polymers for neural interfaces: challenges in developing an effective long-term implant. *Biomaterials* **2008**, 29, 3393-3399.

155. Abidian, M. R.; Kim, D. H.; Martin, D. C. Conducting-polymer nanotubes for controlled drug release. *Advanced Materials* **2006**, 18, 405-409.
156. Ravichandran, R.; Sundarrajan, S.; Venugopal, J. R.; Mukherjee, S.; Ramakrishna, S. Applications of conducting polymers and their issues in biomedical engineering. *Journal of The Royal Society Interface* **2010**, 7, S559-S579.
157. Duarte, A.; Pu, K.-Y.; Liu, B.; Bazan, G. C. Recent advances in conjugated polyelectrolytes for emerging optoelectronic applications. *Chemistry of Materials* **2010**, 23, 501-515.
158. Lee, K.; Povlich, L. K.; Kim, J. Recent advances in fluorescent and colorimetric conjugated polymer-based biosensors. *Analyst* **2010**, 135, 2179-2189.
159. Gerard, M.; Chaubey, A.; Malhotra, B. Application of conducting polymers to biosensors. *Biosensors and Bioelectronics* **2002**, 17, 345-359.
160. Tanriverdi, S.; Tuncagil, S.; Toppare, L. A new amperometric alcohol oxidase biosensor based on conducting polymer of (4, 7-Dithien-2-yl-2, 1, 3-benzothiadiazole). *Journal of Macromolecular Science, Part A* **2012**, 49, 185-190.
161. Stoller, M. D.; Park, S.; Zhu, Y.; An, J.; Ruoff, R. S. Graphene-based ultracapacitors. *Nano Letters* **2008**, 8, 3498-3502.
162. Agrawal, R. C.; Sahu, D. K. Mg 2-ion conducting polymer electrolytes: Materials characterization and all-solid-state battery performance studies. *Journal of Physical Science and Application* **2013**, 3, 9-17.
163. Intemann, J. J.; Hellerich, E. S.; Tlach, B. C.; Ewan, M. D.; Barnes, C. A.; Bhuwarka, A.; Cai, M.; Shinar, J.; Shinar, R.; Jeffries-El, M. Altering the conjugation pathway for improved performance of benzobisoxazole-based polymer guest emitters in polymer light-emitting diodes. *Macromolecules* **2012**, 45, 6888-6897.

164. Kim, Y. H.; Lee, J.; Hofmann, S.; Gather, M. C.; Müller-Meskamp, L.; Leo, K. Achieving high efficiency and improved stability in ITO: Free transparent organic light emitting diodes with conductive polymer electrodes. *Advanced Functional Materials* **2013**.
165. Adhikari, R.; Postma, A.; Li, J. H.; Hirai, T.; Bown, M.; Ueno, K. Thermally cross-linkable copolymer and its evaluation as a hole transport layer in organic light-emitting diode devices. *Journal of the Society for Information Display* **2013**, 21, 151-158.
166. Deutschmann, T.; Oesterschulze, E. Micro-structured electrochromic device based on poly (3, 4-ethylenedioxythiophene). *Journal of Micromechanics and Microengineering* **2013**, 23, 065032.
167. Kateb, M.; Ahmadi, V.; Mohseni, M. Fast switching and high contrast electrochromic device based on PEDOT nanotube grown on ZnO nanowires. *Solar Energy Materials and Solar Cells* **2013**, 112, 57-64.
168. Möller, S.; Perlov, C.; Jackson, W.; Taussig, C.; Forrest, S. R. A polymer/semiconductor write-once read-many-times memory. *Nature* **2003**, 426, 166-169.
169. Nam, S.; Ko, Y.-G.; Hahm, S. G.; Park, S.; Seo, J.; Lee, H.; Kim, H.; Ree, M.; Kim, Y. Organic nonvolatile memory transistors with self-doped polymer energy well structures. *NPG Asia Materials* **2013**, 5, e33.
170. Joo, J.; Lee, C. High frequency electromagnetic interference shielding response of mixtures and multilayer films based on conducting polymers. *Journal of applied physics* **2000**, 88, 513-518.

171. Saini, P.; Choudhary, V. Enhanced electromagnetic interference shielding effectiveness of polyaniline functionalized carbon nanotubes filled polystyrene composites. *Journal of Nanoparticle Research* **2013**, 15, 1-7.
172. Otero, T. F.; Sanchez, J. J.; Martinez, J. G. Biomimetic dual sensing-actuators based on conducting polymers. Galvanostatic theoretical model for actuators sensing temperature. *The Journal of Physical Chemistry B* **2012**, 116, 5279-5290.
173. Janata, J.; Josowicz, M. Conducting polymers in electronic chemical sensors. *Nature Materials* **2003**, 2, 19-24.
174. Ding, J.; Zhou, D.; Spinks, G.; Wallace, G.; Forsyth, S.; Forsyth, M.; MacFarlane, D. Use of ionic liquids as electrolytes in electromechanical actuator systems based on inherently conducting polymers. *Chemistry of Materials* **2003**, 15, 2392-2398.
175. Heinze, J.; Frontana-Uribe, B. A.; Ludwigs, S. Electrochemistry of conducting polymers: Persistent models and new concepts. *Chemical Reviews* **2010**, 110, 4724-4771.
176. Trojanowicz, M. Application of conducting polymers in chemical analysis. *Microchimica Acta* **2003**, 143, 75-91.
177. Schultze, J.; Karabulut, H. Application potential of conducting polymers. *Electrochimica Acta* **2005**, 50, 1739-1745.
178. Shirakawa, H.; McDiarmid, A.; Heeger, A. Twenty-five years of conducting polymers. *Chemical Communications* **2003**, 2003, 1-4.
179. Pron, A.; Rannou, P. Processible conjugated polymers: from organic semiconductors to organic metals and superconductors. *Progress in Polymer Science* **2002**, 27, 135-190.
180. Zhang, M.; Yang, C.; Mishra, A. K.; Pisula, W.; Zhou, G.; Schmaltz, B.; Baumgarten, M.; Müllen, K. Conjugated alternating copolymers containing both donor and acceptor moieties in the main chain. *Chemical Communications* **2007**, 1704-1706.

181. Banerjee, S. Synthesis, swift heavy ion irradiation and characterization of conducting polymer based nanostructured materials for biomedical and sensor applications, Ph.D thesis, Tezpur **2013**.
182. Reid, O. G.; Rumbles, G. Quantitative transient absorption measurements of polaron yield and absorption coefficient in neat conjugated polymers. *The Journal of Physical Chemistry Letters* **2013**, 4, 2348-2355.
183. Geoghegan, M.; Hadziioannou, G. Polymer Electronics, Oxford University Press, 22, **2013**
184. Saini, P.; Choudhary, V. Structural details, electrical properties, and electromagnetic interference shielding response of processable copolymers of aniline. *Journal of materials science* **2013**, 48, 797-804.
185. Moliton, A.; Hiorns, R. C. Review of electronic and optical properties of semiconducting π -conjugated polymers: applications in optoelectronics. *Polymer International* **2004**, 53, 1397-1412.
186. Jaiswal, M.; Menon, R. Polymer electronic materials: a review of charge transport. *Polymer International* **2006**, 55, 1371-1384.
187. Hussain, S. T.; Abbas, F.; Kausar, A.; Khan, M. R. New polyaniline/polypyrrole/polythiophene and functionalized multiwalled carbon nanotube-based nanocomposites Layer-by-layer in situ polymerization. *High Performance Polymers* **2013**, 25, 70-78.
188. Mendonça, P. V.; Serra, A. C.; Silva, C. L.; Simões, S.; Coelho, J. F. Polymeric bile acid sequestrants—synthesis using conventional methods and new approaches based on “controlled”/living radical polymerization. *Progress in Polymer Science* **2012**.

189. Ye, Y.; Choi, K. Y. Dynamic modeling of a moving-packed-bed reactor for the solid-state polymerization of bisphenol-A polycarbonate. *Industrial & Engineering Chemistry Research* **2008**, 47, 3687-3699.
190. Akgün, E.; Hubbuch, J.; Wörner, M. Perspectives of aerosol-photopolymerization: nanoscale polymer particles. *Chemical Engineering Science* **2013**, 101, 248-252.
191. Bozukova, D.; Jérôme, R.; Jérôme, C. A fast and facile synthetic route toward the preparation of nanoparticles of polythiophene and its derivatives. *Journal of Nanoparticle Research* **2013**, 15, 1-18.
192. Terzi, F.; Pasquali, L.; Seeber, R. Studies of the interface of conducting polymers with inorganic surfaces. *Analytical and bioanalytical chemistry* **2013**, 405, 1513-1535.
193. Sapurina, I.; Stejskal, J. The mechanism of the oxidative polymerization of aniline and the formation of supramolecular polyaniline structures. *Polymer International* **2008**, 57, 1295-1325.
194. Zhao, Y.; Tomšík, E.; Wang, J.; Morávková, Z.; Zhigunov, A.; Stejskal, J.; Trchová, M. Self assembly of aniline oligomers. *Chemistry—An Asian Journal* **2013**, 8, 129-137.
195. Stejskal, J.; Gilbert, R. Polyaniline. Preparation of a conducting polymer (IUPAC technical report). *Pure and Applied Chemistry* **2002**, 74, 857-867.
196. Green, R.; Matteucci, P.; Hassarati, R.; Giraud, B.; Dodds, C.; Chen, S.; Byrnes-Preston, P.; Suaning, G.; Poole-Warren, L.; Lovell, N. Performance of conducting polymer electrodes for stimulating neuroprosthetics. *Journal of neural engineering* **2013**, 10, 016009.
197. Otero, T. F. Biomimetic conducting polymers: synthesis, materials, properties, functions, and devices. *Polymer Reviews* **2013**, 53, 311-351.

198. Bardini, L.; Ceccato, M.; Hinge, M.; Pedersen, S. U.; Daasbjerg, K.; Marcaccio, M.; Paolucci, F. Electrochemical polymerization of allylamine copolymers. *Langmuir* **2013**, *29*, 3791-3796.
199. Tran, H. D.; D'Arcy, J. M.; Wang, Y.; Beltramo, P. J.; Strong, V. A.; Kaner, R. B. The oxidation of aniline to produce “polyaniline”: a process yielding many different nanoscale structures. *Journal of Materials Chemistry* **2011**, *21*, 3534-3550.
200. Fusalba, F.; Gouérec, P.; Villers, D.; Bélanger, D. Electrochemical characterization of polyaniline in nonaqueous electrolyte and its evaluation as electrode material for electrochemical supercapacitors. *Journal of the Electrochemical Society* **2001**, *148*, A1-A6.
201. Huang, J.; Virji, S.; Weiller, B. H.; Kaner, R. B. Nanostructured polyaniline sensors. *Chemistry-A European Journal* **2004**, *10*, 1314-1319.
202. Mortimer, R. J.; Dyer, A. L.; Reynolds, J. R. Electrochromic organic and polymeric materials for display applications. *Displays* **2006**, *27*, 2-18.
203. Golmohammadi, M.; Kokabi, M.; Entezami, A. A. Polyaniline-modified montmorillonite nanocomposite as an actuator. *Issues* **2013**, *13*.
204. Cho, S.; Shin, K.-H.; Jang, J. Enhanced electrochemical performance of highly porous supercapacitor electrodes based on solution processed polyaniline thin films. *ACS Applied Materials & Interfaces* **2013**.
205. Machappa, T.; Sasikala, M.; Prasad, M. Impedance & electric modulus of conducting polyaniline/ZnWO₄ composites. *International Journal of Science Research* **2013**, *1*, 113-115.
206. Zhang, D.; Wang, Y. Synthesis and applications of one-dimensional nano-structured polyaniline: An overview. *Materials Science and Engineering: B* **2006**, *134*, 9-19.

207. Li, D.; Kaner, R. B. Shape and aggregation control of nanoparticles: not shaken, not stirred. *Journal of the American Chemical Society* **2006**, 128, 968-975.
208. Scott, J. C. History of conductive polymers. *Nanostructured Conductive Polymers* **2010**, 1-17.
209. Tjahyono, A.; Aw, K.; Travas-Sejdic, J., A novel polypyrrolebased sensor for robotics applications, *Robot Control*, **2012** (unpublished).
210. Scherer, M. R. J. 'Electropolymerization of Conjugated Polymers', *Double-Gyroid-Structured Functional Materials* (Springer), **2013** 135-156.
211. Chiang, J.-C.; MacDiarmid, A. G. 'Polyaniline': Protonic acid doping of the emeraldine form to the metallic regime. *Synthetic Metals* **1986**, 13, 193-205.
212. Chen, X.; Yuan, C.; Wong, C.; Zhang, G., Molecular modeling of the conductivity changes of the emeraldine base polyaniline due to protonic acid doping, Thermal, Mechanical and Multi-Physics Simulation and Experiments in Microelectronics and Microsystems (EuroSimE), 2012 13th International Conference on, **2012** (unpublished).
213. Huang, J.; Kaner, R. B. A general chemical route to polyaniline nanofibers. *Journal of the American Chemical Society* **2004**, 126, 851-855.
214. Tzamalīs, G.; Zaidi, N.; Monkman, A. Applicability of the localization-interaction model to magnetoconductivity studies of polyaniline films at the metal-insulator boundary. *Physical review B* **2003**, 68, 245106.
215. Araujo, J.; Adamo, C.; Robertis, E.; Kuznetsov, O.; Archanjo, B.; Fragneaud, B.; Achete, C.; De Paoli, M.-A. Crystallinity, oxidation states and morphology of polyaniline coated curauá fibers in polyamide-6 composites. *Composites science and technology* **2013**.

216. Fedorko, P.; Trznadel, M.; Pron, A.; Djurado, D.; Planès, J.; Travers, J. New analytical approach to the insulator–metal transition in conductive polyaniline. *Synthetic Metals* **2010**, 160, 1668-1671.
217. Huang, J.; Li, Q.; Wang, Y.; Dong, L.; Xie, H.; Wang, J.; Xiong, C. Fluxible nanoclusters of Fe₃O₄ nanocrystals embedded polyaniline by macromolecule-induced self-assembly. *Langmuir* **2013**, 29, 10223-10228.
218. Stejskal, J.; Sapurina, I.; Trchová, M. Polyaniline nanostructures and the role of aniline oligomers in their formation. *Progress in Polymer Science* **2010**, 35, 1420-1481.
219. Ge, D.; Yang, L.; Tong, Z.; Ding, Y.; Xin, W.; Zhao, J.; Li, Y. Ion diffusion and optical switching performance of 3D ordered nanostructured polyaniline films for advanced electrochemical/electrochromic devices. *Electrochimica Acta* **2013**.
220. Wallace, G. G.; Teasdale, P. R.; Spinks, G. M.; Kane-Maguire, L. A. Conductive electroactive polymers: intelligent polymer systems, CRC press, **2008**
221. Patil, R.; Harima, Y.; Yamashita, K.; Komaguchi, K.; Itagaki, Y.; Shiotani, M. Charge carriers in polyaniline film: a correlation between mobility and in-situ ESR measurements. *Journal of Electroanalytical Chemistry* **2002**, 518, 13-19.
222. Xue, W.; Jiang, X.; Harima, Y. New four-band electrode fabrication to measure in situ electrical property of conducting polymers. *Analytical Chemistry* **2009**, 81, 2364-2372.
223. Shapovalov, V. A.; Shapovalov, V. V.; Rafailovich, M. H.; Piechota, S.; Dmitruk, A. F.; Aksimentyeva, E. I.; Mazur, A. S. Dynamic characteristic of molecular structure of poly (ortho-methoxyaniline) with magnetic probes. *The Journal of Physical Chemistry C* **2013**, 117, 7830-7834.
224. Kebiche, H.; Debarnot, D.; Merzouki, A.; Poncin-Epaillard, F.; Haddaoui, N. Relationship between ammonia sensing properties of polyaniline nanostructures and their deposition and synthesis methods. *Analytica chimica acta* **2012**, 737, 64-71.

225. Stejskal, J.; Sapurina, I. Polyaniline: Thin films and colloidal dispersions (IUPAC Technical Report). *Pure and Applied Chemistry* **2005**, *77*, 815-826.
226. Feng, J.; Jing, X.; Li, Y. Self-assembly of aniline oligomers and their induced polyaniline supra-molecular structures. *Chemical Papers* **2013**, 1-18.
227. Hussain, A. P.; Kumar, A. Electrochemical synthesis and characterization of chloride doped polyaniline. *Bulletin of Materials Science* **2003**, *26*, 329-334.
228. Facchetti, A. π -conjugated polymers for organic electronics and photovoltaic cell applications†. *Chemistry of Materials* **2010**, *23*, 733-758.
229. Ghosh, P.; Datta, K.; Mulchandani, A.; Han, S.-H.; Koinkar, P. M.; Shirsat, M. D. Poly (O-Toluidine) nanowires based organic field effect transistors-a study on influence of anionic size of dopants and SWNTs as a dopant. *The Journal of Physical Chemistry C* **2013**, *117*, 15414-15420.
230. Min, Y.; Yang, Y.; Poojari, Y.; Liu, Y.; Wu, J.-C.; Hansford, D. J.; Epstein, A. J. Sulfonated polyaniline-based organic electrodes for controlled electrical stimulation of human osteosarcoma cells. *Biomacromolecules* **2013**, *14*, 1727-1731.
231. Tóth, P. S.; Samu, G. F.; Endrődi, B.; Visy, C. Hyphenated in situ conductance and spectroelectrochemical studies of polyaniline films in strongly acidic solutions. *Electrochimica Acta* **2013**, *110*, 446-451.
232. Lagoutte, S.; Aubert, P.-H.; Tran-Van, F.; Sallenave, X.; Laffaiteur, C.; Sarrazin, C.; Chevrot, C. Electrochemical and optical properties of poly (3, 4-dimethylthiophene) and its copolymers with 3-methylthiophene in ionic liquids media. *Electrochimica Acta* **2013**, *106*, 13-22.
233. Kumar, A.; Ali, V.; Kumar, S. Effect of the protonation and chemical doping of poly (o-toluidine) with copper sulfate on the spectral and electrical properties of the host polymer. *Journal of Macromolecular Science, Part B* **2013**, *52*, 1107-1114.

234. Dhibar, S.; Sahoo, S.; Das, C.; Singh, R. Investigations on copper chloride doped polyaniline composites as efficient electrode materials for supercapacitor applications. *Journal of Materials Science: Materials in Electronics* **2013**, 24, 576-585.
235. Mathebe, N. G.; Morrin, A.; Iwuoha, E. I. Electrochemistry and scanning electron microscopy of polyaniline/peroxidase-based biosensor. *Talanta* **2004**, 64, 115-120.
236. Morrin, A.; Ngamna, O.; Killard, A. J.; Moulton, S. E.; Smyth, M. R.; Wallace, G. G. An amperometric enzyme biosensor fabricated from polyaniline nanoparticles. *Electroanalysis* **2005**, 17, 423-430.
237. Somerset, V.; Leaner, J.; Mason, R.; Iwuoha, E.; Morrin, A. Development and application of a poly (2, 2'-dithiodianiline)(PDTDA)-coated screen-printed carbon electrode in inorganic mercury determination. *Electrochimica Acta* **2010**, 55, 4240-4246.
238. Silwana, B.; van der Horst, C.; Iwuoha, E.; Somerset, V. (eds.), *Inhibitive determination of metal ions using a horseradish peroxidase amperometric biosensor* (InTech) 2013.
239. Nair, S.; Rajeswari, R.; Natarajan, V.; Mukundan, T. Concentration-dependent growth and morphology of doped polyaniline nanowires. *Journal of Experimental Nanoscience* **2013**, 1-12.
240. Jian, J.; Guo, X.; Lin, L.; Cai, Q.; Cheng, J.; Li, J. Gas-sensing characteristics of dielectrophoretically assembled composite film of oxygen plasma-treated SWCNTs and PEDOT/PSS polymer. *Sensors and Actuators B: Chemical* **2013**.
241. Mishra, S.; Shimpi, N. G.; Sen, T. The effect of PEG encapsulated silver nanoparticles on the thermal and electrical property of sonochemically synthesized polyaniline/silver nanocomposite. *Journal of Polymer Research* **2013**, 20, 1-10.

242. Liu, Y.; Zhu, L.; Luo, Z.; Tang, H. Fabrication of molecular imprinted polymer sensor for chlortetracycline based on controlled electrochemical reduction of graphene oxide. *Sensors and Actuators B: Chemical* **2013**.
243. Rout, C. S.; Kulkarni, G.; Rao, C. Room temperature hydrogen and hydrocarbon sensors based on single nanowires of metal oxides. *Journal of Physics D: Applied Physics* **2007**, 40, 2777.
244. Yu, C.; Hao, Q.; Saha, S.; Shi, L.; Kong, X.; Wang, Z. L. Integration of metal oxide nanobelts with microsystems for nerve agent detection. *Applied Physics Letters* **2005**, 86, 063101-063101-063103.
245. Wang, K.; Weissmüller, J. Composites of nanoporous gold and polymer. *Advanced Materials* **2013**, 25, 1280-1284.
246. Paul, D.; Robeson, L. Polymer nanotechnology: nanocomposites. *Polymer* **2008**, 49, 3187-3204.
247. Sinha Ray, S.; Okamoto, M. Polymer/layered silicate nanocomposites: a review from preparation to processing. *Progress in Polymer Science* **2003**, 28, 1539-1641.
248. Ishida, H.; Campbell, S.; Blackwell, J. General approach to nanocomposite preparation. *Chemistry of Materials* **2000**, 12, 1260-1267.
249. Carrado, K. A. Synthetic organo- and polymer-clays: preparation, characterization, and materials applications. *Applied Clay Science* **2000**, 17, 1-23.
250. Sun, J.; Gerberich, W. W.; Francis, L. F. Electrical and optical properties of ceramic-polymer nanocomposite coatings. *Journal of Polymer Science Part B: Polymer Physics* **2003**, 41, 1744-1761.
251. Catauro, M.; Raucci, M.; De Marco, D.; Ambrosio, L. Release kinetics of ampicillin, characterization and bioactivity of TiO₂/PCL hybrid materials synthesized by sol-gel processing. *Journal of Biomedical Materials Research Part A* **2006**, 77, 340-350.

252. Chung, C. M.; Kim, M. S.; Kim, J. G.; Jang, D. O. Synthesis and photopolymerization of trifunctional methacrylates and their application as dental monomers. *Journal of biomedical materials research* **2002**, 62, 622-627.
253. Zhao, Q.; Samulski, E. T. In situ polymerization of poly (methyl methacrylate)/clay nanocomposites in supercritical carbon dioxide. *Macromolecules* **2005**, 38, 7967-7971.
254. Geim, A. K. Graphene: status and prospects. *Science* **2009**, 324, 1530-1534.
255. Boehm, H.-P.; Clauss, A.; Fischer, G.; Hofmann, U. Das Adsorptionsverhalten sehr dünner Kohlenstoff-Folien. *Zeitschrift für anorganische und allgemeine Chemie* **1962**, 316, 119-127.
256. Singh, V.; Joung, D.; Zhai, L.; Das, S.; Khondaker, S. I.; Seal, S. Graphene based materials: Past, present and future. *Progress in Materials Science* **2011**, 56, 1178-1271.
257. Dresselhaus, M.; Araujo, P. The 2010 Nobel Prize in physics for graphene: some perspectives. *ACS Nano* **2010**, 4, 6297-6302.
258. Madou, M.; Meador, M.; Patra, A.; Rogers, R.; Olds, J.; Zhang, X. Convergence platforms: Foundation science and technology tools. **2013**.
259. Geim, A. K.; Novoselov, K. S. The rise of graphene. *Nature Materials* **2007**, 6, 183-191.
260. Chen, J.-H.; Jang, C.; Adam, S.; Fuhrer, M.; Williams, E.; Ishigami, M. Charged-impurity scattering in graphene. *Nature Physics* **2008**, 4, 377-381.
261. Fradkin, E. Critical behavior of disordered degenerate semiconductors. II. Spectrum and transport properties in mean-field theory. *Physical review B* **1986**, 33, 3263.
262. Novoselov, K.; Geim, A. K.; Morozov, S.; Jiang, D.; Grigorieva, M. K. I.; Dubonos, S.; Firsov, A. Two-dimensional gas of massless Dirac fermions in graphene. *Nature* **2005**, 438, 197-200.

263. Zhang, Y.; Tan, Y.-W.; Stormer, H. L.; Kim, P. Experimental observation of the quantum Hall effect and Berry's phase in graphene. *Nature* **2005**, 438, 201-204.
264. Novoselov, K. S.; Geim, A. K.; Morozov, S.; Jiang, D.; Zhang, Y.; Dubonos, S.; Grigorieva, I.; Firsov, A. Electric field effect in atomically thin carbon films. *Science* **2004**, 306, 666-669.
265. Stankovich, S.; Piner, R. D.; Chen, X.; Wu, N.; Nguyen, S. T.; Ruoff, R. S. Stable aqueous dispersions of graphitic nanoplatelets via the reduction of exfoliated graphite oxide in the presence of poly (sodium 4-styrenesulfonate). *Journal of Materials Chemistry* **2006**, 16, 155-158.
266. Meyer, J. C.; Geim, A.; Katsnelson, M.; Novoselov, K.; Booth, T.; Roth, S. The structure of suspended graphene sheets. *Nature* **2007**, 446, 60-63.
267. Mendham, J.; Mendham, J. *Vogels textbook of quantitative chemical analysis*, Pearson Education India, **2006**
268. Porterfield, W. W. *Inorganic Chemistry*, Access Online via Elsevier, **2013**
269. Atkins, P. W.; Overton, T.; Rourke, J. P.; Weller, M.; Armstrong, F. A. Shriver & Atkins' inorganic chemistry, Oxford University Press, **2010**
270. Buzas, M. A.; Parrish, M. Memorial to Lawrence B. Isham (1922–2011). *The Journal of Foraminiferal Research* **2012**, 42, 107-108.
271. Agrawala, M.; Li, W.; Berthouzoz, F. Design principles for visual communication. *Communications of the ACM* **2011**, 54, 60-69.
272. Mills, A.; Farid, M.; Selman, J.; Al-Hallaj, S. Thermal conductivity enhancement of phase change materials using a graphite matrix. *Applied Thermal Engineering* **2006**, 26, 1652-1661.
273. Enoki, T.; Endo, M.; Suzuki, M. *Graphite intercalation compounds and applications*, Oxford University Press, **2003**

274. Acharya, K. P.; Khatri, H.; Marsillac, S.; Ullrich, B.; Anzenbacher, P.; Zamkov, M. Pulsed laser deposition of graphite counter electrodes for dye-sensitized solar cells. *Applied Physics Letters* **2010**, 97, 201108-201108-201103.
275. Kinder, E.; Moroz, P.; Diederich, G.; Johnson, A.; Kirsanova, M.; Nemchinov, A.; O'Connor, T.; Roth, D.; Zamkov, M. Fabrication of all-inorganic nanocrystal solids through matrix encapsulation of nanocrystal arrays. *Journal of the American Chemical Society* **2011**, 133, 20488-20499.
276. Delhaes, P. Graphite and precursors, CRC Press, 1, **2001**
277. Katsnelson, M. I. Graphene: carbon in two dimensions, Cambridge University Press, **2012**
278. Dresselhaus, M. S.; Dresselhaus, G. Intercalation compounds of graphite. *Advances in Physics* **2002**, 51, 1-186.
279. Balandin, A. A.; Ghosh, S.; Bao, W.; Calizo, I.; Teweldebrhan, D.; Miao, F.; Lau, C. N. Superior thermal conductivity of single-layer graphene. *Nano Letters* **2008**, 8, 902-907.
280. Ghosh, S.; Calizo, I.; Teweldebrhan, D.; Pokatilov, E.; Nika, D.; Balandin, A.; Bao, W.; Miao, F.; Lau, C. N. Extremely high thermal conductivity of graphene: Prospects for thermal management applications in nanoelectronic circuits. *Applied Physics Letters* **2008**, 92, 151911.
281. Bunch, J. S.; Van Der Zande, A. M.; Verbridge, S. S.; Frank, I. W.; Tanenbaum, D. M.; Parpia, J. M.; Craighead, H. G.; McEuen, P. L. Electromechanical resonators from graphene sheets. *Science* **2007**, 315, 490-493.
282. Lee, C.; Wei, X.; Kysar, J. W.; Hone, J. Measurement of the elastic properties and intrinsic strength of monolayer graphene. *Science* **2008**, 321, 385-388.

283. Nair, R.; Blake, P.; Grigorenko, A.; Novoselov, K.; Booth, T.; Stauber, T.; Peres, N.; Geim, A. Fine structure constant defines visual transparency of graphene. *Science* **2008**, 320, 1308-1308.
284. Jobst, J.; Waldmann, D.; Speck, F.; Hirner, R.; Maude, D. K.; Seyller, T.; Weber, H. B. How graphene-like is epitaxial graphene? \ quantum oscillations and quantum hall effect. *arXiv preprint arXiv:0908.1900* **2009**.
285. Wu, X.; Hu, Y.; Ruan, M.; Madiomanana, N. K.; Hankinson, J.; Sprinkle, M.; Berger, C.; de Heer, W. A. Half integer quantum Hall effect in high mobility single layer epitaxial graphene. *Applied Physics Letters* **2009**, 95, 223108-223108-223103.
286. Bai, J.; Huang, Y. Fabrication and electrical properties of graphene nanoribbons. *Materials Science and Engineering: R: Reports* **2010**, 70, 341-353.
287. Seol, J. H.; Jo, I.; Moore, A. L.; Lindsay, L.; Aitken, Z. H.; Pettes, M. T.; Li, X.; Yao, Z.; Huang, R.; Broido, D. Two-dimensional phonon transport in supported graphene. *Science* **2010**, 328, 213-216.
288. Hou, J.; Shao, Y.; Ellis, M. W.; Moore, R. B.; Yi, B. Graphene-based electrochemical energy conversion and storage: fuel cells, supercapacitors and lithium ion batteries. *Physical Chemistry Chemical Physics* **2011**, 13, 15384-15402.
289. Lin, J.; Peng, Z.; Xiang, C.; Ruan, G.; Yan, Z.; Natelson, D.; Tour, J. M. Graphene nanoribbon and nanostructured SnO₂ composite anodes for lithium ion batteries. *ACS Nano* **2013**, 7, 6001-6006.
290. Britnell, L.; Ribeiro, R.; Eckmann, A.; Jalil, R.; Belle, B.; Mishchenko, A.; Kim, Y.-J.; Gorbachev, R.; Georgiou, T.; Morozov, S. Strong light-matter interactions in heterostructures of atomically thin films. *Science* **2013**, 340, 1311-1314.

291. Yan, H.; Li, X.; Chandra, B.; Tulevski, G.; Wu, Y.; Freitag, M.; Zhu, W.; Avouris, P.; Xia, F. Tunable infrared plasmonic devices using graphene/insulator stacks. *Nature Nanotechnology* **2012**, *7*, 330-334.
292. Hecht, D. S.; Hu, L.; Irvin, G. Emerging transparent electrodes based on thin films of carbon nanotubes, graphene, and metallic nanostructures. *Advanced Materials* **2011**, *23*, 1482-1513.
293. Basu, S.; Bhattacharyya, P. Recent developments on graphene and graphene oxide based solid state gas sensors. *Sensors and Actuators B: Chemical* **2012**.
294. Stankovich, S.; Dikin, D. A.; Dommett, G. H.; Kohlhaas, K. M.; Zimney, E. J.; Stach, E. A.; Piner, R. D.; Nguyen, S. T.; Ruoff, R. S. Graphene-based composite materials. *Nature* **2006**, *442*, 282-286.
295. Weick, G.; Woollacott, C.; Barnes, W. L.; Hess, O.; Mariani, E. Dirac-like plasmons in honeycomb lattices of metallic nanoparticles. *Physical review letters* **2013**, *110*, 106801.
296. Partoens, B.; Peeters, F. From graphene to graphite: Electronic structure around the K point. *Physical review B* **2006**, *74*, 075404.
297. Ebrahimi, S.; Montazeri, A.; Rafii-Tabar, H. Molecular dynamics study of the interfacial mechanical properties of the graphene–collagen biological nanocomposite. *Computational Materials Science* **2013**, *69*, 29-39.
298. Lee, J. H.; Park, N.; Kim, B. G.; Jung, D. S.; Im, K.; Hur, J.; Choi, J. W. Restacking-inhibited 3D reduced graphene oxide for high performance supercapacitor electrodes. *ACS Nano* **2013**, *7* 9366–9374.
299. Stankovich, S.; Dikin, D. A.; Piner, R. D.; Kohlhaas, K. A.; Kleinhammes, A.; Jia, Y.; Wu, Y.; Nguyen, S. T.; Ruoff, R. S. Synthesis of graphene-based nanosheets via chemical reduction of exfoliated graphite oxide. *Carbon* **2007**, *45*, 1558-1565.

300. Hernandez, Y.; Nicolosi, V.; Lotya, M.; Blighe, F. M.; Sun, Z.; De, S.; McGovern, I.; Holland, B.; Byrne, M.; Gun'Ko, Y. K. High-yield production of graphene by liquid-phase exfoliation of graphite. *Nature Nanotechnology* **2008**, 3, 563-568.
301. Lotya, M.; Hernandez, Y.; King, P. J.; Smith, R. J.; Nicolosi, V.; Karlsson, L. S.; Blighe, F. M.; De, S.; Wang, Z.; McGovern, I. Liquid phase production of graphene by exfoliation of graphite in surfactant/water solutions. *Journal of the American Chemical Society* **2009**, 131, 3611-3620.
302. Green, A. A.; Hersam, M. C. Solution phase production of graphene with controlled thickness via density differentiation. *Nano Letters* **2009**, 9, 4031-4036.
303. Hassan, M.; Reddy, K. R.; Haque, E.; Minett, A. I.; Gomes, V. G. High-yield aqueous phase exfoliation of graphene for facile nanocomposite synthesis via emulsion polymerization. *Journal of Colloid and Interface Science* **2013**.
304. Bayat, A.; Aghamiri, S. Oil sorption by synthesized exfoliated graphite (EG). *Iranian Journal of Chemical Engineering* **2008**, 5.
305. Su, C.-Y.; Lu, A.-Y.; Xu, Y.; Chen, F.-R.; Khlobystov, A. N.; Li, L.-J. High-quality thin graphene films from fast electrochemical exfoliation. *ACS Nano* **2011**, 5, 2332-2339.
306. Chia, J. S. Y.; Tan, M. T.; SimKhiew, P.; Chin, J. K.; Lee, H.; Bien, D.; Teh, A.; Siong, C. W. Facile synthesis of few-layer graphene by mild solvent thermal exfoliation of highly oriented pyrolytic graphite. *Chemical Engineering Journal* **2013**.
307. Li, X.; Zhang, G.; Bai, X.; Sun, X.; Wang, X.; Wang, E.; Dai, H. Highly conducting graphene sheets and Langmuir–Blodgett films. *Nature Nanotechnology* **2008**, 3, 538-542.

308. Morozov, S.; Novoselov, K.; Katsnelson, M.; Schedin, F.; Ponomarenko, L.; Jiang, D.; Geim, A. Strong suppression of weak localization in graphene. *Physical review letters* **2006**, 97, 016801.
309. Zhou, S.; Gweon, G.-H.; Graf, J.; Fedorov, A.; Spataru, C.; Diehl, R.; Kopelevich, Y.; Lee, D.-H.; Louie, S. G.; Lanzara, A. First direct observation of Dirac fermions in graphite. *Nature Physics* **2006**, 2, 595-599.
310. Eddy Jr, C.; Gaskill, D., 'Silicon carbide as a platform for power electronics, DTIC Document **2009**.
311. Singh, R. S.; Nalla, V.; Chen, W.; Wee, A. T. S.; Ji, W. Laser Patterning of Epitaxial Graphene for Schottky Junction Photodetectors. *ACS Nano* **2011**, 5, 5969-5975.
312. Moon, J.; Curtis, D.; Hu, M.; Wong, D.; McGuire, C.; Campbell, P.; Jernigan, G.; Tedesco, J.; VanMil, B.; Myers-Ward, R. Epitaxial-graphene RF field-effect transistors on Si-face 6H-SiC substrates. *Electron Device Letters, IEEE* **2009**, 30, 650-652.
313. de Parga, A. V.; Calleja, F.; Borca, B.; Passeggi Jr, M.; Hinarejos, J.; Guinea, F.; Miranda, R. Periodically rippled graphene: growth and spatially resolved electronic structure. *Physical review letters* **2008**, 100, 056807.
314. Sutter, P. W.; Flege, J.-I.; Sutter, E. A. Epitaxial graphene on ruthenium. *Nature Materials* **2008**, 7, 406-411.
315. Winterlin, J.; Bocquet, M.-L. Graphene on metal surfaces. *Surface Science* **2009**, 603, 1841-1852.
316. Kim, K. S.; Zhao, Y.; Jang, H.; Lee, S. Y.; Kim, J. M.; Kim, K. S.; Ahn, J.-H.; Kim, P.; Choi, J.-Y.; Hong, B. H. Large-scale pattern growth of graphene films for stretchable transparent electrodes. *Nature* **2009**, 457, 706-710.

317. Reina, A.; Thiele, S.; Jia, X.; Bhaviripudi, S.; Dresselhaus, M. S.; Schaefer, J. A.; Kong, J. Growth of large-area single-and bi-layer graphene by controlled carbon precipitation on polycrystalline Ni surfaces. *Nano Research* **2009**, 2, 509-516.
318. Lahiri, J.; Miller, T. S.; Ross, A. J.; Adamska, L.; Oleynik, I. I.; Batzill, M. Graphene growth and stability at nickel surfaces. *New Journal of Physics* **2011**, 13, 025001.
319. Chen, W.; Yan, L.; Bangal, P. R. Preparation of graphene by the rapid and mild thermal reduction of graphene oxide induced by microwaves. *Carbon* **2010**, 48, 1146-1152.
320. Sun, L.; Fugetsu, B. Massive production of graphene oxide from expanded graphite. *arXiv preprint arXiv:1301.3253* **2013**.
321. Boukhvalov, D. W.; Katsnelson, M. I. Modeling of graphite oxide. *Journal of the American Chemical Society* **2008**, 130, 10697-10701.
322. Szabó, T.; Berkesi, O.; Forgó, P.; Josepovits, K.; Sanakis, Y.; Petridis, D.; Dékány, I. Evolution of surface functional groups in a series of progressively oxidized graphite oxides. *Chemistry of Materials* **2006**, 18, 2740-2749.
323. Lerf, A.; He, H.; Forster, M.; Klinowski, J. Structure of graphite oxide revisited. *The Journal of Physical Chemistry B* **1998**, 102, 4477-4482.
324. Nakajima, T.; Matsuo, Y. Formation process and structure of graphite oxide. *Carbon* **1994**, 32, 469-475.
325. Cai, W.; Piner, R. D.; Stadermann, F. J.; Park, S.; Shaibat, M. A.; Ishii, Y.; Yang, D.; Velamakanni, A.; An, S. J.; Stoller, M. Synthesis and solid-state NMR structural characterization of ¹³C-labeled graphite oxide. *Science* **2008**, 321, 1815-1817.
326. Gao, W.; Alemany, L. B.; Ci, L.; Ajayan, P. M. New insights into the structure and reduction of graphite oxide. *Nature chemistry* **2009**, 1, 403-408.
327. Buchsteiner, A.; Lerf, A.; Pieper, J. Water dynamics in graphite oxide investigated with neutron scattering. *The Journal of Physical Chemistry B* **2006**, 110, 22328-22338.

328. Cervený, S.; Barroso-Bujans, F.; Alegría, A. n.; Colmenero, J. Dynamics of water intercalated in graphite oxide. *The Journal of Physical Chemistry C* **2010**, 114, 2604-2612.
329. Wei, A.; Wang, J.; Long, Q.; Liu, X.; Li, X.; Dong, X.; Huang, W. Synthesis of high-performance graphene nanosheets by thermal reduction of graphene oxide. *Materials Research Bulletin* **2011**, 46, 2131-2134.
330. Liao, K.-H.; Mittal, A.; Bose, S.; Leighton, C.; Mkhoyan, K. A.; Macosko, C. W. Aqueous only route toward graphene from graphite oxide. *ACS Nano* **2011**, 5, 1253-1258.
331. Becerril, H. A.; Mao, J.; Liu, Z.; Stoltenberg, R. M.; Bao, Z.; Chen, Y. Evaluation of solution-processed reduced graphene oxide films as transparent conductors. *ACS Nano* **2008**, 2, 463-470.
332. Bourlinos, A. B.; Gournis, D.; Petridis, D.; Szabó, T.; Szeri, A.; Dékány, I. Graphite oxide: chemical reduction to graphite and surface modification with primary aliphatic amines and amino acids. *Langmuir* **2003**, 19, 6050-6055.
333. Eda, G.; Fanchini, G.; Chhowalla, M. Large-area ultrathin films of reduced graphene oxide as a transparent and flexible electronic material. *Nature Nanotechnology* **2008**, 3, 270-274.
334. Gómez-Navarro, C.; Weitz, R. T.; Bittner, A. M.; Scolari, M.; Mews, A.; Burghard, M.; Kern, K. Electronic transport properties of individual chemically reduced graphene oxide sheets. *Nano Letters* **2007**, 7, 3499-3503.
335. Shin, H. J.; Kim, K. K.; Benayad, A.; Yoon, S. M.; Park, H. K.; Jung, I. S.; Jin, M. H.; Jeong, H. K.; Kim, J. M.; Choi, J. Y. Efficient reduction of graphite oxide by sodium borohydride and its effect on electrical conductance. *Advanced Functional Materials* **2009**, 19, 1987-1992.

336. Willemse, C. M.; Tlhomelang, K.; Jahed, N.; Baker, P. G.; Iwuoha, E. I. Metallo-graphene nanocomposite electrocatalytic platform for the determination of toxic metal ions. *Sensors* **2011**, 11, 3970-3987.
337. Pei, S.; Zhao, J.; Du, J.; Ren, W.; Cheng, H.-M. Direct reduction of graphene oxide films into highly conductive and flexible graphene films by hydrohalic acids. *Carbon* **2010**, 48, 4466-4474.
338. Fan, Z.; Wang, K.; Wei, T.; Yan, J.; Song, L.; Shao, B. An environmentally friendly and efficient route for the reduction of graphene oxide by aluminum powder. *Carbon* **2010**, 48, 1686-1689.
339. Fernandez-Merino, M.; Guardia, L.; Paredes, J.; Villar-Rodil, S.; Solis-Fernandez, P.; Martinez-Alonso, A.; Tascon, J. Vitamin C is an ideal substitute for hydrazine in the reduction of graphene oxide suspensions. *The Journal of Physical Chemistry C* **2010**, 114, 6426-6432.
340. McAllister, M. J.; Li, J.-L.; Adamson, D. H.; Schniepp, H. C.; Abdala, A. A.; Liu, J.; Herrera-Alonso, M.; Milius, D. L.; Car, R.; Prud'homme, R. K. Single sheet functionalized graphene by oxidation and thermal expansion of graphite. *Chemistry of Materials* **2007**, 19, 4396-4404.
341. Kudin, K. N.; Ozbas, B.; Schniepp, H. C.; Prud'Homme, R. K.; Aksay, I. A.; Car, R. Raman spectra of graphite oxide and functionalized graphene sheets. *Nano Letters* **2008**, 8, 36-41.
342. Park, S.; Ruoff, R. S. Chemical methods for the production of graphenes. *Nature Nanotechnology* **2009**, 4, 217-224.
343. Medhekar, N. V.; Ramasubramaniam, A.; Ruoff, R. S.; Shenoy, V. B. Hydrogen bond networks in graphene oxide composite paper: structure and mechanical properties. *ACS Nano* **2010**, 4, 2300-2306.

344. Wang, Z.; Zhou, X.; Zhang, J.; Boey, F.; Zhang, H. Direct electrochemical reduction of single-layer graphene oxide and subsequent functionalisation with glucose oxidase. *The Journal of Physical Chemistry C* **2009**, 113, 14071-14075.
345. Zhou, M.; Wang, Y.; Zhai, Y.; Zhai, J.; Ren, W.; Wang, F.; Dong, S. Controlled synthesis of large area and patterned electrochemically reduced graphene oxide films. *Chemistry-A European Journal* **2009**, 15, 6116-6120.
346. Li, D.; Mueller, M. B.; Gilje, S.; Kaner, R. B.; Wallace, G. G. Processable aqueous dispersions of graphene nanosheets. *Nature Nanotechnology* **2008**, 3, 101-105.
347. Georgakilas, V.; Otyepka, M.; Bourlinos, A. B.; Chandra, V.; Kim, N.; Kemp, K. C.; Hobza, P.; Zboril, R.; Kim, K. S. Functionalisation of graphene: covalent and non-covalent approaches, derivatives and applications. *Chemical Reviews* **2012**, 112, 6156-6214.
348. Kuila, T.; Bose, S.; Mishra, A. K.; Khanra, P.; Kim, N. H.; Lee, J. H. Chemical functionalisation of graphene and its applications. *Progress in Materials Science* **2012**, 57, 1061-1105.
349. Stankovich, S.; Dikin, D. A.; Compton, O. C.; Dommett, G. H.; Ruoff, R. S.; Nguyen, S. T. Systematic post-assembly modification of graphene oxide paper with primary alkylamines. *Chemistry of Materials* **2010**, 22, 4153-4157.
350. Compton, O. C.; Jain, B.; Dikin, D. A.; Abouimrane, A.; Amine, K.; Nguyen, S. T. Chemically active reduced graphene oxide with tunable C/O ratios. *ACS Nano* **2011**, 5, 4380-4391.
351. Sampath, S.; Basuray, A. N.; Hartlieb, K. J.; Aytun, T.; Stupp, S. I.; Stoddart, J. F. Direct exfoliation of graphite to graphene in aqueous media with diazaperopyrenium dication. *Advanced Materials* **2013**.

352. Zhang, B.; Zhang, Y.; Peng, C.; Yu, M.; Li, L.; Deng, B.; Hu, P.; Fan, C.; Li, J.; Huang, Q. Preparation of polymer decorated graphene oxide by γ -ray induced graft polymerization. *Nanoscale* **2012**, 4, 1742-1748.
353. Zheng, W.; Shen, B.; Zhai, W. Surface functionalisation of graphene with polymers for enhanced properties **2013**.
354. Huang, X.; Yin, Z.; Wu, S.; Qi, X.; He, Q.; Zhang, Q.; Yan, Q.; Boey, F.; Zhang, H. Graphene based materials: synthesis, characterization, properties, and applications. *Small* **2011**, 7, 1876-1902.
355. Huang, X.; Qi, X.; Boey, F.; Zhang, H. Graphene-based composites. *Chemical Society Reviews* **2012**, 41, 666-686.
356. Choi, E.-Y.; Han, T. H.; Hong, J.; Kim, J. E.; Lee, S. H.; Kim, H. W.; Kim, S. O. Noncovalent functionalisation of graphene with end-functional polymers. *Journal of Materials Chemistry* **2010**, 20, 1907-1912.
357. Bai, H.; Xu, Y.; Zhao, L.; Li, C.; Shi, G. Non-covalent functionalisation of graphene sheets by sulfonated polyaniline. *Chem. Commun.* **2009**, 1667-1669.
358. Wan, Y.-J.; Tang, L.-C.; Yan, D.; Zhao, L.; Li, Y.-B.; Wu, L.-B.; Jiang, J.-X.; Lai, G.-Q. Improved dispersion and interface in the graphene/epoxy composites via a facile surfactant-assisted process. *Composites science and technology* **2013**.
359. Thickett, S. C.; Zetterlund, P. B. Functionalisation of graphene oxide for the production of novel graphene-based polymeric and colloidal materials. *Current Organic Chemistry* **2013**, 17, 956-974.
360. Jeevananda.T; Jang. Y. K; Lee. J. H; Siddaramaiah; Deepa Urs. M. V; Ranganathaiah. C. Investigation of multi-walled carbon nanotubes reinforced high-density polyethylene/carbon black nanocomposites using electrical DSC and positron lifetime spectroscopy techniques. *Polym Int.* **2009**, 58, 755-780.

361. Thostenson, E. T.; Ren, Z.; Chou, T.-W. Advances in the science and technology of carbon nanotubes and their composites: a review. *Composites science and technology* **2001**, 61, 1899-1912.
362. Chen, L.-Y.; Peng, J.-Y.; Xu, J.-Q.; Choi, H.; Li, X.-C. Achieving uniform distribution and dispersion of high percentage nanoparticles in metal matrix nanocomposites by solidification processing. *Scripta materialia* **2013**, 69, 634–637.
363. Kumar, M.; Singh, K.; Dhawan, S. K.; Tharanikkarasu, K.; Chung, J. S.; Kong, B.-S.; Kim, E. J.; Hur, S. H. Synthesis and characterization of covalently-grafted graphene-polyaniline nanocomposites and its use in a supercapacitor. *Chemical Engineering Journal* **2013**, 231 397–405.
364. Zhou, T.; Qi, X.; Fu, Q. The preparation of the poly (vinyl alcohol)/graphene nanocomposites with low percolation threshold and high electrical conductivity by using the large-area reduced graphene oxide sheets. *Express Polymer Letters* **2013**, 7, 747-755.
365. Kim, H.; Miura, Y.; Macosko, C. W. Graphene/polyurethane nanocomposites for improved gas barrier and electrical conductivity. *Chemistry of Materials* **2010**, 22, 3441-3450.
366. Ramanathan, T.; Abdala, A.; Stankovich, S.; Dikin, D.; Herrera-Alonso, M.; Piner, R.; Adamson, D.; Schniepp, H.; Chen, X.; Ruoff, R. Functionalized graphene sheets for polymer nanocomposites. *Nature Nanotechnology* **2008**, 3, 327-331.
367. Yu, W.; Xie, H.; Wang, X.; Wang, X. Highly efficient method for preparing homogeneous and stable colloids containing graphene oxide. *Nanoscale Research Letters* **2011**, 6, 47.

368. Park, S.; Dikin, D. A.; Nguyen, S. T.; Ruoff, R. S. Graphene oxide sheets chemically cross-linked by polyallylamine. *The Journal of Physical Chemistry C* **2009**, 113, 15801-15804.
369. Cao, Y.; Feng, J.; Wu, P. Preparation of organically dispersible graphene nanosheet powders through a lyophilization method and their poly (lactic acid) composites. *Carbon* **2010**, 48, 3834-3839.
370. Chen, G.; Weng, W.; Wu, D.; Wu, C. PMMA/graphite nanosheets composite and its conducting properties. *European Polymer Journal* **2003**, 39, 2329-2335.
371. Eda, G.; Chhowalla, M. Graphene-based composite thin films for electronics. *Nano Letters* **2009**, 9, 814-818.
372. Kuilla, T.; Bhadra, S.; Yao, D.; Kim, N. H.; Bose, S.; Lee, J. H. Recent advances in graphene based polymer composites. *Progress in Polymer Science* **2010**, 35, 1350-1375.
373. Kalaitzidou, K.; Fukushima, H.; Drzal, L. T. Mechanical properties and morphological characterization of exfoliated graphite-polypropylene nanocomposites. *Composites Part A: Applied Science and Manufacturing* **2007**, 38, 1675-1682.
374. Zhang, H.-B.; Zheng, W.-G.; Yan, Q.; Yang, Y.; Wang, J.-W.; Lu, Z.-H.; Ji, G.-Y.; Yu, Z.-Z. Electrically conductive polyethylene terephthalate/graphene nanocomposites prepared by melt compounding. *Polymer* **2010**, 51, 1191-1196.
375. Zheng, W.; Lu, X.; Wong, S. C. Electrical and mechanical properties of expanded graphite-reinforced high-density polyethylene. *Journal of Applied Polymer Science* **2004**, 91, 2781-2788.
376. Besse, J.-P.; Leroux, F. Poly (styrene sulfonate) layered double hydroxide nanocomposites. Stability and subsequent structural transformation with changes in temperature. *Journal of Materials Chemistry* **2003**, 13, 258-264.

377. Mo, Z.; Zhao, Y.; Zhang, J.; Xie, T. Fabrication of nanoGs/PPy/polymethacrylate (PMMA)-epoxy conductive films. *Materials and Manufacturing Processes* **2012**, *27*, 1324-1328.
378. Pradyot, P., 'Handbook of inorganic chemical compounds; McGraw-Hill:New York **2003**.
379. Zhang, Y.; Tang, Z.-R.; Fu, X.; Xu, Y.-J. TiO₂- graphene nanocomposites for gas-phase photocatalytic degradation of volatile aromatic pollutant: Is TiO₂- graphene truly different from Other TiO₂- carbon composite materials? *ACS Nano* **2010**, *4*, 7303-7314.
380. Rajeshwar, K.; de Tacconi, N. R.; Chenthamarakshan, C. Semiconductor-based composite materials: preparation, properties, and performance. *Chemistry of Materials* **2001**, *13*, 2765-2782.
381. Yao, Y.; Li, G.; Ciston, S.; Lueptow, R. M.; Gray, K. A. Photoreactive TiO₂/carbon nanotube composites: synthesis and reactivity. *Environmental science & technology* **2008**, *42*, 4952-4957.
382. Su, J.; Cao, M.; Ren, L.; Hu, C. Fe₃O₄-graphene nanocomposites with improved lithium storage and magnetism properties. *The Journal of Physical Chemistry C* **2011**, *115*, 14469-14477.
383. Lee, J.-H.; Kim, H.-M.; Kim, K.-B.; Kabe, R.; Anzenbacher, P.; Kim, J.-J. Homogeneous dispersion of organic p-dopants in an organic semiconductor as an origin of high charge generation efficiency. *Applied Physics Letters* **2011**, *98*, 173303.
384. Sun, M.; Xu, N.; Cao, Y.; Yao, J.; Wang, E. Nanocrystalline tungsten oxide thin film: Preparation, microstructure, and photochromic behavior. *Journal of Materials Research* **2000**, *15*, 927-933.

385. Granqvist, C. G. Electrochromic tungsten oxide films: review of progress 1993–1998. *Solar Energy Materials and Solar Cells* **2000**, 60, 201-262.
386. Somani, P. R.; Radhakrishnan, S. Electrochromic materials and devices: present and future. *Materials chemistry and physics* **2003**, 77, 117-133.
387. Bamwenda, G. R.; Arakawa, H. The visible light induced photocatalytic activity of tungsten trioxide powders. *Applied Catalysis A: General* **2001**, 210, 181-191.
388. Avendano, E.; Berggren, L.; Niklasson, G. A.; Granqvist, C. G.; Azens, A. Electrochromic materials and devices: Brief survey and new data on optical absorption in tungsten oxide and nickel oxide films. *Thin Solid Films* **2006**, 496, 30-36.
389. Monk, P.; Mortimer, R.; Rosseinsky, D. Electrochromism and electrochromic devices, Cambridge University Press, **2007**
390. Barik, R.; Bera, A.; Tanwar, A.; Baek, I.; Min, S.; Kwon, O.; Lee, W.; Park, G.-S. A novel approach to synthesis of scandia-doped tungsten nano-particles for high-current-density cathode applications. *International Journal of Refractory Metals and Hard Materials* **2013**, 38 60–66.
391. Antunez, P. D.; Webber, D. H.; Brutchey, R. L. Solution-phase synthesis of highly conductive tungsten diselenide nanosheets. *Chemistry of Materials* **2013**, 25, 2385–2387.
392. Huo, L. H.; Bai, X. H.; Xu, Y. M.; Cheng, X. L.; Zhao, H.; Gao, S.; Ding, J.; Wang, Z. A simple, greens synthesis of photochromic, monoclinic tungsten oxide fiber. *Advanced Materials Research* **2013**, 669, 307-310.
393. Baek, S. H.; Choi, K. S.; Jaramillo, T. F.; Stucky, G. D.; McFarland, E. W. Enhancement of photocatalytic and electrochromic properties of electrochemically fabricated mesoporous WO₃ thin films. *Advanced Materials* **2003**, 15, 1269-1273.

394. Baserga, A.; Russo, V.; Di Fonzo, F.; Bailini, A.; Cattaneo, D.; Casari, C.; Li Bassi, A.; Bottani, C. Nanostructured tungsten oxide with controlled properties: Synthesis and Raman characterization. *Thin Solid Films* **2007**, 515, 6465-6469.
395. Kida, T.; Fujiyama, S.; Suematsu, K.; Yuasa, M.; Shimanoe, K. Pore and particle size control of gas sensing films using SnO₂ nanoparticles synthesized by seed-mediated growth: design of highly sensitive gas sensors. *The Journal of Physical Chemistry C* **2013**, 117, 17574-17582.
396. Porter, J.; Arzberger, P.; Braun, H.-W.; Bryant, P.; Gage, S.; Hansen, T.; Hanson, P.; Lin, C.-C.; Lin, F.-P.; Kratz, T. Wireless sensor networks for ecology. *Bioscience* **2005**, 55, 561-572.
397. Bakker, E. Electrochemical sensors. *Analytical Chemistry* **2004**, 76, 3285-3298.
398. Janata, J. Principles of chemical sensors, Springer, **2009**
399. Stradiotto, N. R.; Yamanaka, H.; Zanon, M. V. B. Electrochemical sensors: a powerful tool in analytical chemistry. *Journal of the Brazilian Chemical Society* **2003**, 14, 159-173.
400. Taillefert, M.; Luther III, G. W.; Nuzzio, D. B. The application of electrochemical tools for in situ measurements in aquatic systems. *Electroanalysis* **2000**, 12, 401-412.
401. Dutta, M.; Das, D. Recent developments in fluorescent sensors for trace-level determination of toxic-metal ions. *TrAC Trends in Analytical Chemistry* **2012**, 32, 113-132.
402. Datta, M.; Goyal, D. Development of biosensor for heavy metal detection, PhD Thesis in Chemistry, Thapar University **2013**.
403. Pigani, L.; Zanfognini, B.; Seeber, R. PEDOT modified microelectrodes. Preparation, characterisation and analytical performances. *Electroanalysis* **2012**, 24, 1340-1347.

404. Bakker, E.; Telting-Diaz, M. Electrochemical sensors. *Analytical Chemistry* **2002**, 74, 2781–2800.
405. Dobrokhotov, V.; Oakes, L.; Sowell, D.; Larin, A.; Hall, J.; Barzilov, A.; Kengne, A.; Bakharev, P.; Corti, G.; Cantrell, T. Thermal and optical activation mechanisms of nanospring-based chemiresistors. *Sensors* **2012**, 12, 5608-5622.
406. Liu, C.-C. Electrochemical sensors. *Biomedical Engineering Handbook*, CRC Press, Boca Raton Fla **1995**, 758-763.
407. Grygolowicz-Pawlak, E.; Crespo, G. A.; Ghahraman Afshar, M.; Mistlberger, G.; Bakker, E. Potentiometric sensors with ion-exchange donnan exclusion membranes. *Analytical Chemistry* **2013**, 85, 6208–6212.
408. De Wael, K.; Daems, D.; Van Camp, G.; Nagels, L. Use of potentiometric sensors to study (bio) molecular interactions. *Analytical Chemistry* **2012**, 84, 4921-4927.
409. Monk, P. M. Fundamentals of electro-analytical chemistry, John Wiley & Sons, 29, **2008**
410. Torralba, E.; Serna, C.; Ortuño, J. Analytical solution for the facilitated ion transfer at the interface between two immiscible electrolyte solutions via successive complexation reactions in any voltammetric technique. application to square wave Voltammetry and cyclic Voltammetry. *Electrochimica Acta* **2013**, 106, 244–257.
411. Zoski, C. G. Handbook of electrochemistry, Access Online via Elsevier, **2007**
412. Heyrovsky, J.; Shikata, M. Researches with the dropping mercury cathode. II. *The polarograph. Recueil des Travaux Chimiques des Pays-Bas et de la Belgique* **1925**, 44, 496-498.
413. Gupta, V. K.; Jain, R.; Radhapyari, K.; Jadon, N.; Agarwal, S. Voltammetric techniques for the assay of pharmaceuticals—a review. *Analytical Biochemistry* **2011**, 408, 179-196.

414. Kounaves, S.P. Voltammetric techniques. In handbook of instrumental techniques for analytical chemistry. *Department of Chemistry, Tufts University*, **2008**.
415. Bard, A. J.; Zoski, C. G. Voltammetry Retrospective. *Analytical Chemistry* **2000**, *72*, 346 A-352 A.
416. Alves, R. D.; Rodrigues, L. C.; Andrade, J. R.; Fernandes, M.; Pinto, J. V.; Pereira, L.; Pawlicka, A.; Martins, R.; Fortunato, E.; de Zea Bermudez, V. Gelatin/Zn (CF₃SO₃)₂ polymer electrolytes for electrochromic devices. *Electroanalysis* **2013**, *25*, 1483-1490.
417. Vielstich, W. Cyclic voltammetry, Wiley Online Library, **2010**
418. González, J.; Molina, A.; Soto, C.; Serna, C. Detection of interaction between redox centers of surface confined molecules by means of cyclic voltammetry and differential staircase voltammetry. *Journal of Electroanalytical Chemistry* **2012**, *664*, 53-62.
419. Viswanathan, V.; Hansen, H. A.; Rossmeisl, J.; Jaramillo, T. F.; Pitsch, H.; Nørskov, J. K. Simulating linear sweep voltammetry from first-principles: application to electrochemical oxidation of water on Pt(111) and Pt₃Ni (111). *The Journal of Physical Chemistry C* **2012**, *116*, 4698-4704.
420. De Souza, D.; Mascaro, L. H.; Fatibello-Filho, O. A comparative electrochemical behaviour study and analytical detection of the p-nitrophenol using silver solid amalgam, mercury, and silver electrodes. *International journal of analytical chemistry* **2011**, 2011.
421. ul Haque, I.; Fatima, M.; Tariq, M. Cyclic Voltammetry of Fluorenones: Simulation. *ECS Transactions* **2013**, *45*, 39-46.
422. Andres, T.; Eckmann, L.; Smith, D. K. Voltammetry of nitrobenzene with cysteine and other acids in DMSO. Implications for the biological reactivity of reduced nitroaromatics with thiols. *Electrochimica Acta* **2013**, *92*, 257-268.

423. Garcia, L. L. C.; Figueiredo-Filho, L. C. S.; Oliveira, G. G.; Fatibello-Filho, O.; Banks, C. E. Square-wave voltammetric determination of paraquat using a glassy carbon electrode modified with multiwalled carbon nanotubes within a dihexadecylhydrogenphosphate (DHP) film. *Sensors and Actuators B: Chemical* **2013**, 181, 306–311.
424. Markovic, N. M. Electrocatalysis: Interfacing electrochemistry. *Nature Materials* **2013**, 12, 101-102.
425. Artero, V.; Fontecave, M. Solar fuels generation and molecular systems: is it homogeneous or heterogeneous catalysis? *Chemical Society Reviews* **2013**, 42, 338-2356.
426. Jia, G.; Gao, Y.; Zhang, W.; Wang, H.; Cao, Z.; Li, C.; Liu, J. Metal-organic frameworks as heterogeneous catalysts for electrocatalytic oxidative carbonylation of methanol to dimethyl carbonate. *Electrochemistry Communications* **2013**, 34, 211–214.
427. Feng, X.; Yan, Z.; Li, R.; Liu, X.; Hou, W. The synthesis of shape-controlled polypyrrole/graphene and the study of its capacitance properties. *Polymer Bulletin* **2013**, 1-14.
428. Monge-Romero, I. C.; Suárez-Herrera, M. F. Electrocatalysis of the hydroquinone/benzoquinone redox couple at platinum electrodes covered by a thin film of poly(3,4-ethylenedioxythiophene). *Synthetic Metals* **2013**, 175, 36-41.
429. Tsakova, V. 'Conductive Polymer-Based Materials for Medical Electroanalytic Applications', *Applications of Electrochemistry in Medicine* (Springer), **2013** 283-342.
430. Zhang, X.; Lai, G.; Yu, A.; Zhang, H. A glassy carbon electrode modified with a polyaniline doped with silicotungstic acid and carbon nanotubes for the sensitive amperometric determination of ascorbic acid. *Microchimica Acta* **2013**, 1-7.

431. Xi, L.; Zhu, Z.; Wang, F. Electrocatalytic oxidation of ascorbic acid on quaternized carbon nanotubes/ionic liquid-polyaniline composite film modified glassy carbon electrode. *Journal of the Electrochemical Society* **2013**, 160, H327-H334.
432. Liu, J.; Tian, S.; Knoll, W. Properties of polyaniline/carbon nanotube multilayer films in neutral solution and their application for stable low-potential detection of reduced β -nicotinamide adenine dinucleotide. *Langmuir* **2005**, 21, 5596-5599.
433. Lee, P.; Compton, R. Electrochemical detection of NADH, cysteine, or glutathione using a caffeic acid modified glassy carbon electrode. *Electroanalysis* **2013**, 25, 1613–1620.
434. Lai, G.; Liu, Y.; Yu, A.; Han, D.; Zhang, H. Simultaneous sensitive determination of dopamine and uric acid in the presence of excess ascorbic acid with a magnetic chitosan microsphere/thionine modified electrode. *Analytical Letters* **2013**, 46
435. Wang, J. Analytical electrochemistry, Wiley. com, **2006**
436. Thévenot, D. R.; Toth, K.; Durst, R. A.; Wilson, G. S. Electrochemical biosensors: recommended definitions and classification. *Biosensors and Bioelectronics* **2001**, 16, 121-131.
437. Chaki, N. K.; Vijayamohan, K. Self-assembled monolayers as a tunable platform for biosensor applications. *Biosensors and Bioelectronics* **2002**, 17, 1-12.
438. Wu, K.; Fei, J.; Hu, S. Simultaneous determination of dopamine and serotonin on a glassy carbon electrode coated with a film of carbon nanotubes. *Analytical Biochemistry* **2003**, 318, 100-106.
439. Ganzorig, C.; Kwak, K.-J.; Yagi, K.; Fujihira, M. Fine tuning work function of indium tin oxide by surface molecular design: Enhanced hole injection in organic electroluminescent devices. *Applied Physics Letters* **2001**, 79, 272-274.

440. Zhang, J.; Vukmirovic, M. B.; Sasaki, K.; Nilekar, A. U.; Mavrikakis, M.; Adzic, R. R. Mixed-metal Pt monolayer electrocatalysts for enhanced oxygen reduction kinetics. *Journal of the American Chemical Society* **2005**, 127, 12480-12481.
441. Cattarin, S.; Musiani, M. Electrosynthesis of nanocomposite materials for electrocatalysis. *Electrochimica Acta* **2007**, 52, 2796-2805.
442. Zhou, M.; Guo, L.-p.; Lin, F.-y.; Liu, H.-x. Electrochemistry and electrocatalysis of polyoxometalate-ordered mesoporous carbon modified electrode. *Analytica chimica acta* **2007**, 587, 124-131.
443. Kant, R.; Kumar, R.; Yadav, V. K. Theory of anomalous diffusion impedance of realistic fractal electrode. *The Journal of Physical Chemistry C* **2008**, 112, 4019-4023.
444. Kazeman, I.; Hasanzadeh, M.; Jafarian, M. Electrochemical impedance of oxygen reduction in acidic solution at silver-modified glassy carbon electrode. *Analytical Bioanalytical Electrochemistry* **2012**, 4, 447 - 456.
445. Macdonald, D. D. Reflections on the history of electrochemical impedance spectroscopy. *Electrochimica Acta* **2006**, 51, 1376-1388.
446. Freger, V.; Bason, S. Characterization of ion transport in thin films using electrochemical impedance spectroscopy: I. Principles and theory. *Journal of membrane science* **2007**, 302, 1-9.
447. Macdonald, D. D. Why electrochemical impedance spectroscopy is the ultimate tool in mechanistic analysis. *ECS Transactions* **2009**, 19, 55-79.
448. Allen, J. B.; Larry, R. F. Electrochemical methods: fundamentals and applications. *Department of Chemistry and Biochemistry University of Texas at Austin, John Wiley & Sons, Inc* **2001**.
449. Orazem, M. E.; Tribollet, B. Electrochemical impedance spectroscopy, Wiley. com, 48, **2011**

450. Ates, M. Review study of electrochemical impedance spectroscopy and equivalent electrical circuits of conducting polymers on carbon surfaces. *Progress in Organic Coatings* **2011**, 71, 1-10.
451. Suni, I. I. Impedance methods for electrochemical sensors using nanomaterials. *TrAC Trends in Analytical Chemistry* **2008**, 27, 604-611.
452. Ates, M.; Sarac, A. S. Electrochemical impedance spectroscopic study of polythiophenes on carbon materials. *Polymer-Plastics Technology and Engineering* **2011**, 50, 1130-1148.
453. Fernández-Sánchez, C.; McNeil, C. J.; Rawson, K. Electrochemical impedance spectroscopy studies of polymer degradation: application to biosensor development. *TrAC Trends in Analytical Chemistry* **2005**, 24, 37-48.
454. Costa, F. R.; Franco, D. V.; Da Silva, L. M. Electrochemical impedance spectroscopy study of the oxygen evolution reaction on a gas-evolving anode composed of lead dioxide microfibers. *Electrochimica Acta* **2013**, 90, 332-343.
455. Magdić, K.; Horvat-Radošević, V. The role of electrochemical impedance spectroscopy in the characterization of electrodes and devices for energy conversion and storage. *Kemija u industriji* **2013**, 62, 81-91.
456. Chang, B.-Y.; Park, S.-M. Electrochemical impedance spectroscopy. *Annual Review of Analytical Chemistry* **2010**, 3, 207-229.
457. Beller, M.; Centi, G.; Sun, L.; Bellussi, G.; Bianchini, C.; Corma, A.; De Angelis, F.; Guldi, D.; Kamm, B.; Sakakura, T. ChemSusChem succeeds Annali di Chimica, a journal of the SocietaChimica Italiana The journal is also supported by the Asian Chemical Editorial Society (ACES). *ChemSusChem* **2013**, 6, 1291-1302.

458. Péter, L.; Arai, J.; Akahoshi, H. Impedance of a reaction involving two adsorbed intermediates: aluminum dissolution in non-aqueous lithium imide solutions. *Journal of Electroanalytical Chemistry* **2000**, 482, 125-138.
459. Hsing, I.-M.; Wang, X.; Leng, Y.-J. Electrochemical impedance studies of methanol electro-oxidation on Pt/C thin film electrode. *Journal of the Electrochemical Society* **2002**, 149, A615-A621.
460. Boukamp, B. A. Electrochemical impedance spectroscopy in solid state ionics: recent advances. *Solid state ionics* **2004**, 169, 65-73.
461. Chen, W.-C.; Wen, T.-C.; Teng, H. Polyaniline-deposited porous carbon electrode for supercapacitor. *Electrochimica Acta* **2003**, 48, 641-649.
462. Levi, M.; Gofer, Y.; Aurbach, D.; Berlin, A. EIS evidence for charge trapping in n-doped poly-3-(3, 4, 5-trifluorophenyl) thiophene. *Electrochimica Acta* **2004**, 49, 433-444.
463. Bramblett, A. L.; S Boeckl, M.; Hauch, K. D.; Ratner, B. D.; Sasaki, T.; Rogers, J. Determination of surface coverage for tetraphenylporphyrin monolayers using ultraviolet visible absorption and x-ray photoelectron spectroscopies. *Surface and interface analysis* **2002**, 33, 506-515.
464. Bogumil, K.; Orphal, J.; Homann, T.; Voigt, S.; Spietz, P.; Fleischmann, O.; Vogel, A.; Hartmann, M.; Kromminga, H.; Bovensmann, H. Measurements of molecular absorption spectra with the SCIAMACHY pre-flight model: Instrument characterization and reference data for atmospheric remote-sensing in the 230–2380 nm region. *Journal of Photochemistry and Photobiology A: Chemistry* **2003**, 157, 167-184.
465. Skoog, D. A.; Holler, F. J.; Crouch, S. R. Instrumental analysis, Brooks/Cole, Cengage Learning, **2007**

466. Pawar, N.; Salunkhe, V. Development and validation of UV spectrophotometric method for simultaneous estimation of rutin and gallic acid in hydroalcoholic extract of triphala churna. *Development* **2013**, 5, 724-729.
467. Griffiths, P.; De Haseth, J. A. Fourier transform infrared spectrometry, John Wiley & Sons, 171,, **2007**
468. Vogel, H.; Rosén, P.; Wagner, B.; Melles, M.; Persson, P. Fourier transform infrared spectroscopy, a new cost-effective tool for quantitative analysis of biogeochemical properties in long sediment records. *Journal of Paleolimnology* **2008**, 40, 689-702.
469. Smith, E.; Dent, G. Modern Raman spectroscopy: a practical approach, Wiley. com, **2005**
470. McCreery, R. L. Raman spectroscopy for chemical analysis, Wiley. com, 225, **2005**
471. Fiechtner, G. J.; Gord, J. R. Absorption and the dimensionless overlap integral for two-photon excitation. *Journal of Quantitative Spectroscopy and Radiative Transfer* **2001**, 68, 543-557.
472. Lang, K.; Hite, D.; Simmonds, R.; McDermott, R.; Pappas, D.; Martinis, J. M. Conducting atomic force microscopy for nanoscale tunnel barrier characterization. *Review of scientific instruments* **2004**, 75, 2726-2731.
473. Gruverman, A.; Wu, D.; Lu, H.; Wang, Y.; Jang, H.; Folkman, C.; Zhuravlev, M. Y.; Felker, D.; Rzechowski, M.; Eom, C.-B. Tunneling electroresistance effect in ferroelectric tunnel junctions at the nanoscale. *Nano Letters* **2009**, 9, 3539-3543.
474. Dufrière, Y. F.; Martínez-Martín, D.; Medalsy, I.; Alsteens, D.; Müller, D. J. Multiparametric imaging of biological systems by force-distance curve-based AFM. *Nature methods* **2013**, 10, 847-854.
475. Eaton, P. J.; West, P. Atomic force microscopy, Oxford University Press New York, **2010**

476. Jenkins, R.; Snyder, R. Introduction to X-ray powder diffractometry, John Wiley & Sons, 267, **2012**
477. He, B. B. Two-dimensional X-ray Diffraction, John Wiley & sons NewYork, , **2011**
478. Als-Nielsen, J.; McMorrow, D. Elements of modern X-ray physics, John Wiley & Sons, **2011**
479. Fultz, B.; Howe, J. M. Transmission electron microscopy and diffractometry of materials, Springer, **2012**
480. Alem, N.; Erni, R.; Kisielowski, C.; Rossell, M. D.; Gannett, W.; Zettl, A. Atomically thin hexagonal boron nitride probed by ultrahigh-resolution transmission electron microscopy. *Physical review B* **2009**, 80, 155425.
481. Huang, P. Y.; Ruiz-Vargas, C. S.; van der Zande, A. M.; Whitney, W. S.; Levendorf, M. P.; Kevek, J. W.; Garg, S.; Alden, J. S.; Hustedt, C. J.; Zhu, Y. Grains and grain boundaries in single-layer graphene atomic patchwork quilts. *Nature* **2011**, 469, 389-392.
482. Straumal, B. B.; Mazilkin, A. A.; Baretzky, B.; Schuetz, G.; Rabkin, E.; Valiev, R. Z. Accelerated diffusion and phase transformations in Co-Cu alloys driven by the severe plastic deformation. *Materials Transactions* **2012**, 53, 63-71.
483. Jiang, W.; Atzmon, M. The effect of compression and tension on shear-band structure and nanocrystallization in amorphous Al₉₀Fe₅Gd₅: a high-resolution transmission electron microscopy study. *Acta materialia* **2003**, 51, 4095-4105.
484. Yuk, J. M.; Park, J.; Ercius, P.; Kim, K.; Hellebusch, D. J.; Crommie, M. F.; Lee, J. Y.; Zettl, A.; Alivisatos, A. P. High-resolution EM of colloidal nanocrystal growth using graphene liquid cells. *Science* **2012**, 336, 61-64.

485. Wells, O. C.; Joy, D. C. The early history and future of the SEM. *Surface and interface analysis* **2006**, 38, 1738-1742.
486. Zhou, M.; Zhai, Y.; Dong, S. Electrochemical sensing and biosensing platform based on chemically reduced graphene oxide. *Analytical Chemistry* **2009**, 81, 5603-5613.
487. Huang, J.; Li, Q.; Wang, Y.; Dong, L.; Xie, H.; Wang, J.; Xiong, C. Fluxible Nanoclusters of Fe₃O₄ Nanocrystals Embedded Polyaniline by Macromolecule-Induced Self-Assembly. *Langmuir* **2013**.
488. Zhang, K.; Zhang, L. L.; Zhao, X.; Wu, J. Graphene/polyaniline nanofiber composites as supercapacitor electrodes. *Chemistry of Materials* **2010**, 22, 1392-1401.
489. Fan, Y.; Liu, J.-H.; Yang, C.-P.; Yu, M.; Liu, P. Graphene–polyaniline composite film modified electrode for voltammetric determination of 4-aminophenol. *Sensors and Actuators B: Chemical* **2011**, 157, 669-674.
490. Al-Mashat, L.; Shin, K.; Kalantar-zadeh, K.; Plessis, J. D.; Han, S. H.; Kojima, R. W.; Kaner, R. B.; Li, D.; Gou, X.; Ippolito, S. J. Graphene/polyaniline nanocomposite for hydrogen sensing. *The Journal of Physical Chemistry C* **2010**, 114, 16168-16173.
491. Pauporte, T.; Soldo-Olivier, Y.; Faure, R. XAS study of amorphous WO₃ formation from a peroxo-tungstate solution. *The Journal of Physical Chemistry B* **2003**, 107, 8861-8867.
492. Zou, B.-X.; Liang, Y.; Liu, X.-X.; Diamond, D.; Lau, K.-T. Electrodeposition and pseudocapacitive properties of tungsten oxide/polyaniline composite. *Journal of Power Sources* **2011**, 196, 4842-4848.
493. Wang, Z.; Liu, E.; Zhao, X. Glassy carbon electrode modified by conductive polyaniline coating for determination of trace lead and cadmium ions in acetate buffer solution. *Thin Solid Films* **2011**, 519, 5285-5289.

494. Li, N.; Xiao, Y.; Xu, C.; Li, H.; Yang, X. Facile preparation of polyaniline nanoparticles via electrodeposition for supercapacitors. *International Journal of Electrochemical Science* **2013**, 8, 1181-1188.
495. Vivekanandan, J.; Mahudeswaran, A.; Vijayanand, P. Synthesis, characterization and conductivity study of polyaniline prepared by chemical oxidative and electrochemical methods. *Archives of Applied Science Research* **2011**, 3, 147-153.
496. Singh, R.; Choi, J. Biosensors development based on potential target of conducting polymers. *Sensors & Transducers Journal* **2009**, 104, 1-18.
497. Kirwan, L. J.; Fawell, P. D.; van Bronswijk, W. An in situ FTIR-ATR study of polyacrylate adsorbed onto hematite at high pH and high ionic strength. *Langmuir* **2004**, 20, 4093-4100.
498. Dórea, H. S.; Bispo, J. R.; Aragão, K. A.; Cunha, B. B.; Navickiene, S.; Alves, J. P.; Romão, L. P.; Garcia, C. A. Analysis of BTEX, PAHs and metals in the oilfield produced water in the State of Sergipe, Brazil. *Microchemical journal* **2007**, 85, 234-238.
499. García, T.; Solsona, B.; Taylor, S. H. Naphthalene total oxidation over metal oxide catalysts. *Applied Catalysis B: Environmental* **2006**, 66, 92-99.
500. Prabhukumar, G.; Pagilla, K. Polycyclic aromatic hydrocarbons in urban runoff—sources, sinks and treatment: A review. *Dep. of Civ., Archit. and Environ. Eng., Inst. of Tech: Chicago, IL* **2010**.
501. Williams, L. L.; Webster, R. D. Electrochemically controlled chemically reversible transformation of α -tocopherol (vitamin E) into its phenoxonium cation. *Journal of the American Chemical Society* **2004**, 126, 12441-12450.
502. Gilje, S.; Han, S.; Wang, M.; Wang, K. L.; Kaner, R. B. A chemical route to graphene for device applications. *Nano Letters* **2007**, 7, 3394-3398.

503. Shen, J.; Hu, Y.; Shi, M.; Lu, X.; Qin, C.; Li, C.; Ye, M. Fast and facile preparation of graphene oxide and reduced graphene oxide nanoplatelets. *Chemistry of Materials* **2009**, 21, 3514-3520.
504. Szabó, T.; Berkesi, O.; Dékány, I. DRIFT study of deuterium-exchanged graphite oxide. *Carbon* **2005**, 43, 3186-3189.
505. Park, S.; An, J.; Piner, R. D.; Jung, I.; Yang, D.; Velamakanni, A.; Nguyen, S. T.; Ruoff, R. S. Aqueous suspension and characterization of chemically modified graphene sheets. *Chemistry of Materials* **2008**, 20, 6592-6594.
506. Guo, P.; Song, H.; Chen, X. Electrochemical performance of graphene nanosheets as anode material for lithium-ion batteries. *Electrochemistry Communications* **2009**, 11, 1320-1324.
507. Pan, D.; Zhang, J.; Li, Z.; Wu, M. Hydrothermal route for cutting graphene sheets into blue luminescent graphene quantum dots. *Advanced Materials* **2010**, 22, 734-738.
508. Rao, C.; Biswas, K.; Subrahmanyam, K.; Govindaraj, A. Graphene, the new nanocarbon. *Journal of Materials Chemistry* **2009**, 19, 2457-2469.
509. Lucchese, M. M.; Stavale, F.; Ferreira, E.; Vilani, C.; Moutinho, M.; Capaz, R. B.; Achete, C.; Jorio, A. Quantifying ion-induced defects and Raman relaxation length in graphene. *Carbon* **2010**, 48, 1592-1597.
510. Ferrari, A.; Robertson, J. Interpretation of raman spectra of disordered and amorphous carbon. *Physical review B* **2000**, 61, 14095.
511. Nian, Y.-R.; Teng, H. Nitric acid modification of activated carbon electrodes for improvement of electrochemical capacitance. *Journal of the Electrochemical Society* **2002**, 149, A1008-A1014.

512. Wang, Y. G.; Li, H. Q.; Xia, Y. Y. Ordered whiskerlike polyaniline grown on the surface of mesoporous carbon and its electrochemical capacitance performance. *Advanced Materials* **2006**, 18, 2619-2623.
513. Shah, A.-u.-H. A.; Holze, R. Spectroelectrochemistry of two-layered composites of polyaniline and poly (o-aminophenol). *Electrochimica Acta* **2008**, 53, 4642-4653.
514. Bard, A. J.; Faulkner, L. R. *Electrochemical methods: fundamentals and applications*, Wiley New York, 2, **1980**
515. Iwuoha, E. I.; Mavundla, S. E.; Somerset, V. S.; Petrik, L. F.; Klink, M. J.; Sekota, M.; Bakers, P. Electrochemical and Spectroscopic Properties of Fly Ash–Polyaniline Matrix Nanorod Composites. *Microchimica Acta* **2006**, 155, 453-458.
516. Ehret, R.; Baumann, W.; Brischwein, M.; Schwinde, A.; Stegbauer, K.; Wolf, B. Monitoring of cellular behaviour by impedance measurements on interdigitated electrode structures. *Biosensors and Bioelectronics* **1997**, 12, 29-41.
517. Kang, X.; Mai, Z.; Zou, X.; Cai, P.; Mo, J. A novel glucose biosensor based on immobilization of glucose oxidase in chitosan on a glassy carbon electrode modified with gold–platinum alloy nanoparticles/multiwall carbon nanotubes. *Analytical Biochemistry* **2007**, 369, 71-79.
518. Wang, L.; Wang, E. Direct electron transfer between cytochrome *c* and a gold nanoparticles modified electrode. *Electrochemistry Communications* **2004**, 6, 49-54.
519. Piro, B.; Haccoun, J.; Pham, M. C.; Tran, L.; Rubin, A.; Perrot, H.; Gabrielli, C. Study of the DNA hybridisation transduction behavior of a quinone-containing electroactive polymer by cyclic voltammetry and electrochemical impedance spectroscopy. *Journal of Electroanalytical Chemistry* **2005**, 577, 155-165.

520. Li, J.; Xie, H.; Li, Y.; Liu, J.; Li, Z. Electrochemical properties of graphene nanosheets/polyaniline nanofibers composites as electrode for supercapacitors. *Journal of Power Sources* **2011**, 196, 10775-10781.
521. Zheming, G.; Ling, Z.; Chunzhong, L. Emulsion polymerization: a new approach to prepare graphite oxide coated with polyaniline. *Journal of Macromolecular Science*® **2009**, 48, 226-237.
522. Yin, J.; Zhao, X.; Xia, X.; Xiang, L.; Qiao, Y. Electrorheological fluids based on nanofibrous polyaniline. *Polymer* **2008**, 49, 4413-4419.
523. Subrahmanyam, K.; Vivekchand, S.; Govindaraj, A.; Rao, C. A study of graphenes prepared by different methods: characterization, properties and solubilization. *Journal of Materials Chemistry* **2008**, 18, 1517-1523.
524. Lian, P.; Zhu, X.; Liang, S.; Li, Z.; Yang, W.; Wang, H. Large reversible capacity of high quality graphene sheets as an anode material for lithium-ion batteries. *Electrochimica Acta* **2010**, 55, 3909-3914.
525. Yan, J.; Wei, T.; Shao, B.; Fan, Z.; Qian, W.; Zhang, M.; Wei, F. Preparation of a graphene nanosheet/polyaniline composite with high specific capacitance. *Carbon* **2010**, 48, 487-493.
526. Bouvrette, P.; Hrapovic, S.; Male, K. B.; Luong, J. H. Analysis of the 16 environmental protection agency priority polycyclic aromatic hydrocarbons by high performance liquid chromatography-oxidized diamond film electrodes. *Journal of Chromatography A* **2006**, 1103, 248-256.
527. Costa, J.; Sant'Ana, A.; Corio, P.; Temperini, M. Chemical analysis of polycyclic aromatic hydrocarbons by surface-enhanced raman spectroscopy. *Talanta* **2006**, 70, 1011-1016.

528. Paddon, C. A.; Banks, C. E.; Davies, I. G.; Compton, R. G. Oxidation of anthracene on platinum macro-and micro-electrodes: Sonoelectrochemical, cryoelectrochemical and sonocryoelectrochemical studies. *Ultrasonics Sonochemistry* **2006**, 13, 126-132.
529. Cordeiro, D. S.; Corio, P. Electrochemical and photocatalytic reactions of polycyclic aromatic hydrocarbons investigated by raman spectroscopy. *Journal of Brazilian Chemical Society* **2009**, 20, 80-87.
530. Mailu, S. N.; Waryo, T. T.; Ndangili, P. M.; Ngece, F. R.; Baleg, A. A.; Baker, P. G.; Iwuoha, E. I. Determination of anthracene on Ag-Au alloy nanoparticles/overoxidized-polypyrrole composite modified glassy carbon electrodes. *Sensors* **2010**, 10, 9449-9465.
531. Ghosh, U.; Gillette, J. S.; Luthy, R. G.; Zare, R. N. Microscale location, characterization, and association of polycyclic aromatic hydrocarbons on harbor sediment particles. *Environmental science & technology* **2000**, 34, 1729-1736.
532. Laska, J.; Widlarz, J. Spectroscopic and structural characterization of low molecular weight fractions of polyaniline. *Polymer* **2005**, 46, 1485-1495.
533. Basavaraja, C.; Kim, W. J.; Kim, Y. D.; Huh, D. S. Synthesis of polyaniline-gold/graphene oxide composite and microwave absorption characteristics of the composite films. *Materials Letters* **2011**, 65, 3120-3123.
534. Wei, H.; Yan, X.; Li, Y.; Gu, H.; Wu, S.; Ding, K.; Wei, S.; Guo, Z. Electrochromic poly (DNTD)/WO₃ nanocomposite films via electropolymerization. *The Journal of Physical Chemistry C* **2012**, 116, 16286-16293.
535. Díaz-Reyes, J.; Dorantes-García, V.; Pérez-Benítez, A.; Balderas-López, J. Obtaining of films of tungsten trioxide (WO₃) by resistive heating of a tungsten filament. *Superficies Vacio* **2008**, 21, 12-17.

536. Balázsi, C.; Pfeifer, J. Development of tungsten oxide hydrate phases during precipitation, room temperature ripening and hydrothermal treatment. *Solid state ionics* **2002**, 151, 353-358.
537. Gao, W.; Wu, G.; Ling, Y.; Sun, J. H₂ sensing properties of Pd modified WO₃Fe₂O₃ nanostructured composite films prepared by amorphous WFe dealloying. *Journal of Nanoscience and Nanotechnology* **2013**, 13, 1190-1193.
538. Pauporté, T.; Goux, A.; Kahn-Harari, A.; De Tacconi, N.; Chenthamarakshan, C.; Rajeshwar, K.; Lincot, D. Cathodic electrodeposition of mixed oxide thin films. *Journal of Physics and Chemistry of Solids* **2003**, 64, 1737-1742.
539. Luo, W.; Fu, X. K.; Ma, L. H. The research on the high quality TiO₂, MoO₃-doped WO₃ electrochromic film. *Chinese Chemical Letters* **2007**, 18, 883-886.
540. Gmati, F.; Fattoum, A.; Manaii, A.; Mohamed, A. B. Effects of the action of hydrogen peroxide on the electrical properties of polyaniline-aluminium composites. *Journal of Physics D: Applied Physics* **2011**, 44, 315405.
541. Piro, B.; Haccoun, J.; Pham, M.C.; Tran, L.D.; Rubin, A.; Perrot, H.; Gabrielli, C. Study of the DNA hybridisation transduction behavior of a quinone-containing electroactive polymer by cyclic voltammetry and electrochemical impedance spectroscopy. *J. Electroanal. Chem* **2005**, 577, 155.
542. Comninellis, C.; Kapalka, A.; Malato, S.; Parsons, S. A.; Poulios, I.; Mantzavinos, D. Advanced oxidation processes for water treatment: advances and trends for R&D. *Journal of Chemical Technology and Biotechnology* **2008**, 83, 769-776.
543. Pumera, M.; Ambrosi, A.; Bonanni, A.; Chng, E. L. K.; Poh, H. L. Graphene for electrochemical sensing and biosensing. *TrAC Trends in Analytical Chemistry* **2010**, 29, 954-965.



UNIVERSITY *of the*
WESTERN CAPE